2018

Robustness Enhancement of Sensory Transduction by Hair Bundles

Andrew Robert Milewski

ROBUSTNESS ENHANCEMENT OF SENSORY TRANSDUCTION BY HAIR BUNDLES

A Thesis Presented to the Faculty of
The Rockefeller University
in Partial Fulfillment of the Requirements for
the degree of Doctor of Philosophy

by
Andrew Robert Milewski
June 2018

Robustness Enhancement of Sensory Transduction by Hair Bundles

Andrew R. Milewski, Ph.D.

The Rockefeller University 2018

How do biological systems ensure robustness of function despite developmental and environmental variation? Our sense of hearing boasts exquisite sensitivity, precise frequency discrimination, and a broad dynamic range. Experiments and modeling imply, however, that the auditory system achieves this performance for only a narrow range of parameter values. Although the operation of some systems appears to require precise control over parameter values, I describe how the function of the ear might instead be made robust to parameter perturbation.

The sensory hair cells of the cochlea are physiologically vulnerable: small changes in parameter values could compromise hair cells' ability to detect stimuli. Most ears, however, remain highly sensitive despite differences in their physical properties. I propose that, rather than exerting tight control over parameters, the auditory system employs a homeostatic mechanism that increases the robustness of its operation to variation in parameter values.

To slowly adjust the response to sinusoidal stimulation, the homeostatic mechanism feeds back to its adaptation process a rectified version of the hair bundle's displacement. When homeostasis is enforced, the range of parameter values for which the sensitivity, tuning sharpness, and dynamic range exceed specified thresholds can increase by more than an order of magnitude. Certain characteristics of the hair cell's behavior might provide a means to determine through experiment whether such a mechanism operates in the auditory system. This homeostatic strategy constitutes a general principle by which many biological systems might ensure robustness of function.

To Caroline and my family.

Acknowledgments

First and foremost I would like to thank my friends and family for their their steadfast support, endless encouragement, and unwavering confidence in me. I would especially like thank to Caroline Huang for filling my days with joy, warmth, and love. Many thanks also to my big brother Chris Milewski for looking out for me all those years that we were growing up.

I am deeply indebted to Dr. Dáibhid Ó Maoiléidigh for his deep insights into dynamical systems theory, generosity with his time, thoughtful comments and suggestions, and invaluable guidance throughout my training. Many ideas presented in this thesis build on Dáibhid's work and many others were clarified through rigorous discussions with him. I greatly admire his commitment to making complicated concepts accessible and I appreciate all of his encouragement.

I owe many thanks to Dr. Joshua Salvi for teaching me everything I know about stimulating hair bundles and for sitting next to me through an uncountable number of failed experiments. Were it not for him, I would never have obtained any meaningful experimental results. Thank you also for your willingness to share advice at any time and for making the journey a little easier for MD-PhD students following closely behind you.

Thank you also to: Dr. Florian Berger for many illuminating conversations, for embarking with me on experimental adventures, and for making it a pleasure to work in our office; Brian Fabella for an unmatched technical know-how, unflappable demeanor in the face of labVIEW crises, and unsurpassed crossword puzzling skills; Beth Dougherty for keeping meticulous track of me and my affairs in the lab, for sharing exciting tales of travel adventures, and for making sure I did not leave the U.S.

without the appropriate malaria prophylaxis; Dr. Julien Azimzadeh for unparalleled kindness and for assistance in applying to grants; and to Dr. Adrian Jacobo for introducing me to the beauty of Turing patterns when I first entered the lab. Thank you also to all of the members of the Hudspeth Laboratory of Sensory Neuroscience for their all of their helpful questions and suggestions and for making for a truly enjoyable lab environment.

I am grateful to a number of mentors outside the laboratory. Thank you to Dr. John Chen for allowing this novice to join his lab, for introducing me to bench research, and for helping me start the journey toward becoming a physician scientist. Thank you to Dr. David Morin for bringing genuine enthusiasm to physics and physics education and for cultivating my passion for teaching–many of my fondest memories of my undergraduate training are working as a teaching fellow for Physics 15a and b. Thank you to Dr. Guang Li for helping me explore the wealth of questions in the biomedical sciences that require quantitative approaches, and for your seemingly endless patience. A very fond thank you to Dr. Thomas Kalman. My work with you through the Weill Cornell Center for Human Rights has been the most meaningful extracurricular activity that I have undertaken. Thank you also for always serving as model of professionalism and compassion and for your commitment to enriching your students' training.

Many thanks to the members of my Faculty Advisory Committee, Prof. Winrich Freiwald, Prof. Stanislas Leibler, and Prof. Christina Leslie, for years worth of advice in matters relating to science and to life. I wish to extend a special thank you to Dr. Andrei Kozlov for joining the committee as my external examiner and for making the long journey across the Atlantic Ocean to be present for my defense.

I have truly enjoyed my time in the Tri-Institutional MD-PhD program. Thank you to the entering class of 2012 for making the journey so much fun. Thank you to Dr. Olaf Andersen and Dr. Ruth Gotian. Their genuine commitment to ensuring their students' well-being and success drew me to the program and has supported me through each phase of the MD-PhD training. I greatly appreciate that both of these individuals are ever looking for ways to do things that ordinary people would consider impossible. Thank you also to Renee Horton and Hannah Silvast in the MD-PhD office and to Kristen Cullen, Stephanie Fernandez, Cris Rosario, and Marta Delgado in the Dean's office of The Rockefeller University for their indispensable help and for being, without exaggeration, the friendliest people on the planet.

Most importantly, I wish to express my deepest thanks to Professor A. James Hudspeth. Thank you Jim, I am so grateful to have benefited from your mentorship. You are without peer in your ability to communicate science to any audience. I was drawn to your lab after attending a lecture you gave to my medical school class; I left the room thinking "that is how I would like to speak about my work." Thank you for helping me find my scientific voice and hone my critical thinking. Thank you also for the numerous fascinating conversations on topics ranging from microtubules to manifolds, I learn something new from each of these interactions and always come away with a deepened interest thanks to your genuine curiosity in the subjects. The reach of your knowledge and the acuity of your physical intuition are staggering, if I achieve even a fraction of either I might finally feel like I know something. Finally, thank you for being a role model who epitomizes the scientist, communicator, and mentor I aspire to become. I hope that I might someday prove to be– in your words–a "tolerable colleague."

Table of Contents

List of Figures

List of Tables

List of Symbols and Abbreviations

$\forall$	for all
$\in$	is a member of
$\pm$	plus or minus
$\ll$	much, much less than
$\{\ldots\}$	indicates a vector, a point, or a set of coordinates
$\mid\ \mid$	magnitude of a complex number
$[\ ,\ )$	parameter-value range, [endpoint included, (endpoint excluded
$\|\|\ \|\|$	magnitude of a vector
$\langle\ \rangle$	inner product or time average
$\equiv$	is equivalent to, or is defined as
$\approx$	is approximately equal to
$\propto$	is proportional to
$\int\ dx$	integral
$\oint\ d\vec{r}$	line integral around a closed loop
∂	partial derivative
$\vec{\nabla}$	gradient vector, $\{\partial_{x_1}, \ldots, \partial_{x_n}\}$, $\vec{\nabla} \times \vec{U}$ is the curl of $\vec{U}$
$\mathbb{C}$	the set of all complex numbers
$\mathbb{I}$	$n \times n$ identity matrix
$\mathbb{R}$	the set of all real numbers
$\mathcal{P}$	generic property of a system
$\mathcal{R}$	areal ratio
ℓ_1	first Lyapunov coefficient
α	adaptation rate in Model I (coefficient to $\|z\|^4 z$, subcritical Hopf)
α_0	value to which α decays in Model I in the absence of homeostasis
β_α	strength of homeostasis in Model I
β_f	strength of homeostasis in Model II
γ	cubic coefficient in the Hopf normal form
δ	$Nk_BT/(Dk_{\text{gs}})$, sets the width of P_o
$\delta(\ )$	Dirac delta function
ϵ	generic exponent
ζ	quantity to determine whether a Hopf is supercritical or subcritical
θ	argument of a complex number, angular variable in polar coordinates
η	symmetric change in P_o about 1/2
λ_x	drag coefficient to the bundle's motion in Model II
λ_y	drag coefficient to the motors' motion in Model II
μ	generic bifurcation or control parameter with critical value μ_c
ν	generic exponent
ξ	generic eigenvalue
κ	multiplicative factor separating characteristic frequencies in the cochlea
Π	product
π	the constant relating a circle's diameter to its circumference
Σ	summation, surface area, $\partial\Sigma$ is a boundary curve

τ	generic timescale
τ_α	timescale of homeostatic mechanism in Model I
τ_f	timescale of homeostatic mechanism in Model II
ϕ	phase of complex number
χ	sensitivity, defined as $\lvert x\rvert/\lvert F\rvert$
χ_0	sensitivity of a linearized system
ω	frequency
$\omega_\pm$	frequency at which $\chi(\omega) = \chi(\omega_R)/\sqrt{2}$
ω_D	driving frequency
ω_R	resonant frequency
$\Delta\omega$	$\omega_+ - \omega_-$
a	channel-gating stiffness in Model I
$\vec{a}_*$	generic equilibrium point
A	$\exp([\Delta G + (k_{\mathrm{gs}}D)^2/(2N)]/k_BT)$, sets horizontal position of P_o
b	adaptation strength in Model I
c_i	generic constant coefficient
cos	cosine
$\cos^{-1}$	arccosine
Curv	curvature of a curve
D	bundle displacement effected by channel gating
det[ ]	matrix determinant
e	the natural number
f	myosin motor force in model II
f_0	value to which f decays in Model II without homeostasis
F_0	offset force or amplitude of driving force
$F(t)$	time-dependent force applied to a bundle
F_c	constant offset force
F_{SF}	force applied through a stimulus fiber
h	dilation factor
ΔG	energy difference between the closed and open states of a MET channel
i	the imaginary number
$I_{\max}$	maximum current through MET channels
$I(t)$	time-dependent current
Im	take the imaginary part
J	$n \times n$ Jacobian matrix with components $J_{i,j}$
k	$k_{\mathrm{e}} + k_{\mathrm{sp}}$
k_B	Boltzmann's constant
k_{e}	stiffness of an external load
k_{es}	stiffness of the extent spring
k_{gs}	stiffness of the gating springs
k_{sp}	stiffness of the stereociliary pivots
lim	limit
m	mass
N	number of stereocilia
MET	mechanoelectrical transduction, as in MET channel

$O(\ )$	abbreviation for terms that grow slower than those contained inside ( )
OAE	otoacoustic emission
P_o	a channel's open probability
ΔP_o^a	amount by which adaptation diminishes ΔP_o^i
ΔP_o^i	change in P_o following a displacement Δx_1
ΔP_o^f	adapted change in P_o
$p_J(\xi)$	$\det[J - \xi\mathbb{I}]$, characteristic polynomial of J
Q	quality factor, defined as $\omega_R/\Delta\omega$
r	magnitude of a complex number, radial variable in polar coordinates
Re[ ]	take the real part
s	distance from a bifurcation
S	strength of calcium-mediation inhibition of myosin motors in Model II
$\sec^{-1}$	arcsecant
sin	sine
t	time
T	temperature
$\tan^{-1}$	arctangent
Tr[ ]	matrix trace
T_k^j	$(\mathrm{Tr}[J^k])^j$
$\vec{u}$	solutions to the linearized system $\dot{\vec{u}} = J(\vec{x}_*)\vec{u}(t)$
$\vec{U}$	generic unit vector field
v	velocity of the bundle in Model II
$\vec{v}_i$	generic eigenvector
x	displacement of a hair bundle's tip along its axis of sensitivity
x_0	initial bundle position
Δx_1	initial bundle displacement
Δx_2	additional bundle displacement owing to adaptation
$\vec{x}$	vector of variables $\{x_1(t), \ldots, x_n(t)\}$ in the system $\dot{\vec{x}} = \vec{F}(\vec{x})$
y	adaptation variable in Model I, position of myosin motors in Model II
y_0	initial horizontal offset of P_o curve
y_{es}	equilibrium length of the extent spring
Δy	horizontal shift in P_o curve owing to adaptation
z	complex number $x + iy$ or $re^{i\theta}$

Variable modifications: A subscript or superscript asterisk denotes the steady-state of a variable, as in x_* or P_o^*. A diacritical dot, as in $\dot{x}$, indicates a temporal derivative, and a diacritical tilde, as in $\widetilde{x}$, indicates the variable has been Fourier transformed. A subscript R or I, as in x_R or x_I, indicates the real and imaginary parts of a variable, respectively. The subscripts H, SN, TC, and BT indicate that the variable pertains to a Hopf bifurcation, a saddle-node bifurcation, a transcritical bifurcation, and a Bogdanov-Takens bifurcation, respectively. $\vec{x}^T$ indicates the vector $\vec{x}$ is transposed. Additional variables appear in Appendix C.

Chapter 1

Hair Bundle Features Essential for Hearing

Our sense of hearing boasts precise frequency discrimination, exquisite sensitivity, and a broad dynamic range. A trained human listener can distinguish tones that differ in frequency by only 0.2 %, a difference one thirtieth of that between the pitches sounded by two neighboring keys on a piano [1]. The softest sounds that we can detect carry energies of the same magnitude as thermal fluctuations [2–5]. We can, however, also process sounds that convey a trillionfold more power [6]. Hair cells, the cells in our cochlea that translate mechanical stimuli into electrical messages, contribute significantly to each of these remarkable features. After briefly introducing how sounds are processed by the ear, this chapter discusses how the design of the hair cell's mechanosensing apparatus, the hair bundle, underlies the sensitivity, frequency selectivity, and broad dynamic range of signal detection by the ear.

1.1 Sound Processing by the Ear

Sound comprises oscillating pressure waves that alternately compress and rarefy the medium through which they propagate. The contours of the external ear direct sound waves toward the tympanic membrane situated at the end of the external auditory canal. As happens for the diaphragm of a microphone, sound waves that impinge on the tympanic membrane cause it to vibrate. By setting the malleus, incus, and stapes into motion, oscillations in the tympanic membrane are carried by the three ossicles to the oval window of the cochlea (Fig. 1.1*A*).

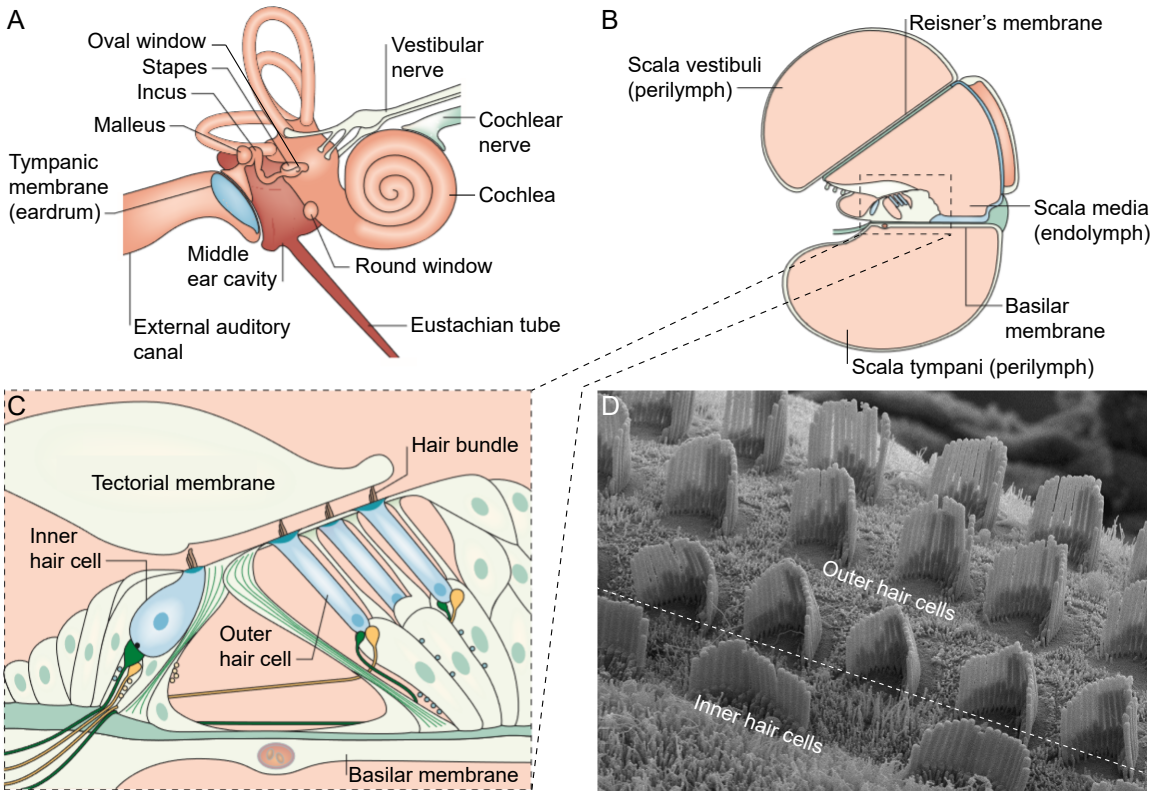

Figure 1.1: The peripheral auditory system (A) The ear is divided into three sections. The pinna and external auditory canal of the outer ear direct sounds toward the tympanic membrane. The three ossicles of the middle ear, the malleus, incus, and stapes, communicate vibrations arriving at the tympanic membrane to the oval window. The inner ear's cochlea, an organ that resembles a snail's shell, translates fluid-pressure waves generated at the oval window into electrical signals. (B) Cross section of one turn of the cochlea. The cochlea comprises three coiled tubes, called scalae, that are separated by Reisner's membrane and by the basilar membrane. The scala media is filled with endolymph, a fluid that is rich in potassium. Perilymph, which resembles the fluid that bathes most neurons, fills the scala vestibuli and scala tympani. (C) A magnified view of the scala media features the organ of Corti, the sensory epithelium that sits atop the basilar membrane and houses the hair cells. The tectorial membrane lies over top of the hair cell bundles. Cochlear hair cells come in two varieties: Inner hair cells receive the majority of afferent innervation and their bundles protrude into a groove on the basal surface of the tectorial membrane. Outer hair cells receive the majority of efferent innervation, have bundles that are physically coupled to the tectorial membrane, and outnumber inner hair cells threefold. (D) A scanning electron micrograph of the organ of Corti's apical surface reveals how the shapes of the inner and outer hair cell bundles differ. Panels $A-C$ modified from [7], panel D modified from [8].

From the Greek *kokhlías* ($\kappa o \chi \lambda \iota \alpha \varsigma$) meaning screw or snail, the cochlea is a spiral-shaped organ whose interior is partitioned by Reissner's membrane and the basilar membrane into three fluid-filled canals called scalae (Fig. 1.1*B*). The scala media contains potassium-rich endolymph and is sandwiched between the scala tympani and scala vestibuli, which are filled instead with perilymph whose composition resembles that of the fluid surrounding most neurons [7].

Within the scala media and resting on the basilar membrane resides the organ of Corti, the sensory epithelium that houses the cochlea's hair cells (Fig. 1.1*C*). There are two varieties of cells in the mammalian cochlea. Inner hair cells synapse onto several afferent neurons and receive little efferent innervation, while the converse is true of outer hair cells [9,10]. Consequently, inner hair cells primarily serve to provide sensory information to the brain and outer hair cells mainly contribute to amplifying incoming signals, as discussed below [7, 11, 12]. The shapes of their mechanosensitive organelles, the hair bundles, also differ: the bundles of inner hair cells are straight, whereas those of outer hair cells are V-shaped (Fg. 1.1*D*) [13]. Although it overlies all of the cochlear hair bundles, the tectorial membrane is physically attached only to the tips of the outer hair cell bundles, whereas the tips of the inner hair cell bundles project into a groove on the tectorial membrane's basal surface [14].

Owing to the pressure difference it generates between the scalae, periodic displacement of the oval window induces vibrations in the basilar membrane that push the hair cells alternately toward and away from the tectorial membrane. The resulting shearing motion between the tectorial and basilar membranes deflects the hair bundles in a plane that is nearly orthogonal to the motion of the hair cells' bodies (Fig. 1.2*A*). Deflection of the bundles affects the electrical state of the hair cells and this information is carried across synapses to afferent neurons and onward to the brain.

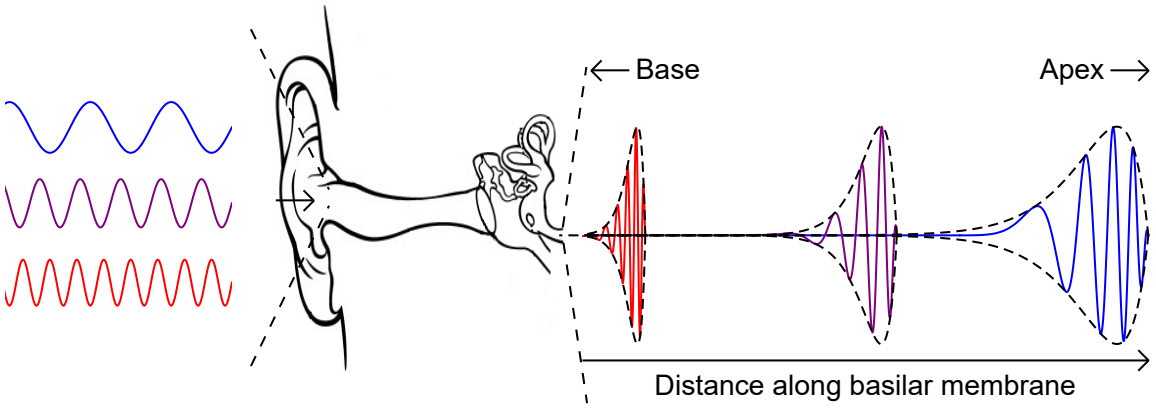

Figure 1.2: Sound processing by the ear. The tympanic membrane receives sound waves and passes these vibrations through the three ossicles to the oval window. Periodic displacement of the oval window generates a fluid pressure wave in the cochlea that induces vibrations in the basilar membrane. (A) The resulting shearing motion between the tectorial and basilar membranes leads to deflection of the hair bundles and, subsequently, effects a change in the hair cells' membrane potential. Image taken from [12]. (B) Tonotopic map indicating the locations along the basilar membrane at which the noted frequencies elicit the largest responses. Frequencies are listed in hertz, image taken from [15]. (C) Because its response to stimuli of different frequencies peaks at different locations, the basilar membrane decomposes sounds into their constitutive frequency components. Ear diagram modified from [16].

The biophysical properties of the basilar membrane, including its width and stiffness, continuously vary along its length: the basilar membrane is narrow and stiff near its base but wide and compliant at its apex [17–19]. Owing to changes in hair bundle morphology, it is likely that the preferred stimulation frequency for the hair cells sitting atop the basilar membrane also systematically decreases from the base to the apex [14, 20–22]. At a given location along the basilar membrane, the active process that is activated by hair bundle stimulation is thus designed to amplify vibrations at only a particular frequency. Together these gradients cause the basilar membrane's response to sinusoidal stimuli of a particular frequency to peak at a specific location along the membrane's length (Fig. 1.2*B*). High-frequency tones, for example, excite traveling waves that peak near the base of the basilar membrane, whereas large responses near the basilar membrane's apex are seen for low-frequency stimuli. The frequency that evokes the largest response at a particular position along the basilar membrane is termed the characteristic frequency for that location. A tonotopic map that spans the range of human hearing can thus be ascribed to the basilar membrane, whose characteristic frequency decreases monotonically from 20 kHz at the base to 20 Hz at the apex.

From Fourier analysis it is well known that any waveform can be mathematically decomposed into oscillating component functions. Because it separates sinusoids whose oscillation frequencies differ, the basilar membrane performs a spectral decomposition that is similar in spirit to a Fourier transform. A complex sound containing multiple frequency components is therefore separated into its constituent components by the basilar membrane, and the membrane's response to the complex stimulus comprises peaks at locations that correspond to the frequencies of the individual components (Fig. 1.2*C*). The hair cells whose locations coincide with the

peaks in the basilar membrane's response receive the greatest stimulation: like chords on a piano, sounds containing multiple frequency components activate multiple hair cells.

Signals propagating through the cochlea must pass through an array of frequency filters, two of which–the basilar membrane and the hair bundle–were introduced in the preceding discussion. Additional frequency selectivity is likely enforced by numerous other stages of signal processing in the peripheral auditory system, including the synaptic release of vesicles by hair cells and the subsequent response of the afferent neuron [23, 24]. Evidently the central frequencies of these filters are closely aligned: afferent neurons and the basilar membrane exhibit nearly identical frequency tuning [25]. How this alignment is orchestrated as the cochlea develops remains an open question.

Filter misalignment does not appear to impair the cochlea's frequency resolution. A simple calculation suggests, rather, that the frequency resolution of hearing in humans is limited by the number of inner hair cells. Let us assume that, as in mice, the place-frequency map of the human cochlea is logarithmic [26], which means that if two positions along the basilar membrane are separated by the same physical distance as another pair of points, then the multiplicative factor that relates the characteristic frequencies of the first two positions matches that of the second pair. For example, if the 20 Hz and 100 Hz places, whose characteristic frequencies differ fivefold, are physically separated by 5 mm, then the 100 Hz and 500 Hz places will also be 5 mm apart. Because they occur at regularly spaced intervals along the organ of Corti, the characteristic frequencies for any pair of adjacent inner hair cells will differ by the same multiplicative factor κ. Considering that human hearing ranges from 20 Hz to 20 kHz and that the cochlea contains $\sim$3,500 inner hair cells, κ is estimated by solving

$20\kappa^{3,500} = 20,000$, which yields $\kappa \approx 1.002$. This result implies that the characteristic frequencies between adjacent inner hair cells differ by 0.2 %, a number that agrees with the frequency resolution measured for trained listeners [1], and thus raises the possibility that our frequency resolution is limited by the number of inner hair cells. This simplified exercise might be inaccurate, however, if the place-frequency maps for humans is not logarithmic as is the case for some mammals [27–29].

Hair cells also reside in our vestibular organs and in the neuromasts of fishes and aquatic amphibians (Fig. 1.3). As in the cochlea, deflection of the hair bundles in these organs instigates depolarization of the hair cells and the ensuing electrical signals are communicated across synapses to afferent neurons; hair cells again translate mechanical stimuli into electrical messages. That hair cells can employ the same mechanism to relay information from diverse sensory modalities is made possible by the varied mechanical features of the organs that house these cells.

Within the utricle and sacculus, the organs that enable us to sense linear acceleration in respectively the horizontal and vertical directions, the hair bundles are physically coupled to an overlying otolithic membrane atop which sit massive calcium carbonate crystals called otoconia (Fig. 1.3A). When our heads accelerate, the inertia of the otoconia causes their motion to lag behind that of the underlying hair cells and results in deflection of the hair bundles.

Hair bundles in the semicircular canals and the neuromasts of fishes are embedded in a gelatinous cupula whose specific gravity matches that of the surrounding fluid (Fig. 1.3A, B). Fluid flow activates the hair cells in these organs by deflecting the cupula and the hair bundles contained therein. Rotational acceleration of the head generates a differential motion between the semicircular canals and the endolymph that fills them: owing to its inertia, the endolymph lags behind the semicircular canals

and consequently deflects the cupula. In fishes, fluid flow across the neuromasts may be generated by the wiggle of nearby prey or by the gulp of an imminently attacking predator [30, 31].

It is of interest to note that because the density of the cupula normally matches that of the surrounding endolymph, the cupula is neutrally buoyant and is not deflected by changing its orientation with respect to the earth's gravitational field. However, as is posited by the "buoyancy hypothesis," ingesting certain fluids, including alcohol and heavy water, can induce a temporary gradient in the specific gravity across the cupula-endolymph boundary because ingested fluids enter these compartments at different rates [32]. This disruption in neutral buoyancy allows linear accelerations to deflect the cupula and consequently to be perceived as rotational accelerations, a phenomenon familiarly known as "the spins."

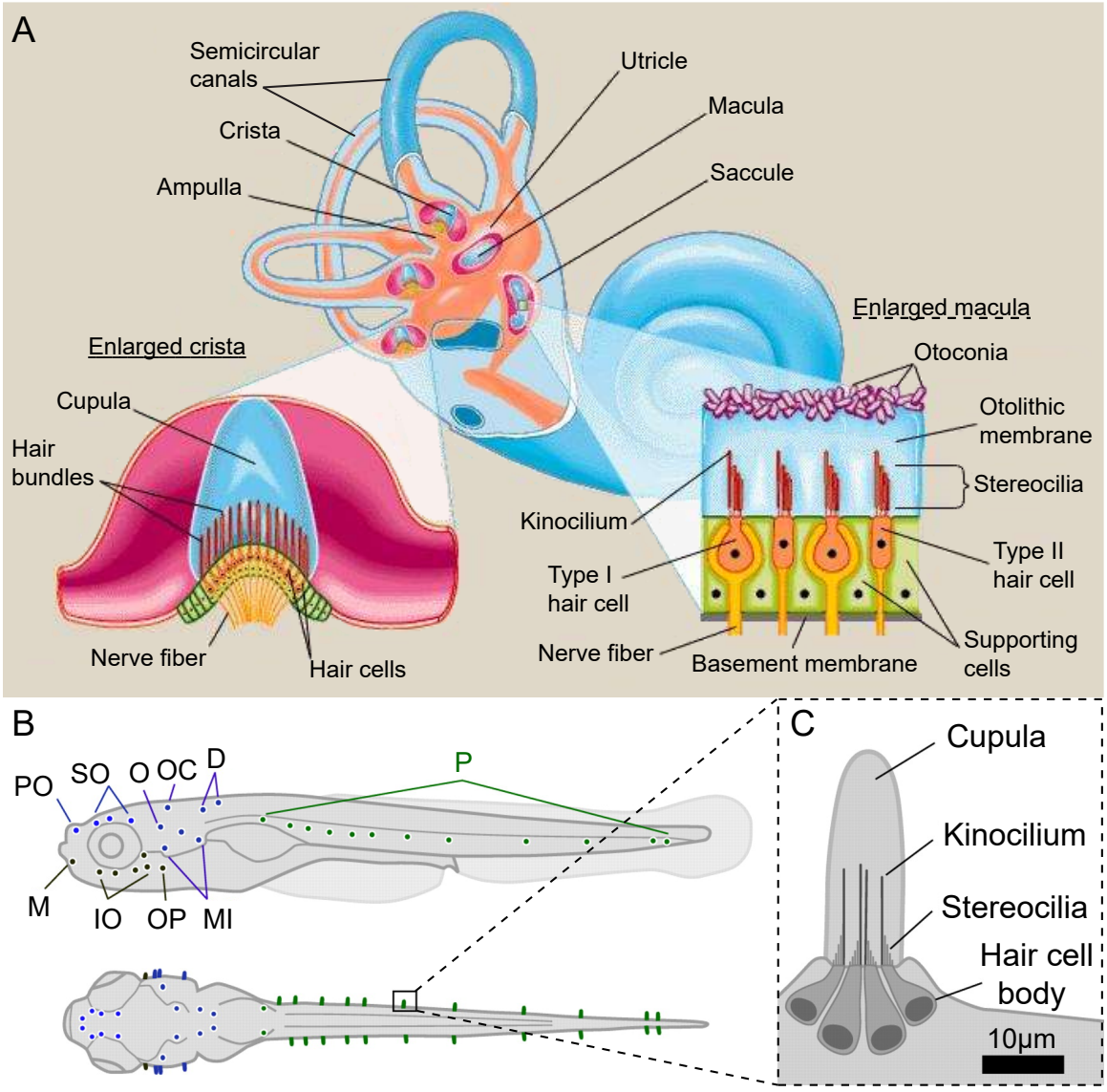

Figure 1.3: Hair cells in the vestibular system and neuromasts. (A) Hair cells residing in the semicircular canals, utricle, and sacculus are activated by the movements of overlying structures. Rotations of the head beget differential motions between the cupula and endolymph within the semicircular canals, which in turn deflect the bundles protruding into the cupula. The otolithic membrane of the utricle and sacculus is weighted down by otoconia. In response to linear accelerations of the head, the motion of the macular hair cell bodies leads that of the otolithic membrane. Because they are coupled to the underside of the otolithic membrane, this motion deflects the hair bundles. Image modified from [33]. (B) Locations of neuromasts in zebrafish larvae. (C) Like in the cristae of semicircular canals, the hair bundles in the neuromasts of fish are embedded in an overlying cupula and are thus sensitive to fluid flow. Panels B and C modified from [34].

1.2 Mechanoelectrical Transduction by Hair Cells

The hair cell derives its name from the hair bundle that protrudes from its apical surface and resembles a tuft of hairs. The hair bundle comprises a set of stereocilia organized into rows that are graded by height (Fig. 1.4*A*). Owing to the tightly packed actin filaments that fill their interiors, stereocilia approximate rigid rods. Near their bases, however, stereocilia taper and are more compliant [35]. When the hair bundle is deflected, each stereocilium pivots about its point of insertion into the hair cell's apical surface (Fig. 1.4*D*) [36].

A proteinaceous tip link runs between each stereocilium and its tallest neighbor (Figs. 1.4*B*, *C*). A dimer of protocadherin-15 embraces a parallel dimer of cadherin-23 in an 'extended handshake' to form this strand [37–41]. Several domains of the tip link embrace calcium ions and the handshake interaction becomes unstable when calcium is absent: chelation of calcium by BAPTA ruptures tip links and abolishes the hair bundle's ability to detect mechanical stimuli [41, 42].

The lower end of every tip link is coupled to two mechanoelectrical transduction (MET) channels (Fig. 1.4*E*) [43], making it likely that each of the tip link's protocadherin-15 monomers is associated with one MET channel. Because each stereocilium is constrained to rotate about a pivot, deflecting the hair bundle toward its taller edge engenders a shearing motion between neighboring stereocilia that increases the tension in every tip link. When the tension becomes great enough, the tip links pull open the MET channels (Fig. 1.4*F*). Once open, these ion channels allow potassium and calcium ions to passively diffuse down their electrochemical gradients into the stereocilia. The ensuing depolarization of the hair cell completes the transduction of a mechanical stimulus into an electrical signal.

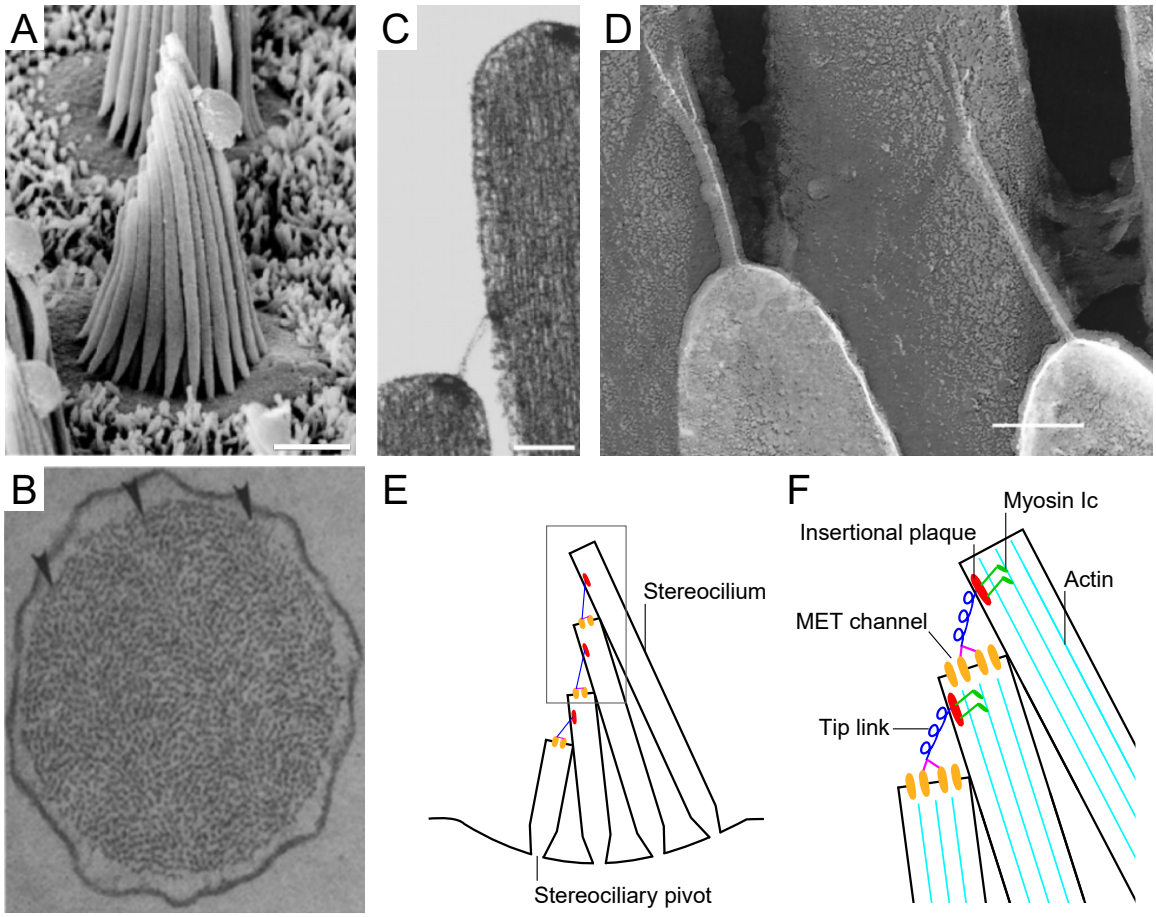

Figure 1.4: Hair bundle structure. (A) Scanning electron micrograph of a saccular hair bundle from the American bullfrog, from [44]. (B) Transmission electron micrograph of a transverse section through a stereocilium from the hair bundle of an alligator lizard's basilar papilla. Paracrystalline packing of actin filaments is seen in stereocilia rather than the hexagonal lattice that occurs in most other actin-containing tissues. Magnification $\times$ 100,000, from [35]. (C, D) Views of the tip link acquired through transmission electron microscopy (C) and freeze-etch imaging (D) [37, 44]. (E) A schematic diagram of a hair bundle illustrating the pivots about which stereocilia rotate. (F) An enlarged view of the area enclosed by the gray box in panel E provides additional details of the bundle's transduction apparatus. Each tip link runs obliquely between two neighboring stereocilia. The lower end of the tip link is somehow coupled to two mechanoelectrical transduction (MET) channels and the upper end attaches to an insertional plaque that harbors myosin motors in some species. The scale bars in panels A, C, and D represent 2 μm, 100 nm, and 100 nm, respectively.

Approximately half of the MET channels in outer hair cells and 30% in other hair cells are open when the hair bundle stands in its equilibrium position [45–47]. Deflection of the hair bundle towards its shorter edge therefore allows channels to close and leads to hyperpolarization of the hair cell. The line that runs from the shorter to the taller edge and coincides with the bundle's plane of mirror symmetry defines the axis of the hair bundle's sensitivity. Virtually no change is measured in the hair cell's membrane potential when its bundle is deflected in a direction orthogonal to this axis [48].

Mechanical deflection of a hair bundle along its axis of sensitivity adjusts the amount of current that enters the hair cell through the MET channels. By inserting a sharp electrode into the hair cell's apical surface, one can measure the incoming current while simultaneously changing the bundle's offset with a glass probe. The current-displacement relationship obtained in this fashion bears a sigmoidal shape. Dividing the ordinate by the maximum current yields the channels' open probability P_o as a function of displacement (Fig. 1.5A). P_o can be interpreted as the fraction of open MET channels or as the probability that any given MET channel is open [49].

P_o is readily fit by a first-order Boltzmann function obtained from a two-state model for channel gating [49–51] and has the form

$$P_o = \frac{1}{1 + Ae^{-(x-y)/\delta}}. \tag{1.1}$$

x is the displacement of the hair bundle's tip along its axis of sensitivity, y is an offset from the bundle's equilibrium position, A depends on the energy needed to open a single channel, and δ gives the length scale over which the channels open. $P_o = 1/2$ when $x = y + \delta \ln[A]$, and a change in P_o from $1/2 - \eta$ to $1/2 + \eta$, $\eta \in [0, 1/2)$, is effected by displacing the bundle's tip through a distance $\delta \ln[(1 + 2\eta)^2/(1 - 2\eta)^2]$.

Gating of the MET channels has important consequences for how the bundle responds to applied forces. A force-displacement relationship can be obtained under displacement-clamp conditions by measuring what forces need to be delivered through a flexible probe to command the bundle to undergo a series of defined displacements [52]. Such experiments reveal the nonlinear relationship between the applied forces and the bundle's resulting displacement (Fig. 1.5B).

Unless otherwise stated, the largest relevant displacements shift the bundle's tip from its equilibrium position by around 100 nm. Displacements of this size cause the stereocilia to rotate about their pivots by only a few degrees. In this regime small-angle approximations approximate the corresponding trigonometric functions with a high degree of accuracy. It is therefore reasonable to consider displacements of the hair bundle's tip as following a straight line rather than as describing an arc. It is also assumed that hydrodynamic coupling, top connectors, and divalent counterion interactions between stereocilia ensure that the entire bundle moves as a single unit [53–57], which allows the position of the bundle to be described by a single variable x.

Because the tension in the tip links and the rigidity of the stereociliary pivots resist changes in the hair bundle's displacement, a fiber must overcome these elastic forces to move the tip of the bundle a distance x. Invoking the small-angle approximation, the force needed to bend the stereocilia with collective pivot stiffness k_{sp} is $k_{\mathrm{sp}}x$. A similar expression, $k_{\mathrm{gs}}x$, would also apply for the tip links with collective stiffness k_{gs} ("gs" here stands for gating springs and accounts for the compliance of elements that lay in series with the tip links), except that opening a channel diminishes the stretch in the tip links. Letting D represent the displacement in the hair bundle's tip that results when all of the MET channels are open and also accounting for a possible offset

y from equilibrium, the gating-spring force becomes $k_{\mathrm{gs}}(x - y - DP_o)$. Lastly, the terms F_0 and $k_{\mathrm{e}}x$ are included to account for any external sources of constant forces or elastic loads, which may include the stimulus fiber or overlying accessory structures. The force applied through a stimulus fiber F_{SF} needed effect a displacement x can thus be represented as

$$F_{\mathrm{SF}} = (k_{\mathrm{e}} + k_{\mathrm{sp}})x + k_{\mathrm{gs}}(x - y - DP_o) + F_0. \tag{1.2}$$

To save space, I will let $k = k_{\mathrm{e}} + k_{\mathrm{sp}}$ hereafter.

The curve described by equation (1.2) accurately describes the experimentally acquired data portrayed in Figure 1.5B and possesses some important features. Owing to its nonlinear shape, the curve crosses the $F_{\mathrm{SF}} = 0$ line in three places. Consequently, this bundle possesses three equilibrium positions: if the bundle is placed in any of these positions and left exactly undisturbed, then the bundle will remain there for all time.[1] Two equilibrium positions, marked by cyan circles, are stable, whereas the central equilibrium position, marked by a red circle, is unstable.

Consider one of the stable equilibrium positions. A force must be applied in the direction that is parallel to the desired displacement to displace the bundle from one of these positions, positive forces are needed, for example to effect positive displacements. If the bundle is displaced a small amount and then released, it will return to one of these stable positions.

The situation is quite different for the unstable equilibrium position: now a negative force is required to maintain a positive displacement away from equilibrium (and vice versa), indicating that the bundle has a tendency to vacate this position. Even the tiniest kick causes the bundle to leave the unstable equilibrium position and not

[1] More generally, if a force F is applied to the bundle, then the number of equilibrium points is given by the number of times the force-displacement relation crosses the line $F_{\mathrm{SF}} = F$.

return. Because it is constantly bombarded by water molecules and subjected to thermal forces, an actual hair bundle cannot remain near the unstable equilibrium point without continually applying forces that push the bundle toward this position.

The stability of a given equilibrium point is determined by the sign of the force-displacement curve's slope at the point in question: the force-displacement curve bears a positive slope at stable equilibria and a negative slope at unstable equilibrium points.[2] The slope of the force-displacement relationship also represents the stiffness of the hair bundle (Fig. 1.5*C*). Therefore, an unstable equilibrium point can exist only if a region of negative stiffness is present in the force-displacement relation. A condition for the existence of negative stiffness, and thus for the existence of the instability, can be found as follows: Noting the useful relation $dP_o/dx = P_o(1-P_o)/\delta$, the slope of $F_{\mathrm{SF}}(x)$ is given by

$$\frac{dF_{\mathrm{SF}}}{dx} \equiv k_{\mathrm{hb}} = k - k_{\mathrm{gs}}[DP_o(1-P_o)/\delta - 1]. \tag{1.3}$$

This expression reaches its minimum value at $x = y + \delta \ln[A]$, which corresponds to $P_o = 1/2$. Because $D/4\delta > 1$, F_{SF} bears a region of negative slope only if

$$k < k_{\mathrm{gs}} \left(\frac{D}{4\delta} - 1 \right). \tag{1.4}$$

The negative stiffness region can thus be abrogated by decreasing k_{gs} or D or by increasing δ or k. These predictions accord with experimental results: rupturing the tip links, equivalent to setting $k_{\mathrm{gs}} = 0$, and blocking the MET channels with aminoglycoside antibiotics, akin to setting $P_o = 0$ [58, 59], both linearize the bundle's force-displacement relation [7, 60, 61].

[2]Because the force-displacement relation is defined as the force needed to displace the bundle and not as the force exerted by the bundle, the stated sign convention is opposite to what is normally employed.

A simple analogy helps explain how the nonlinear shape of the force-displacement relationship arises from MET-channel gating. Imagine attaching a spring to a closed door. Pulling on the spring's free end initially effects a displacement in the puller's hand that is proportional to the applied force. In other words, as is expected for a Hookean spring, there is a linear relationship between the applied force and the resulting displacement. This situation resembles that described by the rightmost part of the black curve in Figure 1.5*B*: The relationship is linear as the applied force acts to stretch or bend elastic elements in the hair bundle, namely stereociliary pivots and tip links.

Returning to our analogy, the force applied to the spring eventually becomes large enough to pull the door open. At the instant the door swings open, the tension in the spring abruptly decreases and causes the puller's hand to lurch forward. Similar events occur for the bundle in Figure 1.5*B* when the applied force is just under 7 pN. This force positions the bundle at around -13 nm, which coincides with the peak of the hump in the force-displacement relation (orange arrow's tail in Fig. 1.5*B*). Increasing the force a tiny bit more opens the MET channels and effects a sudden decrease in tip-link tension [50]. To regain force balance, the bundle abruptly jumps forward to ≈ 27 nm (orange arrow's tip in 1.5*B*) as this constitutes the only stable equilibrium position for the applied force (see footnote 1). Beyond this point the relationship is again linear: further increases in the applied force beget proportionally larger displacements by stretching the elastic elements.

The displacement in the hair bundle's position that follows gating of MET channels merits further discussion. Like a string curving a shaft of wood in a bow, the tension in the tip links provides the force needed to bend the stereocilia at their pivots [62]. Analogous to cutting the bow's string, chelating calcium ruptures tip links and

eliminates the tension they held. Without this tensile force holding them in place, the stereocilia are propelled forward by the elastic energy stored in their pivots [42]. A decrease in tip-link tension can also be realized through MET-channel gating. Only under certain conditions, however, will all the channels open at once and precipitate a large hair bundle displacement. When one channel opens the tension that was previously borne by all of the tip links must now be distributed across one fewer tip links [62]. Consequently, the tension increases in the tip links coupled to still-closed channels. If the increase in tension exceeds the threshold for MET-channel gating, then a cascade of channel openings ensues [62, 63]. If not, then the bundle does not lurch forward, but its compliance increases until half of the channels open. By making hair bundles softer over a certain range of displacements, MET-channel gating introduces into the force-displacement relation a nonlinearity, termed "gating compliance," that manifests itself as a region of shallower slope in this relation. For some bundles the nonlinearity is so extreme that the slope in the shallower region is negative, which in turn permits cooperative opening and closing of the MET channels.

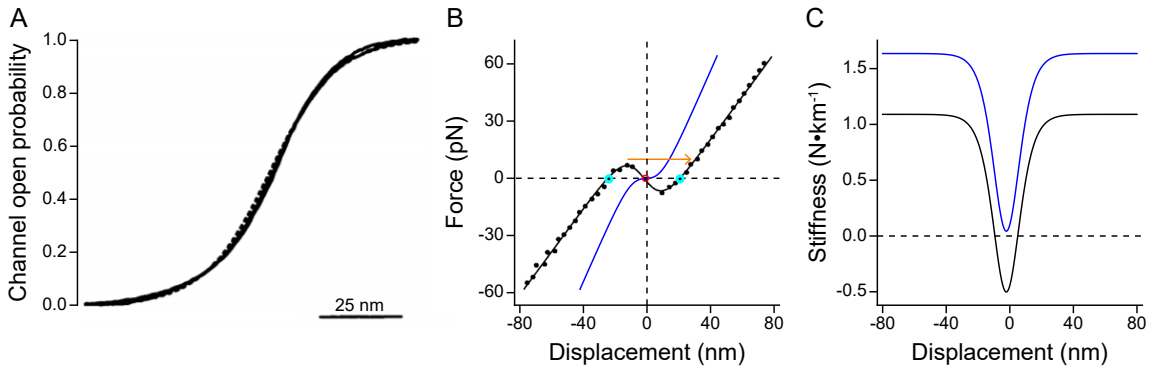

Figure 1.5: Mechanoelectrical transduction by hair cells. (A) Channel open probability as a function of hair bundle displacement. Equation (1.1) fits the data with $\delta = 3.5$ nm. Because the bundle's rest position was not given, A and y are not discernible. Image modified from [49]. (B) The force-displacement relationship measured for a spontaneously oscillating hair bundle whose motion was suppressed by coupling the bundle to a stiff fiber (black). Stable equilibria are marked by cyan circles whereas the red circle denotes an unstable equilibrium position for the black curve. Overlaid is a simulated force-displacement relation obtained by increasing k (blue) This curve does not bear a region of negative slope and contains only one stable equilibrium point (red dot). Image modified from [52]. (C) Slopes of the force-displacement relations depicted in panel B, corresponding curves are color-matched. Under certain conditions, negative hair bundle stiffness can arise from MET-channel gating. The best-fit curves in panels B and C are respectively given by equations (1.2) and (1.3) with parameter values: $A = 2 \times 10^6$, $\delta = 5.7$ nm, $y = 85$ nm, $D = 45$ nm, $k_{\text{gs}} = 816\ \mu\text{N} \cdot \text{m}^{-1}$, $k = 274\ \mu\text{N} \cdot \text{m}^{-1}$, $F_0 = 26$ pN (black), and $k = 819$ nm (blue).

Numerous facets of mechanoelectrical transduction remain unresolved: The molecular identities of the MET channels and the manner in which these proteins couple to the tip links remain unknown. The transmembrane channel-like proteins TMC1 and TMC2 are strong candidates for the pore of the channel, though additional accessory proteins are likely to be involved [64]. Investigations to determine whether the tip link behaves like a spring were being actively pursued at the time that this thesis was written–an answer seems imminent. How the MET channels are gated is also an area of active research. Rather than attributing gating entirely to the conformational change of a channel or of an attached protein gate, it has been suggested that the change in the plasma membrane deformation that follows the opening of one MET channel first encourages opening of the second MET channel and then mediates an attractive force that causes the two channels to slide toward one another [60, 65]. Critically, the latter model can account for the size of the hair bundle's displacement that follows channel gating.

1.3 Adaptation in Hair Cells

In the time immediately following the application of a mechanical force to a hair bundle, the effected displacement grows from its initial value and the inward current diminishes (Fig. 1.6) [66–71]. These changes, termed *slow* adaptation, occur concurrently and with similar time constants. Slow adaptation is mediated by myosin motors associated with the insertional plaque that is coupled to the upper end of each tip link (Fig. 1.5F). In some hair cells these motors are likely myosin Ic [72–76]. The motors' identity remains controversial in mammalian outer hair cells, in which slow adaptation is limited. Myosin VIIa has been advanced as a candidate, but this protein might rather serve as an extent spring that limits the extent of adaptation [7, 77–80].

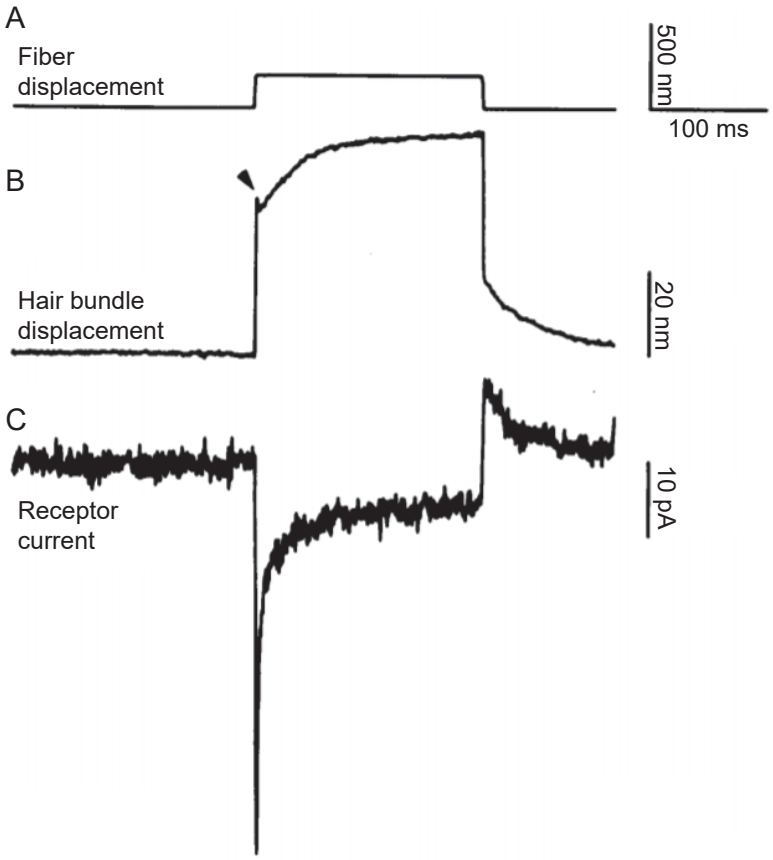

Figure 1.6: Adaptation in the bullfrog's saccular hair cell. (A) A force step was applied to the bundle through a flexible glass fiber. (B, C) At the onset of the force step, the bundle initially responded with a large displacement (B) that coincided with a large inward current (C). Adaptation in the receptor current was observed in the following few tens of milliseconds (C). The bundle's displacement simultaneously grew to a larger value. When the force step abated, the bundle rapidly moved in the negative direction but initially fell short of its rest position and the current overshot its initial value. In the time that followed, however, the current and the bundle's displacement diminished at similar rates to reach their initial values. The twitch indicated by the arrowhead in panel B is a signature of fast adaptation (reviewed in [7, 79]). Image modified from [68].

The mechanism of slow adaptation is thought to proceed as follows (Fig. 1.7). In response to a positive hair bundle deflection, the tensed tip links exert a downward pull on the insertional plaque and open MET channels that allow an influx of calcium ions. In vestibular hair cells of frogs and mammals, calcium has been found to promote slippage of the insertional plaque, likely by weakening myosin's affinity for actin [70, 81, 82]. The downward pull and incoming calcium ions thus cause the insertional plaque to slide down the stereocilia. Owing to this motion, tension in the tip links is relieved, the bundle sags farther in the positive direction, and MET channels close. The experimental correlates of this process are the concurrent shift in the hair bundle's position and adaptation in the receptor current described earlier.

Slow adaptation also operates in the reverse direction. Deflecting the hair bundle toward its shorter edge slackens the tip links and closes MET channels. Partially released from calcium's inhibitory effects, myosin motors then hydrolyze ATP to climb up the actin filaments until force balance on the insertional plaque is restored. As tension returns to the tip links, the bundle pivots farther in the negative direction and reopening MET channels mitigate the hair cell's hyperpolarization (Fig. 1.6).

By shifting the relationship between the channel open probability P_o and the bundle's displacement x (eq. 1.1), slow adaptation enables the bundle to be sensitive to farther deflection in either direction. Effecting a displacement Δx_1 in a bundle positioned at $x = x_0$ and with offset $y = y_0$ initially changes P_o by an amount

$$\Delta P_o^i = \left(1 + Ae^{-(x_0+\Delta x_1-y_0)/\delta}\right)^{-1} - \left(1 + Ae^{-(x_0-y_0)/\delta}\right)^{-1}.$$

As adaptation proceeds, the myosin motors act to change the number of open MET channels and thus effect a horizontal shift Δy in the P_o curve (Fig. 1.7B). The offset y can therefore be regarded as a dynamical variable that represents the positions of

the myosin motors. As the number of open channel changes the bundle also slides a bit farther in the direction of the initial displacement by an amount Δx_2. Some time later, the change in P_o from its unstimulated value has therefore become

$$\Delta P_o^f = \left(1 + Ae^{-(x_0+\Delta x_1+\Delta x_2-y_0-\Delta y)/\delta}\right)^{-1} - \left(1 + Ae^{-(x_0-y_0)/\delta}\right)^{-1},$$

and the amount that P_o has adapted is given by

$$\Delta P_o^a = \Delta P_o^i - \Delta P_o^f = \left(1 + Ae^{-(x_0+\Delta x_1-y_0)/\delta}\right)^{-1} - \left(1 + Ae^{-(x_0+\Delta x_1+\Delta x_2-y_0-\Delta y)/\delta}\right)^{-1}.$$

If adaptation were perfect, then $\Delta y = \Delta x_1 + \Delta x_2$, which would in turn yield $\Delta P_o^f = 0$ and $\Delta P_o^a = \Delta P_o^i$. In actual hair bundles, adaptation is incomplete, i.e. $\Delta y < \Delta x_1 + \Delta x_2$ and $\Delta P_o^f \neq 0$. Importantly, this means that a bundle is equipped to signal both transient and tonic stimuli [7].

Because $P_o \in [0, 1]$, sinusoidal stimuli, like those encountered by hair bundles in the cochlea, are rectified by the hair cell. The sigmoidal shape of the P_o curve additionally means that sinusoidal input to the hair bundle engenders asymmetric oscillations in P_o, except in the case that the bundle is initially poised in a position with exactly half of its channels open. Consequently, the time average of the periodically stimulated P_o differs from the cell's resting P_o value, a feature that might be employed by hair cells tasked with detecting the highest frequencies. Alternatively, a process termed *fast* adaptation, which effects the reclosure of MET channels on a submillisecond timescale after an abrupt stimulus, might enable hair bundle movements that are rapid enough to support high-frequency hearing [7, 79].

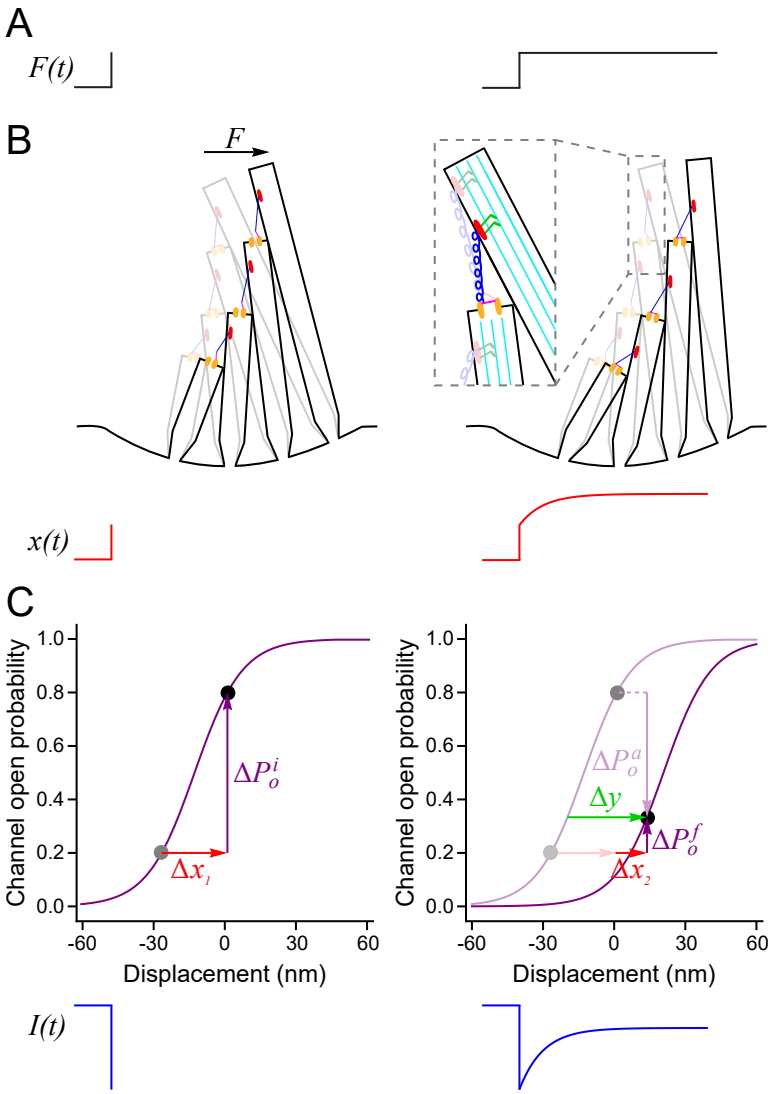

Figure 1.7: Adaptation mechanism. Applying a positive force (A, left) deflects the hair bundle toward its taller edge (B, left). By opening MET channels, this initial displacement Δx_1 changes the channels' open probability by ΔP_o^i, which is evidenced by a large inward current (C, left). During the sustained force step (A, right), the increased tip-link tension and influx of calcium ions cause myosin motors to slide down the actin filaments (B, inset). The consequent slackening of tip-link tension has two concurrent effects: 1. The bundle tilts an amount Δx_2 farther in the positive direction (B, right). 2. Owing to the reclosure of some MET channels, the open probability curve shifts rightward by Δy, which diminishes the probability by ΔP_i^a (C, right). Consequently, the inward current reaches a steady-state value equal to $I_{\max}\Delta P_o^f$. This mechanism is adaptive because it enables the bundle to be sensitive to farther positive deflections. Because $\Delta y < \Delta x_1 + \Delta x_2$, $\Delta P_o^f \neq 0$ and adaptation is incomplete.

1.4 Behavior of the Hair Bundle

Hair bundles are not merely passive receptors. Thanks to an active process, bundles amplify their responses to stimuli and exhibit a menagerie of behaviors. In addition to slow adaptation and twitches, the hair bundles of fishes [83], amphibians [61, 68, 84, 85], and reptiles [86] have been observed to oscillate spontaneously under certain conditions.

Spontaneous hair bundle oscillations arise from the interaction between gating compliance and adaptation [52, 61]. Block of MET-channel conductance by aminoglycoside antibiotics or inhibition of the myosin motors by butanedione monoxime both abolish spontaneous oscillations [61]. This evidence suggests that the motors provide the energy to drive the hair bundle's position back and forth across the instability that arises from the bundle's nonlinear force-displacement relation.

Consider a hair bundle in which the majority of MET channels have just opened in the absence of an external force, marked as position 1 in Figure 1.8*A*. This position is a stable equilibrium. By hastening the detachment of myosin motors from their actin filament targets, the ensuing influx of calcium ions activates slow adaptation. As the insertional plaque slips downward, the bundle tilts farther in the positive direction (sequence of dots proceeding from position 1 to position 2).

The previous section discussed how adaptation effects a horizontal shift Δy in the relation between displacement and channel open probability. Because it depends on P_o, the force-displacement relation also undergoes a shift as adaptation progresses. Specifically, if the bundle has most of its channels open, the curve shifts upward and to the right, as indicated by the progression of curves from blue to red.

If the extent of adaptation is great enough so that the red force-displacement relation is realized, the bundle's position becomes unstable (position 2) and the bundle

abruptly jerks in the negative direction where it comes to rest at the only remaining stable equilibrium (position 3). This rapid displacements occurs if the slippage of the insertional plaque introduces enough slack in the tip links, and does so at the correct pace, to allow most of the MET channels to reclose in rapid succession.

From position 3, slow adaptation, mediated by myosin motors climbing up the actin filaments, causes the bundle to sag farther in the negative direction toward position 4. For the appropriate rate and extent of adaptation, the tension developed in the tip links can engender a cascade of MET-channel gating, thus evoking a large positive displacement in the bundle's position. From the perspective of the force-displacement relation, this rapid movement results when stability is lost at position 4 and necessitates a leap to the only remaining stable equilibrium at position 1. By returning to position 1 the bundle has completed a full cycle and is poised to start again (Fig. 1.8*B*). In this way hair bundles can support spontaneous oscillations indefinitely (Fig. 1.8*C*).

Hair bundles have been found to exhibit a variety of periodic behaviors, including: sinusoidal oscillations, relaxation oscillations (Fig. 1.8*C*), multimodal oscillations, oscillations resembling square waves, and spiking [61, 87–90]. Pseudoperiodic and chaotic behaviors have also been reported, evidence of rich dynamics at play [91].

The characteristics of a bundle's oscillation pattern can be altered systematically by adjusting experimentally accessible parameters. Specifically, the amplitude, frequency, and morphology of bundle oscillations depend on the hair cell's membrane potential [88], the concentration of calcium [61, 87] (Fig. 1.9*A*), and the stiffness or force experienced by the bundle owing to an external load [61, 87, 89, 90] (Figs. 1.9*B*, *C*). Experiments have also confirmed theoretical predictions that spontaneous oscillations occur for only a limited range of parameter values (Fig. 1.9*D*) [51, 89, 92].

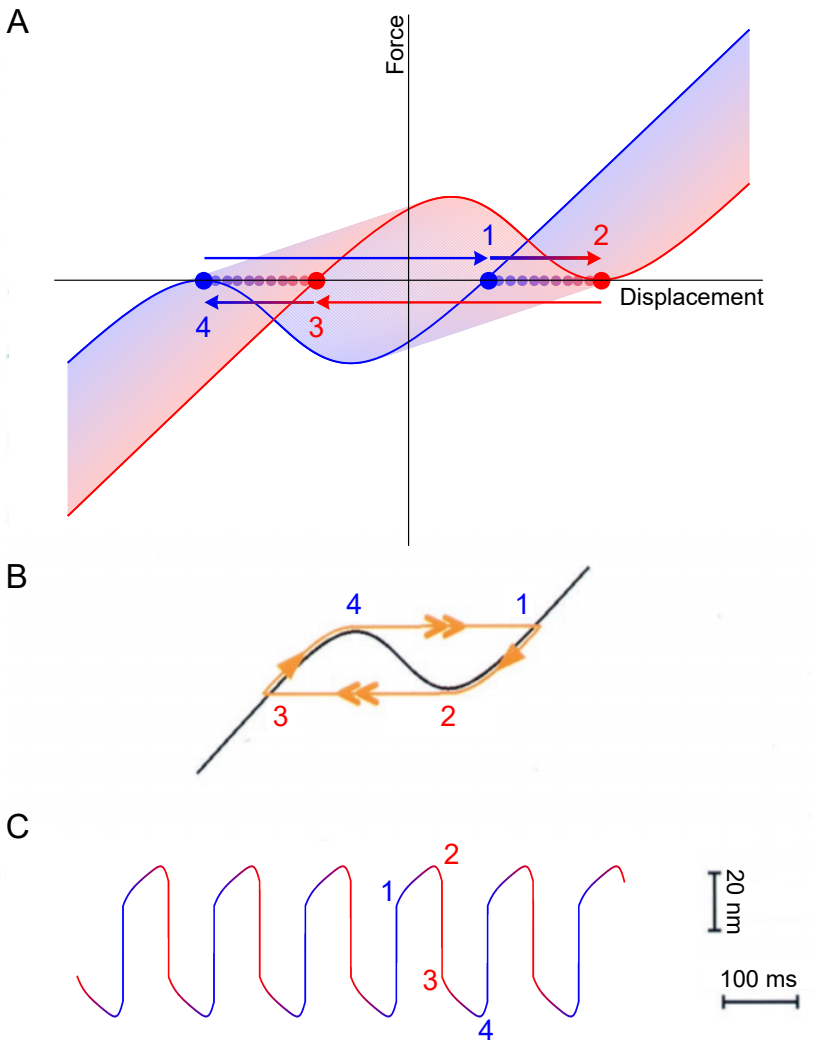

Figure 1.8: Mechanism of hair bundle oscillations. (A) The hair bundle's trajectory follows the numbered points in order, $\cdots 1 \to 2 \to 3 \to 4 \to 1 \cdots$. Slow phases of the bundle's motion occur between points 1 and 2 and between 3 and 4 as adaptation acts to shift the force-displacement relation (blue to red curve between 1 and 2 and red to blue between 3 and 4). When it reaches a maximum or minimum, the bundle's position on the force-displacement curve becomes unstable, and a rapid jerk ensues from 2 to 3 (red arrow) or from 4 to 1 (blue arrow). (B) Keeping the force-displacement curve stationary and mapping the path traced by the bundle with respect to this curve yields the orange trajectory. Double arrows denote the fast phases of the bundle's motion that result from MET-channel gating, whereas single arrows mark the slower segments that arise from slow adaptation. (C) The bundle's measured periodic motion agrees with the model and resembles relaxation oscillations. The color coding of the curve matches that of the arrows in panel A. Image adapted from [52].

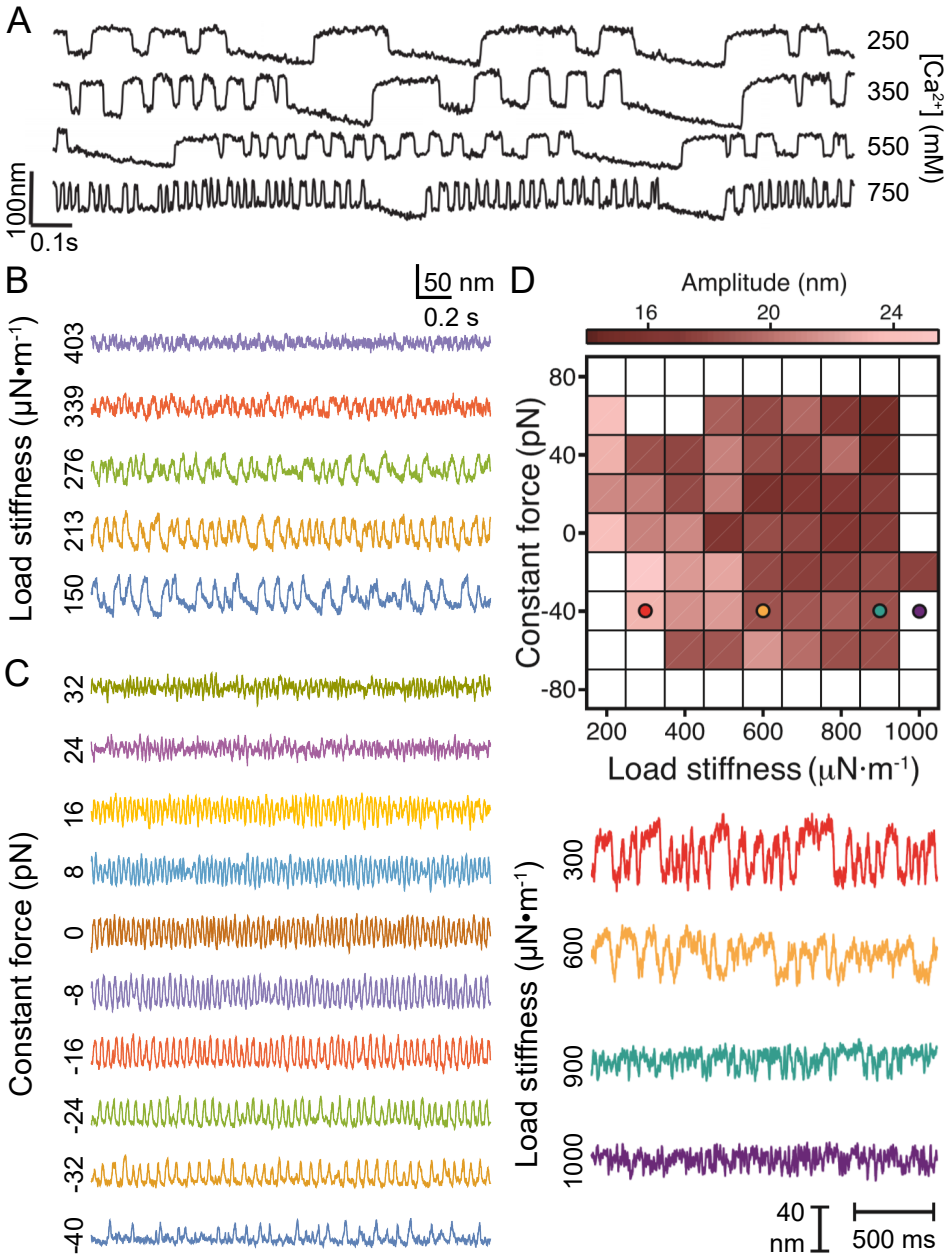

Figure 1.9: Oscillations depend on parameter values. (A) Increasing the endolymph's calcium concentration effects a decrease in amplitude and increase in frequency of the bundle's oscillations. Image modified from [87]. (B, C) Changes in amplitude and frequency are also seen as the stiffness (B) or constant force (C) of an external load is altered. The traces in panel C were obtained from a bundle that was additionally loaded with a few nanograms of tungsten. (D) Systematically adjusting an external load's force and stiffness demonstrates that spontaneous oscillations occur for only a limited range of parameter values, in agreement with theoretical predictions. Image modified from [90].

1.5 Features of Signal Detection by Hair Bundles

The impressive feats that characterize our sense of hearing are made possible by an active process that operates in the cochlea. This fact is made evident by the precipitous decline in amplification, frequency selectivity, and dynamic range that occurs as the cochlea's energy stores are depleted [93]. Without an active process the passive basilar membrane has no mechanism to overcome the viscous drag exerted by the surrounding fluid [94]. Several lines of evidence suggest that self-oscillatory elements residing in the cochlea, namely hair bundles, power the active process.

First, the ears of mammals, birds, reptiles, and amphibians have been found to emit faint sounds, termed otoacoustic emissions (OAEs), both spontaneously and after auditory stimuli [95–100]. These emissions reveal that the ears of many species are actively generating vibrations. Considering that the power needed to generate an OAE is commensurate with that produced by a few dozen hair cells, it is feasible that OAEs emanate from spontaneous bundle oscillations [85, 101]. Modeling studies also demonstrate that synchronized groups of oscillating bundles could serve as the source of the emissions [102, 103]. Somatic motility of outer hair cells, an alternating elongation and contraction of the cell's body that is thought to amplify the basilar membrane's response and is powered by voltage-dependent conformational changes in the membrane-spanning protein prestin, is not required for OAEs: emissions are measurable, though fainter, in mice lacking prestin [104–107].

Second, several parallels have been found between the basilar membrane's response to acoustic stimuli and a hair bundle's response to periodic forcing. Specifically, both amplify their responses to small-amplitude stimuli, the largest responses in both systems are evoked by applying stimuli at a particular frequency, and both employ a power-law compression that allows a thousandfold difference in stimulus amplitude to

be represented by just a tenfold change the system's response (Fig. 1.10) [108, 109].

The following chapters discuss quantitative models that explain how hair bundles attain exquisite sensitivity, precise frequency selectivity, and a broad dynamic range. A few brief qualitative comments, however, may help illuminate how these features would arise naturally in such a system. Because only a small stimulus would be required to elicit a large response, detectors poised on the brink of self-oscillation would be highly sensitive to periodic signals. If it is appropriately tuned, slow adaptation can bring the bundle to the precipice of MET-channel gating. Even a tiny force would then be sufficient to start a cascade of channel openings and elicit a large shift in the bundle's position.

The detector described above would also tend to respond strongly to signals whose periodicity is compatible with the system's preferred oscillation frequency. Like that of a driven harmonic oscillator, the bundle's preferred oscillation frequency is set by the stiffnesses of the stereociliary pivots and the gating springs, as well as by the rate at which the myosin motors drive adaptation.

Finally, the curved shape of the force-displacement relation can engender nonlinear compression in the hair bundle's response to stimuli. For the sake of simplicity, consider a bundle that lacks negative stiffness. Such a bundle will be most compliant when half of its MET channels are open. Because this position is situated at the most gradually varying part of the force-displacement relation, only weak stimuli are needed to effect large hair bundle displacements. As the size of the driving force increases, however, the bundle's displacement begins exploring the steeper parts of the force-displacement relation. Consequently, the amplitude of the bundle's response does not increase in proportion to the change in the size of the driving force.

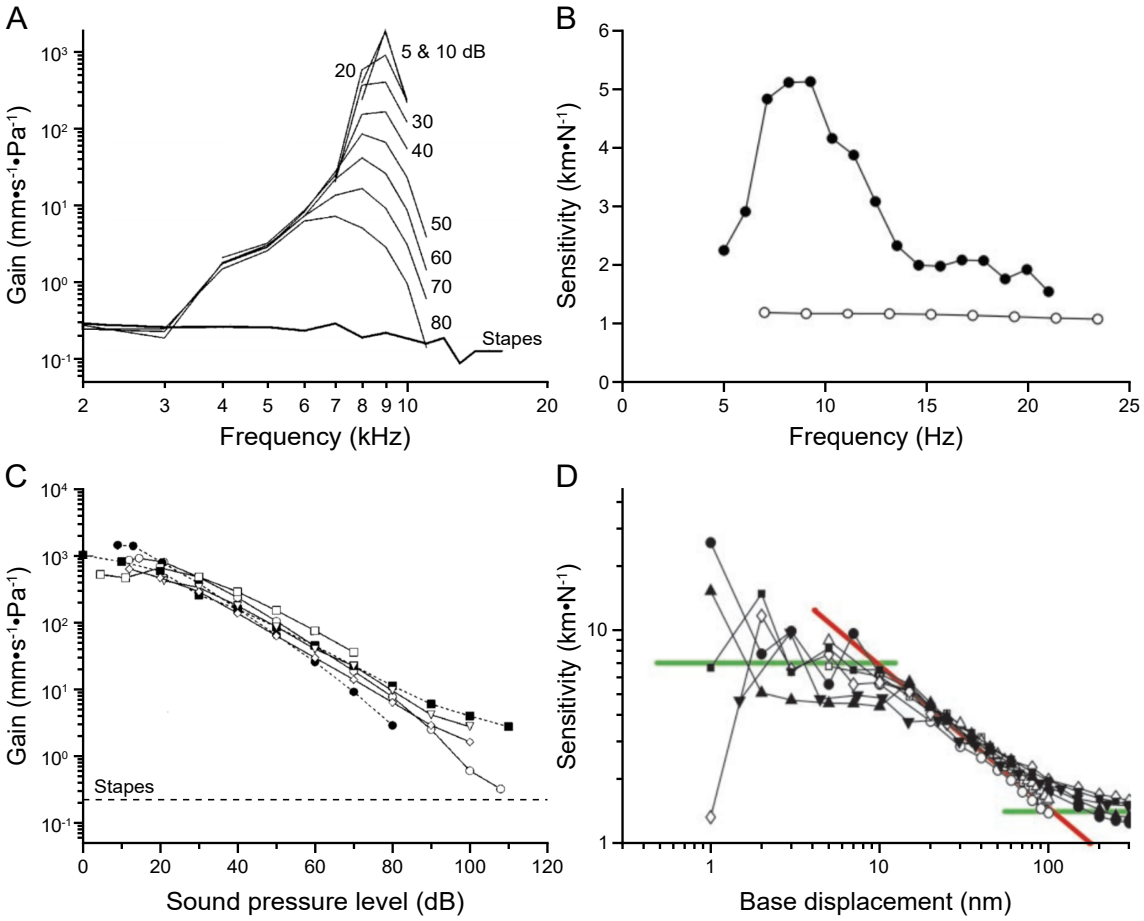

Figure 1.10: Similarities between the basilar membrane and hair bundles. (A) Gain (velocity normalized by the pressure delivered to the tympanic membrane) of the basilar membrane's response at the 9 kHz place in the cochlea of an anesthetized chinchilla. The curves show frequency selectivity, high gain around the characteristic frequency at low sound pressure levels, and much lower gain at high sound pressure levels. The labels note the sound pressure level in decibels that was employed to generate each curve. (B) An active hair bundle's sensitivity (response amplitude divided by the size of the driving force) also exhibits amplification and frequency selectivity near the bundle's natural frequency (filled circles). These features are absent in a passive bundle (open circles). Data obtained from bullfrog saccular hair bundles are shown in panels B and D. (C) Multiple examples demonstrating that the gain in the basilar membrane's response as a function of the input's amplitude exhibits nonlinear compression that follows a negative two-thirds power law. (D) The same two-thirds power law occurs in the dependence of a bundle's sensitivity on stimulus amplitude (red line), though linear regimes are also seen for very small and very large driving forces (green lines). Panels A and C modified from [108] and B and D from [109].

Chapter 2

Mathematical Preliminaries

Biological systems exhibit fantastically diverse behaviors. Describing such a system often entails formulating a system of differential equations $\dot{\vec{x}}(t) = \vec{F}(\vec{x})$ that captures how the dynamical variables $\vec{x}(t) = \{x_1(t), \ldots, x_n(t)\}$ evolve in time[1]. Tools from dynamical systems theory grant insight into the mathematical behavior of these equations and thus help illuminate phenomena observed in the physical systems they represent. This chapter introduces those tools that are essential for the analyses undertaken in later chapters. More comprehensive treatments can be found in references [110] and [111].

2.1 Equilibrium Points, Limit Cycles, Stability

If left undisturbed, a dynamical system $\vec{x}(t)$ approaches a steady-state behavior. Example behaviors include trajectories that hurtle away toward infinity and paths that remain within a bounded region of space. Which of these is possible for $\vec{x}(t)$ depends on the existence and nature of a special collection of points, curves, or manifolds. When they exist, these special points, called equilibrium points, are coordinates at which the system will reside for all time if not otherwise perturbed.

Consider the system $\dot{\vec{x}}(t) = \vec{F}(\vec{x})$, $\vec{x}(t) = \{x_1(t), \ldots, x_n(t)\}$. This expression states that the rate of change of each dynamical variable $x_i(t)$ is governed by the differential equation[2] $\dot{x}_i(t) = F_i(\vec{x})$ in which F_i is a function that can depend on time and on

[1] A diacritical dot over a variable, as in $\dot{\vec{x}}$, will be used to indicate a time derivative, i.e. $d\vec{x}/dt$, throughout this text. A variable's time dependence, i.e. $\vec{x}(t)$, will not always be stated explicitly.

[2] More generally, the F_i may also depend explicitly on time, as would be the case for systems that contain driving terms. Systems containing explicit time dependences will possess equilibrium points only if those dependences decay to zero. Explicit time dependences will therefore be considered external perturbations of the underlying autonomous system and will be treated separately.

any of the dynamical variables in the system. From this system can n-dimensional phase space can be constructed in which each dynamical variable $x_i(t)$ is assigned an axis. The time evolution of $\vec{x}(t)$ can then be represented by trajectories in this phase space.

The phase-space trajectory of a system situated at an equilibrium point is that single point. Remaining at an equilibrium point requires that all the dynamical variables are constant in time, $x_i(t) = c_i \; \forall i, t$. Consequently, the time derivatives of all the x_i must be zero, i.e. $\dot{\vec{x}}(t) = 0$. This provides a condition for locating equilibrium points: $\vec{x}_* = \{x_1^*, \ldots, x_n^*\}$ is an equilibrium point if $\vec{F}(\vec{x}_*) = 0$. Trajectories close enough in phase space may be attracted or repelled by $\vec{x}_*$. If all trajectories within some distance ϵ of $\vec{x}_*$ approach $\vec{x}_*$, then $\vec{x}_*$ is a stable equilibrium point and is unstable otherwise.

The stability of an equilibrium point can be determined through linear stability analysis. This strategy constructs a linear system of differential equations from the first-order Taylor expansions of the F_i around an equilibrium point:

$$\dot{x}_i(t) = F_i(\vec{x}) \approx F_i(\vec{x}_*) + \sum_{j=1}^{n} \left.\frac{\partial F_i(\vec{x})}{\partial x_j}\right|_{\vec{x}=\vec{x}_*} (x_j - x_j^*). \tag{2.1}$$

By definition, $\vec{F}(\vec{x}) = 0$ at an equilibrium point, so all the constant terms in Equation 2.1 vanish. Letting $J_{i,j}(\vec{x}_*) = \partial F_i(\vec{x})/\partial x_j|_{\vec{x}=\vec{x}_*}$, the approximation becomes

$$\dot{x}_i(t) \approx \sum_{j=1}^{n} J_{i,j}(\vec{x}_*)(x_j - x_j^*).$$

Identifying the $J_{i,j}(\vec{x}_*)$ with the elements of a matrix $J(\vec{x}_*)$, called the Jacobian matrix, reveals that the above equation is one component of the matrix equation

$\dot{\vec{x}}(t) \approx J(\vec{x}_*)(\vec{x}(t) - \vec{x}_*)$. Making the substitution $\vec{u}(t) = \vec{x}(t) - \vec{x}_*$ finally yields

$$\dot{\vec{u}}(t) \approx J(\vec{x}_*)\vec{u}(t). \tag{2.2}$$

The coordinate transformation effected in this last step sets the origin at $\vec{x}_*$.

Although they are approximate[3], the solutions $\vec{u}(t)$ to Equation 2.2 closely resemble the solutions of the original system of equations near the equilibrium point $\vec{x}_*$. In contrast to the original system, the solutions $\vec{u}(t)$ are readily obtained:

$$\vec{u}(t) = \sum_{i=1}^{n} c_i \vec{v}_i e^{\xi_i t}, \tag{2.3}$$

where ξ_i and $\vec{v}_i$ are the eigenvalues and eigenvectors[4] of $J(\vec{x}_*)$, and c_i are scalar constants that are determined by the initial state of the system. If $\vec{u}(0)$ is known, then c_i can be obtained by solving the system of equations $\vec{u}(0) = \sum_{i=1}^{n} c_i \vec{v}_i$. λ_i and $\vec{v}_i$ may be complex-valued. When they are real, the eigenvectors define lines through the origin along which phase-space trajectories are directly attracted to or repelled from the equilibrium point.

A condition for the stability of the equilibrium point $\vec{x}_*$ is apparent from Equation 2.3: The equilibrium point $\vec{x}_*$ is stable if and only if $\mathrm{Re}[\xi_i] < 0 \ \forall i$. When this condition is satisfied all of the exponential terms in Equation 2.3, and thus all nearby phase-space trajectories, decay to zero, the location of $\vec{x}_*$ in the linearized coordinate system, as t approaches infinity. If even one of the eigenvalues of $J(\vec{x}_*)$ has a positive real part, then there exists at least one nearby phase-space trajectory that is repelled from $\vec{x}_*$ and the equilibrium point is consequently unstable.

[3]Because the models analyzed in this dissertation contain only differentiable functions, it is assumed that all partial derivatives of the F_i exist.

[4]It is assumed that $J(\vec{x}_*)$ is diagonalizable. Solutions $\vec{u}(t)$ still exist if this assumption is violated and have the form of exponentials multiplied into polynomials of t.

Taking this analysis further in systems of two dynamical variables reveals more interesting properties. In this case the Jacobian matrix is 2×2 and analytical expressions can be found for ξ_i by identifying the roots of J's characteristic polynomial $p_J(\xi)$:

$$p_J(\xi) = \det[J - \xi \mathbb{I}_2] = \xi^2 - (J_{1,1} + J_{2,2})\xi + (J_{1,1}J_{2,2} - J_{1,2}J_{2,1}). \tag{2.4}$$

$\mathbb{I}_2$ is the 2×2 identity matrix. The constant coefficients in Equation 2.4 are well-known properties of a 2×2 matrix: $J_{1,1}+J_{2,2} = \mathrm{Tr}[J]$, the trace of J, and $(J_{1,1}J_{2,2}-J_{1,2}J_{2,1}) = \det[J]$, the determinant of J. These matrix properties can also be expressed in terms of the eigenvalues of the matrix:

$$\mathrm{Tr}[J_{n\times n}] = \sum_{i=1}^{n} \xi_i, \qquad \det[J_{n\times n}] = \prod_{i=1}^{n} \xi_i.$$

The two eigenvalues $\xi_{1,2}$ of J are then given by finding the roots of $p_J(\xi) = \xi^2 - \mathrm{Tr}[J]\xi + \det[J]$:

$$\xi_{1,2} = \frac{1}{2}\left(\mathrm{Tr}[J] \pm \sqrt{(\mathrm{Tr}[J])^2 - 4\det[J]}\right). \tag{2.5}$$

From Equation 2.5 it is evident that if $\mathrm{Tr}[J] > 0$ then $\mathrm{Re}[\xi_i] > 0$ for at least one eigenvalue. Specifically, the real parts of both eigenvalues are positive if additionally $\det[J] > 0$, whereas only one eigenvalue has a positive real part if $\det[J] < 0$. and in either case the equilibrium point is unstable. Similarly, if $\mathrm{Tr}[J] < 0$ and $\det[J] < 0$, then one eigenvalue has $\mathrm{Re}[\xi_i] > 0$ and $\vec{x}_*$ is again an unstable equilibrium point. Thus, $\vec{x}_*$ is a stable equilibrium point only if $\mathrm{Tr}[J] < 0$ and $\det[J] > 0$.

Equation 2.5 also reveals that complex-valued eigenvalues occur when $\det[J] > 4(\mathrm{Tr}[J])^2$, i.e. $\xi_{1,2} = \xi_R \pm i\xi_I$. In this case, the eigenvectors must have the form $\vec{v}_{1,2} = \vec{v}_R \pm i\vec{v}_I$ and the constants determined by initial conditions are $c_{1,2} = c_R \pm ic_I = |c|e^{\pm i\phi_c}$. Substituting the complex eigenvalues, eigenvectors, and constants into

Equation 2.3 yields phase-space trajectories that spiral inward or outward depending on the sign of ξ_R:

$$\vec{u}(t) = 2|c|e^{\xi_R t}\left[\vec{v}_R \cos(\xi_I t + \phi_c) - \vec{v}_I \sin(\xi_I t + \phi_c)\right]. \tag{2.6}$$

Two borderline cases merit mention. If $\mathrm{Tr}[J] = 0$ and $\det[J] > 0$, then $\xi_{1,2} = \pm i\xi_I$ and the system describes closed orbits (circles or ellipses) in phase space. Because they are neutrally stable, nearby trajectories are neither attracted nor repelled by the orbits and the origin: if perturbed away from an orbit, the system simply assumes a new orbit. The second borderline case occurs when $\det[J] = 0$. In this case one eigenvalue is zero and a continuous series of equilibrium points occur along a line passing through the origin that is parallel to the eigenvector associated with the zero eigenvalue. The equilibrium points are stable if the nonzero eigenvalue is negative and unstable otherwise. Figure 2.1 summarizes the possible behaviors of a system of two linear differential equations.

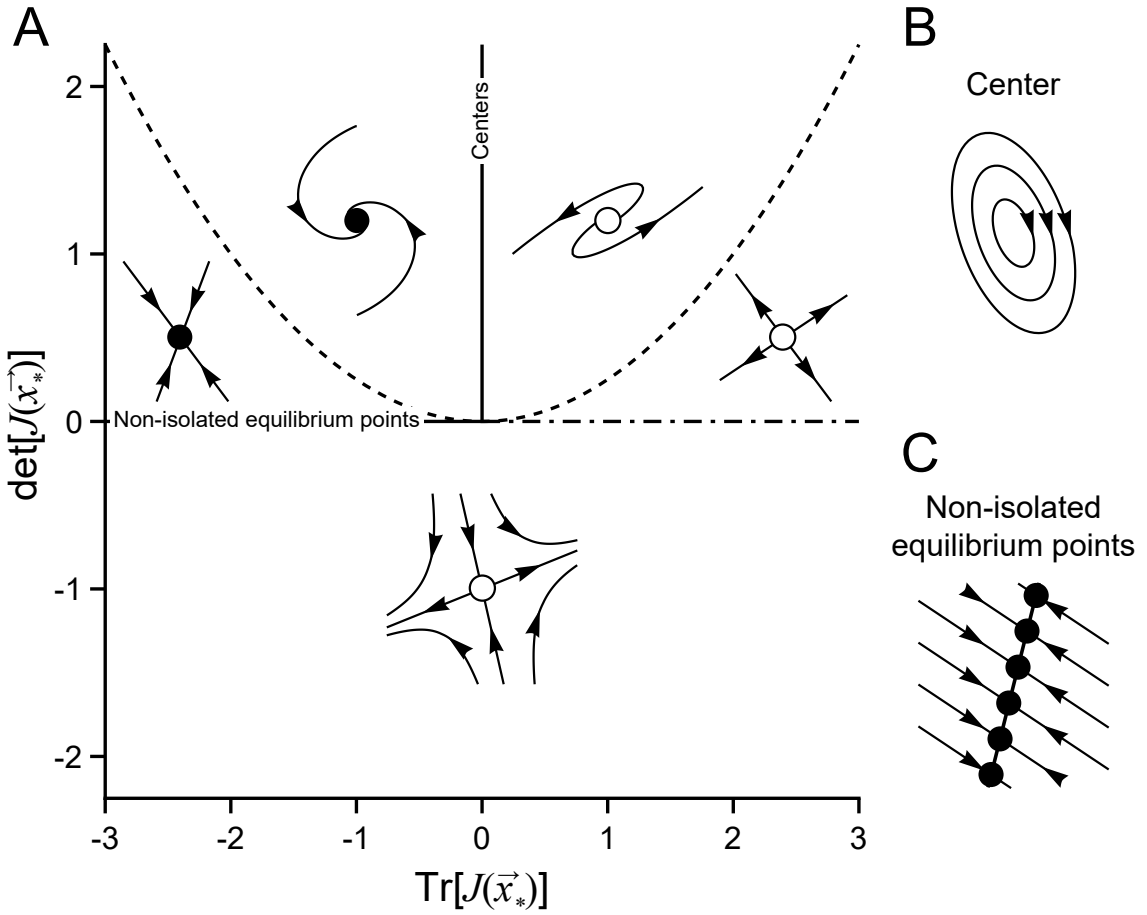

Figure 2.1: Characterization of linear systems of differential equations. (A) Systems of two linear differential equations can be completely characterized by two parameters, the trace and the determinant of the system's Jacobian matrix. This analysis also applies near equilibrium points $\vec{x}_*$ of nonlinear systems. The diagrams in each region of the figure portray phase portraits in which the trajectories of a few example solutions are shown. Only a few behaviors are possible. The equilibrium point $\vec{x}_*$ is stable if $\mathrm{Tr}[J(\vec{x}_*)] < 0$ and $\det[J(\vec{x}_*)] > 0$. $\vec{x}_*$ is otherwise unstable, except at the borderline case $\det[J(\vec{x}_*)] = 0$ and $\mathrm{Tr}[J(\vec{x}_*)] < 0$ for which a line of stable equilibrium points is seen (C). Spirals occur if $\det[J(\vec{x}_*)] > (\mathrm{Tr}[J(\vec{x}_*)])^2/4$ (dashed curve), and they are inward if $\mathrm{Tr}[J(\vec{x}_*)] < 0$ and outward if $\mathrm{Tr}[J(\vec{x}_*)] > 0$. Neutrally attracting closed orbits (ellipses) occur in this region if $\mathrm{Tr}[J(\vec{x}_*)] = 0$ (B). Lines of unstable equilibrium points occur when $\det[J(\vec{x}_*)] = 0$ and $\mathrm{Tr}[J(\vec{x}_*)] > 0$ (double-dashed line). The phase portrait for this phenomenon resembles that depicted in panel C except that all of the equilibrium points repel nearby trajectories.

In nonlinear systems, additional phenomena exist that cannot be characterized by linear stability analysis. Because trajectories in phase space cannot cross, only one additional behavior exists in systems of two differential equations: limit cycles are closed loops in phase space that attract all nearby trajectories (stable) or repel at least some trajectories (unstable). The following equations constitute one of the simplest systems in which a limit cycle occurs:

$$\begin{aligned} \dot{x} &= \mu x - \omega_0 y - \gamma x(x^2 + y^2) \\ \dot{y} &= \omega_0 x + \mu y - \gamma y(x^2 + y^2). \end{aligned} \tag{2.7}$$

Expressing equations 2.7 in a different form aids in locating the limit cycle. Multiplying the $\dot{y}$ equation by i and adding it to the $\dot{x}$ equation yields

$$\dot{x} + i\dot{y} = (\mu + i\omega_0)(x + iy) - \gamma(x + iy)(x^2 + y^2).$$

Letting $z = x + iy$ simplifies the expression:

$$\dot{z} = (\mu + i\omega_0)z - \gamma|z|^2 z. \tag{2.8}$$

If a circular limit cycle exists, then the ansatz solution $z(t) = r(t)e^{i\theta(t)}$ will satisfy Equation 2.8:

$$\dot{r}\cancel{e^{i\theta}} + ir\dot{\theta}\cancel{e^{i\theta}} = (\mu + i\omega_0)r\cancel{e^{i\theta}} - \gamma r^3\cancel{e^{i\theta}}.$$

Canceling the exponents on both sides and satisfying the real and imaginary parts of the equation separately leads to

$$\begin{aligned} \dot{r} &= \mu r - \gamma r^3 \\ \dot{\theta} &= \omega_0. \end{aligned} \tag{2.9}$$

Switching to polar coordinates succeeded in uncoupling the system of differential equations. The $\dot{\theta}$ equation is solved by $\theta(t) = \omega_0 t + \theta_0$. The $\dot{r}$ equation has two

equilibrium solutions, $r = 0$ and $r = \sqrt{\mu/\gamma}$. Assuming $\gamma > 0$ and $\mu > 0$, the system possesses a limit cycle given by $z_*(t) = \sqrt{\mu/\gamma}e^{i(\omega_0 t+\theta_0)}$. The steady-state solution $z_*(t)$ represents a phase-space trajectory that rotates clockwise around the origin at a constant angular velocity ω_0 and at a constant radius $\sqrt{\mu/\gamma}$. A limit cycle thus arises from the cubic term in the $\dot{r}$ equatio: limit cycles are an entirely nonlinear phenomenon and cannot occur in systems of linear differential equations.

Because $\dot{r} > 0$ when $0 < r < \sqrt{\mu/\gamma}$ and $\dot{r} < 0$ when $r > \sqrt{\mu/\gamma}$, the limit cycle is stable. Letting $\mu = \gamma = 1$ and $r(0) = r_0$, the full solution to Equation 2.9 is given by

$$z(t) = r(t)e^{i\theta(t)} = \frac{e^{(1+i\omega_0)t}}{\sqrt{e^{2t} + r_0^{-2} - 1}}. \tag{2.10}$$

If $r_0 = 0$ then $z(t) = 0$, if $r_0 = 1$ then $z(t) = e^{i\omega_0 t}$, and if r_0 is any other value then $z(t)$ spirals toward the limit cycle, i.e. $\lim_{t\to\infty} z(t) = e^{i\omega_0 t}$ (Fig. 2.2*A*).

Negating the right-hand sides of equations 2.7 produces a system with an unstable limit cycle. In polar coordinates this system is described by $\dot{r} = -\mu r + \gamma r^3$ and $\dot{\theta} = -\omega_0$. Because $\dot{r} < 0$ when $0 < r < \sqrt{\mu/\gamma}$ and $\dot{r} > 0$ when $r > \sqrt{\mu/\gamma}$, the limit cycle $z(t) = \sqrt{\mu/\gamma}e^{-\omega_0 t}$ repels nearby trajectories and is thus unstable (Fig. 2.2*B*). Letting $\mu = \gamma = 1$ and $r(0) = r_0$, solutions to this system are given by

$$z(t) = e^{i\omega_0 t}\left[1 + \left(r_0^{-2} - 1\right)e^{2t}\right]^{-1/2}.$$

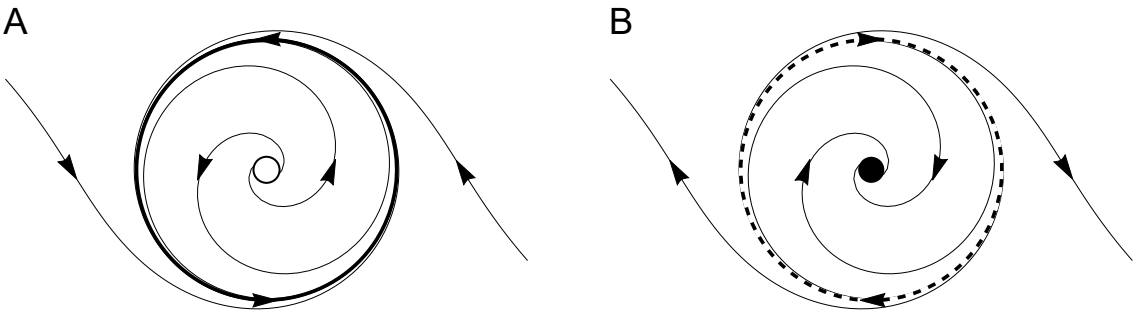

Figure 2.2: Limit cycles. (A) Phase portrait for a stable limit cycle (thick circle). Trajectories inside and outside the closed path spiral toward the limit cycle. The trajectories inside the limit cycle are also repelled by an unstable equilibrium point. (B) In contrast, nearby trajectories are repelled by an unstable limit cycle (dashed circle). The trajectories inside the cycle are additionally attracted to a stable equilibrium point. An unstable limit cycle might also repel trajectories within its bounds, but attract trajectories that are outside the closed path, or vice versa. A system may possess multiple limit cycles. For instance, the system $\dot{r} = r(r-1)(r-2)(r-3)(r-4)$ $\dot{\theta} = \omega_0$ contains nested limit cycles of alternating stability at $r = 1, 2, 3$, and 4. Of course, limit cycles need not be nested.

The limit cycles discussed above are among the simplest: limit cycles need not be centered around the origin and can trace close paths with highly irregular shapes. It is thus often necessary to resort to numerical simulations to characterize limit cycles. Determining whether a system possesses limit cycles can also be a nontrivial endeavor. Subsequent sections of this chapter discuss analytical tools that are devoted to this task.

This section closes with a brief discussion of phenomena that can occur in systems of three or more dynamical variables. Because trajectories in three-dimensional (and higher) phase spaces have room to spread out, multimodal limit cycles and chaos can occur. The Rössler system, which contains only a single nonlinearity, provides one of the simplest systems that supports these phenomena [112]:

$$\begin{aligned} \dot{x} &= -y - z \\ \dot{y} &= x + ay \\ \dot{z} &= b + z(x - c). \end{aligned} \tag{2.11}$$

For $a = b = 0.2$ and $c = 4$ the system exhibits autonomous multimodal oscillations (Fig. $2.3A, C$). Changing c to 5 evokes an aperiodic behavior termed chaos (Fig. $2.3B, D$). In both phenomena phase-space trajectories are pulled toward attractors whose topologies are more complicated than those possible in systems of two dynamical variables. Multimodal oscillations arise from closed-loop limit cycles that have at least one twist. Trajectories in a chaotic system are pulled toward a strange attractor: a fractal embedded in a folded manifold that occupies a bounded volume of phase space.

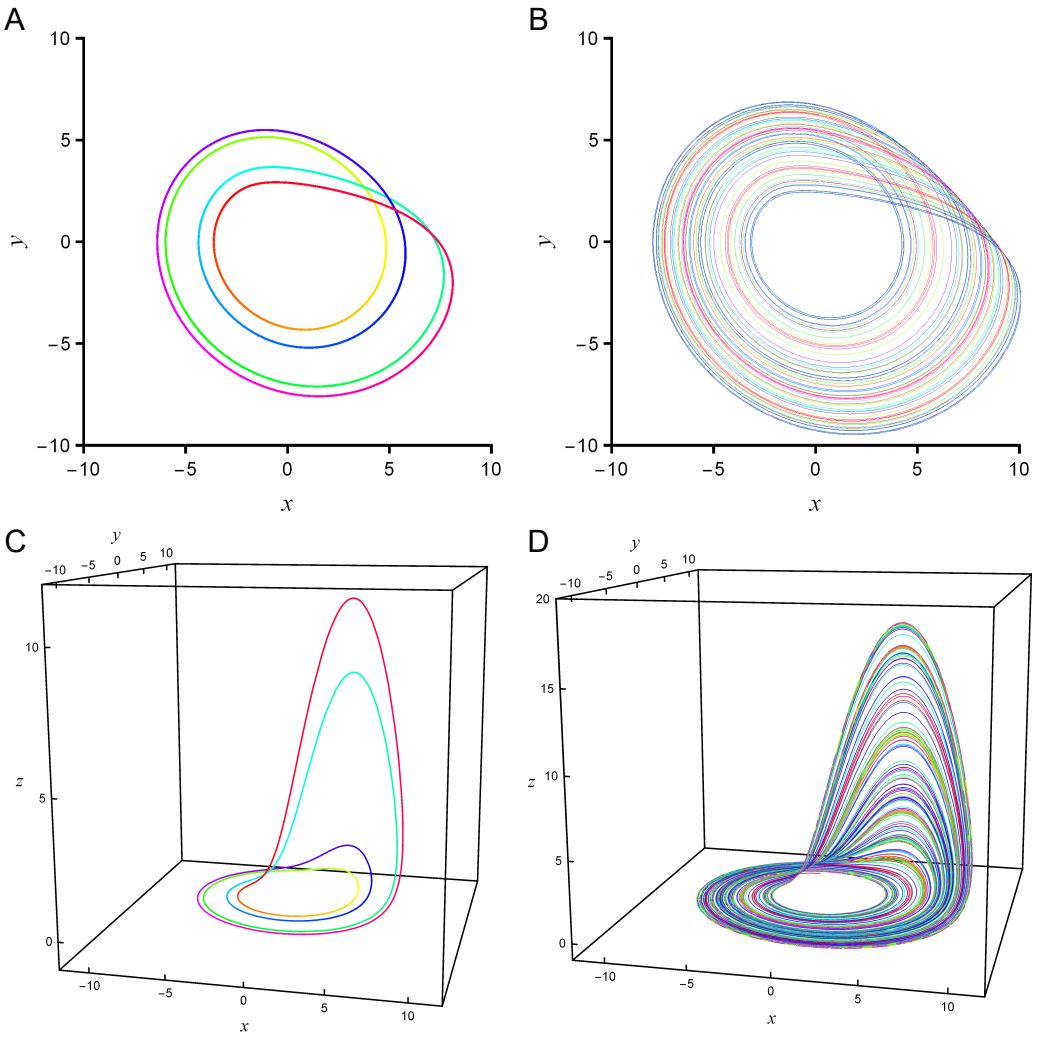

Figure 2.3: More complicated attractors. (A, B) Phase-space trajectories projected onto the xy-plane for the Rössler system when $a = b = 0.2$ and $c = 4$ (A) or $c = 5$ (B). Because phase-space trajectories cannot intersect, the crossings indicate that the system cannot be fully described by two dynamical variables. Panel A depicts a multimodal oscillation: the system traces a path that makes four loops before repeating itself. Aperiod or chaotic behavior is portrayed in panel B. The trajectory remains within a bounded region but never repeats itself. (C, D) In the full phase space it is apparent how the trajectories shown in panels A and B can avoid self-crossings. The attractor in panel C is a closed loop that has been twisted a few times. Panel D depicts a strange attractor. The fractal nature of this attractor can be appreciated by cutting perpendicularly through the trajectory: If the system is allowed to evolve forever, then the phase-space trajectory eventually crosses this cut an infinite number of times and an infinite number of crossings occurs between every pair of crossings. Because phase-space trajectories can never touch, the set of crossing points cannot be continuous.

2.2 Bifurcations

Many systems of differential equations depend on adjustable parameters. If smoothly changing a parameter μ effects an abrupt change in the system's qualitative behavior at some particular value μ_c, then the system is said to undergo a bifurcation. In such a system, μ is called a bifurcation parameter and μ_c, the value of μ at which the bifurcation occurs, is termed the critical value of μ.

A phase portrait depicts representative solutions to a system of differential equations in phase space. The topologies of the phase portraits on either side of a bifurcation are inequivalent: passing μ through its critical value causes a topological change in the system's phase portrait that alters the system's qualitative behavior. Topological changes that constitute bifurcations include switching the stability of an equilibrium point or limit cycle, altering the number of equilibrium points or limit cycles, converting a limit cycle into an aperiodic attractor, and a number of other, more exotic transitions. This section discusses several bifurcations that arise in the hair bundle models that are introduced in Chapter 4.

Consider the following system of differential equations

$$\begin{aligned} \dot{x} &= \mu + x^2 \\ \dot{y} &= -y. \end{aligned} \tag{2.12}$$

Equations 2.12 have equilibrium points at $\vec{x}_* = \{\pm\sqrt{\text{-}\mu}, 0\}$. These equilibrium points exist only if $\mu < 0$. Assuming this is true, the Jacobian at $\vec{x}_*$ is

$$J(\{\pm\sqrt{\text{-}\mu}, 0\}) = \begin{bmatrix} \pm\sqrt{\text{-}\mu} & 0 \\ 0 & \text{-1} \end{bmatrix}. \tag{2.13}$$

Because this is a diagonal matrix, the eigenvalues of J can be read off its diagonal entries: $\xi_{1,2} = \{\pm\sqrt{\text{-}\mu}, \text{-1}\}$. Thus, the equilibrium point at $\vec{x}_* = \{-\sqrt{\text{-}\mu}, 0\}$ is stable,

whereas $\vec{x}_* = \{\sqrt{\text{-}\mu}, 0\}$ marks an unstable equilibrium point. As μ is increased from a negative value toward zero the two equilibrium points get closer in phase space. Exactly at $\mu = 0$ the two equilibrium points coalesce into a saddle node, so called because the trajectories on one side of the point are attracted to the saddle node and those on the other side are repelled. If μ becomes even the slightest bit positive, the equilibrium points vanish entirely. In summary, as the bifurcation parameter μ is adjusted from negative to positive, the stable and unstable equilibrium points collide (when μ takes on its critical value $\mu_c = 0$) and annihilate. Viewed in reverse, as μ is decreased from a positive value, two equilibrium points suddenly pop into existence when the system crosses the saddle-node bifurcation.

Another way to see how changing μ precipitates the saddle-node bifurcation is to graphically visualize the $\dot{x}$ equation. This parabola has real roots, corresponding to two equilibrium points, when $\mu < 0$. Increasing the value of μ effects a vertical shift of the parabola in the positive direction. When $\mu = 0$ the function has a single root, and when $\mu > 0$ the function no longer has any real roots. Figure 2.4*A* shows these changes together with representative phase portraits for each value of μ and a bifurcation diagram that provides a convenient shorthand for conveying all this information.

Equations 2.12 constitute the normal form for the saddle-node bifurcation. Saddle-node bifurcations can occur in other systems. However, in the vicinity of a saddle node, these other systems will closely resemble the saddle-node normal form when their respective bifurcation parameters are nearly critical. More precisely, the topologies (i.e. phase portraits) of all saddle nodes are equivalent. Exactly at a saddle-node bifurcation, the system reduces to the saddle-node normal form, which represents the simplest system that permits a saddle-node bifurcation.

An example of a saddle-node bifurcation was seen in Chapter 1: Slow adaptation shifts the hair bundle's force-displacement relation, which can cause an unstable equilibrium position to collide with and annihilate a stable position (Fig. 1.8). For simplicity, consider adaptation in the positive direction, which shifts the relation upward. In the force-displacement relation (Eq. 1.2), a local minimum occurs at

$$x_{\min} = y + \delta \ln\left[\frac{Ak_{\mathrm{gs}}D(1+\eta)}{2\delta(k+k_{\mathrm{gs}})} - A\right], \qquad \eta = \sqrt{1 - \frac{4\delta(k+k_{\mathrm{gs}})}{k_{\mathrm{gs}}D}}.$$

The well surrounding this minimum constitutes the relevant part of the curve: This region is bounded on the left by an unstable equilibrium point and on the right by an equilibrium point that is stable. This part of the relation resembles a parabola. Taylor expansion of the function around $x_{\min}$ to second order yields

$$F_{\mathrm{SF}}(x) \approx F_0 + ky + \frac{k_{\mathrm{gs}}D}{2}(1+\eta) + \delta(k+k_{\mathrm{gs}}) \ln\left[\frac{Ak_{\mathrm{gs}}D(1+\eta)}{2\delta(k+k_{\mathrm{gs}})} - A\right] + \frac{k+k_{\mathrm{gs}}}{2\delta}\eta(x-x_{\min})^2.$$

Restricting x to values that lie near $x_{\min}$ renders higher-order terms negligible. Collecting constants gives the more wieldy expression

$$F_{\mathrm{SF}}(x) \approx ky + F_0 - C_0 + C_2(x - x_{\min})^2.$$

Close to the bifurcation, the locations of the equilibrium points are given by

$$x_* \approx x_{\min} \pm \sqrt{\frac{C_0 - ky - F_0}{C_2}}.$$

From this expression it is apparent that two equilibrium points vanish at $y = (C_0 - F_0)/k$ or at $F_0 = C_0 - ky$, confirming that slow adaptation or applying the appropriate external force coaxes the system across a saddle-node bifurcation.

The saddle-node bifurcation is a local bifurcation, meaning the topological change underlying the bifurcation occurs at an equilibrium point. The stability and number

of equilibrium points can change in a variety of ways. However, if several ways are topologically equivalent, then they all represent the same local bifurcation and can be described by the same normal form. The remainder of this section proceeds by discussing several other important local bifurcations and also includes a brief discussion of a couple global bifurcations.

A (supercritical) pitchfork bifurcation occurs in the system

$$\dot{x} = \mu x - x^3$$
$$\dot{y} = -y. \tag{2.14}$$

For $\mu < 0$ equations 2.14 possess a single, stable equilibrium point at $\vec{x}_* = \{0, 0\}$ ($J(\vec{x}_*$ has $\xi_{1,2} = \{\mu, \text{-}1\}$). When μ crosses zero, the equilibrium point at $\vec{x}_* = \{0, 0\}$ becomes unstable, and two stable equilibria at $\vec{x}_* = \{\pm\sqrt{\mu}, 0\}$ are born. This bifurcation gets its name from the pitchfork appearance of its bifurcation diagram (Fig. 2.4*B*).

A pitchfork bifurcation occurs when a function resembling a cubic polynomial becomes monotonic. Such a bifurcation occurs when the hair bundle's force-displacement relation loses its region of negative stiffness, i.e. when $k = k_{\text{gs}}(D/4\delta - 1)$.

The normal form for a transcritical bifurcation is given by

$$\dot{x} = \mu x - x^2$$
$$\dot{y} = -y. \tag{2.15}$$

This system possesses equilibrium solutions at $\vec{x}_* = \{0, 0\}$, $\xi_{1,2} = \{\mu, \text{-}1\}$, and at $\vec{x}_* = \{\mu, 0\}$, $\xi_{1,2} = \{\text{-}\mu, \text{-}1\}$. For $\mu < 0$ the equilibrium point at the origin is stable and the other equilibrium point is unstable. At the bifurcation, $\vec{x}_* = \{\mu, 0\}$ passes through the equilibrium point at the origin and the two exchange stability: for $\mu > 0$ the origin is unstable and the other point is a stable equilibrium. Figure 2.4*C* portrays the bifurcation diagram for this system.

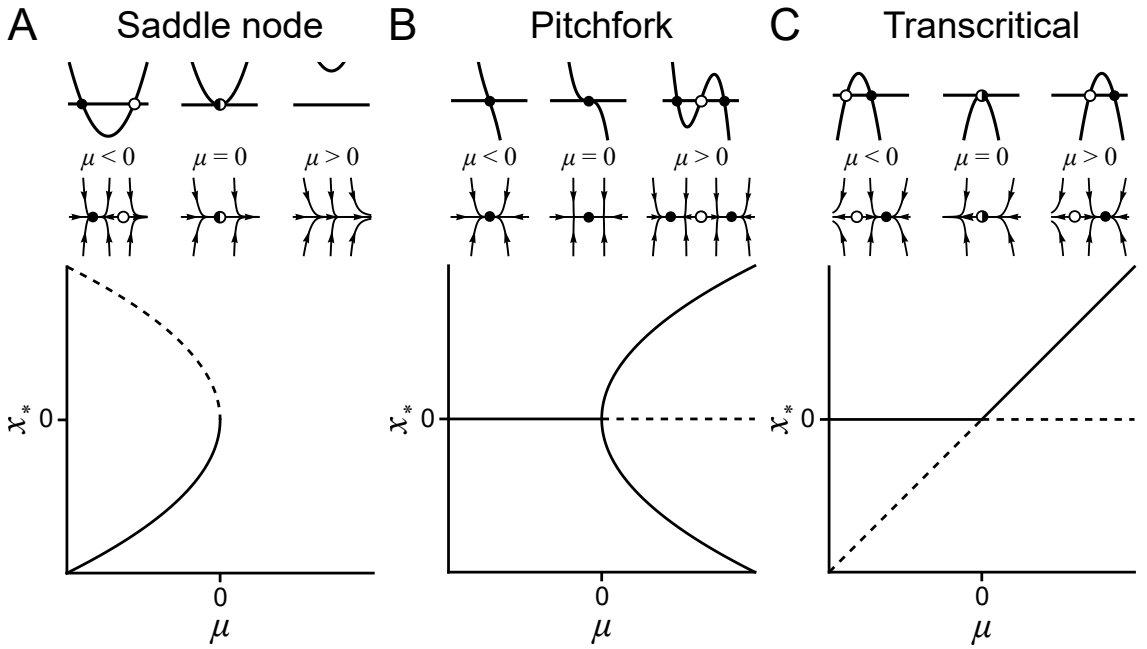

Figure 2.4: Three local bifurcations. $(A - C)$ Graphical representations, phase portraits, and bifurcation diagrams for the saddle-node (A), pitchfork (B), and transcritical (C) normal forms. The curves in a bifurcation diagram indicate the values of the equilibrium points x_*; because $y_* = 0$ throughout, this value is not shown. Continuous lines mark the locations of stable equilibrium points as a function of the bifurcation parameter μ, and the locations of unstable equilibrium points are indicated by dashed lines. (A) The parabola $\dot{x}(\mu) = \mu + x^2$ (top) is shown for negative (left), zero (center), and positive μ. The corresponding phase portraits (middle) show two equilibrium points that collide and annihilate as μ passes through zero. The bifurcation diagram for the saddle-node normal form (bottom) contains this information and also indicates the square-root dependence of x_* on μ. This latter feature is approximately true in other systems only near the saddle-node bifurcation. (B) Same as panel A except for the supercritical pitchfork bifurcation. A subcritical pitchfork bifurcation occurs instead for the system $\dot{x} = \mu x + x^3$, $\dot{y} = -y$, which differs from the supercritical case only in the sign of the cubic term. The bifurcation diagram of the subcritical pitchfork normal form resembles that of the supercritical pitchfork, except it is reflected across the line $\mu = 0$ and each curve displays the opposite stability. (C) In a transcritical bifurcation, two equilibrium points pass through each other and exchange stability. As is revealed by the normal form $\dot{x}(\mu) = \mu x - x^2$, this can occur when the slope of a linear term added to a quadratic term changes sign (top).

A real eigenvalue changes sign as a system crosses a saddle-node, pitchfork, or transcritical bifurcation. Thus, exactly at the bifurcation, the system must have a zero eigenvalue and the determinant of the system's Jacobian matrix, which is equal to the product of its eigenvalues, must also be zero. This property, together with the number of equilibrium points that exist before and after the bifurcation, allows for the identification of each of these three bifurcations.

If the Jacobian possesses complex eigenvalues, then a change in the sign of the eigenvalues' real part constitutes another way to alter the stability of an equilibrium point. A bifurcation of this kind occurs in the supercritical Hopf normal form:

$$\dot{z} = (\mu + i\omega_0)z - (\gamma_R + i\gamma_I)|z|^2 z, \qquad \gamma_R > 0. \tag{2.16}$$

Because $z(t) = x(t) + iy(t) = r(t)e^{i\theta(t)}$, Equation 2.16 is represents a system of two differential equations. In Cartesian coordinates the system is described by

$$\begin{aligned} \dot{x} &= \mu x - \omega_0 y - \gamma_R x(x^2 + y^2) + \gamma_I y(x^2 + y^2) \\ \dot{y} &= \omega_0 x + \mu y - \gamma_I x(x^2 + y^2) - \gamma_R y(x^2 + y^2), \end{aligned} \tag{2.17}$$

and in polar coordinates by

$$\begin{aligned} \dot{r} &= r(\mu - \gamma_R r^2) \\ \dot{\theta} &= \omega_0 - \gamma_I r^2. \end{aligned} \tag{2.18}$$

These equations are nearly identical to those discussed in the previous section (Eqs. 2.7-2.9), except here it is not assumed that the coefficient of the cubic term is real.

The Hopf normal form possesses an equilibrium point at $\vec{x}_* = \{0, 0\}$, at which point the Jacobian matrix is

$$J(\{0,0\}) = \begin{bmatrix} \mu & -\omega_0 \\ \omega_0 & \mu \end{bmatrix},$$

with eigenvalues $\xi_\pm = \mu \pm i\omega_0$. Thus, $\vec{x}_* = \{0, 0\}$ is stable for $\mu < 0$ and unstable for $\mu > 0$. Because the eigenvalues are complex, trajectories near the equilibrium point describe spirals.

Analysis in the previous section revealed that a stable limit cycle occurs when $\mu > 0$. For the Hopf normal form the limit cycle is described by $z_*(t) = \sqrt{\mu/\gamma_R} e^{i(\omega_0 - \gamma_I \mu/\gamma_R)t}$, where the subscript asterisk demarcates a steady-state solution. In summary, phase-space trajectories spiral toward the equilibrium point when $\mu < 0$, but this equilibrium becomes unstable and a stable limit cycle is born when μ passes through zero and becomes positive (Fig. 2.5*A*). A quiescent system can thus begin to oscillate spontaneously if it crosses a Hopf bifurcation, a phenomenon that has been observed in hair bundles.

The amplitude of the limit cycle's oscillation grows from zero at $\mu = 0$ and follows a square-root dependence on the bifurcation parameter. This scaling is approximately true near supercritical Hopf bifurcations in other systems. Very close to the bifurcation the limit cycle's oscillation frequency[5] is approximately equal to the imaginary part of the eigenvalues $\mathrm{Im}[\xi_\pm] = \omega_0$.

Rather than rising from nothing, a limit cycle oscillation can also appear abruptly. Such behavior is seen as a system crosses a subcritical Hopf bifurcation, whose normal form is given by

$$\dot{z} = (\mu + i\omega_0)z + (\gamma_R + i\gamma_I)|z|^2 z - (\alpha_R + i\alpha_I)|z|^4 z, \qquad \alpha_R > 0. \tag{2.19}$$

Because they primarily affect the system's angular velocity and not the locations of limit cycles, γ_I and α_I are set to zero to simplify the discussion. Equations 2.19 are

[5]When $\gamma_I \neq 0$, the angular velocity of the phase-space trajectories depends on their distance from the origin. Interestingly, it is possible to kill the rotation exactly at the limit cycle by setting $\gamma_I = \omega_0 \gamma_R / \mu$.

given respectively in Cartesian and polar by

$$\dot{x} = \mu x - \omega_0 y + \gamma_R x(x^2 + y^2) - \alpha_R x(x^2 + y^2)^2$$
$$\dot{y} = \omega_0 x + \mu y + \gamma_R y(x^2 + y^2) - \alpha_R y(x^2 + y^2)^2, \tag{2.20}$$

and

$$\dot{r} = r(\mu + \gamma_R r^2 - \alpha_R r^4)$$
$$\dot{\theta} = \omega_0. \tag{2.21}$$

As for the supercritical Hopf normal form, the origin is a fixed point that loses stability when μ becomes positive; the Jacobian matrix is the same as above and the eigenvalues are again $\xi_\pm = \mu \pm i\omega_0$. The amplitude of the stable limit cycle, however, is nonzero at the bifurcation. Setting $\dot{r} = 0$ when $\mu = 0$ yields $r = \sqrt{\gamma_R/\alpha_R}$. In crossing a subcritical Hopf bifurcation, a system rapidly jumps from a stable equilibrium point to a large-amplitude limit cycle.

A few additional properties of this system merit mention. The $\dot{r}$ equation reveals that the system permits both a stable and an unstable limit cycle over a certain range of μ:

$$\text{Stable:} \qquad r = \sqrt{\frac{1}{2\alpha_R}\left(\gamma_R + \sqrt{\gamma_R^2 + 4\mu\alpha_R}\right)}, \qquad -\frac{\gamma_R^2}{4\alpha_R} < \mu$$
$$\text{Unstable:} \qquad r = \sqrt{\frac{1}{2\alpha_R}\left(\gamma_R - \sqrt{\gamma_R^2 + 4\mu\alpha_R}\right)}, \qquad -\frac{\gamma_R^2}{4\alpha_R} < \mu < 0. \tag{2.22}$$

At $\mu = 0$ the unstable limit cycle collides with the stable equilibrium point at the origin and leaves behind an unstable equilibrium point. Because the stable limit cycle exists for negative values of μ, the system exhibits hysteresis. Starting from $\mu < -\gamma_R^2/4\alpha_R$, the system settles on the stable equilibrium point until μ exceeds zero, at which point the system jumps to the stable limit cycle. If μ is then decreased, the

stable limit cycle persists beyond $\mu = 0$ and does not return to the stable equilibrium until $\mu < -\gamma_R^2/4\alpha_R$ (Fig. 2.5B).

Owing to the presence of multiple attractors, bistability arises for $-\gamma_R^2/4\alpha_R < \mu < 0$, termed the coexistence region. If a perturbation is large enough to drive the system across the unstable limit cycle, then the system's behavior can be switched from quiescent to self-oscillatory and vice versa.

A second bifurcation occurs in the subcritical Hopf's normal form. As μ is decreased past $-\gamma_R^2/4\alpha_R$ the stable and unstable limit cycles collide and annihilate in a saddle-node of limit cycles bifurcation. Because it does not involve changing the stability or number of equilibrium points, the saddle-node of limit cycles bifurcation is a global bifurcation. The homoclinic bifurcation provides another example of a global bifurcation. This bifurcation occurs when an equilibrium point collides with and subsequently breaks a limit cycle. Analytical criteria do not always exist for identifying the critical parameter value that precipitates a global bifurcation. Numerical simulations of a system's behavior are thus frequently employed to locate these oft-elusive bifurcations.

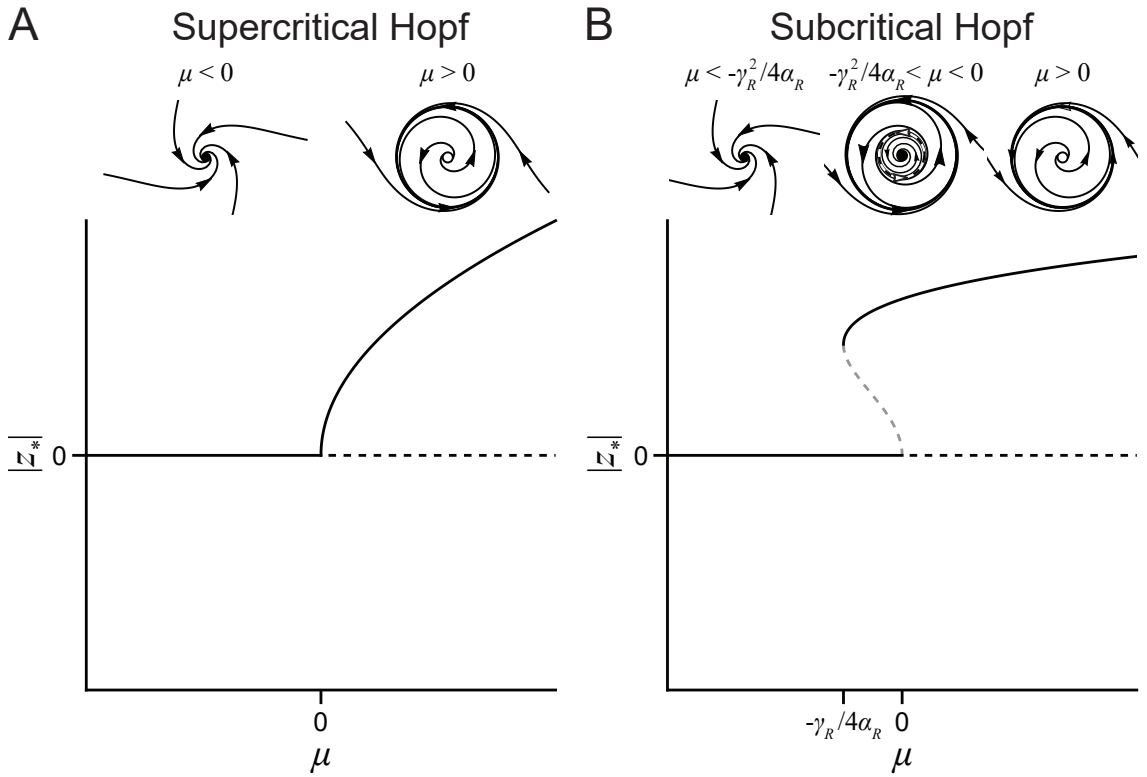

Figure 2.5: Hopf bifurcations. (A) Bifurcation diagram for the supercritical Hopf normal form. Representative phase portraits for $\mu < 0$ and $\mu > 0$ are shown above the diagram. The ordinate indicates the steady-state solution's magnitude. The origin is a stable equilibrium point when $\mu < 0$ (solid half line). As the bifurcation parameter passes its critical value $\mu_c = 0$, the origin becomes unstable (dashed half line) and a stable limit cycle $z_*(t) = \sqrt{\mu/\gamma_R}e^{i(\omega_0 - \gamma_I\mu/\gamma_R)t}$ (solid curve) is born. (B) Representative phase portraits and bifurcation diagram for the subcritical Hopf normal form. As in the supercritical case, the origin loses stability as μ is increased through 0 (solid and dashed half lines). However, the stable limit cycle (solid curve) emerges with a non-zero amplitude and exists for some negative values of μ, specifically for $\mu > -\gamma_R^2/4\alpha_R$. This value of μ also coincides with a saddle-node of limit cycles bifurcation. The unstable limit cycle (gray, dashed curve) that arises from this bifurcation is annihilated by the stable equilibrium point when $\mu = 0$.

Both the supercritical and subcritical Hopf bifurcations occur when the Jacobian's eigenvalues displays a zero real part. Although this criterion affords the detection of a Hopf bifurcation, it is therefore insufficient to distinguish between the supercritical and subcritical varieties. This ambiguity can be resolved by finding the sign of

$$16\zeta \equiv f_{xxx} + f_{xyy} + g_{xxy} + g_{yyy} + \frac{1}{\omega}[f_{xy}(f_{xx} - f_{yy}) - g_{xy}(g_{xx} + g_{yy}) - f_{xx}g_{xx} + f_{yy} + g_{yy}], \tag{2.23}$$

in which f contains the nonlinear terms of the $\dot{x}$ equation, g contains the nonlinear terms of the $\dot{y}$ equation, and the subscripts indicate successive partial differentiation with respect to the variables listed. The quantity ζ represents, in essence, the coefficient of a system's cubic term when the system is poised at a Hopf bifurcation. If $\zeta < 0$, then the Hopf bifurcation is supercritical, whereas $\zeta > 0$ indicates a subcritical bifurcation.

Applying Equation 2.23 to the subcritical Hopf normal form yields $\zeta = \gamma_R$. Evidently, this normal form is subcritical only when $\gamma_R > 0$ and is supercritical otherwise. Indeed, both the size of the coexistence region and the amplitudes of the limit cycles contained therein shrink has γ_R approaches zero. At $\mu = \gamma_R = 0$ the subcritical Hopf bifurcation and the saddle-node of limit cycles meet a supercritical Hopf bifurcation at a point called a Bautin bifurcation.

Until now, only codimension-1 bifurcations have been discussed. The codimension of a bifurcation is equal to the number of parameters that need to simultaneously achieve their critical values to effect the bifurcation. The Buatin point is a codimension-2 bifurcation and the criteria for its occurrence are: 1. the real parts of a pair of complex eigenvalues vanish ($\mu = 0$ in our example), and 2. the system's cubic term vanishes[6] ($\zeta = 0$).

[6]More accurately, the first Lyapunov coefficient vanishes, see Appendix A.

For systems in which multiple bifurcations occur, a graphical representation called a state diagram aids in visualizing how bifurcations relate to each other. Consider a system that possesses two bifurcation parameters μ_1 and μ_2. Assigning each an axis constructs a parameter space. A state diagram partitions the parameter space into sectors that contain topologically equivalent phase portraits (Fig. 2.6). Different sectors are separated by bifurcation curves that indicate the values of the parameters at which that particular bifurcation occurs.

Another codimension-2 bifurcation encountered in this work is the Bogdanov-Takens point, whose normal form is given by

$$\begin{aligned} \dot{x} &= \mu_1 + \mu_2 y + y^2 - xy \\ \dot{y} &= x. \end{aligned} \tag{2.24}$$

Equilibrium points for this systems are located at

$$\vec{x}_* = \left\{ 0, \frac{1}{2}\left(-\mu_2 \pm \sqrt{\mu_2^2 - 4\mu_1} \right) \right\}.$$

If $\mu_1 > \mu_2^2/4$ there are no equilibrium points, but two equilibrium points exist when $\mu_1 < \mu_2^2/4$, indicating that a saddle-node bifurcation occurs at $\mu_1 = \mu_2^2/4$. For $\mu_1 = 0$ the equilibrium points are $\vec{x}_* = \{0, 0\}$ and $\{0, \mu_2\}$. The eigenvalues of $J(\{0, 0\})$ are $\xi_{1,2} = \pm\sqrt{\mu_2}$. These eigenvalues are completely imaginary when $\mu_2 < 0$, thus a Hopf bifurcation occurs for $\mu_1 = 0$, $\mu_2 < 0$. The limit cycle that arises from the Hopf bifurcation breaks when it touches a saddle node in a homoclinic bifurcation. The homoclinic bifurcation is approximately located at $\mu_1 \approx -6\mu_2^2/25$ [111]. The saddle-node, Hopf, and homoclinic bifurcations all collide at a Bogdanov-Takens point at $\mu_1 = \mu_2 = 0$. Only a single equilibrium point, $\vec{x}_* = \{0, 0\}$, exists for these parameter values and $J(\{0, 0\})$ has two zero eigenvalues.

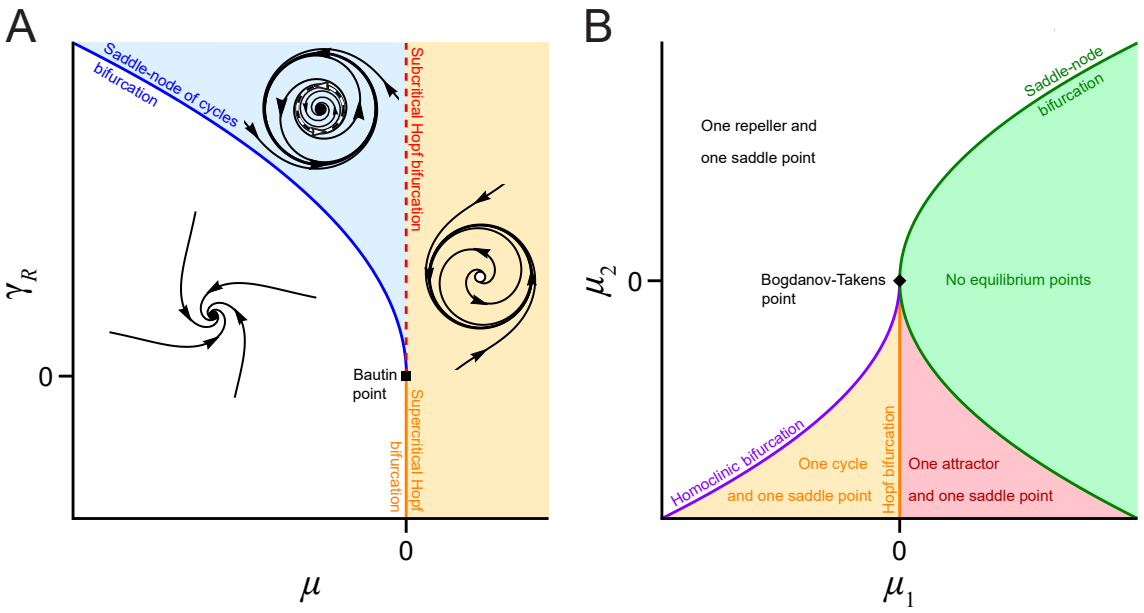

Figure 2.6: Example state diagrams. The axes of a state diagram give the values of bifurcation parameters. Bifurcation curves divide a state diagram into regions that contain steady-state behaviors of the system that are topologically equivalent. In other words, a system's coordinates in state space dictate the system's steady-state behavior. For this reason, bifurcation parameters are also called control parameters: the values of such parameters set the fate of the system. The qualitative character of the steady-state behavior can be changed by coaxing the system across a bifurcation. In two-dimensional state diagrams, codimension-1 bifurcations are represented by curves and codimension-2 bifurcations are indicated by points. (A) State diagram near a Bautin point (black square). This codimension-2 bifurcation occurs at the intersection of a supercritical Hopf (solid, orange line), a subcritical Hopf (red, dashed line), and a saddle-node of limit cycles bifurcation (solid, blue curve). Representative phase portraits are shown in each region. (B) A Bogdanov-Takens point (black diamond) occurs when a homoclinic (purple curve) and a Hopf bifurcation (orange line) meet at a saddle-node bifurcation (green curve). For convenient viewing, each region of the state diagram is shaded a different color and labeled by the topology of the steady-state behavior. The saddle-node of limit cycles (A) and homoclinic (B) bifurcations are global bifurcations and can often be located only through numerical simulations. A variety of options often exist when selecting control parameters for a system. Given its mathematical connection to several bifurcations, the real part of an eigenvalue is sometimes a suitable choice. In other cases, an experimental observable that appears as a coefficient in the system might be preferred.

2.3 Generic Responses Near a Hopf Bifurcation

That adjusting a parameter can engender spontaneous oscillations by a hair bundle suggests that the bundle is poised near a Hopf bifurcation. If it does in fact govern a bundle's dynamics, then a Hopf bifurcation should also account for the experimentally measured features of a bundle's response to periodic stimuli. Specifically, the presence of a Hopf bifurcation must allow signal detection by hair bundles to be sensitive, frequency selective, and operational over a broad dynamic range.

To evaluate whether it is beneficial for a periodic-signal detector to operate near a Hopf bifurcation, a sinusoidal stimulus $F(t) = F_0 e^{i\omega_D t}$ with driving amplitude F_0 and frequency ω_D must be added to the Hopf normal form:

$$\begin{aligned} \dot{x} &= \mu x - \omega_0 y - \gamma_R x(x^2 + y^2) + F_0 e^{i\omega_D t} \\ \dot{y} &= \omega_0 x + \mu y - \gamma_R y(x^2 + y^2). \end{aligned} \tag{2.25}$$

Because a typical experiment entails delivering forces to a hair bundle, the driving term is added to only the $\dot{x}$ equation. The variable x can thus be likened to the hair bundle's position and y can be considered a (perhaps unmeasurable) internal variable. The focus of this thesis centers around what transpires on the side of the Hopf bifurcation that contains a single, stable equilibrium point, termed the "stable side" of the bifurcation; the side containing the limit cycle is instead called the "unstable side". It is thus assumed that $\mu < 0$ in what follows.

To determine the system's response to small-amplitude stimuli it is assumed that the driving term $F_0 e^{i\omega_D t}$ is small and thus elicits only small displacements from the equilibrium point $\vec{x}_* = \{0, 0\}$. In this regime, equations 2.25 closely resemble their linearized counterparts

$$\dot{x} = \mu x - \omega_0 y + F_0 e^{i\omega_D t}$$

$$\dot{y} = \omega_0 x + \mu y. \tag{2.26}$$

This approximation has the advantage of allowing analytical solutions. Applying a Fourier transform converts the system of differential equations in to a more tenable system of algebraic equations:

$$i\omega\widetilde{x} = \mu\widetilde{x} - \omega_0\widetilde{y} + F_0\delta(\omega_D - \omega)$$

$$i\omega\widetilde{y} = \omega_0\widetilde{x} + \mu\widetilde{y}. \tag{2.27}$$

The diacritical tildes indicate that the variables are Fourier transformed. The system's response in frequency space $\widetilde{x}$ is now easily isolated as

$$\widetilde{x}(\omega) = F_0\delta(\omega_D - \omega)\left[i\omega - \mu + \frac{\omega_0^2}{i\omega - \mu}\right]^{-1}. \tag{2.28}$$

An inverse Fourier transformation yields the corresponding response in the time domain

$$\begin{aligned} x(\omega_D, t) =& F_0 e^{i\omega_D t}\left[i\omega_D - \mu + \frac{\omega_0^2}{i\omega_D - \mu}\right]^{-1} + e^{\mu t}(c_1\cos[\omega_0 t] + c_2\sin[\omega_0 t]) \\ =& \frac{F_0 e^{i(\omega_D t+\phi)}\sqrt{\omega_D^2+\mu^2}}{\sqrt{(\omega_D^2+\mu^2)^2 - \omega_0^2(2\omega_d^2 - 2\mu^2 - \omega_0^2)}} + e^{\mu t}(c_1\cos[\omega_0 t] + c_2\sin[\omega_0 t]), \\ \phi =& \tan^{-1}\left[\frac{\omega_D(\mu^2+\omega_D^2-\omega_0^2)}{\mu(\mu^2+\omega_D^2+\omega_0^2)}\right]. \end{aligned} \tag{2.29}$$

The coefficients c_1 and c_2 are determined by the initial conditions. Because $\mu < 0$, the transient response $e^{\mu t}(c_1\cos[\omega_0 t] + c_2\sin[\omega_0 t])$ decays at a rate that is proportional to the system's distance from the Hopf bifurcation in parameter space. As the bifurcation parameter nears its critical value, more time is needed for the system to reach steady state.

The phase difference between the stimulus and the response ϕ equals zero when $\omega_d = \sqrt{\omega_0^2 - \mu^2}$, which differs slightly from the system's resonant frequency (see Equation 2.32 below). When stimulated at the resonance frequency and when $\mu \ll 1$, $\phi \approx (\mu/\omega_0)[1 - (11/6)(\mu/\omega_0)^2 + O(\mu^4)]$.

The sensitivity χ of a system's response to forcing is defined as the amplitude of the system's output divided by the amplitude of the driving force:

$$\chi \equiv \frac{|x|}{|F|}. \tag{2.30}$$

The same driving force elicits a larger response in a system that is more sensitive. The sensitivity of the linearized Hopf normal form is given by

$$\chi(\omega_D, \mu) = \sqrt{\frac{\omega_D^2 + \mu^2}{(\omega_D^2 + \mu^2)^2 - \omega_0^2(2\omega_d^2 - 2\mu^2 - \omega_0^2)}}. \tag{2.31}$$

By definition, a system's resonant frequency ω_R is the driving frequency that elicits the greatest response. The Hopf's linear sensitivity (Eq. 2.31) reaches its maximum value at

$$\omega_R(\mu) = \left[\omega_0\sqrt{4\mu^2 + \omega_0^2} - \mu^2\right]^{1/2}. \tag{2.32}$$

When driven at its resonant frequency, the system attains the sensitivity

$$\chi(\omega_D = \omega_R, \mu) = \chi_{\max}(\mu) = \frac{1}{\sqrt{2\omega_0\sqrt{\mu^2 + \omega_0^2} - 2\omega_0^2}} \approx \frac{1}{|\mu|} + O(\mu), \tag{2.33}$$

in which the approximation is given for $\mu \ll 1$. Near a Hopf bifurcation a system's maximum sensitivity is thus inversely proportional to the system's distance from the bifurcation in parameter space.

The sharpness of a system's frequency selectivity can be quantified by the quality factor Q

$$Q \equiv \frac{\omega_R}{\Delta\omega}, \tag{2.34}$$

in which $\Delta\omega = \omega_+ - \omega_-$ is the range of frequencies over which the system's response exceeds $1/\sqrt{2}$ times its maximum. The boundary frequencies $\omega_\pm$ can be obtained by solving

$$\chi(\omega_\pm) = \frac{1}{\sqrt{2}}\chi(\omega_R). \tag{2.35}$$

Sharper frequency selectivity is indicated by larger values of Q.

Substituting ω_R into Equation 2.35 reveals that

$$\omega_\pm = \left[2\omega_0\sqrt{4\mu^2+\omega_0^2} - \mu^2 - \omega_0^2 \pm 2\omega_0\sqrt{3\mu^2+\omega_0^2-\omega_0\sqrt{4\mu^2+\omega_0^2}}\right]^{1/2}. \tag{2.36}$$

For $\mu \ll 1$, $\omega_R \approx \omega_0 + \mu^2/2\omega_0 + O(\mu^4)$ and $\Delta\omega = \omega_+ - \omega_- \approx 2|\mu|[1+(\mu/\omega_0)^6 + O(\mu^8)]$, which in turn means that, close to the Hopf bifurcation,

$$Q = \frac{\omega_R}{\Delta\omega} \approx \frac{\omega_0}{2|\mu|} + O(\mu). \tag{2.37}$$

A system poised near a Hopf bifurcation thus exhibits frequency selectivity whose sharpness is inversely proportional to the system's distance from the bifurcation in parameter space[7].

To evaluate how the Hopf normal form responds to a range of driving amplitudes it is necessary to reintroduce the system's nonlinear terms, for these are no longer negligible when the stimulus amplitude is large:

$$\dot{z} = (\mu + i\omega_0)z - \gamma_R|z|^2 z + F_0 e^{i\omega_D t}. \tag{2.38}$$

[7]Generally speaking, a bifurcation parameter's critical value μ_c need not coincide with zero. It would thus be more accurate for equations 2.33 and 2.37 to read $\chi_{\max}(\mu) \approx 1/|\mu - \mu_c|$ and $Q \approx \omega_0/2|\mu - \mu_c|$, respectively.

The ansatz $z(t) = re^{i(\omega_D t+\phi)}$ constitutes a phase-locked solution to this differential equation. Inserting the solution into Equation 2.38 yields

$$i\omega_D re^{i(\omega_D t+\phi)} = (\mu + i\omega_0)re^{i(\omega_D t+\phi)} - \gamma_R r^3 e^{i(\omega_D t+\phi)} + F_0 e^{i\omega_D t}$$

$$i\omega_D re^{i\phi} = (\mu + i\omega_0)re^{i\phi} - \gamma_R r^3 e^{i\phi} + F_0. \tag{2.39}$$

Simple rearrangement leads to

$$F_0 = re^{i\phi}[\mu - \gamma_R r^2 + i(\omega_0 - \omega_D)].$$

Calculating the squared magnitude of both sides produces a relation between the amplitude of the driving force F_0 and that of the system's response r [113]:

$$F_0^2 = \gamma_R^2 r^6 - 2\mu\gamma_R r^4 + r^2[\mu^2 + (\omega_0 - \omega_D)^2]. \tag{2.40}$$

This expression is cubic in r^2 and is thus exactly solvable, though the algebraic form of the solution is less than illuminating[8]. Appropriate limits, however, uncover the salient features of the system's response.

For small enough forcing F_0, the amplitude of the system's response r is also small and thus dominated by the r^2 term, so that

$$r \approx \frac{F_0}{\sqrt{\mu^2 + (\omega_0 - \omega_d)^2}}, \qquad \frac{r}{F_0} = \chi \approx \frac{1}{\sqrt{\mu^2 + (\omega_0 - \omega_d)^2}}. \tag{2.41}$$

For small forcing the system's response is linearly proportional to the stimulus's amplitude, and the sensitivity is thus constant. Driving the system at $\omega_D = \omega_0$ yields $\chi \approx 1/|\mu|$, which accords with Equation 2.33.

[8]The solution to Equation 2.40 is

$$r = \sqrt{\frac{2}{3}\mu + \frac{(\text{-}2)^{1/3}}{6}(4\mu^2\Gamma^{\text{-}1} - \Gamma)}, \quad \Gamma = \left[2\mu^3 - 27F_0^2\left(1 - \sqrt{3F_0^2 - f\mu^3/4}\right)\right]^{1/3}.$$

For large forcing, or very close to the bifurcation ($\mu \ll 1$), the system's response is dominated by the r^6 term that arises from the normal form's cubic nonlinearity:

$$r \approx \left(\frac{F_0}{\gamma_R}\right)^{1/3}, \qquad \frac{r}{F_0} = \chi \approx \frac{F_0^{-2/3}}{\gamma_R^{1/3}}. \tag{2.42}$$

Close to the Hopf bifurcation, expressions 2.42 reveal that a thousandfold increase in the amplitude of the driving force begets only a tenfold increase in the system's response. The cubic nonlinearity in the Hopf normal form thus allows the system to compress a range of stimuli spanning three orders of magnitude into a range of responses that span only one order of magnitude, a phenomenon termed nonlinear compression. Consequently, the system's sensitivity follows a negative two-thirds power law near the bifurcation.

In summary, near a supercritical Hopf bifurcation a system's sensitivity to periodic stimuli is approximately constant for small-amplitude forcing and follow a negative two-thirds power law for large-amplitude driving (Fig. 2.7B). This enables such a system to amplify weak stimuli and, through nonlinear compression, to faithfully operate over a broad dynamic range. Because any system poised near a Hopf bifurcation can be reduced to the Hopf normal form, the sensitivity, frequency selectivity, and nonlinear compression that characterize the Hopf normal form are generic features of any system that permits a Hopf bifurcation.

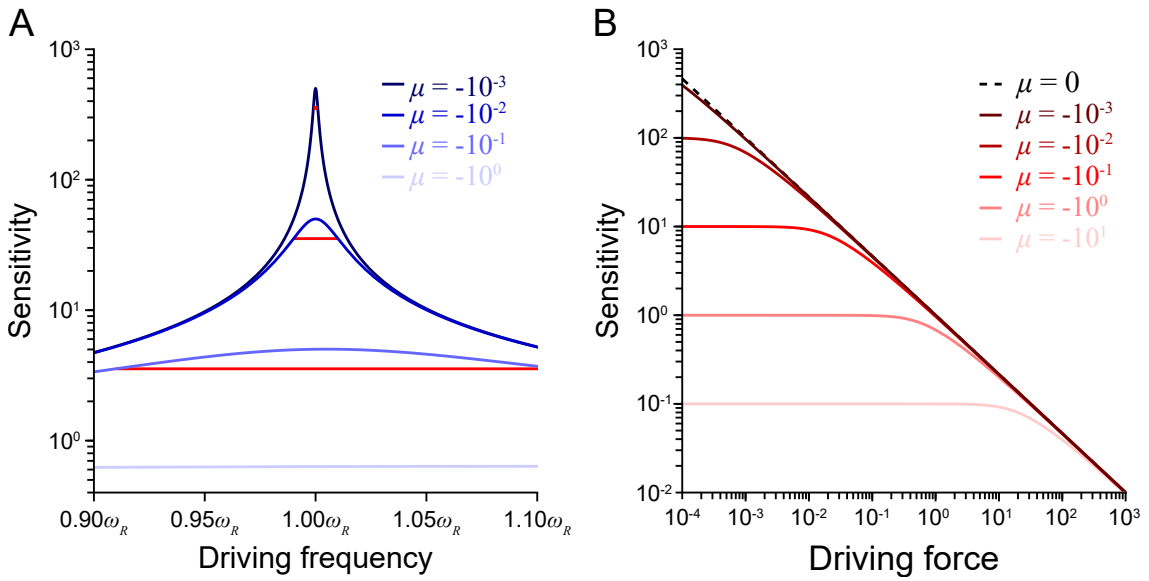

Figure 2.7: Generic properties near a supercritical Hopf bifurcation. (A) As the supercritical Hopf normal form nears its bifurcation at $\mu_c = 0$, the system exhibits greater peak sensitivity. The peak linear sensitivity increases nearly tenfold for every tenfold decrement in the system's distance to the bifurcation in parameter space, thus approximating the relation $\chi \propto |\mu - \mu_c|^{-1}$. The horizontal red lines span $\Delta\omega$ for each sensitivity curve, and decrease in length by a factor of ten for each tenfold reduction in $|\mu - \mu_c|$. Because the resonance frequency ω_R remains nearly constant, $Q = \omega_R/\Delta\omega$, which measures the sharpness of a system's frequency selectivity, is also inversely proportional to $|\mu - \mu_c|$. (B) Close to the bifurcation and for large enough stimuli, the Hopf normal form exhibits nonlinear compression that follows a negative two-thirds power law, $\chi \propto F_0^{-2/3}$. Compression of this kind permits a system to represent stimuli spanning three orders of magnitude with responses that span a hundredfold smaller range. Because the cubic nonlinearity of the Hopf normal form does not saturate, the negative two-thirds power law extends indefinitely as the driving-force amplitude grows. The force-displacement relation measured for actual hair bundles (Eq. 1.2) exhibits a saturating nonlinearity. Nonlinear compression in hair bundles is therefore operational over only a finite range of stimulus amplitudes. The response properties discussed in this figure are generic features of systems that operate near a supercritical Hopf bifurcation and a correlate of each has been measured in hair bundles (c.f. Fig. 1.10).

2.4 Hopf Bifurcations in Three Dimensions

The bifurcation that figures most prominently in this work is the (supercritical) Hopf. This section is therefore devoted to describing an efficient method for locating Hopf bifurcations in systems of three dynamical variables.

It has already been shown how a Hopf bifurcation arises in a system of two dynamical variables: letting $J(\vec{x}_*)$ be the Jacobian matrix evaluated at the equilibrium point $\vec{x}_*$, a Hopf bifurcation occurs when the eigenvalues of $J(\vec{x}_*)$ are completely imaginary, i.e. $\xi_\pm = \{\pm i\xi_I\}$. Considering that summing the eigenvalues produces the trace of the associated matrix and that their product yields the matrix determinant, this condition can be recast as $\mathrm{Tr}[J(\vec{x}_*)] = i\xi_I - i\xi_I = 0$ and $\det[J(\vec{x}_*)] = (i\xi_I)(\text{-}i\xi_I) = \xi_I^2 > 0$. Let $T_n = \mathrm{Tr}[J(\vec{x}_*)^n]$. Making use of the relation $\det[J(\vec{x}_*)] = \frac{1}{2}(T_1^2 - T_2)$, the second condition can also be expressed as $T_2 < T_1^2$. Together the two conditions are

$$T_1 = 0, \qquad T_2 < 0. \tag{2.43}$$

Of course, a stabilizing nonlinearity must also be present for the system to undergo spontaneous oscillations, which can be confirmed through numerical simulations.

In systems of three or more dynamical variables, a stable equilibrium point $\vec{x}_*$ also undergoes a Hopf bifurcation when $J(\vec{x}_*)$ has a pair of purely imaginary eigenvalues. The surest way to locate Hopf bifurcations is to track how all of the eigenvalues of $J(\vec{x}_*)$ change as the values of the chosen parameters are altered. Because formulas do not exist for the roots of polynomials of degree five and higher, calculating eigenvalues in systems with five or more dynamical variables usually requires numerical methods. In systems of three dynamical variables, however, Hopf bifurcations can be found analytically and the formulae are be fairly simple.

A system of three dynamical variables possesses a 3×3 Jacobian matrix. Consequently, the characteristic polynomial $p_J(\xi)$ is a cubic relation:

$$p_J(\xi) = c_1\xi^3 + c_2\xi^2 + c_3\xi + c_4\,.$$

Letting $T_n = \mathrm{Tr}[J(\vec{x}_*)^n]$, the polynomial's coefficients are c_1 = -1, $c_2 = T_1$, $c_3 = \frac{1}{2}(T_2 - T_1^2)$, and $c_4 = \frac{1}{6}(T_1^3 - 3T_1T_2 + 2T_3) = \det[J(\vec{x}_*)]$. Exactly at the Hopf bifurcation, the real part of a pair of complex conjugate eigenvalues is zero. In other words, at the bifurcation there is a pair of purely imaginary eigenvalues, $\{i\xi_I, -i\xi_I\}$, that satisfy $p_J(\xi) = 0$. Substituting $\xi = i\xi_I$ into the characteristic equation yields

$$-ic_1\xi_I^3 - c_2\xi_I^2 + ic_3\xi_I + c_4 = 0\,.$$

The real and imaginary parts of the above equation must be satisfied simultaneously:

$$\begin{aligned} -ic_1\xi_I^3 + ic_3\xi_I &= 0 \\ -c_2\xi_I^2 + c_4 &= 0 \end{aligned} \qquad \Rightarrow \qquad \xi_I^2 = \frac{c_3}{c_1} = \frac{c_4}{c_2}.$$

After substituting the expressions given above for c_1, c_2, c_3, and c_4, this equality becomes:

$$-\frac{T_2 - T_1^2}{2} = \frac{T_1^3 - 3T_1T_2 + 2T_3}{6T_1} \Rightarrow T_1^3 = T_3.$$

As a check, let $J(\vec{x}_*)$ have eigenvalues ξ_1, ξ_2, and ξ_3, then $p_J(\xi)$ can be written as

$$\begin{aligned} p_J(\xi) &= c_1\xi^3 + c_2\xi^2 + c_3\xi + c_4 = (\xi_1 - \xi)(\xi_2 - \xi)(\xi_3 - \xi) \\ &= -\xi^3 + (\xi_1 + \xi_2 + \xi_3)\xi^2 - (\xi_1\xi_2 + \xi_1\xi_3 + \xi_2\xi_3)\xi + \xi_1\xi_2\xi_3 = 0. \end{aligned}$$

Equating coefficients reveals $c_1 = -1$, $c_2 = \xi_1 + \xi_2 + \xi_3$, $c_3 = -(\xi_1\xi_2 + \xi_1\xi_3 + \xi_2\xi_3)$, and $c_4 = \xi_1\xi_2\xi_3$, which are well known results from linear algebra.

The condition $c_3/c_1 = c_4/c_2$ is satisfied if $\xi_3 = -\xi_2$:

$$c_1 = -1, \;\; c_2 = \xi_1, \;\; c_3 = \xi_2^2, \;\; c_4 = -\xi_1\xi_2^2 \;\; \Rightarrow \;\; \frac{c_3}{c_1} = -\xi_2^2 = \frac{c_4}{c_2}.$$

The condition $T_3 = T_1^3$ therefore characterizes not only curves of Hopf bifurcations, but also curves along which $J(\vec{x}_*)$ has two real eigenvalues that are equal in magnitude and opposite in sign. To distinguish between these two possibilities, note that when $\xi_2 \in \mathbb{R}$, $c_3 = \xi_2^2 = \frac{1}{2}(T_2 - T_1^2) > 0$, whereas if ξ_2 is completely imaginary (i.e. $\xi_2 = i\xi_I$, $\xi_I \in \mathbb{R}$), then $c_3 = (i\xi_I)^2 = -\xi_I^2 = \frac{1}{2}(T_2 - T_1^2) < 0$. Therefore, the conditions to find curves of Hopf bifurcations are:

$$T_3 = T_1^3 \quad \text{and} \quad T_2 < T_1^2. \tag{2.44}$$

The trace of $J(\vec{x}_*)$ and its powers are functions of the system's parameters. If μ_1 and μ_2 are bifurcation parameters, then the relation $T_3(\mu_1, \mu_2) = T_1(\mu_1, \mu_2)^3$ locates a curve of Hopf bifurcations in the μ_1-μ_2 parameter space (provided $T_2(\mu_1, \mu_2) < T_1(\mu_1, \mu_2)^2$ is also satisfied).

Assuming that $J(\vec{x}_*)$ is an $n\times$n diagonalizable matrix,

$$T_k^m = \left(\sum_{i=1}^{n} \xi_i^k \right)^m.$$

Conditions 2.44 can then be written:

$$T_3 = T_1^3 : \qquad \xi_1^3 + \xi_2^3 + \xi_3^3 = (\xi_1 + \xi_2 + \xi_3)^3$$

$$T_2 < T_1^2 : \qquad \xi_1^2 + \xi_2^2 + \xi_3^2 < (\xi_1 + \xi_2 + \xi_3)^2.$$

The first condition enforces that $\xi_1 = -\xi_2$. Equality in the second condition is achieved only if $\xi_1 = \xi_2 = 0$. Thus, the criterion $T_2 = T_1^2$ locates a Bogdanov-Takens point in systems of three dynamical variables. In passing through a Bogdanov-Takens point along the manifold $T_1^3 = T_3$, the eigenvalues of $J(\vec{x}_*)$ undergo the transition $\{i\xi_I, \text{-}i\xi_I, \xi_3\} \to \{0, 0, \xi_3\} \to \{\xi_R, \text{-}\xi_R, \xi_3\}$, $\xi_I, \xi_R \in \mathbb{R}$.

A saddle-node bifurcation occurs when a real eigenvalue of $J(\vec{x}_*)$ becomes zero. This requires $\xi_1\xi_2\xi_3 = \det[J(\vec{x}_*)] = \frac{1}{6}[T_1^3 - 3T_1T_2 + 2T_3] = 0$. If the saddle-node

bifurcation curve meets a Hopf bifurcation curve, this condition can be satisfied in two ways. Noting that the Hopf bifurcation requires $T_3 = T_1^3$, the condition becomes

$$T_1^3 - 3T_1T_2 + 2T_3 = T_1^3 - 3T_1T_2 + 2T_1^3 = T_1(T_1^2 - T_2) = 0.$$

So either $T_2 = T_1^2$, as occurs at a Bogdanov-Takens point, or $T_1 = 0$. In the latter case, the eigenvalues of $J(\vec{x}_*)$ are $\{i\xi_I, -i\xi_I, 0\}$, indicating that this saddle-node bifurcation affects the stability of the equilibrium point in a direction outside of the manifold that contains the limit cycle.

Appendix A: Locating a Bautin Bifurcation

Derivations of the results presented in this Appendix can be found in [111]. Consider a system of n nonlinear differential equations $\dot{\vec{x}} = \vec{F}(\vec{x}, \vec{\mu})$ that governs the behavior of n dynamical variables $\vec{x} = \{x_1(t), \ldots, x_n(t)\}$ and depends on p parameters $\vec{\mu} = \{\mu_1, \ldots, \mu_p\}$. Assume that the appropriate change of variables has been performed so that an equilibrium point $\vec{x}_*$ occurs at the origin. The vector function $\vec{F}(\vec{x}, \vec{\mu})$ can be expanded in a Talor series about the equilibrium point $\vec{x}_* = \vec{0}$:

$$\vec{F}(\vec{x}, \vec{\mu}) = J(\vec{\mu})\vec{x} + \frac{1}{2}\vec{B}(\vec{x}, \vec{x}, \vec{\mu}) + \frac{1}{6}\vec{C}(\vec{x}, \vec{x}, \vec{x}, \vec{\mu}) + O(||\vec{x}||^4),$$

in which $J(\vec{\mu})$ is the Jacobian matrix at $\vec{x}_* = 0$,

$$B_j(\vec{x}, \vec{y}, \alpha) = \sum_{k,l=1}^{n} \left.\frac{\partial^2 F_j(\vec{q}, \vec{\mu})}{\partial q_k \partial q_l}\right|_{\vec{q}=0} x_k y_l, \text{ and}$$

$$C_j(\vec{x}, \vec{y}, \vec{z}, \vec{\mu}) = \sum_{k,l,m=1}^{n} \left.\frac{\partial^3 F_j(\vec{q}, \vec{\mu})}{\partial q_k \partial q_l \partial q_m}\right|_{\vec{q}=0} x_k y_l z_m.$$

Define the inner product between two vectors $\langle \vec{v}, \vec{w} \rangle \equiv \bar{\vec{v}}^T \vec{w}$, where the bar denotes complex conjugation as the vectors $\vec{v}, \vec{w} \in \mathbb{C}^n$ may be complex valued. Let $J(\vec{\mu})$

have an eigenvector $\hat{v}_\mu$ corresponding to the eigenvalue $\xi_\mu = \xi_R(\vec{\mu}) + i\xi_I(\vec{\mu})$, i.e. $J(\vec{\mu})\hat{v}_\mu = \xi_\mu \hat{v}_\mu$. Here the diacritical hat indicates that the vector has unit length: $\langle \hat{v}_\mu, \hat{v}_\mu \rangle = 1$. Lastly, define the adjoint eigenvector $\hat{w}_\mu \in \mathbb{C}^n$: $J(\vec{\mu})^T \hat{w}_\mu = \bar{\xi}_\mu \hat{w}_\mu$, and $\langle \hat{w}_\mu, \hat{v}_\mu \rangle = 1$. The first Lyapunov coefficient is defined to be

$$\ell_1(\vec{\mu}) = \frac{\mathrm{Re}[\mathcal{Z}(\vec{\mu})]}{\xi_I(\vec{\mu})} - \xi_R(\vec{\mu}) \frac{\mathrm{Im}[\mathcal{Z}(\vec{\mu})]}{(\xi_I(\vec{\mu}))^2},$$

in which

$$\begin{aligned} \mathcal{Z}(\vec{\mu}) \; = \tfrac{1}{2} \Big[& \langle \hat{w}_\mu, \vec{C}(\hat{v}_\mu, \hat{v}_\mu, \bar{\hat{v}}_\mu, \vec{\mu}) \rangle + 2 \langle \hat{w}_\mu, \vec{B}(\hat{v}_\mu, ((\xi_\mu + \bar{\xi}_\mu)\mathbb{I}_n - J(\vec{\mu}))^{-1} \vec{B}(\hat{v}_\mu, \bar{\hat{v}}_\mu, \vec{\mu}), \vec{\mu}) \rangle \\ & + \langle \hat{w}_\mu, \vec{B}(\bar{\hat{v}}_\mu, (2\xi_\mu \mathbb{I}_n - J(\vec{\mu}))^{-1} \vec{B}(\hat{v}_\mu, \hat{v}_\mu, \vec{\mu}), \vec{\mu}) \rangle \Big], \end{aligned}$$

and $\mathbb{I}_n$ is the $n \times n$ identity matrix. If the first Lyapunov coefficient is evaluated along a curve of Hopf bifurcations, then a Bautin bifurcation occurs when $\ell_1(\vec{\mu}) = 0$. In other words, because $\xi_R(\vec{\mu}) = 0$ at a Hopf bifurcation, it must be true that $\mathrm{Re}[\mathcal{Z}(\vec{\mu})] = 0$ at the Bautin point.

Chapter 3

Statement of the Problem

The previous chapter discussed how a Hopf bifurcation could underlie a hair bundle's exquisite sensitivity, sharp frequency selectivity, and broad dynamic range. Since the concept was advanced, however, a major criticism of a Hopf bifurcation in hearing has been the precise parameter tuning necessary to reach the level of performance observed in our cochlea [51, 114–121]. The auditory system's ability to detect sound could be compromised by small changes in parameter values that move the system away from a Hopf bifurcation. In other words, the system's function might not be robust to changes in parameter values. Acoustic trauma or pharmacological insults, which undoubtedly affect the system's parameters, can indeed disrupt our hearing [122, 123]. Nonetheless, our hearing ability is less vulnerable than our current understanding of the auditory system might suggest. The present chapter frames the problem faced by a system whose function relies on operating near a Hopf bifurcation: how can such a system be robust to parameter-value perturbations? Possible solutions, old and new, are also introduced.

3.1 High Performance within a Narrow Range

Recent work has shown that individual hair bundles can operate close to a Hopf bifurcation (1.9) [89, 90]. In accord with experimental predictions, it has also been demonstrated that a bundle's peak sensitivity, quality factor, and dynamic range diminish as experimentally accessible parameters are adjusted in manner that shifts the bundle's operating point away from the Hopf bifurcation [89, 92, 124]. Figure 3.1 presents an example of this phenomenon.

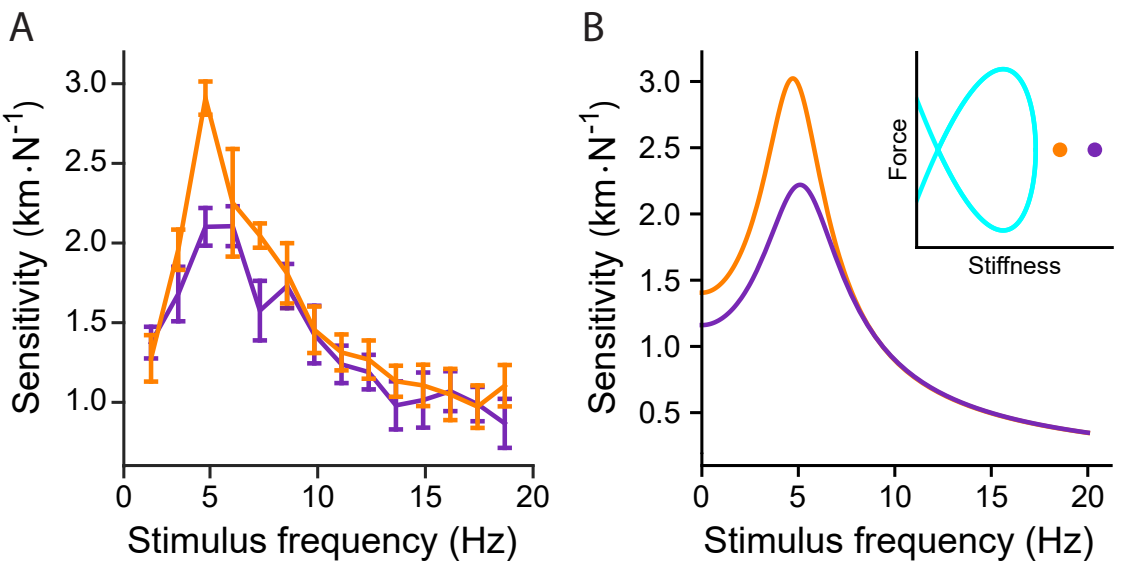

Figure 3.1: The sensitivity of a hair bundle to sinusoidal stimulation. (*A*) Tuning curves for an actual hair bundle from the bullfrog's sacculus commanded to operate at stiffness values closer to (orange, 900 μN·m^{-1}) or farther from (purple, 1000 μN·m^{-1}) the self-oscillation region. The sensitivity of the hair bundle's response to periodic forcing was calculated as the bundle's motion at the driving frequency $\widetilde{x}(\omega_D)$ divided by the amplitude of the stimulus at the driving frequency $\widetilde{F}(\omega_D)$ averaged over replications. The magnitude of the resulting number was taken as $|\bar{\chi}(\omega_D)| = \left|\left\langle \frac{\widetilde{x}(\omega_D)}{\widetilde{F}(\omega_D)} \right\rangle\right|$. The control parameter is the bundle's load stiffness and this bundle traverses a Hopf bifurcation at 710 μN·m^{-1} (Appendix B). Error bars represent the standard errors of the means of four repeated measurements on the same hair bundle. Sinusoidal stimuli 10 pN in amplitude were delivered to the hair bundle directly using a glass fiber (Chapter 6). (*B*) Sensitivity of a hair bundle model close to (orange, 750 μN·m^{-1}) or farther from (purple, 900 μN·m^{-1}) a Hopf bifurcation. The inset schematically depicts the model's state diagram, whose axes are the size of a constant force applied to the bundle and the combined stiffness of the bundle and its overlying load; only positive stiffness values are represented. The Hopf bifurcation curve (cyan) encloses operating points at which the bundle oscillates spontaneously. These tuning curves were obtained from Model II without homeostasis (Eqs. 4.3 and 4.4) with the parameter values listed in Table 4.2, except $\lambda_x = 25$ μN · s · m^{-1}, $\lambda_y = 125$ μN · s · m^{-1}, $P_o^* = 0.5$, and $f = 220$ pN. For this set of parameter values, a Hopf bifurcation occurs at a static deflection, or constant force, of 0 pN and a load stiffness of 248 μN·m^{-1}. From [124].

Imagine that we wish to design a system that can detect very soft sounds while also using only a hundredfold range of response amplitudes to faithfully register tones whose amplitudes span nearly six orders of magnitude. The first specification is achieved if the system's sensitivity surpasses the requisite threshold (Fig. 3.2*A*), and a compressive nonlinearity following a one-third power law can satisfy the second criterion if the compression operates over at least the specified range of stimulus amplitudes (Fig. 3.2*B*). By operating close to a Hopf bifurcation a system can readily attain this level of performance.

However, because such a system's sensitivity and dynamic range decline steeply with increasing distance from the bifurcation ($\approx \mu^{-1}$, Eqs. 2.33 and 2.37), the high performance level will be possible within only a limited range of parameter values. The range may be so narrow that the parameter-value selection and maintenance demanded of the system are incommensurate with the level of precision that is possible for a biological system. In this scenario the system would fail to be robust to parameter variation, for small parameter-value changes could significantly impair the system's ability to detect signals.

The hair bundle is relentlessly bombarded by water molecules and continually subjected to thermal fluctuations in its macromolecular constituents. Owing to stochastic variations during their development, hair bundles exhibit biophysical parameters that embrace a range of values across members of the same species. Despite numerous sources of parameter-value perturbations, hair bundles exhibit high-performance signal detection over several decades of continuous operation in the vast majority of individuals. It is therefore hypothesized that some mechanism ensures the robustness of the hair bundle's signal detection.

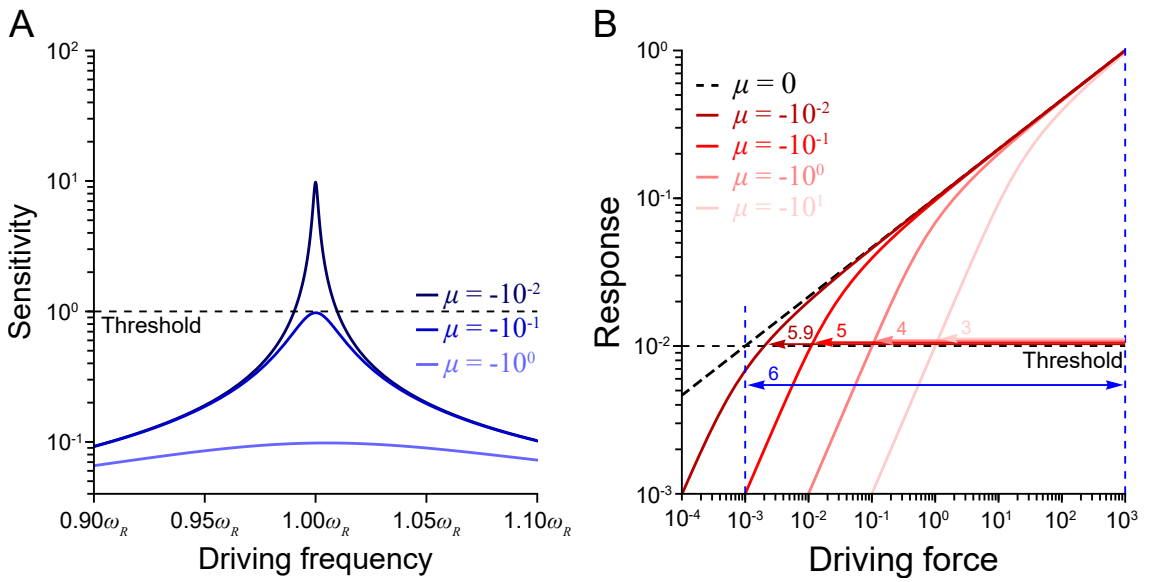

Figure 3.2: High performance within a narrow parameter range. (A) Simulated tuning curves for a hair bundle whose operating point is situated various distances from the Hopf bifurcation. Darker shades of blue indicate operating points that are closer to the bifurcation located at $\mu = 0$. A bundle detects a faint sound if the bundle's sensitivity exceeds the prescribed threshold (dashed line). In the example shown, the hypothetical signal can be detected only when $|\mu| < 0.1$. (B) A bundle has only a limited range of response amplitudes at its disposal, say two orders of magnitude, to represent stimuli: subthreshold responses do not effect a detectable change in the hair cell's membrane potential and responses that exceed the range's maximum damage the bundle. By employing a compressive nonlinearity, a bundle can utilize a limited range of responses to code a much broader range of driving-force amplitudes. A one-third power law arises naturally near a Hopf bifurcation (Eq. 2.42). Unless the bundle is poised exactly at the Hopf bifurcation (dashed, black line, $\mu = 0$), the compressive nonlinearity operates over only a finite range of stimulus amplitudes and the size of this range decreases approximately in proportion to the system's distance from the bifurcation. Consequently, the bundle's dynamic range, defined as the range of stimulus amplitudes that can be represented, is narrower at operating points farther from the bifurcation. Each curve is labeled by the number of orders of magnitude in the span of its dynamic range, which runs from the blue, dashed line on the right to the point at which the curve crosses threshold. A dynamic range spanning six orders of magnitude is obtained exactly at the bifurcation, blue arrow. A bundle might require a dynamic range that covers at least five orders of magnitude. This specification is achieved in this example only if $|\mu| < 0.1$. High performance, as measured by either metric, therefore occurs within only a narrow range of parameter values.

3.2 Previous Solutions and Caveats

The narrow range of parameter values within which the bundle attains the desired performance level corresponds to a thin zone in parameter space–termed the high-performance zone–that abuts the self-oscillation region (Fig. 3.3A). It has previously been suggested that a parameter-tuning mechanism can dynamically adjust a hair bundle's operating point in state space, thus ensuring that the bundle is always poised within the high-performance zone (Fig. 3.3B, C) [51, 115–120, 125]. A parameter-value perturbation activates the mechanism and the value of the offending parameter is tuned back to its set point.

This strategy suffers, however, from a number of difficulties. First, several implementations require the bundle to maintain a representation of the bifurcation's location so that the tuning mechanism stops at the appropriate parameter value [115, 116, 120]. If the tuning mechanism is permitted to cross the Hopf bifurcation then the ensuing hair bundle oscillations would provide an obvious biological readout of the bifurcation's location. Keeping track of critical parameter values becomes more challenging, however, if the system is required to conduct its tuning entirely on the stable of the bifurcation. Other authors have resolved this issues by demonstrating that a system can successfully tune parameters to their critical values without having knowledge of the bifurcation's location [118, 119].

Second, robustness to parameter variation will be guaranteed only for parameters that possess a tuning mechanism. The system would then require a separate tuning mechanism for each bifurcation parameter.

Third, the strategy assumes that the bundle has the ability to adjust the parameters that are responsible for its proximity to the bifurcation. The control parameters

that set the bundle's operating point are often not themselves dynamical variables; technically this is actually never the case (see below).

Finally, the analyses applied to systems that employ this strategy assume that the tuning dynamics do not appreciably change the state diagram, which is shown to not be true in general in Chapter 4. The picture shown in Figure 3.3*B* could be entirely wrong: conferring dynamics upon control parameter 1 could drastically shift or reshape the Hopf bifurcation or other features of the state diagram.

On a more technical note, it is an abuse of terms to call a dynamical variable a control parameter. Because the values of the control parameters dictate a system's steady-state behavior, the system need not be at steady state if a control parameter is dynamic, which contradicts the definition of a control parameter. For a given set of parameter values and initial conditions the system follows a prescribed trajectory. A change in a dynamical variable's value merely reflects the system's time evolution along this trajectory and cannot affect the system's fate–that can be achieved only by adjusting parameter values or by choosing a different set of initial conditions, both of which constitute processes that are external to the system.

In other words, a system's internal dynamics cannot change a system's operating point in the state diagram, for it is precisely the location of the operating point that specifies the behavior to which the system tends as it approaches a steady state. If the operating point's location evolves in time then it is unclear which steady-state behavior the system possesses. "Control parameters" upon which dynamics have been conferred should be counted among the system's internal dynamical variables and not as parameters that determine the system's steady-state behavior, nor should they appear on the axes of state diagrams.

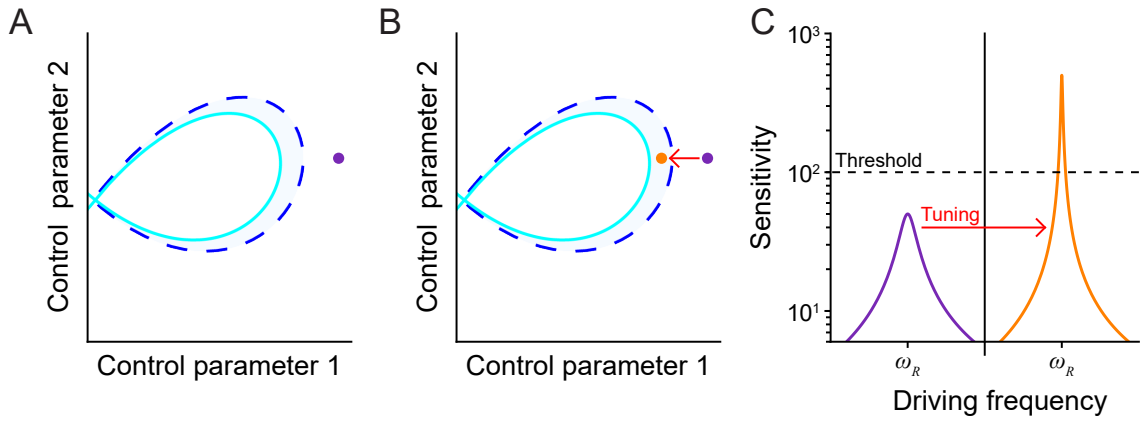

Figure 3.3: Robustness through parameter tuning. (*A*) State diagram for a hair bundle that permits a loop of Hopf bifurcations (solid, cyan curve) that in turn encloses a set of parameter values at which spontaneous oscillations occur. The self-oscillation region is bordered by a zone of high performance (lightly shaded blue area between the Hopf bifurcation curve and the dashed, blue curve). The bundle's sensitivity, for example, exceeds a specified threshold in this region. Because it lies outside of the high-performance zone, the purple dot marks an operating point at which the bundle performs poorly as a signal detector (*C*, left). (*B*) To ensure it maintains a high level of performance, a bundle may be able to dynamically adjust parameter values (red arrow). By tuning parameters to be near their critical values, such a strategy would enable a system to maintain its proximity to a Hopf bifurcation (orange dot). (*C*) In moving its operating point closer to the Hopf bifurcation, the bundle would attain a higher level of performance (left to right).

3.3 Robustness Enhancement by Homeostasis

Rather than tuning parameters to their critical values, I propose that a homeostatic mechanism increases the range of parameter values for which a bundle is sufficiently sensitive to periodic stimuli. This strategy, which I call robustness enhancement, in essence broadens the range of the Hopf bifurcation's influence and consequently eases the demands on the system to precisely set its control parameter values (Fig. 3.4). By decreasing the steepness of various performance metrics' decline with increasing distance from the bifurcation, this mechanism endows the system with a means of maintaining effective operation, termed homeostasis of function.

Considering that the high-performance zone envelops the self-oscillation region, one might heuristically expect that enlarging the latter would effect a concomitant expansion of the former. The remainder of this section undertakes a general analysis to validate this hypothesis. Two homeostatic mechanisms employed in disparate models of hair bundle motility are discussed in detail in the following chapter. In addition to being biologically plausible, both mechanisms render the bundle's signal detection more robust to parameter variation by enlarging the self-oscillation region. The following calculations suggest that this constitutes a general strategy that can be applied to any system that depends on a Hopf bifurcation to function effectively.

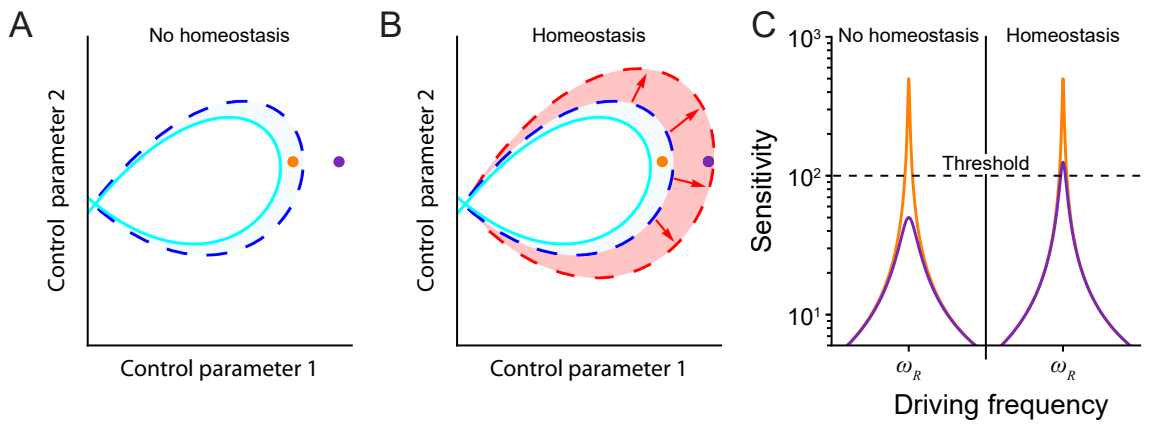

Figure 3.4: Robustness enhancement by means of homeostasis. (*A*) Without homeostasis, the bundle is capable of high-performance signal detection within only a narrow range of parameter values (lightly shaded blue region). Because the bundle's sensitivity declines with increasing distance from the Hopf bifurcation (cyan curve), a small-amplitude stimulus may be detected by a bundle operating at the orange point but not at the purple point (*C*, left). (*B*) When engaged, a homeostatic mechanism could broaden the influence of the Hopf bifurcation, thereby expanding the high-performance zone. Portrayed is a realization of such a strategy that has added the lightly shaded red region to the high-performance zone, which now contains the purple operating point (*C*, right). The boundary of the new high-performance zone (dashed, red curve) is static: the proposed homeostatic mechanism does not dynamically adjust the positions of contours or operating points in parameter space. Rather, different realizations of the homeostatic mechanism augments the high-performance zone by different degrees. (*C*). The decline in the bundle's sensitivity with increasing distance from the bifurcation is rendered less steep by the homeostatic mechanism. Signal detection is consequently more robust because a high level of performance is achieved for a broader range of parameter values. Middle panel modified from [124].

Consider a system that depends on parameters $\vec{\mu}$ and permits Hopf bifurcations along the parametric curve $\vec{\mu}_c(\theta) = \{\mu_{c,x}(\theta), \mu_{c,y}(\theta)\} = \mu_c(\theta)\hat{\mu}_c(\theta)$, $\mu_c(\theta) = |\vec{\mu}_c(\theta)| = \sqrt{\mu_{c,x}^2(\theta) + \mu_{c,y}^2(\theta)}$, in parameter space $\{\mu_x, \mu_y\}$. Let this curve form a closed loop, i.e. $\vec{\mu}_c(\theta_-) = \vec{\mu}_c(\theta_+)$, and let the signed curvature of $\vec{\mu}_c$ be nonnegative on the interval $\theta \in [\theta_-, \theta_+]$:

$$\text{Curv}(\theta) = \frac{\partial_\theta \mu_{c,x} \partial_\theta^2 \mu_{c,y} - \partial_\theta \mu_{c,y} \partial_\theta^2 \mu_{c,x}}{[(\partial_\theta \mu_{c,x})^2 + (\partial_\theta \mu_{c,y})^2]^{3/2}} \geq 0 \ \ \forall \ \theta \in [\theta_-, \theta_+].$$

Designate the inside of the loop as the unstable side of the Hopf bifurcation so that spontaneous oscillations occur in the system for only a finite range of parameter values $\vec{\mu}$. Finally, let the system possess a property whose value $\mathcal{P}$ has a power-law dependence on the system's distance s from the Hopf bifurcation when measured along a line of constant θ:

$$\mathcal{P}(s) = |(s\hat{\mu}_c(\theta) + \vec{\mu}_c(\theta)) - \vec{\mu}_c(\theta)|^\nu = |s|^\nu, \qquad s > 0.$$

This analysis is restricted to the stable side of the bifurcation by requiring $s > 0$. Requiring that $\text{Curv}(\theta) \geq 0 \ \forall \ \theta \in [\theta_-, \theta_+]$ ensures that $\mathcal{P}$ is a single-valued function outside the bifurcation loop. $\mathcal{P}(s)$ could, for instance, represent the system's sensitivity to sinusoidal stimulation.

Next, inflate the size of the loop by a dilation factor h: $\vec{\mu}_c(\theta) \to h\vec{\mu}_c(\theta)$. This scaling multiplies the area within $\vec{\mu}_c(\theta)$ by h^2. Assume, however, that the power-law dependence of $\mathcal{P}$ does not change:

$$\mathcal{P}(s) = |(s\hat{\mu}_c(\theta) + h\vec{\mu}_c(\theta)) - h\vec{\mu}_c(\theta)|^\nu = |s|^\nu.$$

At some point $\vec{\mu}$ outside the loop, $\mathcal{P}$ takes on the value $\mathcal{P} = |\vec{\mu}(\theta) - h\vec{\mu}_c(\theta)|^\nu$. Solving for $\vec{\mu}$ yields contours of constant $\mathcal{P}$ values

$$\vec{\mu}(\mathcal{P}, h, \theta) = h\vec{\mu}_c(\theta) + \mathcal{P}^{1/\nu}\hat{\mu}_c(\theta) = (h\mu_c(\theta) + \mathcal{P}^{1/\nu})\hat{\mu}_c(\theta), \tag{3.1}$$

which can also be written as $\vec{\mu}(\mathcal{P}, h, \theta) = (h\mu_c(\theta) + s)\hat{\mu}_c(\theta)$.

Assuming it forms a closed loop, the area contained within $\vec{\mu}(\mathcal{P}, h, \theta)$ can be found using Stoke's theorem. Let $\vec{U}$ be a vector field with $\vec{\nabla} \times \vec{U}$ a unit vector field perpendicular to the surface Σ. Stoke's theorem then states that

$$\oint_{\partial\Sigma} \vec{U} \cdot d\vec{r} = \iint_{\Sigma} \vec{\nabla} \times \vec{U} \cdot d\vec{\Sigma} = \Sigma, \tag{3.2}$$

in which $\partial\Sigma$ is the boundary curve of Σ with the normal vector field $d\vec{\Sigma}$ and $\vec{r}$ is a parameterization of $\partial\Sigma$. Stoke's theorem reveals that the area Σ can be found by performing a line integral around the boundary of Σ. The curve of interest is

$$\vec{r} = \vec{\mu}(\mathcal{P}, h, \theta) = (h\mu_c(\theta) + \mathcal{P}^{1/\nu})\hat{\mu}_c(\theta) = \left(h + \frac{P^{1/\nu}}{\mu_c(\theta)}\right)\{\mu_{c,x}(\theta), \mu_{c,y}(\theta)\}.$$

The differential tangent-vector field along the curve $\vec{r}$ is then

$$d\vec{\mu} = \frac{\partial}{\partial\theta}\{\mu_x(\theta), \mu_y(\theta)\}d\theta = \frac{\partial}{\partial\theta}\left\{\left(h + \frac{P^{1/\nu}}{\mu_c(\theta)}\right)\mu_{c,x}(\theta), \left(h + \frac{P^{1/\nu}}{\mu_c(\theta)}\right)\mu_{c,y}(\theta), 0\right\}d\theta,$$

Various vector fields $\vec{U}$ may be used in the line integral; any whose curl is 1 suffices. Two simple examples are

$$\vec{U} = \{0, \mu_x(\theta), 0\} \quad \text{or} \quad \vec{U} = \{-\mu_y(\theta), 0, 0\}.$$

The area enclosed by the loop is then given by

$$\text{Area}(\mathcal{P}, h) = \int_{\theta_1}^{\theta_2} \left(h + \frac{P^{1/\nu}}{\mu_c(\theta)}\right)\mu_{c,x}(\theta)\frac{\partial}{\partial\theta}\left[\left(h + \frac{P^{1/\nu}}{\mu_c(\theta)}\right)\mu_{c,y}(\theta)\right]d\theta, \tag{3.3}$$

$$\text{or by} \quad \text{Area}(\mathcal{P}, h) = -\int_{\theta_1}^{\theta_2} \left(h + \frac{P^{1/\nu}}{\mu_c(\theta)}\right)\mu_{c,y}(\theta)\frac{\partial}{\partial\theta}\left[\left(h + \frac{P^{1/\nu}}{\mu_c(\theta)}\right)\mu_{c,x}(\theta)\right]d\theta, \tag{3.4}$$

in which θ_1 and θ_2 are the values at which the curve crosses itself. Noting that $\mu_c(\theta) = \sqrt{\mu_{c,x}^2(\theta) + \mu_{c,y}^2(\theta)}$, these integrals become

$$\text{Area}(\mathcal{P}, h) =$$

$$h^2 \int_{\theta_1}^{\theta_2} \mu_{c,x} \partial_\theta \mu_{c,y} \, d\theta + h\mathcal{P}^{1/\nu} \int_{\theta_1}^{\theta_2} [(2\mu_{c,x}^2 + \mu_{c,y}^2)\partial_\theta \mu_{c,y} - \mu_{c,x}\mu_{c,y}\partial_\theta \mu_{c,x}] \frac{\mu_{c,x}}{\mu_c^3} \, d\theta$$

$$+ \mathcal{P}^{2/\nu} \int_{\theta_1}^{\theta_2} [\mu_{c,x}\partial_\theta \mu_{c,y} - \mu_{c,y}\partial_\theta \mu_{c,x}] \frac{\mu_{c,y}^2}{\mu_c^4} \, d\theta \text{ and} \tag{3.5}$$

$$\text{Area}(\mathcal{P}, h) =$$

$$- h^2 \int_{\theta_1}^{\theta_2} \mu_{c,y} \partial_\theta \mu_{c,x} \, d\theta + h\mathcal{P}^{1/\nu} \int_{\theta_1}^{\theta_2} [\mu_{c,y}\mu_{c,x}\partial_\theta \mu_{c,y} - (2\mu_{c,y}^2 + \mu_{c,x}^2)\partial_\theta \mu_{c,x}] \frac{\mu_{c,y}}{\mu_c^3} \, d\theta$$

$$+ \mathcal{P}^{2/\nu} \int_{\theta_1}^{\theta_2} [\mu_{c,x}\partial_\theta \mu_{c,y} - \mu_{c,y}\partial_\theta \mu_{c,x}] \frac{\mu_{c,x}^2}{\mu_c^4} \, d\theta. \tag{3.6}$$

The integrals multiplying the h^2 terms in equations 3.5 and 3.6 give the area contained within the loop of Hopf bifurcations and must therefore be positive. The other integrals contain $\mu_{c,x}\partial_\theta \mu_{c,y}$ and -$\mu_{c,y}\partial_\theta \mu_{c,x}$ multiplied by positive numbers ($\mu_{c,x}^2$ or $\mu_{c,y}^2$ divided by powers of μ_c) and are thus also positive, confirming that dilating the self-oscillation region generically effects a concomitant expansion of the high-performance zone, the area contained within a given $\mathcal{P}$ contour.

How the size of the high-performance region depends on the dilation factor h can be found as follows. Each integral in Equation 3.5 evaluates to some positive number that depends only on the geometry of the bifurcation loop. Replacing each integral with a constant, with A_0 representing the area enclosed by $\vec{\mu}_c$,

$$\text{Area}(\mathcal{P}, h) = A_0 h^2 + c_1 \mathcal{P}^{1/\nu} h + c_2 \mathcal{P}^{2/\nu}. \tag{3.7}$$

Dilating each dimension of the bifurcation loop by h effects an increase in the area contained within a constant-$\mathcal{P}$ contour by the factor

$$\frac{\text{Area}(\mathcal{P},h)}{\text{Area}(\mathcal{P},1)} \equiv \mathcal{R}(\mathcal{P},h) = \frac{A_0h^2 + c_1\mathcal{P}^{1/\nu}h + c_2\mathcal{P}^{2/\nu}}{A_0 + c_1\mathcal{P}^{1/\nu} + c_2\mathcal{P}^{2/\nu}}. \tag{3.8}$$

The quadratic form of Equation 3.8 is expected: scaling each dimension of a two-dimensional object by h scales the object's area by h^2.

Appropriate limits reveal that $\mathcal{R}(\mathcal{P},h)$ is always greater than 1, but cannot exceed h^2 (Fig. 3.5*A*). Assuming $\mathcal{P} > 1$ and $h > 1$:

$$\lim_{\nu\to 0^+} \mathcal{R}(\mathcal{P},h) = 1 \;<\; \lim_{\nu\to\pm\infty} \mathcal{R}(\mathcal{P},h) = \frac{A_0h^2 + c_1h + c_2}{A_0 + c_1 + c_2} \;<\; \lim_{\nu\to 0^-} \mathcal{R}(\mathcal{P},h) = h^2. \tag{3.9}$$

The $\nu \to 0^+$ and $\nu \to 0^-$ limits are switched if $\mathcal{P} < 1$. Assuming $\nu < 0$ and $h > 1$:

$$\lim_{\mathcal{P}\to 0^+} \mathcal{R}(\mathcal{P},h) = 1 \;<\; \mathcal{R}(1,h) = \frac{A_0h^2 + c_1h + c_2}{A_0 + c_1 + c_2} \;<\; \lim_{\mathcal{P}\to\infty} \mathcal{R}(\mathcal{P},h) = h^2. \tag{3.10}$$

If instead $\nu > 0$, the $\mathcal{P} \to 0^+$ and $\mathcal{P} \to \infty$ limits are exchanged. If $\mathcal{P} = 1$, $\mathcal{R}(1,h)$ is independent of ν: the range of possible parabolas collapses to the single parabola given above.

Excluding the area enclosed by the bifurcation loop yields

$$\text{Area}_{\mathcal{P}}(h) = A_0h^2 + c_1h\mathcal{P}^{1/\nu} + c_2\mathcal{P}^{2/\nu} - A_0h^2 = c_1h\mathcal{P}^{1/\nu} + c_2\mathcal{P}^{2/\nu}. \tag{3.11}$$

As h increases, this area grows as

$$\frac{\text{Area}_{\mathcal{P}}(h)}{\text{Area}_{\mathcal{P}}(1)} \equiv \mathcal{R}_{\mathcal{P}}(h) = \frac{c_1h + c_2\mathcal{P}^{1/\nu}}{c_1 + c_2\mathcal{P}^{1/\nu}}, \tag{3.12}$$

which is linear in the dilation factor h. This dependence is also expected. Imagine partitioning the annular region between $\vec{\mu}(\mathcal{P},h,\theta)$ and $\vec{\mu}_c(\theta)$ into infinitesimal slices

within which θ is approximately constant. The area of such a slice dA at a particular θ will be approximately equal to the width of the slice $|\vec{\mu}(\mathcal{P}, h, \theta) - h\vec{\mu}_c(\theta)|$ times the infinitesimal arc length passing through the middle of the slices, $d\vec{r} \approx d\theta\,[\vec{\mu}(\mathcal{P}, h, \theta) + h\vec{\mu}_c(\theta)]/2$. Substitution yields:

$$dA \approx \mathcal{P}^{1/\nu}(h\mu_c(\theta) + \mathcal{P}^{1/\nu}/2)\,d\theta. \tag{3.13}$$

The entire area involves integrating out θ, but this does not change the dependence of dA on h. Thus, $\text{Area}_{\mathcal{P}}(h) \propto h$.

Taking the same limits as above reveals that $\mathcal{R}_{\mathcal{P}}(h)$ must lie between 1 and h (Fig. 3.5*B*). Assuming $\mathcal{P} > 1$ and $h > 1$:

$$\lim_{\nu\to 0^+} \mathcal{R}_{\mathcal{P}}(h) = 1 \;<\; \lim_{\nu\to\pm\infty} \mathcal{R}_{\mathcal{P}}(h) = \frac{c_1 h + c_2}{c_1 + c_2} \;<\; \lim_{\nu\to 0^-} \mathcal{R}_{\mathcal{P}}(h) = h. \tag{3.14}$$

The $\nu \to 0^+$ and $\nu \to 0^-$ limits are switched if $\mathcal{P} < 1$. Assuming $\nu < 0$ and $h > 1$:

$$\lim_{\mathcal{P}\to 0^+} \mathcal{R}_{\mathcal{P}}(h) = 1 \;<\; \mathcal{R}_1(h) = \frac{c_1 h + c_2}{c_1 + c_2} \;<\; \lim_{\mathcal{P}\to\infty} \mathcal{R}_{\mathcal{P}}(h) = h. \tag{3.15}$$

If instead $\nu > 0$, the $\mathcal{P} \to 0^+$ and $\mathcal{P} \to \infty$ limits are again exchanged.

The preceding calculations demonstrate that if dilating the bifurcation loop does not change the power-law dependence between $\mathcal{P}$ and s (i.e. ν does not depend on h), then the area enclosed by $\mathcal{P}$ contours is guaranteed to increase. Relaxing this requirement, it is possible to find an upper bound on the change in ν that would still allow the area enclosed by a $\mathcal{P}$ contour to expand. Assuming the change is uniform in θ, $\Delta\nu$ can be found from Equation 3.11:

$$\text{Area}_{\mathcal{P}}(h, \nu + \Delta\nu) = \text{Area}_{\mathcal{P}}(1, \nu) \quad\Rightarrow\quad c_1 h \mathcal{P}^{1/(\nu+\Delta\nu)} + c_2 \mathcal{P}^{2/(\nu+\Delta\nu)} = c_1 \mathcal{P}^{1/\nu} + c_2 \mathcal{P}^{2/\nu}.$$

Solving for $\Delta\nu$

$$|\Delta\nu| < \left| \nu - \frac{\ln[\mathcal{P}]}{\ln\left[\frac{1}{2c_1 h}\left(\sqrt{c_2^2 + 4c_1 c_2 h \mathcal{P}^{1/2\nu} + 4c_1^2 h \mathcal{P}^{1/\nu}} - c_2\right)\right]} \right|. \tag{3.16}$$

If this inequality is satisfied, the area between $\vec{\mu}(,h,\nu+\Delta\nu,\theta)$ and $\vec{\mu}_c(h,\theta)$ expands[1].

Two examples confirm the findings of the preceding calculations. First, let $\vec{\mu}_c(\theta)$ describe a circle with radius μ_c (Figs. 3.5C, D):

$$\vec{\mu}_c(\theta) = \{\mu_c \cos\theta, \mu_c \sin\theta\}, \quad |\vec{\mu}_c(\theta)| = \mu_c, \quad \frac{\vec{\mu}_c(\theta)}{\mu_c} \equiv \hat{\mu}_c(\theta) = \{\cos\theta, \sin\theta\}.$$

Dilating the circle is achieved by multiplying h into $\vec{\mu}_c(\theta)$. As before, let the system possess some property whose value is governed by $\mathcal{P} = |\vec{\mu}(\theta) - h\vec{\mu}_c(\theta)|^\nu$. Then $\vec{\mu}(\mathcal{P}) = h\vec{\mu}_c + \mathcal{P}^{1/\nu}\hat{\mu}_c$, and

$$\text{Area}(\mathcal{P}, h) = \pi|\vec{\mu}(\mathcal{P})|^2 = \pi(h\mu_c + \mathcal{P}^{1/\nu})^2. \tag{3.17}$$

Note that the above result is 2π times Equation 3.13: the approximation given for dA is exact when the bifurcation loop is a circle. For a dilation factor h, the area contained within a $\mathcal{P}$ contour is multiplied by

$$\frac{\text{Area}(\mathcal{P}, h)}{\text{Area}(\mathcal{P}, 1)} \equiv \mathcal{R}(\mathcal{P}, h) = \left(\frac{h\mu_c + \mathcal{P}^{1/\nu}}{\mu_c + \mathcal{P}^{1/\nu}}\right)^2, \tag{3.18}$$

which is Equation 3.8 with $A_0 = \pi\mu_c^2$, $c_1 = 2\pi\mu_c$, and $c_2 = \pi$. Subtracting the area enclosed by the bifurcation curve yields

$$\text{Area}_\mathcal{P}(h) = \pi(h\mu_c + \mathcal{P}^{1/\nu})^2 - \pi h^2 \mu_c^2 = \pi(2h\mu_c \mathcal{P}^{1/\nu} + \mathcal{P}^{2/\nu}), \tag{3.19}$$

[1] If the area contained within $\vec{\mu}_c(h,\theta)$ is included, then the inequality becomes

$$|\Delta\nu| < \left| \nu - \frac{\ln[\mathcal{P}]}{\ln\left[\frac{1}{2c_1 h}\left(\sqrt{c_2^2 + 4c_1 c_2 h \mathcal{P}^{1/2\nu} + 4c_1 h(A_0 - A_0 h^2 - c_1 \mathcal{P}^{1/\nu})} - c_2\right)\right]} \right|,$$

which is possible only if $h < \sqrt{1 + \frac{c_2}{A_0}\mathcal{P}^{1/2\nu} + \frac{c_1}{A_0}\mathcal{P}^{1/\nu}}$. In other words, for large enough h the area is guaranteed to increase.

and the scaling factor for the remaining annular region is

$$\frac{\text{Area}_{\mathcal{P}}(h)}{\text{Area}_{\mathcal{P}}(1)} \equiv \mathcal{R}_{\mathcal{P}}(h) = \frac{2h\mu_c + \mathcal{P}^{1/\nu}}{2\mu_c + \mathcal{P}^{1/\nu}}. \tag{3.20}$$

The limiting values of equations 3.18 and 3.20 are the same as those given for the general case.

A second example, which resembles more closely the situation in models of hair bundle motility, is given by (Figs. $3.5E, F$):

$$\vec{\mu}_c(\theta) = \{\mu_c \cos(3\theta)\cos(\theta), \mu_c \cos(3\theta)\sin(\theta)\}, \quad \theta \in [\text{-}\pi/6, \pi/6],$$

$$|\vec{\mu}_c(\theta)| = \mu_c|\cos(3\theta)|, \quad \frac{\vec{\mu}_c(\theta)}{\mu_c} \equiv \hat{\mu}_c(\theta) = \text{sign}[\cos(3\theta)]\{\cos\theta, \sin\theta\}.$$

On the interval $\text{-}\pi/6 \leq \theta \leq \pi/6$, $\text{sign}[\cos(3\theta)] \geq 0$, so this term can be dropped for now. The dilated loop is $h\vec{\mu}_c(\theta)$, $\mathcal{P} = |\vec{\mu}(\theta) - h\vec{\mu}_c(\theta)|^\nu$, and

$$\vec{\mu}(\mathcal{P}, \theta) = h\vec{\mu}_c(\theta) + \mathcal{P}^{1/\nu}\hat{\mu}_c(\theta) = \left(h\mu_c \cos(3\theta) + \mathcal{P}^{1/\nu}\right)\{\cos\theta, \sin\theta\}.$$

The infinitesimal tangent vector is then

$$d\vec{\mu} = \big\{ - 3h\mu_c \sin(3\theta)\cos(\theta) - \left(h\mu_c\cos(3\theta) + \mathcal{P}^{1/\nu}\right)\sin(\theta),$$
$$- 3h\mu_c \sin(3\theta)\sin(\theta) + \left(h\mu_c\cos(3\theta) + \mathcal{P}^{1/\nu}\right)\cos(\theta), 0\big\}.$$

Finally, $\vec{U} = \{0, \mu_x, 0\} = \{0, (h\mu_c\cos(3\theta) + \mathcal{P}^{1/\nu})\cos(\theta), 0\}$ serves as the vector field in the line integrals. Because $\vec{\mu}(\mathcal{P}, \theta)$ does not form a closed loop on the interval $\text{-}\pi/6 \leq \theta \leq \pi/6$, the path can be closed a few different ways. One option is to extend the interval of integration to $\theta \in [\text{-}\cos^{\text{-}1}[-\mathcal{P}^{1/\nu}/h\mu_c]/3, \cos^{\text{-}1}[-\mathcal{P}^{1/\nu}/h\mu_c]/3]$, where it is assumed that $\mu_c > 1$, $h > 1$, $\chi > 1$, and $\nu < 0$, or that $\mu_c > 1$, $h > 1$, $\nu > 0$, and $\chi < 1$ to ensure $\cos^{\text{-}1}[-\mathcal{P}^{1/\nu}/h\mu_c]$ is real-valued. In this case, the area contained

within a $\mathcal{P}$ contour is

$$\text{Area}(\mathcal{P},h)=\int_{-\cos^{-1}\left[-\frac{\mathcal{P}^{1/\nu}}{h\mu_c}\right]/3}^{\cos^{-1}\left[-\frac{\mathcal{P}^{1/\nu}}{h\mu_c}\right]/3}\Big[(h\mu_c\cos(3\theta)+\mathcal{P}^{1/\nu})^2\cos^2(\theta)$$

$$-(h\mu_c\cos(3\theta)+\mathcal{P}^{1/\nu})\cos(\theta)3h\mu_c\sin(3\theta)\sin(\theta)\Big]\,d\theta, \tag{3.21}$$

$$\text{Area}(\mathcal{P},h)=\frac{1}{6}\left[(\mu_c^2h^2+2\mathcal{P}^{2/\nu})\sec^{-1}\left[-\frac{\mu_ch}{\mathcal{P}^{1/\nu}}\right]+3\mathcal{P}^{1/\nu}\mu_ch\sqrt{1-\left(\frac{\mathcal{P}^{1/\nu}}{\mu_ch}\right)^2}\right]. \tag{3.22}$$

Assuming $\mathcal{P}^{1/\nu}/\mu_ch$ is small,

$$\text{Area}(\mathcal{P},h)\approx\frac{1}{12}\left[\pi\mu_c^2h^2+2\mathcal{P}^{1/\nu}\mu_ch+6\mathcal{P}^{1/\nu}+2\pi\mathcal{P}^{2/\nu}\right], \tag{3.23}$$

$$\mathcal{R}(\mathcal{P},h)\approx\frac{\pi\mu_c^2h^2+2\mathcal{P}^{1/\nu}\mu_ch+6\mathcal{P}^{1/\nu}+2\pi\mathcal{P}^{2/\nu}}{\pi\mu_c^2+2\mathcal{P}^{1/\nu}\mu_c+6\mathcal{P}^{1/\nu}+2\pi\mathcal{P}^{2/\nu}}. \tag{3.24}$$

The area contained withing the bifurcation curve is equal to $\pi h^2\mu_c^2/12$:

$$\text{Area}_{\mathcal{P}}(h)\approx\frac{1}{6}\left[\mathcal{P}^{1/\nu}\mu_ch+3\mathcal{P}^{1/\nu}+\pi\mathcal{P}^{2/\nu}\right], \tag{3.25}$$

$$\mathcal{R}_{\mathcal{P}}(h)\approx\frac{\mu_ch+3+\pi\mathcal{P}^{1/\nu}}{\mu_c+3+\pi\mathcal{P}^{1/\nu}}. \tag{3.26}$$

Another way to close the loop is to perform integral 3.21 over the interval -$\pi/6\leq\theta\leq\pi/6$, then integrate down the ray $\theta=\pi/6$ to the origin, and finally from the origin along the ray $\theta=-\pi/6$ to join the beginning of the path. Along the rays, $\vec{\mu}(r,\pm\pi/6)=\{r,r\tan[\pm\pi/6]\}=\{r,\pm r/\sqrt{3}\}$, $d\vec{\mu}(r,\pm\pi/6)=\{1,\pm1/\sqrt{3},0\}$, $\vec{U}=\{0,r,0\}$, and $r\in[\pm\sqrt{3}\mathcal{P}^{1/\nu}/2,0]$. The desired area is thus:

$$\begin{aligned}\text{Area}(\mathcal{P},h) = &\int_{\text{-}\pi/6}^{\pi/6} \Big[(h\mu_c\cos(3\theta)+\mathcal{P}^{1/\nu})^2\cos^2(\theta) \\ &- (h\mu_c\cos(3\theta)+\mathcal{P}^{1/\nu})\cos(\theta)3h\mu_c\sin(3\theta)\sin(\theta)\Big]\,d\theta \\ &+ \int_{\sqrt{3}\mathcal{P}^{1/\nu}/2}^{0} \frac{r}{\sqrt{3}}\,dr - \int_{0}^{\text{-}\sqrt{3}\mathcal{P}^{1/\nu}/2} \frac{r}{\sqrt{3}}\,dr,\end{aligned}$$

$$\text{Area}(\mathcal{P},h) = \frac{1}{12}\left[\pi\mu_c^2h^2 + 8\mathcal{P}^{1/\nu}\mu_c h + 2\pi\mathcal{P}^{2/\nu}\right], \text{ and} \tag{3.27}$$

$$\mathcal{R}(\mathcal{P},h) = \frac{\pi\mu_c^2h^2 + 8\mathcal{P}^{1/\nu}\mu_c h + 2\pi\mathcal{P}^{2/\nu}}{\pi\mu_c^2 + 8\mathcal{P}^{1/\nu}\mu_c + 2\pi\mathcal{P}^{2/\nu}}. \tag{3.28}$$

Finally,

$$\text{Area}_{\mathcal{P}}(h) = \frac{1}{6}\left[4\mathcal{P}^{1/\nu}\mu_c h + \pi\mathcal{P}^{2/\nu}\right] \text{ and } \mathcal{R}_{\mathcal{P}}(h) = \frac{4\mu_c h + \pi\mathcal{P}^{1/\nu}}{4\mu_c + \pi\mathcal{P}^{1/\nu}}. \tag{3.29}$$

It is not immediately apparent whether one method for closing the loop should be favored over the other. The second method is slightly more computationally intensive and excludes significant portions of the state diagram, but yields a more tractable, closed-form solution. In extending the $\mathcal{P}$ contours the first method requires a violation of the assumption $\mathcal{P} = s^{\nu}$: points in the state diagram outside $\text{-}\pi/6 \leq \theta \leq \pi/6$ do not reside on lines of constant θ that intersect the bifurcation curve. This difficulty might, however, be an artifact of how the problem was framed: in other systems there might exist a natural way to extend contours to form closed loops.

The analyses in this section were restricted to power-law dependences. The stated results, however, should hold for any monotonic function. Namely, the area of a region that resides between some property's contour and a curve of Hopf bifurcations should increase in proportion to the multiplicative factor that scales the area enclosed by

the bifurcation curve. This effect arises entirely from geometry and is universal; different geometries merely determine the details of the proportionality constant. Some geometries will allow for a more efficient expansion of the high-performance zone. For example, a greater dilation of the high-performance zone is seen in the circular geometry than in the loop geometry for any dilation factor $h > 1$.

If the dependence of the bundle's sensitivity on the system's distance from the bifurcation is unaffected by dilating the self-oscillation region, then expanding this region guarantees that the area contained by the sensitivity contours also increases, and in turn renders the bundle's sensitivity more robust to parameter-value variations. If the relation is affected, gains in robustness can still be achieved if the change in the power law is not too great (Eq. 3.16). On the other hand, changes in the correct direction, i.e. ν becoming less negative when $\mathcal{P} > 1$, could engender additional robustness enhancement, possibly above the calculated upper limit (Eqs. 3.14), or even supralinear improvements.

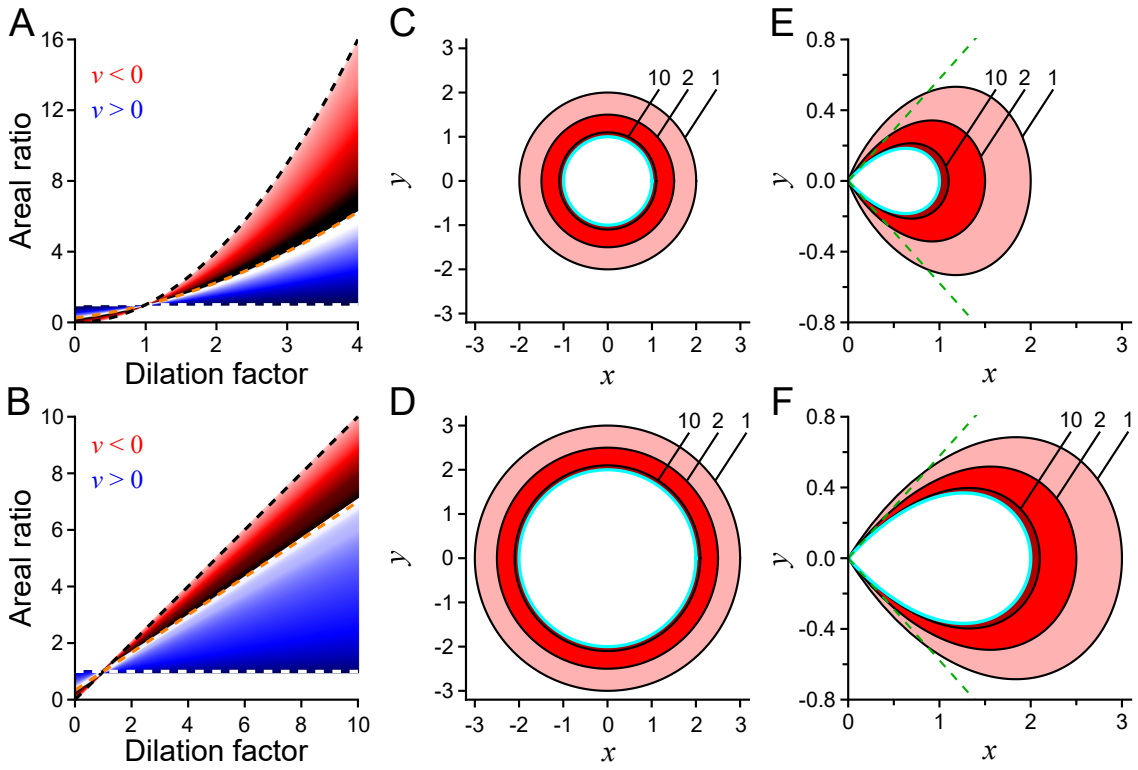

Figure 3.5: Heuristic solution. (A) The ratio $\mathcal{R}(\mathcal{P}, h)$ of the areas contained by the $\mathcal{P} = 10$ contour before and after the Hopf bifurcation curve was scaled by a dilation factor h. A power-law dependence with exponent ν is assumed between $\mathcal{P}$ and the system's distance from the bifurcation curve. Red shades indicate $\nu < 0$ and blue shades indicate $\nu > 0$. When $h > 1$, the upper limit is h^2 (black, dashed line, $\nu \to 0^-$), and the lower bound is 1 (white, dashed line, $\nu \to 0^+$). The orange, dashed line marks $\mathcal{R}(\mathcal{P}, h)$ in the limit that $\nu \to \pm\infty$, which coincides with $\mathcal{R}(\mathcal{P} = 1, h)$. A particular realization of the general case is shown. The specific location of the orange, dashed line is determined by the geometry of the bifurcation curve and by the value of $\mathcal{P}$. If instead $\mathcal{P} < 1$, the red shades indicate $\nu > 0$ and the blue shades indicate $\nu < 0$, but the orange, dashed curve still marks $\mathcal{R}(\mathcal{P}, h)$ in the limit that $\nu \to \pm\infty$. (B) Same as panel A except for $\mathcal{R}_{\mathcal{P}}(h)$, in which the area enclosed by the bifurcation curve is excluded. (C, D) $\mathcal{P}$ contours around a circular Hopf bifurcation curve before (C) and after (D) the curve has been dilated by a factor of two. The area enclosed by a given contour is larger after dilating the bifurcation curve. (E, F) Same as panels C and D except for a different geometry. The green, dashed lines mark $\theta = \pm\pi/6$. In panels $C - F$ the bifurcation curve is shown in cyan and each contour is labeled by its $\mathcal{P}$ value.

Appendix B: Experimental Localization of a Hopf Bifurcation

Hartigans' dip statistic may be employed to experimentally identify the stiffness value at which an actual hair bundle exhibits a supercritical Hopf bifurcation [89, 90, 126]. The position distribution for a quiescent bundle is unimodal, whereas a spontaneously oscillating bundle yields a multimodal distribution. Larger values of the dip statistic arise from multimodal distributions; unimodal distributions possess smaller values. The transition from unimodal to multimodal, which occurs when the dip statistic reaches a statistically significant value, signals a bifurcation. Setting the p-value threshold at 0.01 yields statistically significant dip values, and thus indicates spontaneous oscillations, for stiffnesses less than 710 μN$\cdot$m^{-1} (Fig, 3.6).

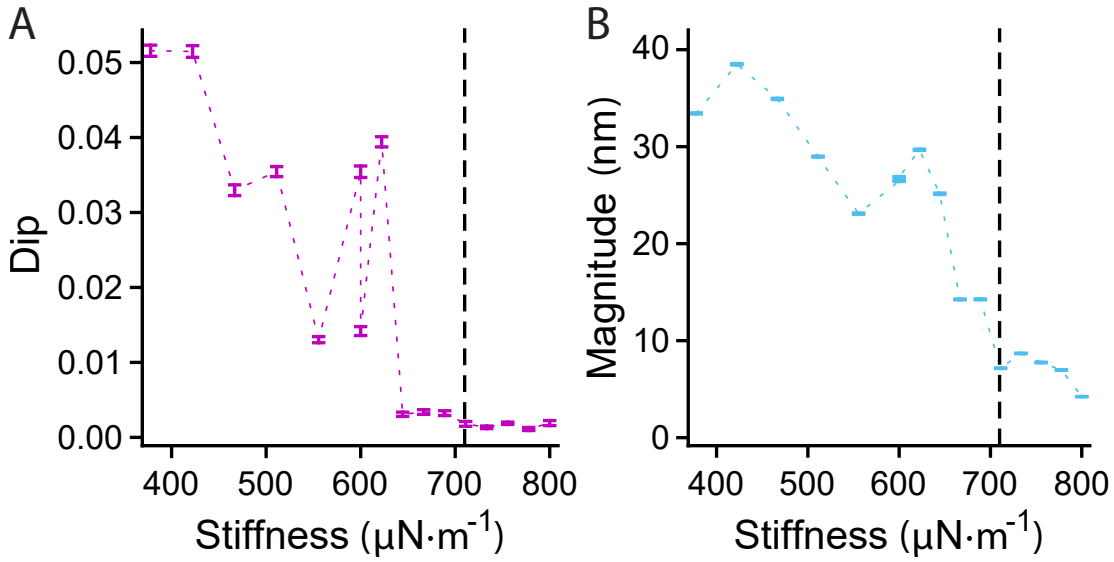

Figure 3.6: Experimental localization of a supercritical Hopf bifurcation in an actual hair bundle. (*A*) To the left of the dashed line at 710 μN·m^{-1} the hair bundle oscillates spontaneously. (*B*) The dependence of a hair bundle's root-mean-square magnitude of oscillation on load stiffness. In qualitative agreement with the behavior expected in the vicinity of a supercritical Hopf bifurcation, the bundle's movement rises as its operating point is poised deeper within the oscillatory region. Each data point represents the average over a 10 s interval. Error bars stem from 1000 bootstrap repetitions. From [124].

Chapter 4

Two Models of Hair Bundle Dynamics

Previous studies have shown that two features of a hair bundle, a nonlinear region of negative stiffness in the bundle's force-displacement relationship and an active adaptation process, are sufficient to capture many aspects of hair bundle dynamics, including spontaneous oscillation [92]. Negative stiffness is a passive consequence of channel gating, whereas adaptation pumps mechanical energy into the system to amplify the hair bundle's response to stimulation.

To determine general principles associated with homeostasis of function, I introduce homeostatic mechanisms into two existing models of hair bundle motility. Model I possesses the simplest realizations of the hair bundle's two essential features and exhibits dynamics that qualitatively agree with those of experimentally observed hair bundles [92]. The simplicity of Model I allows me to determine which elements of the model are sufficient to achieve robustness enhancement. Model II incorporates quantitative biophysical properties of the hair bundle [51]. Adding homeostasis to Model II allows me to determine which effects of homeostasis are generalizable from Model I and to quantify the impact of homeostasis. Analyzing how these models differ in structure further facilitates an understanding of homeostatic mechanisms.

4.1 A Phenomenological Model

Model I without homeostasis is given by [92] (Appendix C):

$$\dot{x} = a(x - y) - (x - y)^3 - kx + F_c + F(t)\,, \tag{4.1}$$

$$\dot{y} = \alpha(bx - y)\,. \tag{4.2}$$

Here x is the hair bundle's displacement, $k = k_e + k_{\mathrm{sp}}$ is the combined stiffness of an external load k_e and of the bundle k_{sp}, a is a stiffness arising from channel gating, F_c is a constant force applied to the bundle, and $F(t)$ is an external force that varies in time [92]. The diacritical dots represent temporal derivatives. Because inertial forces are considered negligible, second-order time derivatives do not appear in the equations.

Equation 4.2 describes the dynamics of adaptation y, which produces a force on the bundle. The coefficient b determines how strongly adaptation depends on bundle displacement, whereas the rate of the adaptation is set by α.

The bundle's instantaneous force-displacement relation is given by $F(x) = kx - ax + x^3 + \mathrm{const}$. This expression bears the label "instantaneous" because it is obtained over a time scale that is too short to allow appreciable changes in the adaptation force. Owing to the cubic term, negative stiffness appears in the bundle's instantaneous force-displacement relation when $k < a$.

It has previously been shown that the mechanical load experienced by a hair bundle sets the bundle's operating point and thus determines its biological function as a step detector, an oscillator, or a sinusoidal-signal detector [89, 90, 92]. The parameters k and F_c were additionally found to control the bundle's sensitivity to periodic stimulation [89, 90, 92]. In light of the experimental accessibility, k and F_c are chosen as the system's bifurcation parameters in both Modles I and II.

4.2 A Biophysically Motivated Model

Model II without homeostasis is given by [51] (Appendix C):

$$\lambda_x \dot{x} = -k_{\text{gs}}(x - y - DP_o) - kx + F_c + F(t)\,, \tag{4.3}$$

$$\lambda_y \dot{y} = k_{\text{gs}}(x - y - DP_o) - k_{\text{es}}(y - y_{\text{es}}) - f(1 - SP_o)\,, \tag{4.4}$$

$$P_o = \frac{1}{1 + Ae^{-(x-y)/\delta}}\,, \tag{4.5}$$

in which x, k, F_c, and $F(t)$ bear the same meanings as in Model I. k_{gs} is the collective stiffness of the gating springs that connect mechanotransduction channels to bundle displacement. D is the displacement of the hair bundle's tip that results when a channel opens, and P_o is the probability that a channel is open. The open probability is described by a Boltzmann function, Equation 4.5, derived from a two-state channel model: if ΔG is the difference in energy between the two states, k_B Boltzmann's constant, T temperature, and N the number of stereocilia in the hair bundle, then $A \equiv \exp([\Delta G + (k_{\text{gs}}D)^2/(2N)]/k_BT)$ and $\delta \equiv Nk_BT/(Dk_{\text{gs}})$ [51]. A controls the sigmoid's horizontal position and δ controls its width. Channel gating introduces into the system nonlinearity, the first essential ingredient, through the sigmoidal shape of P_o: negative stiffness appears in the bundle's force-displacement relation when $k < k_{\text{gs}}(D/4\delta - 1)$ (Eq. 1.4).

The second vital ingredient, adaptation, is powered by a Ca^{2+} gradient and myosin motors that exert forces f to open the channels. The position of the motors serves as the adaptation variable y (Eq. 4.4). The influx of Ca^{2+} through open channels inhibits the motors, resulting in channel reclosure. This arrangement constitutes an adaptation mechanism, for it allows the hair bundle to remain sensitive to farther deflection. An increase in x tends to increase y, which in turn tends to diminish the

difference $x - y$. As $x - y$ decreases, the size of the channel-gating term decreases, as does P_o, corresponding to lessening of tip-link tension and closing of MET channels, respectively. Further, the $1 - SP_o$ term enforces the partial inhibition of the myosin motors by calcium: P_o increases as x increases, which in turn reduces the effect of the myosin motors through the shrinking $1 - SP_o$ coefficient of f. S determines the strength of Ca^{2+} inhibition. To account for the fact that adaptation is incomplete, an extent spring with stiffness k_{es} and equilibrium length y_{es} is included [127].

Because the entire system is submerged in fluid, the hair bundle and the insertional plaque experience the drag forces $\lambda_x \dot{x}$ and $\lambda_y \dot{y}$, each with its respective drag coefficient λ_x and λ_y. Slow adaptation occurs on a slower time scale than channel dynamics and is readily apparent only in mechanical deflections lasting approximately 10 ms or longer [7]. To account for this difference in time scales, λ_y is set to a value larger than λ_x. When the bundle is stationary $\dot{x} = 0$, and, identifying $F(t)$ as F_{SF}, the force applied to the bundle by the stimulus fiber (Eq. 1.2) is recovered.

4.3 The Hopf Depends on Parameter Values

Linear stability analysis was employed to locate curves of Hopf bifurcations in each model (Section 2.4). Letting $T_n = \text{Tr}[J(\vec{a}_*)^n]$, in which $J(\vec{a}_*)$ is the system's Jacobian matrix evaluated at the equilibrium point $\vec{a}_*$, a Hopf bifurcation occurs in a system of two dynamical variables when $T_1 = 0$ and $T_2 < 0$ (Eq. 2.43). For Model I without homeostasis, a curve of Hopf bifurcations is given by [92]

$$F_{c,\text{H}\pm}(k) = \pm \left[(k - a(1-b)) \left(\frac{a - \alpha - k}{3(1-b)^2} \right)^{1/2} + (1-b)^3 \left(\frac{a - \alpha - k}{3(1-b)^2} \right)^{3/2} \right], \quad (4.6)$$

when

$$k > \frac{\alpha}{b}(1-b). \tag{4.7}$$

Adjusting the adaptation rate α changes the size of the oscillatory region (Fig. 4.1A).

$F_{c,\mathrm{H}\pm}(k)$ crosses the $F_c = 0$ axis at $k = (1-b)(2a+\alpha)/(2+b)$ and at $k = a - \alpha$. The area enclosed by $F_{c,\mathrm{H}\pm}(k)$ between these intersection points is

$$\begin{aligned}\mathrm{Area}_i(\alpha, b) &= 2\int_{(1-b)(2a+\alpha)/(2+b)}^{a-\alpha} F_{c,\mathrm{H}+}(k)\,dk \\ &= \frac{8(ab-\alpha)^{5/2}}{5|1-b|(2+b)^{3/2}}.\end{aligned} \tag{4.8}$$

The above expression reveals that the Hopf bifurcation curve forms a closed loop when $\alpha < ab$; when $\alpha = ab$ the endpoints of the integration interval coincide, and when $\alpha > ab$ the real parts of $F_{c,\mathrm{H}\pm}(k)$ intersect the $F_c = 0$ axis only at $k = (1-b)(2a+\alpha)/(2+b)$. Equation (4.8) quantifies how changing the adaptation rate α or strength b affects the size of the oscillatory region (Fig. 4.1A, B).

As long as the underdamped region does not become too small (Section 4.5), the area enclosed by a contour of constant peak sensitivity increases monotonically as the oscillatory region grows (Fig. 4.2A). Define the dilation factor h as the square root of ratio of the area enclosed by the Hopf bifurcation curve when $\alpha < 1$ to that when $\alpha = 1$. In accord with the results presented in Section 3.3, the area between the Hopf bifurcation curve and a peak sensitivity contour grows nearly in proportion to h (Fig. 4.2B). The divergence from linearity arises from the sensitivity contours running into the boundary of the underdamped region. In this situation, the contour is made into a closed loop by integrating along the boundary of the underdamped region between the two points that it intersects the sensitivity contour. As was discussed in Section 3.3, closing the loop in this way excludes parts of parameter space that could otherwise

be enveloped by sensitivity contours. Because contours of lower sensitivity values are farther from the Hopf bifurcation, a greater length of the underdamped region's boundary is needed to complete the loop and thus a greater area of parameter space is excluded.

For Model II without homeostasis, and letting

$$k_{\mathrm{H}}(P_o^*) = \frac{1}{\delta\lambda_y}\left(P_o^*(1-P_o^*)(Dk_{\mathrm{gs}}(\lambda_x+\lambda_y) - fS\lambda_x) - \delta k_{\mathrm{es}}\lambda_x - \delta k_{\mathrm{gs}}(\lambda_x+\lambda_y)\right), \quad (4.9)$$

a Hopf bifurcation occurs when

$$\begin{aligned} F_{c,\mathrm{H}}(P_o^*) =& \frac{1}{\delta}\ln\left[\frac{AP_o^*}{1-P_o^*}\right]\left(k_{\mathrm{gs}} - k_{\mathrm{H}}(P_o^*)\left(1+\frac{k_{\mathrm{gs}}}{k_{\mathrm{es}}}\right)\right) \\ &+ k_{\mathrm{H}}(P_o^*)\left(\frac{k_{\mathrm{gs}}}{k_{\mathrm{es}}}DP_o^* - y_{\mathrm{es}} + \frac{f}{k_{\mathrm{es}}}(1-SP_o^*)\right) - k_{\mathrm{gs}}DP_o^*, \end{aligned} \quad (4.10)$$

so long as

$$\begin{aligned} &\lambda_x[(1-P_o^*)P_o^*(fS - Dk_{\mathrm{gs}}) + \delta(k_{\mathrm{es}}+k_{\mathrm{gs}})]^2 \\ &\qquad < \lambda_y k_{\mathrm{gs}}(D(1-P_o^*)P_o^* - \delta)[(1-P_o^*)P_o^*(fS - Dk_{\mathrm{gs}}) + \delta k_{\mathrm{gs}}]. \end{aligned} \quad (4.11)$$

In the above equations, P_o^* is the steady-state channel open probability. Given a point $\{k, F_c\}$ in the state diagram and values for all the other parameters, P_o^* can be found by solving the following equation numerically:

$$F_c = \frac{1}{\delta}\ln\left[\frac{AP_o^*}{1-P_o^*}\right]\left(k_{\mathrm{gs}} - k\left(1+\frac{k_{\mathrm{gs}}}{k_{\mathrm{es}}}\right)\right) + k\left(\frac{k_{\mathrm{gs}}}{k_{\mathrm{es}}}DP_o^* - y_{\mathrm{es}} + \frac{f}{k_{\mathrm{es}}}(1-SP_o^*)\right) - k_{\mathrm{gs}}DP_o^*. \quad (4.12)$$

Alternatively, P_o^* at the Hopf bifurcation can be found from equation (4.9):

$$P_{o,\mathrm{H}\pm}^*(k) = \frac{1}{2}\left[1 \pm \sqrt{\frac{(Dk_{\mathrm{gs}} - 4\delta)(\lambda_x+\lambda_y) - fS\lambda_x - 4\delta(k_{\mathrm{es}}\lambda_x + \lambda_y k)}{Dk_{\mathrm{gs}}(\lambda_x+\lambda_y) - fS\lambda_x}}\right]. \quad (4.13)$$

Using $P^*_{o,\mathrm{H}\pm}(k)$, it is possible to express the Hopf bifurcation curve in terms of the two functions

$$F_{c,\mathrm{H1}}(k) = \frac{1}{\delta}\ln\left[\frac{AP^*_{o,\mathrm{H}+}(k)}{1-P^*_{o,\mathrm{H}+}(k)}\right]\left(k_{\mathrm{gs}} - k\left(1+\frac{k_{\mathrm{gs}}}{k_{\mathrm{es}}}\right)\right) + k\left(\frac{k_{\mathrm{gs}}}{k_{\mathrm{es}}}DP^*_{o,\mathrm{H}+}(k) - y_{\mathrm{es}} + \frac{f}{k_{\mathrm{es}}}(1-SP^*_{o,\mathrm{H}+}(k))\right) - k_{\mathrm{gs}}DP^*_{o,\mathrm{H}+}(k), \quad (4.14)$$

$$F_{c,\mathrm{H2}}(k) = \frac{1}{\delta}\ln\left[\frac{AP^*_{o,\mathrm{H}-}(k)}{1-P^*_{o,\mathrm{H}-}(k)}\right]\left(k_{\mathrm{gs}} - k\left(1+\frac{k_{\mathrm{gs}}}{k_{\mathrm{es}}}\right)\right) + k\left(\frac{k_{\mathrm{gs}}}{k_{\mathrm{es}}}DP^*_{o,\mathrm{H}-}(k) - y_{\mathrm{es}} + \frac{f}{k_{\mathrm{es}}}(1-SP^*_{o,\mathrm{H}-}(k))\right) - k_{\mathrm{gs}}DP^*_{o,\mathrm{H}-}(k). \quad (4.15)$$

Adjusting the adaptation-motor strength f changes the location and size of the self-oscillation region (Fig. 4.1C).

The functions $F_{c,\mathrm{H1}}(k)$ and $F_{c,\mathrm{H2}}(k)$ intersect at two values of k. One value, which bounds the region of spontaneous oscillations on the right, is

$$k_{\mathrm{R}} = \frac{k_{\mathrm{gs}}(\lambda_x+\lambda_y)(D-4\delta) - \lambda_x(fS+4k_{\mathrm{es}}\delta)}{4\delta\lambda_y}. \quad (4.16)$$

The second value, k_{L}, which bounds the region of spontaneous oscillations on the left, can be found numerically. The area enclosed by the Hopf bifurcation loop can then be calculated numerically from the integral

$$\mathrm{Area}_{ii}(f,S) = \int_{k_{\mathrm{L}}}^{k_{\mathrm{R}}} [F_{c,\mathrm{H1}}(k,f,S) - F_{c,\mathrm{H2}}(k,f,S)]\, dk. \quad (4.17)$$

Note that $F_{c,\mathrm{H1}}(k,f,S) \geq F_{c,\mathrm{H2}}(k,f,S)$ on the interval $k \in [k_{\mathrm{L}}, k_{\mathrm{R}}]$. Changing the adaptation-motor strength f or efficacy of Ca^{2+} inhibition S affects the size and location of the oscillatory region (Fig. 4.1D).

As the size of the oscillatory region grows, the area enclosed by a curve of constant peak sensitivity increases (Fig. 4.2D), as long as the underdamped region does not become too small (Section 4.5). The divergence from linearity is greater than in Model I (Fig. 4.2), reflecting a narrower space between the Hopf bifurcation and the boundary of the underdamped region.

Changing any of the models' parameter values affects the size and position of the self-oscillation region (Appendix D, Fig. 4.8). However, a hair bundle may not have the ability to control some of these parameters, such as the number of stereocilia. Because experimental manipulations have been shown to affect adaptation [79, 87, 128], homeostatic feedback is applied to the models' adaptation mechanisms. Specifically, the models are modified to account for the dynamics of the rate of adaptation α in Model I and of the strength of the myosin motors f in Model II, as is described in the next section.

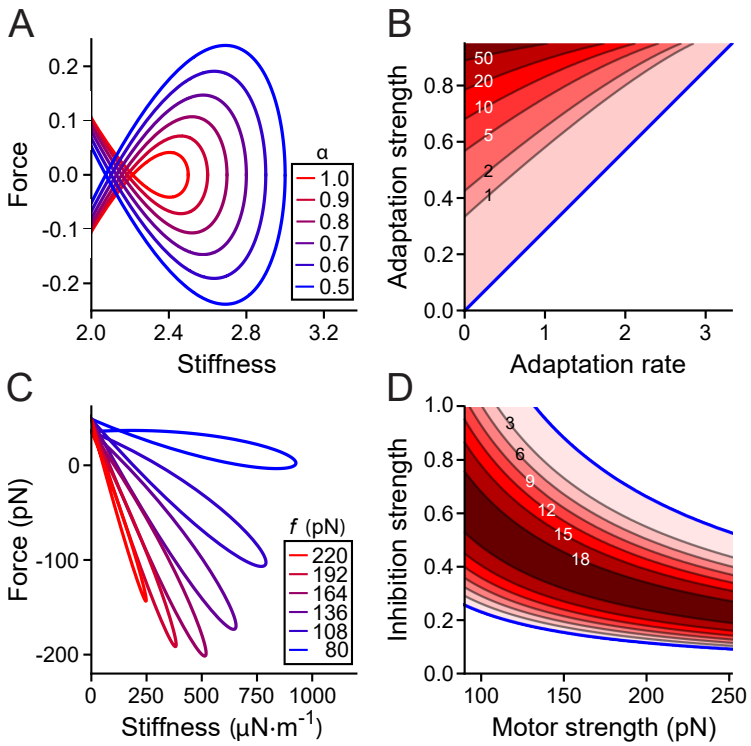

Figure 4.1: Hopf bifurcation curves without homeostasis. (A) Hopf bifurcation curves in the state diagram of Model I for various values of the adaptation rate α. (B) Area enclosed by the Hopf bifurcation loop as a function of adaptation strength b and adaptation rate α. Darker shades of red indicate larger areas and each contour is labeled with its area. The blue line marks where $\alpha = ab$. In the white region of the plot, for which $\alpha > ab$, the Hopf bifurcation curve does not encircle a bounded region of state space. (C) Hopf bifurcation curves in Model II for various values of the adaptation-force strength f. (D) Area enclosed by the Hopf bifurcation loop as a function of motor strength f and of the strength of Ca^{2+} mediated inhibition S. Darker shades of red indicate larger areas and each contour is labeled with its area in units of $\mu N^2 \cdot km^{-1}$. The Hopf bifurcation curve does not enclose a bounded region for values located in the white region of the plot. As f increases from 80 pN the area of the oscillatory region initially increases to a maximum and then decreases for large enough values of f. All parameter values are listed in Tables 4.1 and 4.2. From [124].

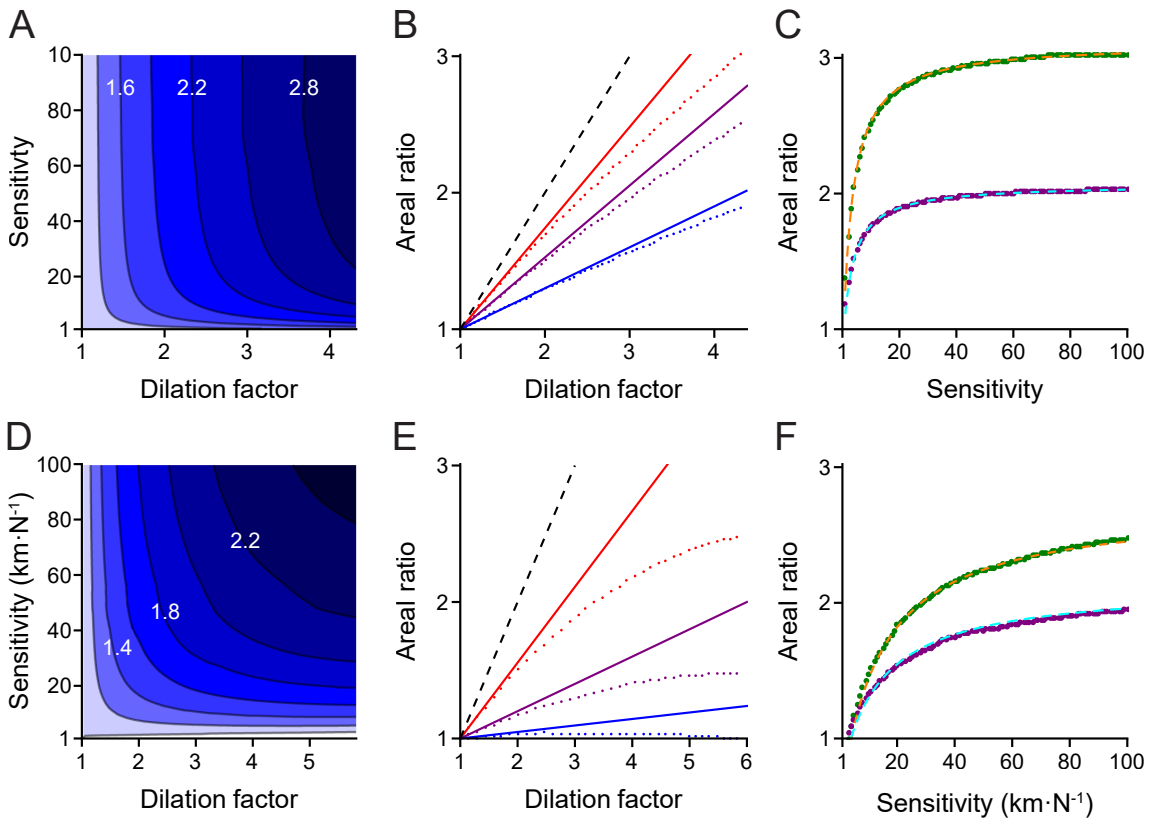

Figure 4.2: Comparison between the general case and the models. (A) Area contained within peak-sensitivity contours relative to that contained in contours when $\alpha = 1$ $(\mathcal{R}_\chi(h))$, as a function of the peak sensitivity and of the dilation factor of the oscillatory region $h = [\text{Area}_i(\alpha, b)/\text{Area}_i(1, b)]^{1/2}$ in Model I. α ranges from 1.0, at a normalized area of 1, to 0.5 at the maximum normalized area shown. Darker shades of blue indicate larger areal ratios. (B) Areal ratios (dots) for $\chi = 100$ (red), 10 (purple) and 3 (blue). Straight lines whose slopes match that of the dots for small dilation factors are shown for comparison. The black, dashed line marks $\mathcal{R}_\chi(h) = h$. (C) Areal ratios for $h = 5.8$ (green dots) and 3.2 (purple dots). (D) Area contained within peak-sensitivity contours relative to that contained in the contours when $f = 250$ pN $(\mathcal{R}_\chi(h))$, as a function of the peak sensitivity and $h = [\text{Area}_{ii}(f, S)/\text{Area}_{ii}(250pN, S)]^{1/2}$. f ranges from 250 pN at a normalized area of 1 to 180 pN at the maximum normalized area shown. The calculations in panels A and D exclude the area of the self-oscillation region and were performed numerically. These panels are modified from [124]. Dilating the self-oscillation region effects a more efficient expansion of the high-performance zone in Model I than in Model II. (E, F) Same as panels B and C except for Model II and $h = 4.3$ (green) and 2.5 (purple). The lines and dashed curves in panels B, C, E, and F were obtained from the general case (Eq. 3.12), except the curves in C and F were scaled by a constant.

4.4 Homeostatic Mechanisms

The goal is to render the hair bundle's ability to detect periodic stimuli more robust to changes in control parameters. To achieve this objective, I accounted for the dynamics of α and f:

$$\text{Model I:} \qquad \tau_\alpha \dot{\alpha} = \alpha_0 - \alpha - \beta_\alpha x^2 \,, \tag{4.18}$$

$$\text{Model II:} \qquad \tau_f \dot{f} = f_0 - f - \beta_f f_0 P_o \,. \tag{4.19}$$

Equations 4.18 and 4.19 are termed homeostatic mechanisms because, as I will show in Chapter 5, their inclusion imparts homeostasis of function to the models.

The timescale of the homeostatic mechanism in Model I is set by τ_α and α_0 gives the value to which α would decay in the absence of homeostasis. Homeostasis is inactive when $\beta_\alpha = 0$ and active when $\beta_\alpha > 0$. Information about the hair bundle's oscillation amplitude is captured by squaring the bundle's displacement, imparting to the homeostasis equation a means of determining whether the bundle is receiving sinusoidal stimulation.

Equation 4.19 describes the dynamics of the myosin motor force f in Model II. The form of Equation 4.19 parallels that of Equation 4.18: τ_f sets the timescale of the homeostatic process, f decays to f_0 in the absence of homeostasis, and β_f determines how strongly the current state of the system affects the homeostatic mechanism. Homeostasis is inactive when $\beta_f = 0$ and operational when $\beta_f > 0$. In contrast to Equation 4.18, Equation 4.19 employs a saturating nonlinearity: the bundle's oscillation amplitude is measured by the sigmoidal function P_o. Equation 4.19 has a physical interpretation: the motor force f is set by the average Ca^{2+}-concentration gradient across the hair cell's plasma membrane, which is adjusted by the ion's influx through the channels. Because homeostasis depends on the transduction current, β_f

could depend on the Ca^{2+}-concentration gradient and the membrane potential.

To minimize its effects on the dynamical response of the bundle to sinusoidal stimulation, both homeostatic mechanisms operate slowly. The homeostatic mechanisms in both models employ a nonlinear term to rectify time-dependent changes in the hair bundle's position. Thanks to this rectification, the terms in the homeostasis equations measuring the current state of the system are non-zero when averaged over time, even for inputs whose time averages are zero. In this way, the homeostasis equations can detect whether the bundle is being stimulated. In contrast, if rectification was absent from the homeostasis equations, for example if x^2 were replaced with x, then sinusoidal driving of the hair bundle would average to zero and the homeostatic mechanisms, on average, would not engage to adjust α or f.

Linear-stability analysis was again employed to locate curves of Hopf bifurcations in parameter space. Model I with homeostasis is given by:

$$\dot{x} = a(x-y) - (x-y)^3 - kx + F_c + F(t)\,, \tag{4.20}$$

$$\dot{y} = \alpha(bx - y)\,, \tag{4.21}$$

$$\tau_\alpha \dot{\alpha} = \alpha_0 - \alpha - \beta_\alpha x^2. \tag{4.22}$$

The conditions $T_3 = T_1^3$ and $T_2 < T_1^2$ (Eqs. 2.44) locate Hopf bifurcations in systems of three dynamical variables. In Model I, when the steady-state adaptation rate α^* exceeds zero, the system's equilibrium points are given by

$$y_* = b\,x_* \tag{4.23}$$

$$\alpha_* = \alpha_0 - \beta_\alpha x_*^2 \tag{4.24}$$

$$F_c = kx_* - a(1-b)x_* + (1-b)^3 x_*^3. \tag{4.25}$$

At these fixed points, a Hopf bifurcation occurs when

$$F_{c,\mathrm{H}\pm}(k) = \pm\left[(k - a(1-b))\left(\frac{a-\alpha_0-k}{3(1-b)^2-\beta_\alpha}\right)^{1/2} + (1-b)^3\left(\frac{a-\alpha_0-k}{3(1-b)^2-\beta_\alpha}\right)^{3/2}\right], \tag{4.26}$$

and when

$$k > \frac{3\alpha_0(1-b)^3 - a\beta_\alpha(1-b)}{3b(1-b)^2-\beta_\alpha}. \tag{4.27}$$

Note that setting $\beta_\alpha = 0$ reproduces Eqs. (4.6) and (4.7). Adjusting the homeostasis strength β_α shifts the position and size of the Hopf bifurcation curve; $\beta_\alpha = 0$ corresponds to inactive homeostasis (Fig. 4.3*A*).

The values of the parameters a, b, α_0, τ_α, and β_α need to be determined, a choice guided by the effect that each parameter has on the self-oscillation region. The Hopf bifurcation curve, $F_{c,\mathrm{H}}(k)$, crosses $F_c = 0$ at

$$[k_0] = \left\{\frac{(1-b)^3(2a+\alpha_0) - a(1-b)\beta_\alpha}{2-3b+b^3-\beta_\alpha}, a-\alpha_0\right\}.$$

The area of the region of spontaneous oscillation is then

$$\begin{aligned}\mathrm{Area}_\mathrm{I}(b,\beta_\alpha) &= 2\int_{[k_0]_1}^{[k_0]_2} F_{c,\mathrm{H}+}(k)\,dk \\ &= \frac{8}{15}|3(1-b)^2-\beta_\alpha|\frac{(ab-\alpha_0)^{5/2}}{(2-3b+b^3-\beta_\alpha)^{3/2}}.\end{aligned} \tag{4.28}$$

The above expression is valid only if $b > \alpha_0/a$ and $\beta_\alpha < \alpha_0(2+b)(1-b)^2/(ab)$. If $b = \alpha_0/a$, then $[k_0]_1 = [k_0]_2$ and a Hopf bifurcation loop does not exist at smaller values of b. At $\beta_\alpha = \alpha_0(2+b)(1-b)^2/(ab)$, $[k_0]_1$ collides with two Bogdanov-Takens points, and the Hopf bifurcation does not form a closed loop when $\beta_\alpha > \alpha_0(2+b)(1-b)^2/(ab)$. Dividing $\mathrm{Area}_\mathrm{I}(b,\beta_\alpha)$ by $\mathrm{Area}_\mathrm{I}(b,0)$, the area of the oscillatory region

when the homeostatic mechanism is inactive, yields the expansion factor, or relative increase in area effected by setting the homeostasis parameter to β_α:

$$\frac{\text{Area}_\text{I}(b, \beta_\alpha)}{\text{Area}_\text{I}(b, 0)} = \frac{|3(1-b)^2 - \beta_\alpha|(2 - 3b + b^3)^{3/2}}{3(1-b)^2(2 - 3b + b^3 - \beta_\alpha)^{3/2}}. \tag{4.29}$$

The expansion factor, which corresponds to h^2 from Section 3.3, depends on only the parameters b and β_α and is independent of a, α_0, and τ_α. Therefore, a was set to 3.5 [92], α_0 was set to 1 for simplicity, and τ_α was set to 1000 to ensure separation between the timescale governing the homeostatic mechanism and the other timescales present in the system: homeostasis was assumed to be a relatively slow process.

The expansion factor depends on the parameters b and β_α, the adaptation strength and homeostasis strength, respectively (Fig. 4.3*B*). The value of b was set to 0.35 and that of β_α to 3/4. This choice of values for b and β_α yields an expansion factor exceeding three. Although even greater expansion factors are possible, the values selected render the increase in area robust to variations in b or β_α. However, the specified parameter values do not optimize the expansion factor or its robustness to changes in parameter values. Optimization is avoided in this work to illustrate that a biological system would not need to exert tight control over parameter values to achieve its performance specifications. A summary of the parameter values used in Model I is given in Table 4.1.

Table 4.1: Parameter Values in Model I

a	3.5	b	0.35	τ_α	10^3
α_0	1	* β_α	0.75		

Model II with homeostasis is given by:

$$\lambda_x \dot{x} = -k_{\rm gs}(x - y - DP_o) - kx + F_c + F(t)\,, \tag{4.30}$$

$$\lambda_y \dot{y} = k_{\rm gs}(x - y - DP_o) - k_{\rm es}(y - y_{\rm es}) - f(1 - SP_o)\,, \tag{4.31}$$

$$\tau_f \dot{f} = f_0 - f - \beta_f P_o\,, \tag{4.32}$$

$$P_o = \frac{1}{1 + Ae^{-(x-y)/\delta}}\,, \tag{4.33}$$

and equilibrium points are found from

$$\begin{cases} f_* = f_0 - \beta_f P_o^* \\ k_{\rm es} y_* = k_{\rm gs}\left(\dfrac{1}{\delta}\ln\left[\dfrac{AP_o^*}{1-P_o^*}\right] - DP_o^*\right) + k_{\rm es} y_{\rm es} - (f_0 - \beta_f P_o^*)(1 - SP_o^*) \\ kx_* = F_c - k_{\rm gs}\left(\dfrac{1}{\delta}\ln\left[\dfrac{AP_o^*}{1-P_o^*}\right] - DP_o^*\right), \end{cases}$$

$$x_* = y_* + \frac{1}{\delta}\ln\left[\frac{AP_o^*}{1-P_o^*}\right],$$

$$\begin{aligned} \Rightarrow F_c =& \frac{1}{\delta}\ln\left[\frac{AP_o^*}{1-P_o^*}\right]\left(k_{\rm gs} - k\left(1 + \frac{k_{\rm gs}}{k_{\rm es}}\right)\right) \\ &+ k\left(\frac{k_{\rm gs}}{k_{\rm es}} DP_o^* - y_{\rm es} + \frac{1}{k_{\rm es}}(f_0 - \beta_f P_o^*)(1 - SP_o^*)\right) - k_{\rm gs} DP_o^* \end{aligned} \tag{4.34}$$

Given a point $\{k, F_c\}$ in state space and values for all the other parameters, equation (4.34) can be solved numerically for P_o^*, and $f_* = f_0 - \beta_f P_o^*$ then follows.

A Hopf bifurcation occurs for Model II when

$$\begin{aligned} F_{c,\rm H}(P_o^*) =& \frac{1}{\delta}\ln\left[\frac{AP_o^*}{1-P_o^*}\right]\left(k_{\rm gs} - k_{\rm H}(P_o^*)\left(1 + \frac{k_{\rm gs}}{k_{\rm es}}\right)\right) \\ &+ k_{\rm H}(P_o^*)\left(\frac{k_{\rm gs}}{k_{\rm es}} DP_o^* - y_{\rm es} + \frac{1}{k_{\rm es}}(f_0 - \beta_f P_o^*)(1 - SP_o^*)\right) - k_{\rm gs} DP_o^*. \end{aligned} \tag{4.35}$$

The expressions for $k_{\rm H}(P_o^*)$ and the $T_2 < T_1^2$ condition are given in Appendix F (Eqs. 5.15 and 5.16). Setting $\beta_f = 0$ reproduces the parametric curve $\left(k_{\rm H}(P_o^*), F_{c,\rm H}(P_o^*)\right)$

found in the absence of homeostasis. Changing the homeostasis strength β_f shifts the position and size of the Hopf bifurcation curve (Fig. 4.3C).

Values for the parameters k_{gs}, k_{es}, δ, D, N, A, T, ΔG, and y_{es} were taken from [92] or [51] and are based on biophysical measurements or estimates of hair bundle parameter values in sacculi of American bullfrogs. The value for S was chosen to ensure the existence of a region of spontaneous oscillation for a broad range of myosin-motor strengths f (Fig. 4.1E). Values for λ_x and λ_y were chosen to ensure that the maximum frequency of spontaneous oscillations was less than 200 Hz. Choices for the remaining parameters, f_0 and β_f, are described below.

When $\beta_f \neq 0$ it is not possible to express the parametric curve $\Big(k_{\mathrm{H}}(P_o^*), F_{c,\mathrm{H}}(P_o*)\Big)$ in terms of a set of elementary functions. Therefore, the parametric equations, $k_{\mathrm{H}}(P_o^*)$ and $F_{c,\mathrm{H}}(P_o*)$, and Stokes's theorem were used to calculate the area enclosed by the Hopf bifurcation loop for various values of f_0 and β_f. Let $\vec{U}$ be a vector field with $\vec{\nabla} \times \vec{U}$ a unit vector field perpendicular to the surface Σ. Stoke's theorem states that

$$\oint_{\partial\Sigma} \vec{U} \cdot d\vec{r} = \iint_{\Sigma} \vec{\nabla} \times \vec{U} \cdot d\vec{\Sigma} = \Sigma,$$

in which $\partial\Sigma$ is the boundary curve of Σ with the normal vector field $d\vec{\Sigma}$ and $\vec{r}$ is a parameterization of $\partial\Sigma$. The Hopf bifurcation curve is given by:

$$\vec{r} = \Big(k_{\mathrm{H}}(P_o^*, f_0, \beta_f), F_{c,\mathrm{H}}(P_o^*, f_0, \beta_f), 0\Big),$$

in which P_o^* is a variable and f_0 and β_f are parameters. The differential tangent-vector field along the curve $\vec{r}$ is then

$$d\vec{r} = \frac{\partial}{\partial P_o^*}\Big(k_{\mathrm{H}}(P_o^*, f_0, \beta_f), F_{c,\mathrm{H}}(P_o^*, f_0, \beta_f), 0\Big)\, dP_o^*,$$

meaning the area of a surface Σ can be found by line integration around the boundary of Σ. Two options for the vector field $\vec{U}$ are

$$\vec{U} = \Big(0, k_{\mathrm{H}}(P_o^*, f_0, \beta_f), 0\Big) \quad \text{or} \quad \vec{U} = \Big(- F_{c,\mathrm{H}}(P_o^*, f_0, \beta_f), 0, 0\Big).$$

The area enclosed by the Hopf bifurcation loop is then given by

$$\mathrm{Area}_{\mathrm{II}}(f_0, \beta_f) = \int_{[P_o^*]_1}^{[P_o^*]_2} k_{\mathrm{H}}(P_o^*, f_0, \beta_f) \frac{\partial}{\partial P_o^*} F_{c,\mathrm{H}}(P_o^*, f_0, \beta_f)\, dP_o^*, \tag{4.36}$$

$$\text{or} \quad \mathrm{Area}_{\mathrm{II}}(f_0, \beta_f) = - \int_{[P_o^*]_1}^{[P_o^*]_2} F_{c,\mathrm{H}}(P_o^*, f_0, \beta_f) \frac{\partial}{\partial P_o^*} k_{\mathrm{H}}(P_o^*, f_0, \beta_f)\, dP_o^*, \tag{4.37}$$

in which $[P_o^*]_1$ and $[P_o^*]_2$ are the values of the parameter P_o^* where the Hopf bifurcation curve crosses itself. These values are found numerically. Three fixed points exist at this intersection, two of which, corresponding to $[P_o^*]_1$ and $[P_o^*]_2$, are stable. As P_o^* is increased from $[P_o^*]_1$, the bundle crosses a saddle-node bifurcation (Section 4.5), beyond which the fixed point associated with $[P_o^*]_1$ persists whereas that associated with $[P_o^*]_2$ vanishes. As P_o^* is increased further toward $[P_o^*]_2$, the remaining stable fixed point shifts continuously toward the fixed point originally associated with $[P_o^*]_2$. When P_o^* nears $[P_o^*]_2$, the bundle again crosses a saddle-node bifurcation, at which point the fixed point originally associated with $[P_o^*]_1$ materializes. Integrating along the Hopf bifurcation curve from $[P_o^*]_1$ to $[P_o^*]_2$ tracks the bundle's position as it transitions smoothly from the $[P_o^*]_1$ fixed point to the $[P_o^*]_2$ fixed point.

The expansion factor of the self-oscillation region,

$$\frac{\mathrm{Area}_{\mathrm{II}}(f_0, \beta_f)}{\mathrm{Area}_{\mathrm{II}}(f_0, 0)}, \tag{4.38}$$

depends on the homeostasis strength β_f and on the adaptation-motor strength f_0 in the absence of homeostasis (Fig. 4.3*D*). The value of f_0 was chosen to be 220 pN

and β_f was set to 110 pN. This choice of parameter values results in a more than tenfold expansion factor while striking a balance with the robustness of this expansion factor to changes in f_0 or β_f. Once again, the parameter values were not optimized; other choices would yield a larger expansion factor as well as render this increase more robust to changes in f_0 and β_f. Unless otherwise stated, Table 4.2 gives the parameter values used in Model II.

Table 4.2: Parameter Values in Model II

k_{gs}	816	$\mu\text{N}\cdot\text{m}^{-1}$	k_{es}	150	$\mu\text{N}\cdot\text{m}^{-1}$
λ_x	500	$\text{nN}\cdot\text{s}\cdot\text{m}^{-1}$	λ_y	2500	$\text{nN}\cdot\text{s}\cdot\text{m}^{-1}$
* δ	5.16	nm	D	49	nm
† A	2.53		S	0.5	
N	50		T	295	K
ΔG	10	k_BT	k_B	1.4×10^{-23}	$\text{J}\cdot\text{K}^{-1}$
y_{es}	0	m	τ_f	0.2	s
‡ β_f	110	pN	f_0	220	pN

* $\delta = Nk_BT/(Dk_{\text{gs}})$

† $A = \exp[(\Delta G + k_{\text{gs}}D^2)/(2Nk_BT)]$

‡ $\beta_f = 0$ when homeostasis is off

The shapes of the Hopf bifurcation curves exhibited by the system when homeostasis is active (Fig. 4.3) differ from those when homeostasis is absent (Fig. 4.1), thus invalidating the assumption that conferring dynamics upon a parameter does not appreciably change the system's state diagram, even when the timescale of those dynamics greatly exceeds the timescales of every other process described by the system. Figure 4.4 provides an explanation for the particular shapes of the Hopf bifurcation curves when homeostasis is active.

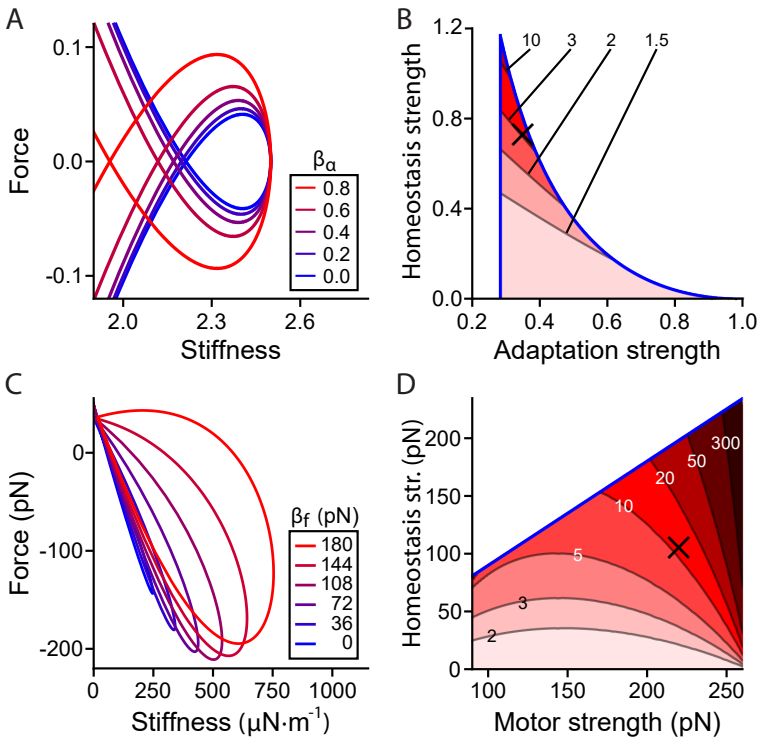

Figure 4.3: Hopf bifurcation curves with homeostasis. (A) Hopf bifurcation curves in the state diagram of Model I for various values of homeostatic strength β_α. (B) Expansion factor, Eq. (4.29), as a function of the strength of adaptation b and homeostasis strength β_α. Darker shades of red indicate larger expansion factors. The $\times$ symbol marks the chosen values of $b = 0.35$ and $\beta_\alpha = 0.75$. The blue curves bound the set of values at which a closed Hopf bifurcation loop exists. (C) Hopf bifurcation curves in the state diagram of Model II for various values of β_f. (D) Expansion factor, Eq. (4.38), as a function of the baseline motor strength f_0 and homeostasis strength β_f. Darker shades of red indicate larger expansion factors. The region encircled by a Hopf bifurcation curve is bounded at all values shown. The chosen values for $f_0 = 220$ pN and $\beta_f = 110$ pN are marked by the $\times$ symbol. Parameter values are listed in Tables 4.1 and 4.2. From [124].

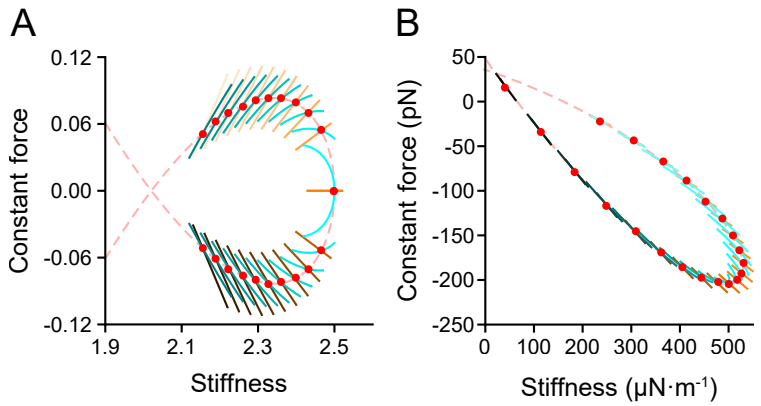

Figure 4.4: Shape of the Hopf bifurcation curves with homeostasis. (A) Segments of the Hopf bifurcation curves without homeostasis for Model I are shown for various values of α (cyan) as are segments of curves along which x_* is constant (orange), with darker shades indicating smaller values of both α and x_*. Each point on the Hopf bifurcation curve when homeostasis is active (dashed, red curve) occurs at the intersection of a cyan curve with an x_* contour (red dots). If, for example, $x_* = 1/2$, then $\alpha_* = \alpha_0 - \beta_\alpha/4$ and this point on the bifurcation curve when homeostasis is active coincides with the point displaying the same x_* value on the curve without homeostasis only if the static parameter α is set to $\alpha_0 - \beta_\alpha/2$. ($B$) Similarly, the point corresponding to a particular P_o^* value on the Hopf bifurcation curve in Model II when homeostasis is active (dashed, red curve) occurs at the intersection (red point) of that P_o^* contour (orange) and the Hopf bifurcation curve exhibited by the system in the absence of homeostasis when the static parameter f is set to $f_0 - \beta_f f_0 P_o^*$ (cyan). Darker shades of orange indicate smaller values of P_o^*, whereas darker shades of cyan denote larger values of f.

4.5 State Diagram Boundaries

All calculations in Chapter 5 were performed within the underdamped region of the state diagram, the set of operating points at which the bundle exhibits ringing in response to small force steps. Outside the underdamped region the bundle exhibits little amplification of periodic stimuli. The boundary of the underdamped region occurs when the discriminant of the Jacobian's characteristic polynomial is equal to zero, whereupon the system is critically damped. This condition can be expressed as

$$-T_1^6 + 9T_1^4T_2 - 21T_1^2T_2^2 - 8T_1^3T_3 + 36T_1T_2T_3 + 3T_2^3 - 18T_3^2 = 0. \tag{4.39}$$

The boundary of the underdamped region in Model I is given by

$$k_{\mathrm{U}\pm}(x_*) = a + \alpha_0 - x_*^2[3(1-b)^2 + \beta_\alpha] \pm 2\sqrt{b[a - 3(1-b)^2x_*^2][\alpha_0 - x_*^2\beta_\alpha]}, \tag{4.40}$$

$$F_{c,\mathrm{U}\pm}(x_*) = [k_{\mathrm{U}\pm}(x_*) - a(1-b)]x_* + (1-b)^3x_*^3. \tag{4.41}$$

Figure 4.5 depicts the underdamped region for the homeostasis off ($\beta_\alpha = 0$) and on ($\beta_\alpha = 3/4$) conditions.

For Model II, when homeostasis is inactive, the boundary of the underdamped region is given by

$$\begin{aligned} k_{U\pm}(P_o^*) =& \frac{1}{\lambda_y\delta}\Big[k_{\mathrm{gs}}[D(1-P_o^*)P_o^* - \delta](\lambda_y - \lambda_x) + \lambda_x[f_0(1-P_o^*)P_o^*S + k_{\mathrm{es}}\delta] \\ & \pm 2\sqrt{k_{\mathrm{gs}}[D(1-P_o^*)P_o^* - \delta][(1-P_o^*)P_o^*(f_0S - Dk_{\mathrm{gs}}) + k_{\mathrm{gs}}\delta]\lambda_y\lambda_x}\Big], \end{aligned} \tag{4.42}$$

$$\begin{aligned} F_{c,U\pm} =& \frac{1}{\delta}\ln\left[\frac{AP_o^*}{1-P_o^*}\right]\left(k_{\mathrm{gs}} - k_{U\pm}(P_o^*)\left(1 + \frac{k_{\mathrm{gs}}}{k_{\mathrm{es}}}\right)\right) \\ & + k_{U\pm}(P_o^*)\left(\frac{k_{\mathrm{gs}}}{k_{\mathrm{es}}}DP_o^* - y_{\mathrm{es}} + \frac{f}{k_{\mathrm{es}}}(1 - SP_o^*)\right) - k_{\mathrm{gs}}DP_o^*. \end{aligned} \tag{4.43}$$

When homeostasis is active, the expression for $k_{U\pm}(P_o^*)$ is very large, and is therefore omitted to conserve space. Curves bounding the underdamped region are shown in Figure 4.6.

Regions of the state diagram in which multiple stable manifolds coexist were excluded from the compressive-range calculations. Sinusoidal forcing in these regions causes the bundle to jump back and forth between stable manifolds so that the amplitude of the bundle's motion is not well-defined.

The bundle is bistable in a region where two stable fixed points coexist. This bistable region is bordered by a curve of saddle node bifurcations, which occur when $\det[J(\vec{a}_*)] = 0$. Equations for these bifurcation curves are given below. The bistable region allows the Hopf bifurcation curve to form a closed loop (Fig. 4.7). The bistable region is divided into lower and upper parts by the line $F_c = 0$ in Model I and by $P_o^* = 1/2$ in Model II. The sensitivity and quality factor for the lower half of the bistable region were calculated at the equilibrium position corresponding to lesser deflection, whereas the equilibrium position corresponding to greater bundle deflection was employed in the upper half of the bistable region.

A stable fixed point coexists with a stable limit cycle within a region, termed the coexistence region, wedged between a saddle node of limit cycles (SNLC) bifurcation curve and a subcritical Hopf bifurcation curve. These two curves collide with each other and a supercritical Hopf bifurcation curve at a Bautin point. A coexistence region is present in Model II whether homeostasis is on or off. In Model I, however, a coexistence region exists when $\beta_\alpha = 0$ but is absent when $\beta_\alpha = 3/4$ (Figs. 4.5 and 4.6). Bautin points for both models were found as described in Appendix A and SNLC-bifurcation curves were calculated numerically. Finally, when homeostasis is active in Model I, a region exists in which the bundle exhibits multimodal oscillations

in response to periodic forcing (Fig. 5.6B).

The condition $\det[J(\vec{a}_*)] = 0$ identifies both saddle node and transcitical bifurcations. In Model I, curves along which these bifurcations occur are given by

$$F_{c,\mathrm{SN}}(k) = \pm\left[(k - a(1-b))\left(\frac{a(1-b)-k}{3(1-b)^3}\right)^{1/2} + (1-b)^3\left(\frac{a(1-b)-k}{3(1-b)^3}\right)^{3/2}\right], \tag{4.44}$$

$$F_{c,\mathrm{TC}}(k) = \pm\sqrt{\frac{\alpha_0}{\beta_\alpha}}\left[k - a(1-b) + (1-b)^3\frac{\alpha_0^2}{\beta_\alpha^2}\right], \text{ when } \beta_\alpha \neq 0. \tag{4.45}$$

At $F_{c,\mathrm{SN}}(k)$ the number of x_* solutions abruptly changes from 1 to 3, whereas at $F_{c,\mathrm{TC}}(k)$ two equilibrium points pass through each other and exchange stability. When $\beta_\alpha < 3(1-b)^2\alpha_0/a$ the Hopf bifurcation curve terminates when it intersects $F_{c,\mathrm{SN}}(k)$ at the Bogdanov-Takens points

$$\left(k_{\mathrm{BT}}, F_{c,\mathrm{BT}}\right) = \left\{\frac{3\alpha_0(1-b)^3 - a\beta_\alpha(1-b)}{3b(1-b)^2 - \beta_\alpha}, \pm 2(1-b)^3\left(\frac{ab-\alpha_0}{3b(1-b)^2-\beta_\alpha}\right)^{3/2}\right\}. \tag{4.46}$$

When $\beta_\alpha > 3(1-b)^2\alpha_0/a$ the Bogdanov-Takens points occur at

$$\left(k_{\mathrm{BT}}, F_{c,\mathrm{BT}}\right) = \left\{a - 3\frac{\alpha_0}{\beta_\alpha}(1-b)^2, \pm\left[ab\sqrt{\frac{\alpha_0}{\beta_\alpha}} - \left(\frac{\alpha_0}{\beta_\alpha}\right)^{3/2}(b^3 - 3b + 1)\right]\right\}, \tag{4.47}$$

where the Hopf bifurcation curve intersects with $F_{c,\mathrm{TC}}(k)$. Additional bifurcations are accessible when α is zero or negative, conditions that are unphysical. These additional bifurcations are discussed in Appendix E.

The Hopf frequency is

$$\omega_{\mathrm{H}} = \sqrt{\frac{[3(1-b)^2\alpha_0 + (k-a)\beta_\alpha][3(1-b)^2(bk - \alpha_0(1-b)) + \beta_\alpha(k - a(1-b))]}{(3(1-b)^2 - \beta_\alpha)^2}}. \tag{4.48}$$

$\omega_{\mathrm{H}} = 0$ if $k = k_{\mathrm{BT}}$. When $\beta_\alpha < 3\alpha_0 b(1-b)^2/(2\alpha_0 - ab)$, ω_{H} increases monotonically from 0 at $k = k_{\mathrm{BT}}$ to $\sqrt{\alpha_0(\alpha_0 - ab)}$ at $k = a - \alpha_0$. Otherwise, ω_{H} achieves a maximum value of

$$\omega_{\mathrm{H,max}} = \frac{b}{2}\sqrt{\frac{[a\beta_\alpha - 3\alpha_0(1-b)^2]^2}{\beta_\alpha[\beta_\alpha - 3(1-b)^2]}} \tag{4.49}$$

$$\text{at } k = \frac{a(2-b)\beta_\alpha^2 - 3(1-b)^2(ab + (2-b)\alpha_0)\beta_\alpha + 9\alpha_0 b(1-b)^4}{2\beta_\alpha^2 - 6b(1-b)^2\beta_\alpha},$$

which is the largest value of k at which a Hopf bifurcation occurs. Detailed state diagrams for Model I are shown in Figure 4.5. Determining all global bifurcations is beyond the scope of this work.

In Model II, a saddle node bifurcation curve is described by

$$k_{\mathrm{SN}}(P_o^*) = \frac{k_{\mathrm{es}}k_{\mathrm{gs}}[DP_o^*(1-P_o^*) - \delta]}{P_o^*(1-P_o^*)[f_0 S + \beta_f - 2P_o^* S\beta_f - Dk_{\mathrm{gs}}] + \delta(k_{\mathrm{es}} + k_{\mathrm{gs}})}, \tag{4.50}$$

$$\begin{aligned} F_{c,\mathrm{SN}}(P_o^*) =& \frac{1}{\delta}\ln\left[\frac{AP_o^*}{1-P_o^*}\right]\left(k_{\mathrm{gs}} - k_{\mathrm{SN}}(P_o^*)\left(1 + \frac{k_{\mathrm{gs}}}{k_{\mathrm{es}}}\right)\right) \\ &+ k_{\mathrm{SN}}(P_o^*)\left(\frac{k_{\mathrm{gs}}}{k_{\mathrm{es}}}DP_o^* - y_{\mathrm{es}} + \frac{1}{k_{\mathrm{es}}}(f_0 - \beta_f P_o^*)(1 - SP_o^*)\right) - k_{\mathrm{gs}}DP_o^*. \end{aligned} \tag{4.51}$$

Bogdanov-Takens points can be found for Model II numerically either from the $T_2 = T_1^2$ condition or by equating the components of $\big(k_{\mathrm{H}}(P_o^*), F_{c,\mathrm{H}}(P_o^*)\big)$ with those of $\big(k_{\mathrm{SN}}(P_o^*), F_{c,\mathrm{SN}}(P_o^*)\big)$.

An analytical expression exists for the Hopf frequency in Model II, but is omitted here to conserve space. Using the parameter values given in Table 4.2, ω_{H} reaches a maximum value of 136 Hz when homeostasis is inactive ($\beta_f = 0$) and 169 Hz when homeostasis is active. These maximum values occur when $P_o^* \approx 1/2$ in both cases, which corresponds to the point $\big(k_{\mathrm{H}}(1/2), F_{c,\mathrm{H}}(1/2)\big)$ in state space. Detailed state diagrams for Model II are shown in Figure 4.6.

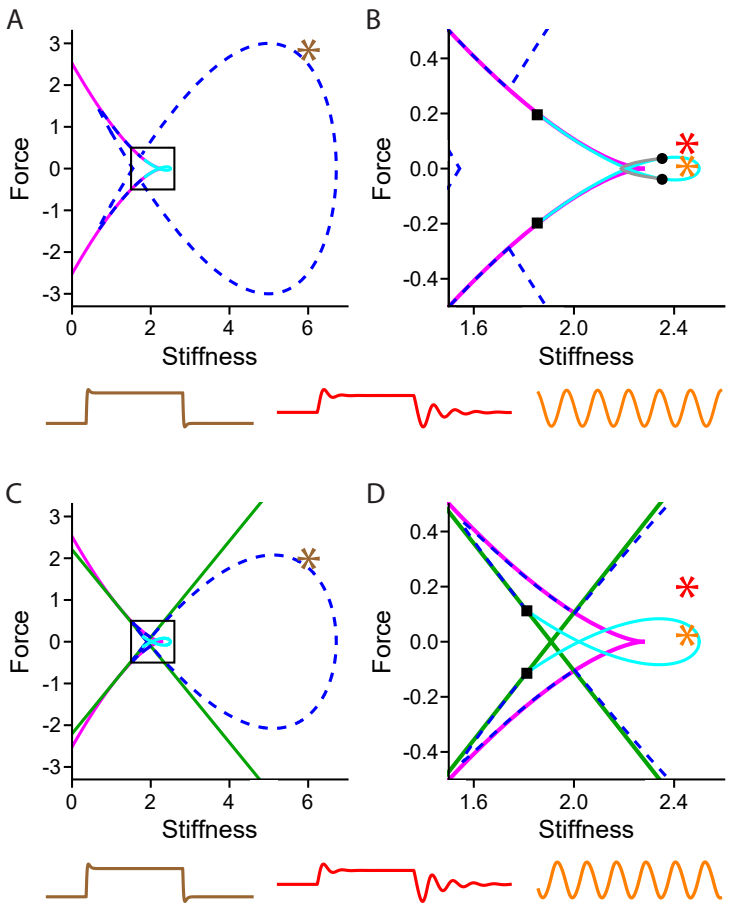

Figure 4.5: Detailed state diagrams for Model I. State diagrams when homeostasis is either inactive (A,B) or active (C,D). In all panels, the blue dashed curves bound the underdamped region, Hopf bifurcation curves are colored cyan, and saddle-node bifurcation curves are magenta. (A,C) The entire underdamped region is shown. The brown traces depict the hair bundle's response to a force step when the bundle is poised at the operating point marked by brown asterisks. At these operating points the bundle does not exhibit any ringing in response to a force step. (B,D) Magnified view of the region enclosed by the box in panel A (B) or in panel C (D). Bogdanov-Takens points are marked by black squares. When homeostasis is inactive, the bundle's state diagram possesses a saddle node bifurcation of limit cycles (SNLC bifurcation) curve found numerically, shown in gray, and Bautin points (Appendix A) indicated by black circles. When the homeostasis-strength parameter is set to $\beta_\alpha = 3/4$, the model's state diagram lacks Bautin points and SNLC bifurcations, but possesses transcritical bifurcations that are colored green in panels C and D. The red traces, obtained at the operating points marked by red asterisks, depict ringing in the hair bundle's response to a force step. Spontaneous oscillations occur at operating points within the Hopf bifurcation curve (orange asterisks and traces). From [124].

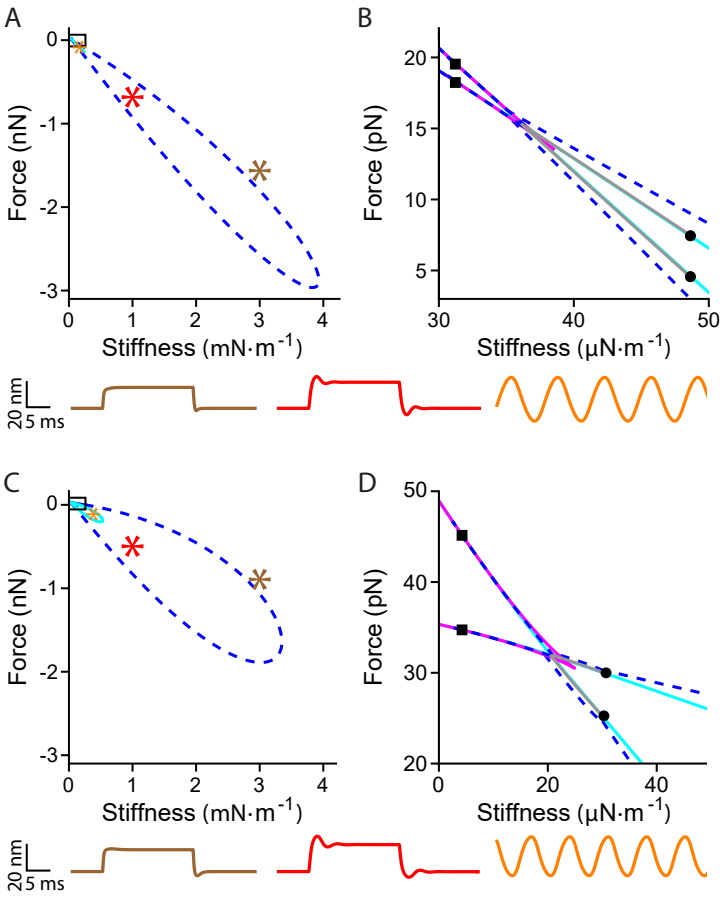

Figure 4.6: Detailed state diagrams for Model II. State diagrams when homeostasis is either inactive (A,B) or active (C,D). In all panels, the blue dashed curves bound the underdamped region, Hopf bifurcation curves are colored cyan, and saddle-node bifurcation curves are magenta. (A,C) The entire underdamped region is shown. The brown traces depict the hair bundle's response to a force step when the bundle is poised at the operating point marked by brown asterisks. At these operating points the bundle does not exhibit any ringing in response to a force step. Red traces, obtained at the operating points marked by the red asterisks, depict ringing in the hair bundle's response to a force step. Simulating the behavior of a bundle poised at the operating points marked with an orange asterisk yields the orange traces, confirming that the model exhibits spontaneous oscillations at operating points within the Hopf bifurcation curve. (B,D) Magnified view of the region enclosed by the box in panel A (B) or in panel C (D). Bogdanov-Takens points are marked by black squares, Bautin points by black circles, and SNLC-bifurcation curves are colored gray. From [124].

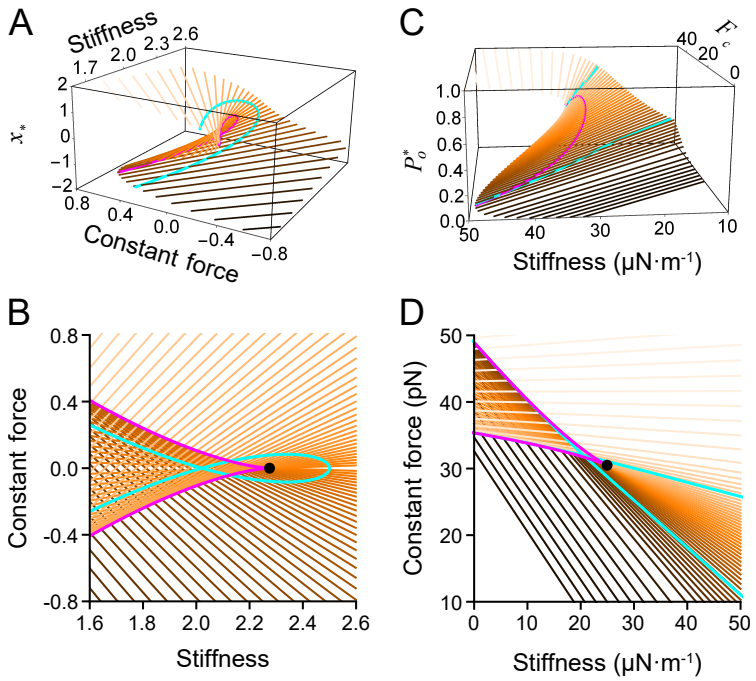

Figure 4.7: Equilibrium-point manifolds. (A) Level curves of the x_* manifold for Model I are shown. Owing to the cubic dependence of Equation 4.25 on x_*, there is a region in parameter space in which x_* is multivalued. Specifically, within the region bounded by saddle-node bifurcation curves (magenta), x_* can take on three values for any given coordinate $\{k, F_c\}$. Two of these values represent stable equilibrium points, whereas the third is an unstable equilibrium. (B) Projection of panel A onto the k-F_c plane. The level curves are lighter for larger values of x_*. The two branches of the saddle-node bifurcation meet at a cusp bifurcation (black dot). Three level curves intersect at any point within the region bounded by the saddle-node bifurcation curves. A single equilibrium point cannot undergo a double Hopf bifurcation in a system of three dynamical variables, for this bifurcation requires two pairs of imaginary values and can therefore occur only in systems with four or more variables. The Hopf bifurcation curve therefore cannot cross itself in the part of parameter space that contains only one equilibrium point. The cubic nonlinearity is thus essential in permitting the Hopf bifurcation curve to form a closed loop. (C, D) Level curves of the P_o^* manifold for Model II and their projection onto the k-F_c plane. The more complicated nonlinearity employed in Model II resembles a cubic function and permits closure of the Hopf bifurcation loop. A curve of Hopf bifurcations is colored cyan in every panel.

Appendix C: Model Modifications

This Appendix describes the modifications made to the models developed in [92] and [51] to generate Models I and II without homeostasis. Model I was closely based on the system

$$m\ddot{x} = -\gamma\dot{x} - kx + a(x - f) - (x - f)^3 + F_c, \tag{4.52}$$

$$\tau\dot{f} = bx - f, \tag{4.53}$$

in which m gives the mass of an overlying load, γ is the total damping experienced by the loaded bundle, τ sets the time scale of adaptation, and all other parameters and variables are defined as in the main text of this paper. Except in Section 5.7, it is assumed that the hair bundle is not loaded with a mass and that the mass of the bundle itself is negligible ($m = 0$). Additionally, γ is scaled to unity and the "rate of adaptation" is defined as $\alpha = 1/\tau$.

The following model of hair bundle dynamics was presented in reference [51]:

$$\lambda\dot{X} = -K_{\mathrm{gs}}(X - X_{\mathrm{a}} - DP_o) - K_{\mathrm{sp}}x + F_{\mathrm{ext}} + \eta,$$

$$\lambda_{\mathrm{a}}\dot{X}_{\mathrm{a}} = K_{\mathrm{gs}}(X - X_{\mathrm{a}} - DP_o) - \gamma N_{\mathrm{a}} f p(C) + \eta_{\mathrm{a}},$$

$$\tau\dot{C} = C_0 - C + C_M P_o + \delta c.$$

First, the noise terms η, η_{a}, and δc are neglected and several variables and parameters are renamed: $X \to x$, $\lambda \to \lambda_x$, $X_a \to y$, $\lambda_a \to \lambda_y$, $F_{\mathrm{ext}} \to F_c$ $K_{\mathrm{gs}} \to k_{\mathrm{gs}}$, $K_{\mathrm{sp}} \to k_{\mathrm{sp}}$, $N_a \to N_m$, $f \to f_m$, and $\gamma \to g$. The system now reads

$$\lambda_x\dot{x} = -k_{\mathrm{gs}}(x - y - DP_o) - k_{\mathrm{sp}}x + F_c, \tag{4.54}$$

$$\lambda_y\dot{y} = k_{\mathrm{gs}}(x - y - DP_o) - gN_m f_m p(C), \tag{4.55}$$

$$\tau_C\dot{C} = C_0 - C + C_M P_o. \tag{4.56}$$

The term $gN_m f_m p(C)$ in Equation 4.55 describes the average force of all the myosin motors at stall: N_m is the number of myosin motors, f_m is the force generated by

a single motor, $g = 0.14$ is the geometrical gain of the stereociliary shear motion, and $p(C) \approx p_0 + p_1 C$, to linear order, is the probability that a motor binds an actin filament. Equation 4.56 describes the dynamics of the intracellular calcium concentration C: When MET channels are closed the intracellular calcium concentration decays to C_0, $C_M \gg C_0$ is the largest possible calcium concentration at the motors, and τ_C sets the time scale of calcium dynamics.

Several additional modifications were made to this model. First, the changes in C are assumed to be very rapid, so that $\tau_C \dot{C} \approx 0$ and $C \approx C_0 + C_M P_o$. Then

$$g N_m f_m p(C) \approx g N_m f_m p_0 + g N_m f_m p_1 (C_0 + C_M P_o).$$

The authors define $f_{\max} = N_m f_m p_0$ and $S = -C_M p_1 / p_0$, which leads to

$$g N_m f_m p(C) \approx g f_{\max} \left(1 + C_0 \frac{p_1}{p_0} - S P_o \right) = g f_{\max} \left(1 - S \frac{C_0}{C_M} - S P_o \right).$$

Because $C_0 \ll C_M$, the $S C_0 / C_M$ term is negligible and, defining $f = g f_{\max}$, the expression $g N_m f_m p(C) \approx f(1 - S P_o)$ results. With these modifications Equation 4.56 drops out and Equation 4.55 becomes $\lambda_y \dot{y} = k_{\mathrm{gs}}(x - y - D P_o) - f(1 - S P_o)$. An elastic-element term $-k_{\mathrm{es}}(y - y_{\mathrm{es}})$ is added to Equation 4.55 to account for the fact that the adaptation provided by the myosin motors is incomplete [127]. A final modification was made to Equation 4.54. In addition to providing a constant offset force F_c, an external load also subjects the bundle to an external stiffness through the term $-k_{\mathrm{e}} x$.

Appendix D: Dependence of the Hopf Bifurcation Curve on Other Parameters

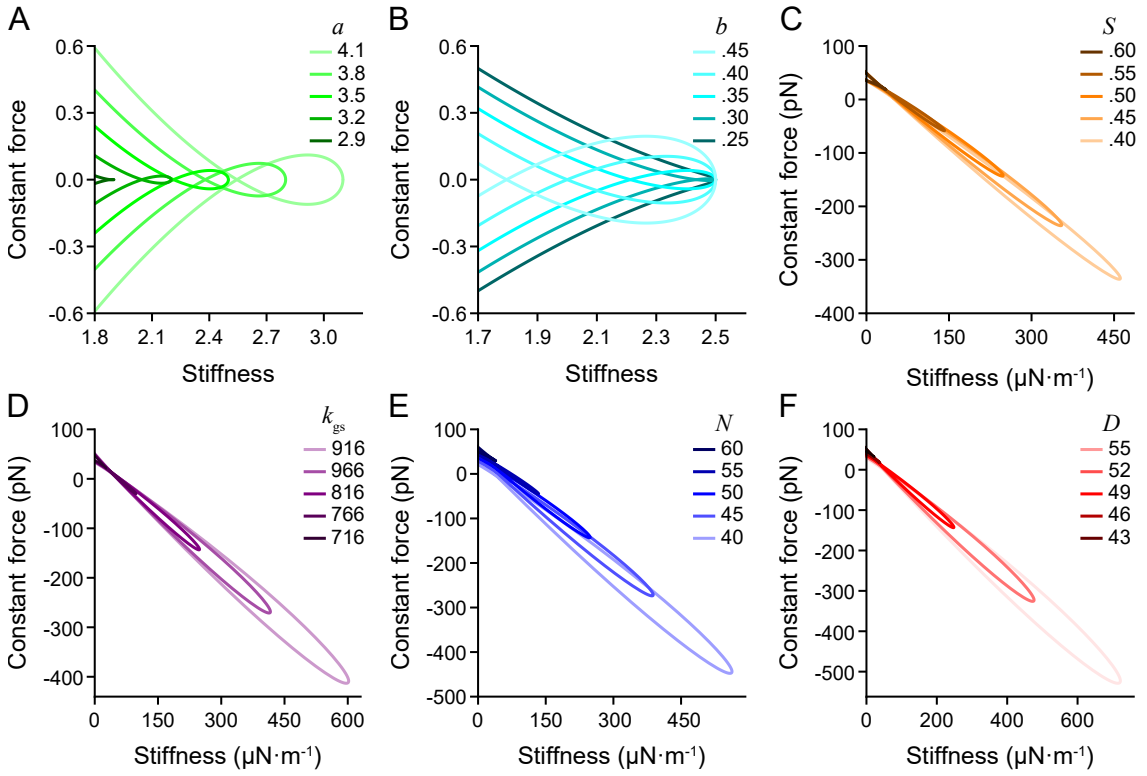

Figure 4.8: Dependence of the Hopf bifurcation curve on other parameters. $(A-F)$ The size and position of the Hopf bifurcation curve in Models I and II are affected by changing any of the system's parameter values. The effect of adjusting α in Model I and f in Model II is discussed in Figure 4.1. Shown are Hopf bifurcation curves for various values of the channel-gating stiffness a (A) or adaptation strength b (B) in Model I and for the strength of Ca^{2+}-mediated inhibition of myosin motors S (C), gating-spring stiffness k_{gs} (D), number of stereocilia N (E), and gating swing D (F) in Model II. Each loop encloses the bundle's self-oscillation region, which is entirely absent for some parameter values.

Appendix E: Additional Bifurcations in Model I

When α^* in Model I is allowed to be zero, additional fixed points exist:

$$\begin{cases} \alpha_* = 0 \\ x_* = \pm\sqrt{\alpha_0/\beta_\alpha} \\ F_c = \pm k\sqrt{\alpha_0/\beta_\alpha} - a(\pm\sqrt{\alpha_0/\beta_\alpha} - y_*) + (\pm\sqrt{\alpha_0/\beta_\alpha} - y_*)^3. \end{cases}$$

These fixed points give rise to two transcritical-bifurcation curves and four saddle node-bifurcation curves:

$$F_{c,\mathrm{TC}\pm}(k) = \pm\sqrt{\frac{\alpha_0}{\beta_\alpha}}\left[k - a(1-b) + \frac{\alpha_0}{\beta_\alpha}(1-b)^3\right], \tag{4.57}$$

$$F_{c,\mathrm{SN}+}(k) = \pm 2\left(\frac{a}{3}\right)^{3/2} + \sqrt{\frac{\alpha_0}{\beta_\alpha}}, \tag{4.58}$$

$$F_{c,\mathrm{SN}-}(k) = \pm 2\left(\frac{a}{3}\right)^{3/2} - \sqrt{\frac{\alpha_0}{\beta_\alpha}}. \tag{4.59}$$

The expressions $F_{c,\mathrm{TC}+}(k)$ and $F_{c,\mathrm{SN}+}(k)$ are associated with the equilibrium point in which $x_* = \sqrt{\alpha_0/\beta_\alpha}$, and $F_{c,\mathrm{TC}-}(k)$ and $F_{c,\mathrm{SN}-}(k)$ with $x_* = -\sqrt{\alpha_0/\beta_\alpha}$. The following Hopf bifurcation curves also occur:

$$\begin{aligned} k_{\mathrm{H}+}(y_*) =& -3\frac{\alpha_0}{\beta_\alpha} - \frac{1}{2\tau_\alpha} + a - 3y_*^2 + 6y_*\sqrt{\frac{\alpha_0}{\beta_\alpha}} \\ &+ \frac{1}{2\beta_\alpha}\sqrt{2\alpha_0\left[3y_*^2(2+b) + ab + \frac{3b\alpha_0}{\beta_\alpha}\right] - 2y_*\sqrt{\frac{\alpha_0}{\beta_\alpha}}\left[3\alpha_0(1+2b) - a\beta_\alpha + 3y_*^2\beta_\alpha\right]} \end{aligned} \tag{4.60}$$

$$F_{c,\mathrm{H}}(y_*) = k_{\mathrm{H}+}(y_*)\sqrt{\alpha_0/\beta_\alpha} - a(\sqrt{\alpha_0/\beta_\alpha} - y_*) + (\sqrt{\alpha_0/\beta_\alpha} - y_*)^3, \tag{4.61}$$

when $\alpha_* = 0$, $x_* = \sqrt{\alpha_0/\beta_\alpha}$, and $b\sqrt{\alpha_0/\beta_\alpha} \leq y_* \leq \sqrt{a/3} + \sqrt{\alpha_0/\beta_\alpha}$, and

$$k_{\mathrm{H}-}(y_*) = -3\frac{\alpha_0}{\beta_\alpha} - \frac{1}{2\tau_\alpha} + a - 3y_*^2 - 6y_*\sqrt{\frac{\alpha_0}{\beta_\alpha}} + \frac{1}{2\beta_\alpha}\sqrt{2\alpha_0\left[3y_*^2(2+b) - ab + \frac{3b\alpha_0}{\beta_\alpha}\right] + 2y_*\sqrt{\frac{\alpha_0}{\beta_\alpha}}\left[3\alpha_0(1+2b) - a\beta_\alpha + 3y_*^2\beta_\alpha\right]} \tag{4.62}$$

$$F_{c,\mathrm{H}}(y_*) = -k_{\mathrm{H}-}(y_*)\sqrt{\alpha_0/\beta_\alpha} + a(\sqrt{\alpha_0/\beta_\alpha} + y^*) - (\sqrt{\alpha_0/\beta_\alpha} + y_*)^3, \tag{4.63}$$

when $\alpha_* = 0$, $x_* = -\sqrt{\alpha_0/\beta_\alpha}$, and $-\sqrt{a/3} - \sqrt{\alpha_0/\beta_\alpha} \leq y_* \leq -b\sqrt{\alpha_0/\beta_\alpha}$.

The fixed points in Model I are given by the following three equations:

$$F_c = ky_*/b - ay_*(1/b - 1) + y_*(1/b - 1)^3,$$

$$F_c = k\sqrt{\alpha_0/\beta_\alpha} - a(\sqrt{\alpha_0/\beta_\alpha} - y_*) + (\sqrt{\alpha_0/\beta_\alpha} - y_*)^3,$$

$$F_c = -k\sqrt{\alpha_0/\beta_\alpha} + a\sqrt{\alpha_0/\beta_\alpha} + y_*) - (\sqrt{\alpha_0/\beta_\alpha} + y_*)^3.$$

Because the manifolds above are represented by cubic equations, each can contribute between one and three fixed points. Any region of the state diagram therefore contains between three and nine fixed points. The number of stable fixed points in each part of the state diagram is shown in Figure 4.9 together with the local bifurcations present in Model I.

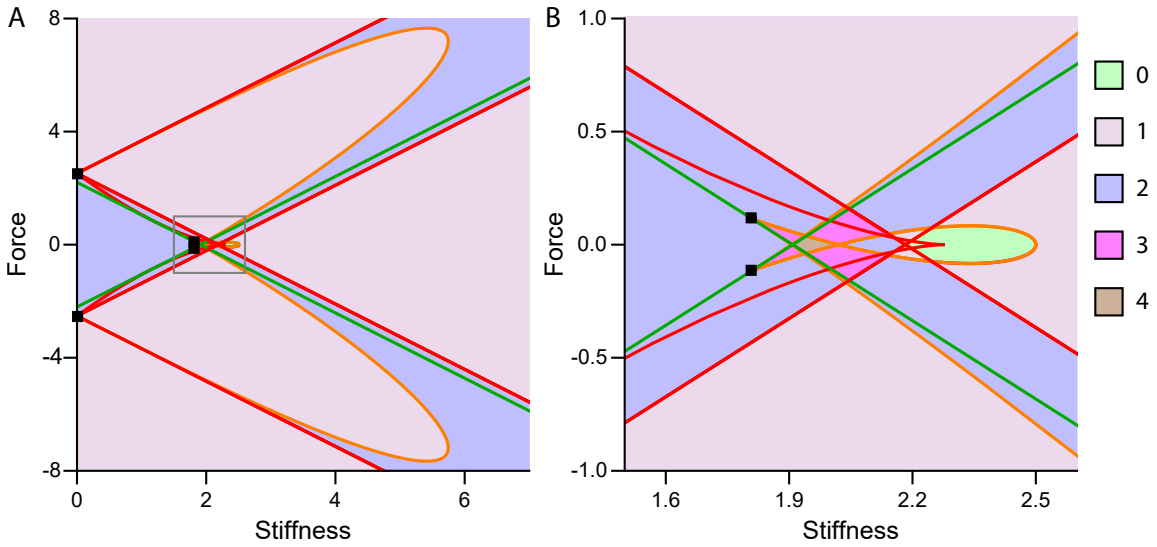

Figure 4.9: Local bifurcations and stable fixed points in Model I, when $\alpha_* = 0$. (A) Homeostasis is active. (B) A magnified view of the area enclosed by the gray box in panel A. In both panels Hopf bifurcation curves are colored orange, saddle node bifurcation curves are red, and transcritical-bifurcation curves are green. The color with which each part of state space is shaded indicates the number of stable fixed points that reside there. From [124].

Chapter 5

Robustness Enhancement by Homeostasis

I evaluated the effects of the homeostatic mechanism on three measures: sensitivity, quality factor, and compressive range. Rendering each of these properties more robust to parameter variations achieves the goal of enhancing the robustness of the system's overall performance as a periodic-signal detector.

5.1 Sensitivity

The sensitivity $|\widetilde{\chi}(\omega)|$ of a system driven by a sinusoidal driving force $F(t) = F_0 \cos(\omega t)$ is defined as the amplitude $|\widetilde{x}(\omega)|$ of the system's phase-locked response at the driving frequency ω divided by the amplitude of the driving force F_0: $|\widetilde{\chi}(\omega)| = |\widetilde{x}(\omega)|/F_0$. A tilde above a variable indicates the Fourier transform of that quantity. Larger sensitivity values indicate a lower input threshold for signal detection.

The sensitivity $|\chi_0(\omega)|$ for weak stimulation is maximized when the system is driven at its resonant frequency ω_R. The hair bundle's peak sensitivity, $|\chi_0(\omega_R)|$, was calculated for operating points on the quiescent side of the Hopf bifurcation in the underdamped region of the state diagram (Section 4.5).

In Model I, the peak sensitivity of the linearized system is

$$\left|\chi_0(\omega_R)\right| = \left|\frac{\alpha_* + i\omega_R}{\alpha_* \widehat{a}\, b + (\alpha_* + i\omega_R)(k - \widehat{a} + i\omega_R)}\right|, \text{ or}$$

$$\left|\chi_0(\omega_R)\right| = \sqrt{\frac{\alpha_*^2 + \omega_R^2}{\omega_R^4 + \omega_R^2[k^2 + \alpha_*^2 - 2\widehat{a}(k + \alpha_* b) + \widehat{a}^2] + \alpha_*^2[k - \widehat{a}(1-b)]^2}}\,, \qquad (5.1)$$

in which $\alpha_* = \alpha_0 - \beta_\alpha x_*^2$, $\widehat{a} = a - 3(1-b)^2 x_*^2$, and the resonant frequency ω_R is

$$\omega_R = \sqrt{-\alpha_*^2 + \sqrt{\widehat{a}\, b[\widehat{a}(b-2) + 2(k+\alpha_*)]\alpha_*^2}}\,. \tag{5.2}$$

For quiescent bundles, the sensitivity is larger for operating points near the Hopf bifurcation. The peak sensitivity inside the region of spontaneous oscillation in the state diagram exceeds that in the quiescent region.

A hair bundle can detect a stimulus if the bundle's response exceeds a threshold value. A curve of constant sensitivity encloses a region in the state diagram within which the bundle's sensitivity exceeds some specified threshold. The larger this region, the more robust is signal detection to changes in the values of control parameters. Homeostasis dilates the area contained within each curve of constant peak sensitivity (Figs. 5.1*A*,*B* and 5.8*A*) and effects more gradual changes in sensitivity along lines of constant k (Fig. 5.1*C*) or F_c (Fig. 5.1*D*). Homeostasis through the adaptation rate α thus renders the hair bundle's sensitivity more robust to changes in the control parameters.

The peak sensitivity of the linearized system for Model II is given by

$$\left|\chi_0(\omega_R)\right| = \left| \frac{\widehat{\beta}_f + (k_{\rm es}\delta + \widehat{k}_{\rm gs}\delta + f_*\widehat{S} + i\omega_R\delta\lambda_y)(1 + i\omega_R\tau_f)}{(k + \widehat{k}_{\rm gs} + i\omega_R\lambda_x)[\widehat{\beta}_f + (f_*\widehat{S} + \delta[k_{\rm es} + \widehat{k}_{\rm gs} + i\omega_R\lambda_y])\widehat{\zeta}] - \widehat{k}_{\rm gs}[\widehat{\beta}_f + (\widehat{k}_{\rm gs}\delta + f_*\widehat{S})\widehat{\zeta}]} \right|, \tag{5.3}$$

in which $f_* = f_0 - \beta_f P_o^*$, $\widehat{k}_{\rm gs} = k_{\rm gs}[1 - DP_o^*(1-P_o^*)/\delta]$, $\widehat{\beta}_f = \beta_f(1-P_o^*)(1-P_o^* S)P_o^*$, $\widehat{S} = SP_o^*(1-P_o^*)$, and $\widehat{\zeta} = 1 + i\omega_R\tau_f$. An analytical expression exists for ω_R but is omitted to conserve space.

Curves of constant peak sensitivity in Model II's state diagram reveal that engaging the homeostatic mechanism augments the areas contained within each contour

(Figs. 5.1*E*,*F* and 5.8*D*). Moreover, when evaluated along a line of constant stiffness (Fig. 5.1*G*) or force (Fig. 5.1*H*), the peak sensitivity changes more slowly when homeostasis is operational than when it is inactive. When homeostasis is active, the bundle can accommodate larger perturbations in the values of control parameters while still maintaining its ability to detect small signals. Although Model II takes into account the dynamics of the active force f rather than the rate of adaptation α, these results echo those found for Model I.

Model I possesses a state diagram that is symmetric about the line $F_c = 0$. Because of the symmetric dependence of Equation 4.18 on the bundle's displacement, the symmetry is unaffected by the homeostatic mechanism (Fig. 4.4*A*). Homeostasis consequently changes the size but not the orientation of the contours. Model II lacks symmetry owing to an asymmetry inherent to hair bundle physiology, namely the sigmoidal relation of the channel open probability to hair bundle displacement. Because Eq. 4.19 is not symmetric with respect to displacement, engaging the homeostatic mechanism in Model II dilates, reshapes, and reorients the oscillatory region (Fig. 4.4*B*).

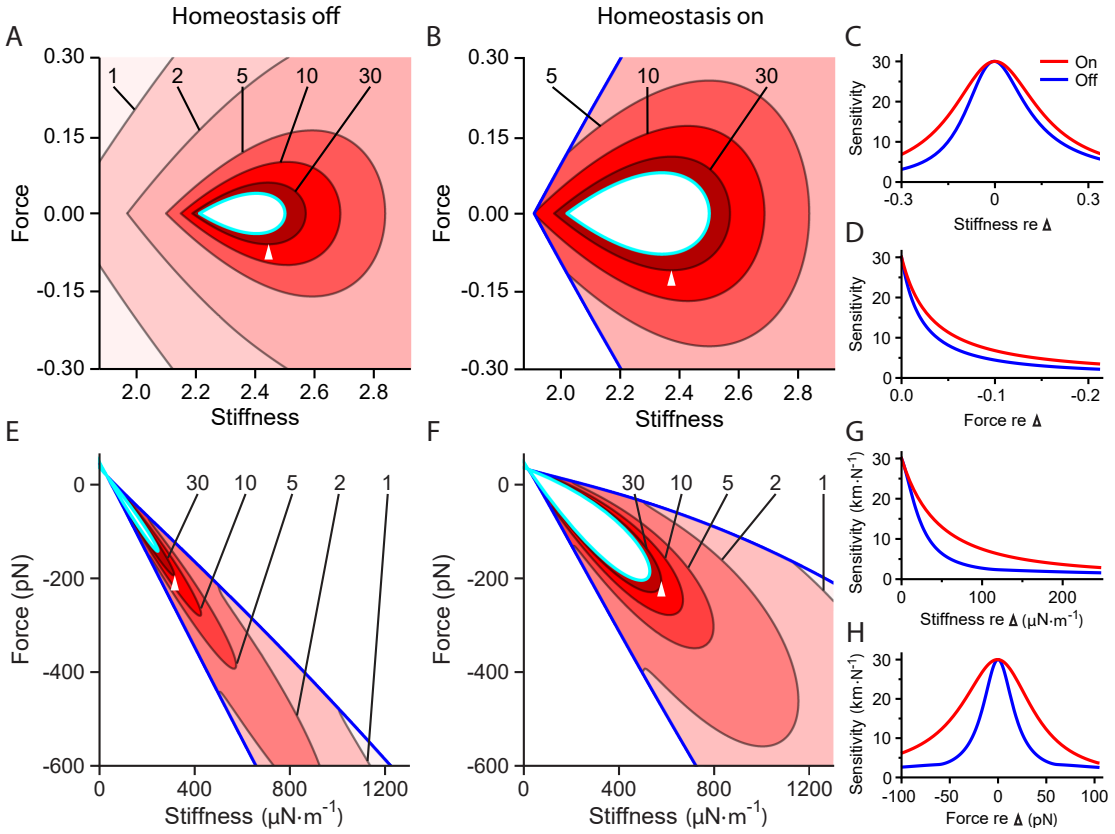

Figure 5.1: Homeostasis increases the robustness of a hair bundle's sensitivity. (A, B) Sensitivity as a function of constant force F_c and stiffness k for Model I when homeostasis is off (A) or on (B). Darker shades of red indicate larger values of the peak sensitivity $\chi_0(\omega_R)$. Contours are labeled by their respective peak sensitivity values. The Hopf bifurcation curve is colored cyan and the blue curve marks the boundary of the underdamped region. Homeostasis enhances the robustness of the hair bundle's sensitivity to small-amplitude sinusoidal signals by expanding the areas enclosed by the sensitivity contours. (C,D) The peak sensitivities along a horizontal (C) or vertical (D) slice through the state diagram when homeostasis is inactive (blue) or active (red). The red and blue curves correspond to slices though the reference operating points indicated in panel A and B respectively (apices of white triangles). The peak sensitivity is larger and changes more slowly along these transects when homeostasis is active. $(E$-$H)$ The results for Model II are portrayed as for panels A-D. The contour labels in panels E and F bear units of km·N^{-1}. All parameter values are listed in Tables 4.1 and 3.2. Additional bifurcation lines that occur in these regions of the state diagram are not shown (Appendix E). From [124].

5.2 Frequency Selectivity

I next examined how the hair bundle's frequency selectivity is affected by the homeostatic mechanisms. The quality factor Q is defined as the system's resonant frequency ω_R divided by the frequency bandwidth $\Delta\omega = \omega_+ - \omega_-$ over which the oscillation's power exceeds half the maximum at resonance: $Q \equiv \omega_R/(\omega_+ - \omega_-)$, in which $\omega_\pm$ is found by solving $\left|\chi_0(\omega_\pm)\right| = \left|\chi_0(\omega_R)\right|/\sqrt{2}$ for $\omega_\pm$ (Appendix F, Eq. 5.14). Large values of Q indicate that a system is sharply tuned. Quality factors as large as 30 have been measured in the mammalian cochlea [129].

I delineate the quality factor contours within the quiescent, underdamped region of the hair bundle's state diagram. Frequency tuning is sharper at operating points that are closer to the self-oscillation region (Figure 5.2), and sharper still inside the oscillatory region. Endowing Model I with its homeostatic mechanism renders Q more robust to changes in the values of the control parameters. When the homeostatic mechanism is engaged, Q contours enclose larger areas in the state diagram than when homeostasis is off (Figures 5.2*A*,*B*). Homeostasis also reduces the rate of change of Q along lines of constant stiffness or force (Figures 5.2*C*,*D*).

For Model II the homeostatic mechanism enlarges the regions contained within Q contours (Figures 5.2*E*,*F*) and diminishes the steepness of Q's dependence on each control parameter (Figures 5.2*G*,*H*). The precision needed in selecting the hair bundle's operating point to ensure sharp frequency selectivity is therefore reduced by each of the two distinct homeostatic mechanisms employed in Model I and Model II.

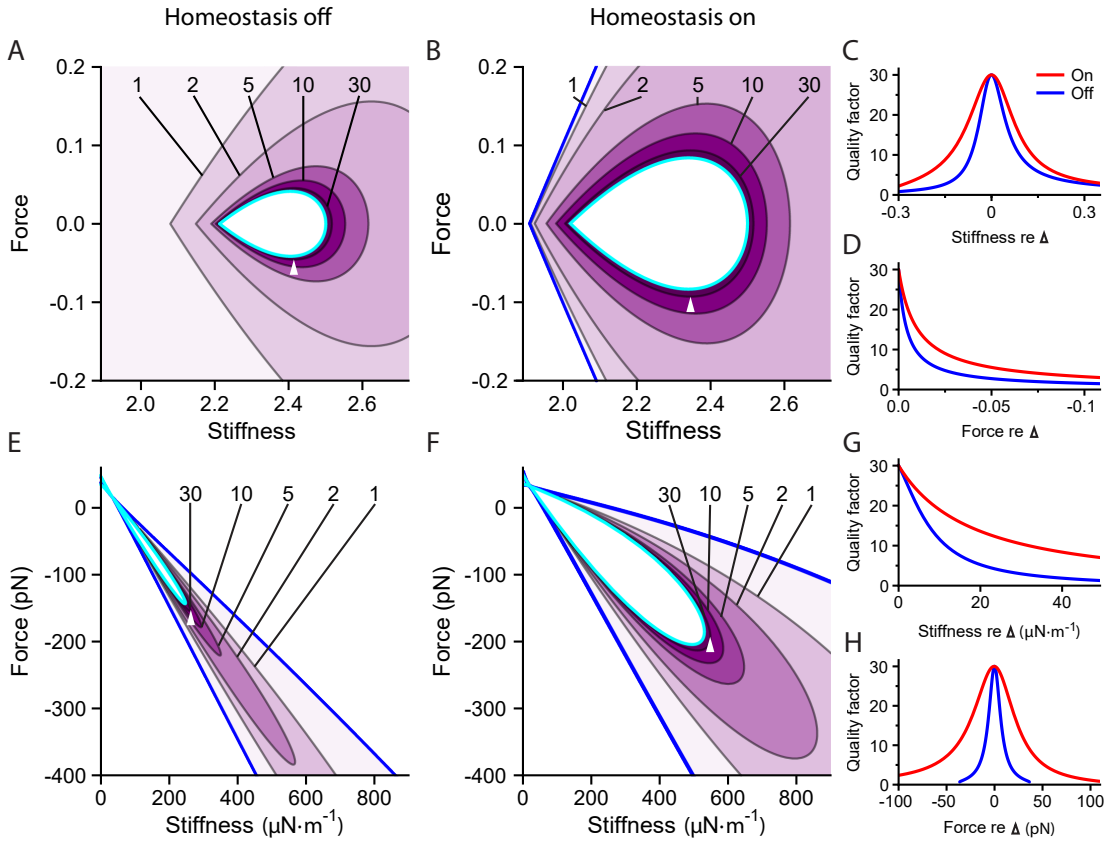

Figure 5.2: Homeostasis increases the robustness of a bundle's frequency selectivity. (A,B) Contours of the quality factor Q are shown in the state diagram of Model I for homeostasis off (A) and homeostasis on (B). Each contour is labeled with its respective value of Q and darker shades of purple indicate larger Q values. (C,D) The quality factor along horizontal (C) or vertical (D) slices that pass through the reference operating points indicated in panels A and B (white triangle apices) when homeostasis is off (blue) or on (red). ($E-H$) The results for Model II are portrayed as for panels $A-D$. In each contour plot the Hopf bifurcation curve is colored cyan and the blue curve marks the boundary of the underdamped region of the state diagram. All parameter values are listed in Tables 4.1 and 4.2 and the alignment of the curves in panels C, D, G, and H is as described in Figure 5.1. Additional bifurcation lines that occur in these regions of the state diagram are not shown (Appendix E). From [124].

5.3 Response Time Trade-Off

The quality factor Q increases monotonically with the length of time that a system requires to reach its steady state: sharper frequency selectivity is obtained at the expense of a slowed response onset. By rendering Q more robust, the homeostatic mechanism in either model reduces the set of operating points at which the bundle can respond quickly to stimuli. Frequency discrimination is improved at the expense of temporal resolution. Owing to greater robustness enhancement, homeostasis causes larger proportional increases in response times in Model II than in Model I. The following analysis reveals, however, that sharper frequency selectivity can be obtained at a slightly lower cost in relaxation time for Model II than for Model I.

For small perturbations, the timescales of a system's response are given by the real parts of the negative reciprocals of the Jacobian matrix's eigenvalues. In Model I, the eigenvalues are $\xi_\alpha = -1/\tau_\alpha$ and

$$\xi_\pm = \frac{1}{2}\Big[a - k - \alpha_0 + x_*^2(\beta_\alpha - 3(1-b)^2) \pm \sqrt{\big(k - a + \alpha_0 + x_*^2[3(1-b)^2 - \beta_\alpha]\big)^2 - 4[k - a(1-b) + 3(1-b)^3 x_*^2](\alpha_0 - x_*^2\beta_\alpha)}\Big]. \tag{5.4}$$

The relevant timescales are therefore τ_α and

$$\tau = 2\left[k - a + \alpha_0 + x_*^2(3(1-b)^2 - \beta_\alpha)\right]^{-1}. \tag{5.5}$$

τ_α is relevant only when $\beta_\alpha \neq 0$ because stimulating the bundle does not engage the homeostatic mechanism when $\beta_\alpha = 0$.

By a similar calculation, τ for Model II when homeostasis is off is given by

$$\tau = \frac{2\delta\lambda_x\lambda_y}{f_0(1-P_o^*)P_o^*S\lambda_x + (k_{\rm es} + k_{\rm gs})\delta\lambda_x + (k + k_{\rm gs})\delta\lambda_y - Dk_{\rm gs}(1-P_o^*)P_o^*(\lambda_x + \lambda_y)}. \tag{5.6}$$

As for Model I, τ_f is irrelevant when homeostasis is inactive.

At operating points far from the Hopf bifurcation, the timescales τ_α and τ_f substantially exceed τ and determine the relaxation time when the bundle's displacement x is greatly perturbed (Fig. 5.9). Small perturbations, however, do not engender large changes in the homeostatic variables α or f.

In both models, τ specifies the approximate time required for the amplitude of the bundle's response to a small perturbation to decay by a factor of $1/e$. Homeostasis increases the set of operating points at which τ exceeds a threshold (Fig. 5.3). Therefore, the cost of enhancing the robustness of the bundle's frequency selectivity is a slowed reaction stimuli. This cost is proportionally smaller in Model II than in Model I.

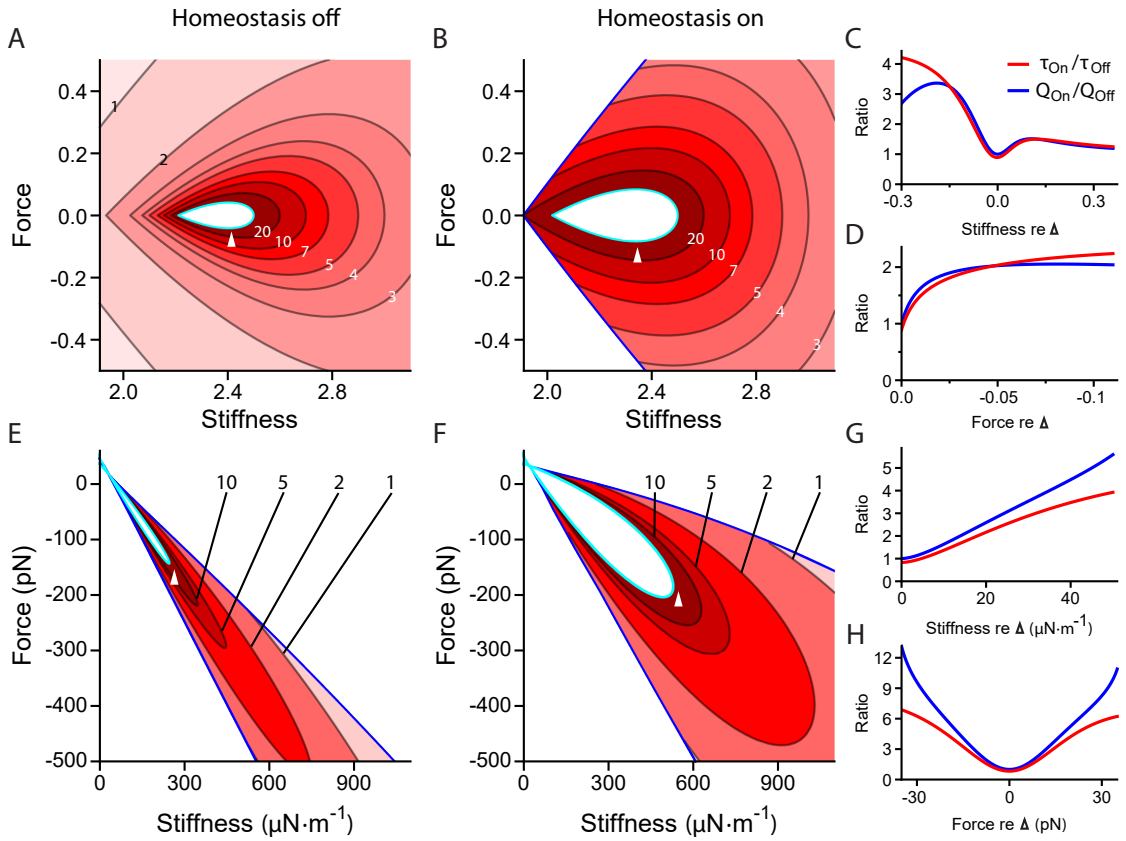

Figure 5.3: Homeostasis increases the time needed to reach a steady state. (A, B) The time τ for the bundle's response to a small perturbation to decay to $1/e$ times the initial amplitude of the response in Model I when homeostasis is off (A) or on (B). Darker shades of red indicate larger τ values. Contours are labeled by their respective τ values. The Hopf bifurcation curve is colored cyan and the blue curve marks the boundary of the underdamped region. Enhanced robustness of signal detection is achieved through homeostasis by sacrificing how quickly the system can respond to stimuli, as evidenced by the expanded areas enclosed by the τ contours. (C,D) Ratios of τ (red) and quality factor Q (blue) values along horizontal (C) or vertical (D) slices through the reference operating points indicated in panels A and B (apices of the white triangles). The selected slices are the same as in Figure 5.2. The τ ratio is similar to the Q ratio, illustrating that the enhanced frequency selectivity attained through homeostasis coincides with a slower approach to steady state. $(E-H)$ Same description as panels $A-D$ but for Model II. The τ ratio is less than the Q ratio for Model II, whereas for Model I the τ ratio can exceed the Q ratio, demonstrating that enhanced frequency selectivity can be attained for Model II at a proportionally lower cost in reaction time than for Model I. The contour labels in panels E and F bear units of ms. All parameter values are listed in Tables 4.1 and 4.2. From [124].

5.4 Compressive Range

A hair bundle can detect signals over a finite range of amplitudes, defined as the bundle's dynamic range. If the amplitude $|\widetilde{x}(\omega)|$ of a system's response to stimulation is proportional to $|\widetilde{F}(\omega)|$, then the system's dynamic range must be restricted by the range of permissible response amplitudes. A broader dynamic range can be attained if the system's response amplitude grows more slowly with stimulus amplitude, compressing a wide range of inputs into a narrower range of outputs.

A system that operates at a Hopf bifurcation exhibits nonlinear compression that obeys the one-third power law $|\widetilde{x}(\omega)| \sim |\widetilde{F}(\omega)|^{1/3}$ [113]. Such a system represents six orders of stimulus magnitude with only two orders of magnitude in the amplitude of the response. Near the bifurcation, nonlinear compression occurs for a limited range of stimulus amplitudes, termed the compressive range (Figure 5.4). This range is defined to be the span, in logarithmic units, of stimulus amplitudes over which the amplitude of the response grows according to $|\widetilde{x}(\omega)| \sim |\widetilde{F}(\omega)|^{\nu}$, in which the exponent ν falls in the interval $(0, 1/2]$. This condition restricts our analysis to strong compression and avoids numerical complications that are described below.

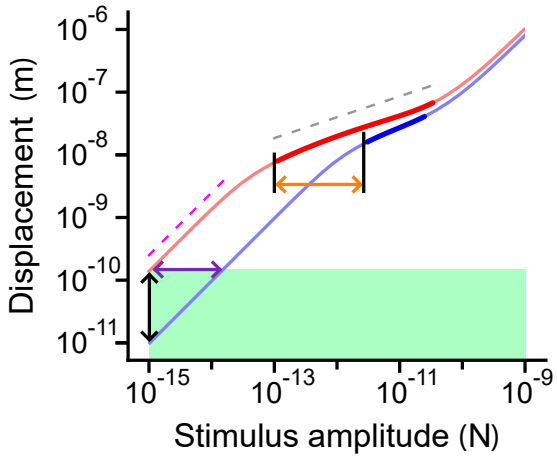

Figure 5.4: Increasing the compressive range broadens a bundle's dynamic range. The responses of Model II, absent homeostasis, to periodic stimulation at the resonant frequency are shown for operating points closer to (red) and farther from (blue) the self-oscillation region. The response $|\widetilde{x}| \sim |\widetilde{F}|^{\nu}$, in which ν is the slope of the curves in the doubly logarithmic plot. Thin portions of the curves possess slopes between 1/2 and 1, whereas thick portions bear slopes between 0 and 1/2. For comparison, the relations $|\widetilde{x}| \sim |\widetilde{F}|$ (dashed magenta line) and $|\widetilde{x}| \sim |\widetilde{F}|^{1/3}$ (dashed gray line) are shown. The horizontal span of the thick part of each curve defines that operating point's compressive range. Points on the curves above the area shaded green exceed some particular threshold in sensitivity. The dynamic range of the red curve equals the width of the green rectangle; the dynamic range of the blue curve is smaller by one order of magnitude (purple double arrow). This difference stems from the red curve's larger compressive range (orange double arrow). Extending the dynamic range renders the bundle more sensitive to low-amplitude stimuli (black double arrow). From [124].

Calculating the compressive range required simulation of each model's response to sinusoidal stimulation spanning a large range of amplitudes at many control-parameter values. The driving term $F_0 \cos[\omega_R(k, F_c)\, t]$, in which F_0 is the driving amplitude and the driving frequency is the bundle's resonance frequency $\omega_R(k, F_c)$ at the control parameter values $\{k, F_c\}$, was added to Equation 4.20 or 4.30 of the main text. Mathematica's `NDSolve` function was then used to numerically solve equations 4.20 - 4.22 or 4.30 - 4.33 of the main text. A maximum step size of 10^{-3} in Model I or of 0.25 μs in Model II was used to ensure faithful reproduction of the nonlinear response; smaller step sizes yielded the same results. Each simulation was allowed to reach steady state, then a lengthy time segment of the simulation was analyzed: in Model I the length of the analyzed segment was 8.5 million steps and in Model II it was 4 million steps or 1 s. These segments contained at least 50 stimulus cycles, and generally many more.

After the Fast Fourier transform had been applied to the resulting time series, the peak of the transform's absolute value at the driving frequency was found. The height of this peak divided by the magnitude of the driving force yielded the bundle's sensitivity at that operating point and stimulus amplitude. This procedure was repeated for a set of stimulus amplitudes spanning the ranges depicted in Figure 5.5. The stimulus amplitudes were logarithmically spaced: each was smaller than the next by a factor of $\sqrt{10}$, except in the regime where the bundle's response transitioned from linear to nonlinear, for which the spacing factor was $10^{1/64}$.

A curve of sensitivity *versus* stimulus amplitude, termed a compression curve, was interpolated through splines in doubly logarithmic space from the sensitivity values calculated at each operating point. The bundle's compressive range at this operating point was finally extracted from the bundle's compression curve, as described below.

Spline interpolation over the compressive-range values calculated on a grid of points in a state diagram yielded the plots shown in Figure 5.6.

Compressive range is defined to be the range of driving-force amplitudes over which the slope of the sensitivity compression curve is between -1 and -1/2 (Fig. 5.5). Model I employs two nonsaturating nonlinearities: Equation 4.20 bears a cubic term and Equation 4.22 is quadratic in the bundle's displacement. A consequence of the first nonlinearity is the absence of an intrinsic upper bound on the hair bundle's compressive range. A value of 1 was chosen so that the compressive range in Model I was comparable to that of Model II. The second nonlinearity results in unbounded responses to very large forces when homeostasis is active. When x is large, α becomes negative. If $\alpha < 0$ and $y > bx$, y grows exponentially quickly, which in turn causes x to grow rapidly. Choosing the maximum driving force amplitude to be 1 ensures that the unphysical situation of $\alpha < 0$ is avoided. Both of these issues are resolved in Model II by employing the saturating nonlinearity P_o, which more closely approximates reality.

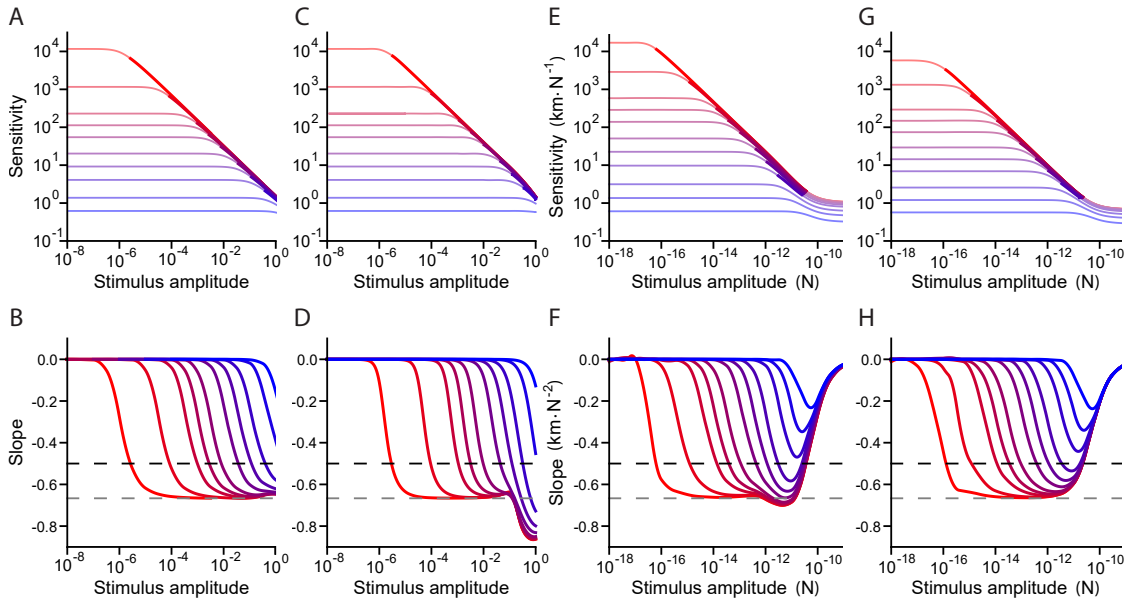

Figure 5.5: Sensitivity as a function of the amplitude of driving in Model I when homeostasis is either off (A) or on (C), and in Model II in the absence (E) or presence (G) of the homeostatic mechanism. From red to blue, the compression curves were generated at operating points located progressively farther from the oscillatory region. The bundle's response is linearly related to the stimulus amplitude when the compression curves are flat, whereas a negative slope indicates nonlinear compression. Compression curves are thicker when their slopes lie in the interval (-1,-1/2], or $\chi(F) \sim F^{\epsilon}$, in which $-1 < \epsilon \leq -1/2$ ($\epsilon = \nu - 1$). The slope of each compression curve in panels A, C, E, and G is shown in panels B, D, F, and H, respectively. The dashed black lines in panels B, D, F, and H marks a slope of -1/2 and a slope of -2/3 is indicated by the dashed gray lines. (A-D) Curves obtained at $F_c = 0$. (E-H) The curves in panels E-F were generated at operating points that fell on the line in which $P_o^* = 0.35$ and $P_o^* = 0.5$ in panels G-H. Curves of the same color correspond to operating points whose Jacobian matrices possess complex eigenvalues with the same real parts. The upper bound on the stimulus amplitude was 1 for all compressive range calculations in Model I. From [124].

Curves of constant compressive range for each model show that operating points close to the Hopf bifurcations in the state diagrams possess a broad compressive range (Figure 5.6). The homeostatic mechanism employed in Model I expands the range of parameter values over which the compressive range exceeds a threshold. Furthermore, the compressive range changes more slowly in size at most values of stiffness or constant force. For Model II the compressive-range contours encompass larger regions when homeostasis is active than when homeostasis is inactive (Figure 5.6*E*,*F*), and the slope of the bundle's compressive range as a function of either stiffness or force is significantly less steep when homeostasis is operational (Figure 5.6*G*,*H*). Both homeostatic mechanisms succeed in rendering the bundle's dynamic range more robust to changes in the control parameters.

The saddle-node bifurcations, saddle-node bifurcations of limit cycles, and multimodal response boundaries shown in Figure 5.6 were excluded from Figures 5.1 are 5.2 for the sake of clarity; in these three figures, the diagrams contain the same set of bifurcations. The Hopf bifurcation curve comprises supercritical and subcritical parts (SI Appendix 8). The advantages and disadvantages of poising a bundle near the supercritical or subcritical portions of the Hopf bifurcation curve are discussed elsewhere [90].

Figure 5.6: Homeostasis increases the robustness of a hair bundle's dynamic range. (A) Contour plot showing curves of constant compressive range for Model I when homeostasis is off. (A,B) Compressive range is shown as a function of the stiffness (abscissa) and constant force (ordinate). The contour labels indicate the size of the compressive range in orders of magnitude of the periodic forcing amplitude; see Figure 5.4 for examples. Darker shades of green indicate broader compressive ranges. The purple curve is a line of saddle-node bifurcations; saddle-node bifurcations of limit cycles are colored red. (B) A contour plot of compressive range when homeostasis is on. Multimodal oscillations occur in response to sinusoidal forcing within the region on the left-hand side of the magenta curves. The purple curve is a line of saddle-node bifurcations. The apices of the white triangles indicate the reference operating points through which horizontal and vertical slices were taken to generate the curves for panels C and D, respectively. (E-H) Compressive range for Model II when homeostasis is inactive (E) or active (F). Panels G and H show the compressive range of the bundle along either a horizontal (G) or vertical (H) slice through the apices of the white triangles in panels E and F. The Hopf bifurcation curve is colored cyan in each contour plot, and the blue curve marks the boundary of the underdamped region of the state diagrams. At each operating point, sinusoidal stimuli were delivered at the bundle's resonant frequency, which varied as a function of stiffness and constant force. The stimulus frequency was not changed to match possible shifts in the peak frequency as the forcing amplitude increases. The compressive range was not calculated within the white regions of state space. "Compression" signifies the compressive range in panels C, D, G, and H. Additional information about the excluded regions can be found in Section 4.5. All parameter values are listed in Tables 4.1 and 4.2, and the alignment of the curves in panels C, D, G, and H is as described in Figure 5.1. Additional bifurcation lines that occur in these regions of the state diagram are not shown (Appendix E). From [124].

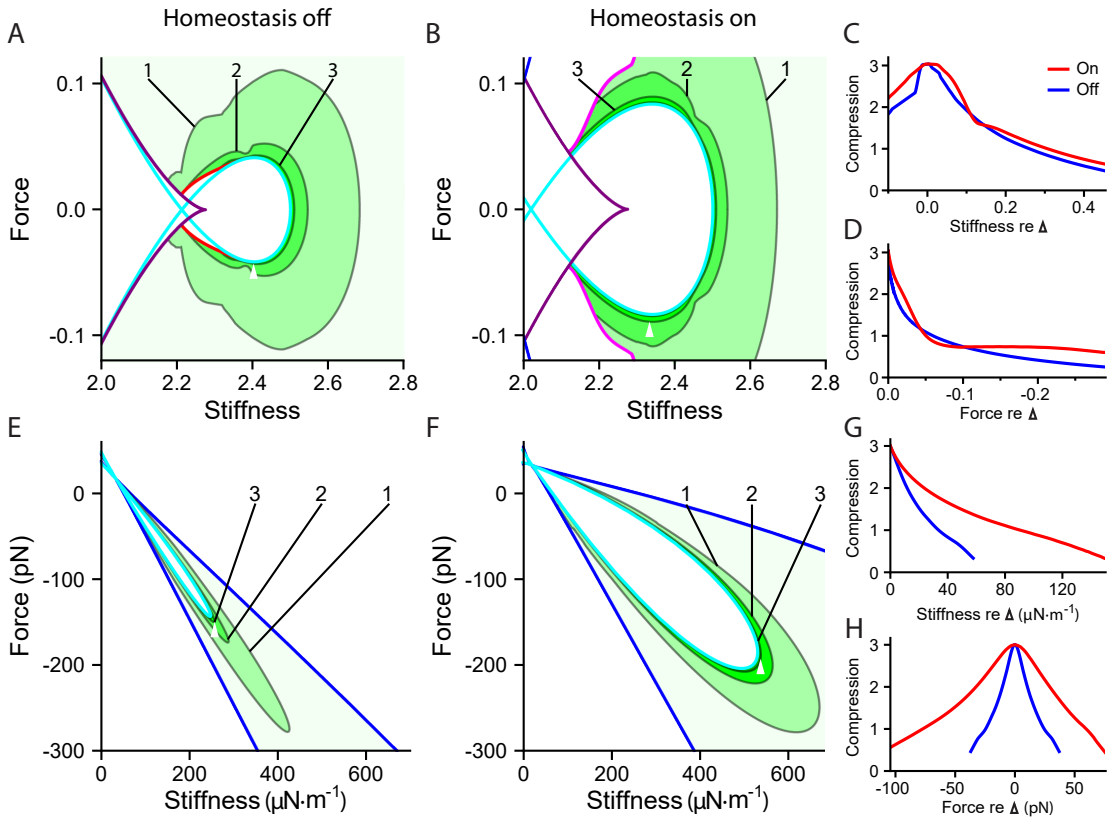

Figure 5.6: Homeostasis increases the robustness of a hair bundle's dynamic range.

5.5 Quantification of Robustness Enhancement

To quantify the degree of robustness enhancement, I calculated the areas contained within contours of peak sensitivity, sharp tuning, and compressive range. The ratio of the areas in the "homeostasis on" state diagram to those of the "homeostasis off" state diagram yielded a measure of robustness enhancement termed the areal ratio. The areal ratios for peak sensitivity, frequency tuning, and compressive range always exceed one and become greater for contours closer to the self-oscillation region (Fig. 5.7). The size of this effect can be increased by changing the values of the parameters that control homeostasis (Figs. 5.8A, D). Both homeostatic strategies thus render the hair bundle's ability to detect signals more robust to parameter variation, with the greatest enhancement occurring for operating points located close to the line of Hopf bifurcations.

It is unclear whether the self-oscillation region of the state diagram is utilized by hair bundles responsible for detecting sinusoidal signals. Including the area of self-oscillation mildly affects the enhancement for Model I: areal ratios are slightly greater than or comparable to values found when the self-oscillation region is excluded. In Model II, however, including the regions of spontaneous oscillation yields much larger areal ratios, particularly for greater values of peak sensitivity, tuning sharpness, and compressive range (Fig. 5.7). When the self-oscillation regions are included, the areal ratios for both models approach the factor by which homeostasis dilates the size of the oscillatory region for large values of sensitivity, tuning sharpness, and compressive range. At small values of these measures, the oscillatory region makes only a small contribution to the area enclosed by the contours and therefore does not significantly affect the areal ratios.

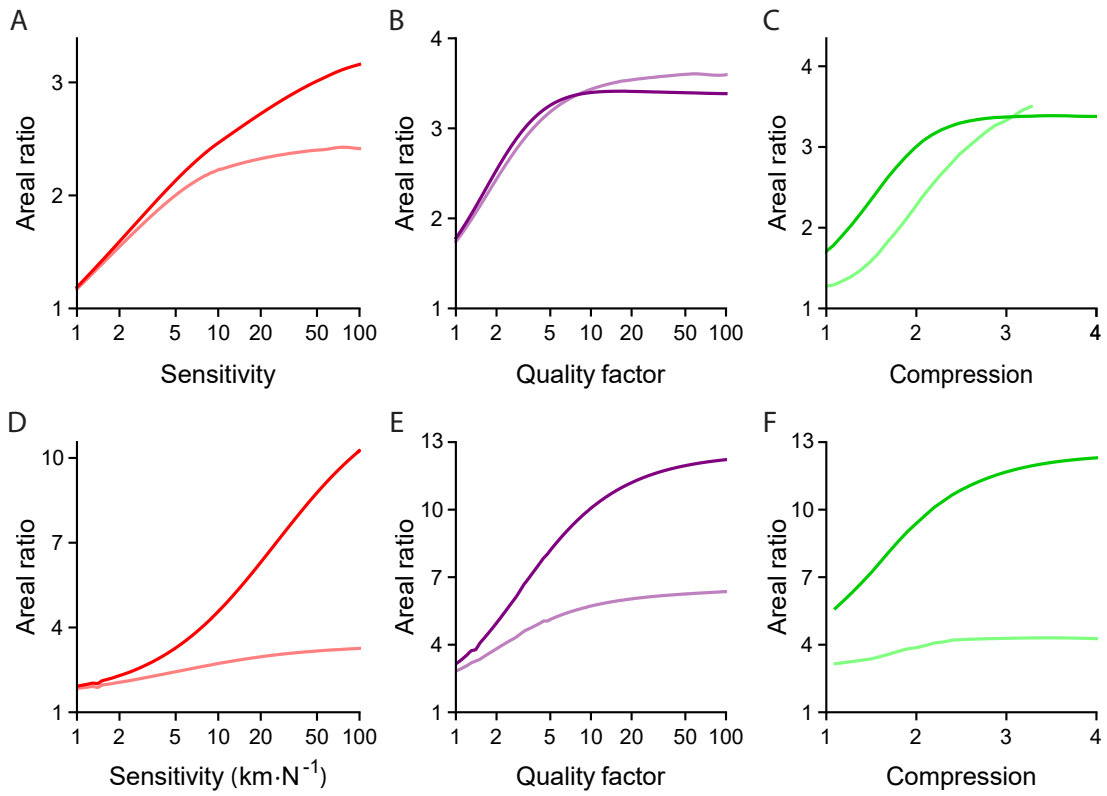

Figure 5.7: Quantification of robustness enhancement. (*A*-*F*) Ratios of areas enclosed by contours in the homeostasis on state diagram to areas bounded by contours in the homeostasis off state diagram. The oscillatory region of the state diagram was either included (darker) or excluded (lighter). (*A*-*C*) Areal ratios for Model I: (*A*) peak sensitivity, (*B*) quality factor, and (*C*) compressive range. (*D*-*F*) Areal ratios for Model II: (*D*) peak sensitivity, (*E*) quality factor, and (*F*) compressive range. The entire areas enclosed by some contours are not shown in Figures 5.1, 5.2, and 5.6, but are included in our calculation of areal ratios. From [124].

Numerical calculations suggest that $|\chi(\omega_R)|$ is inversely proportion to the distance in parameter space between the system's operating point and the Hopf bifurcation along a line of constant x_* in Model I or of constant P_o^* in Model II[1] Because this power-law dependence does not appear to be affected by the presence of the homeostatic mechanisms, it is unsurprising that dilating the self-oscillation region effects a concomitant expansion of the area contained withing sensitivity contours. Two phenomena did, however, prove surprising.

First, the homeostatic mechanisms were more efficient in expanding the sensitivity contours than simply adjusting the value of α in Model I or f in Model two in the absence of homeostasis. In others words, for the same dilation factor, the areal ratios obtained through the homeostatic mechanisms exceeded those acquired through adjusting parameter values. This effect can be seen by comparing figures $5.8B, E$ to figures $4.2B, E$; the data points in the former approximate lines with greater slopes. The areal ratios for Model II also adhere more closely to a linear relation when robustness enhancement is effected through the homeostatic mechanism (Figs. $4.2E$ and $5.8E$). The result may be related to how the homeostatic mechanism reshapes the boundary of the underdamped region.

Second, the areal ratios obtained for Model I exceeded the upper limit found in Section 3.3. That the self-oscillation region is not uniformly scaled by the homeostatic mechanism might account for this finding.

[1]In Model I the line $x_* = 0$ corresponds to $F_c = 0$. Taylor expansion along this line is tractable and reveals that $|\chi(\omega_R)| \propto 1/(k - a + \alpha_0)$, where $a - \alpha_0$ is the k-axis intercept of the Hopf bifurcation curve.

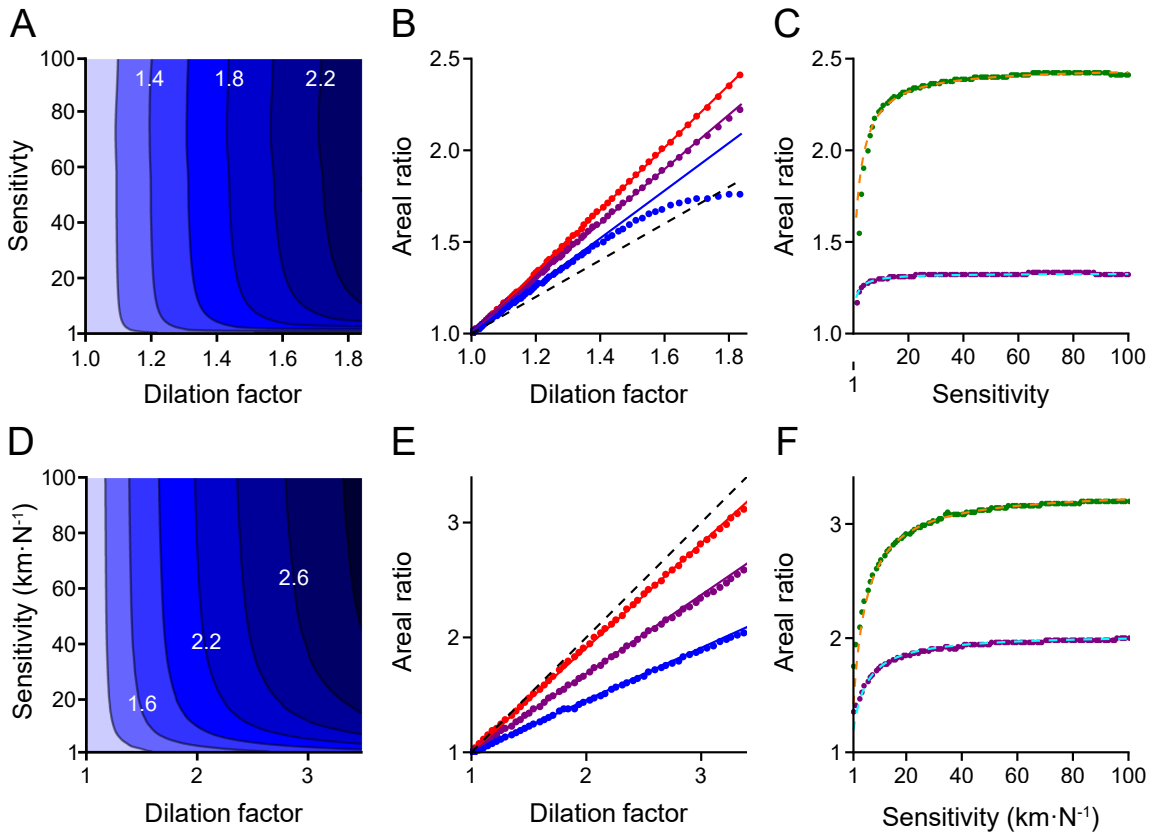

Figure 5.8: Comparison between the general case and the models with homeostasis. (*A*) Peak-sensitivity areal ratios as a function of the peak sensitivity and of the oscillatory region's dilation factor h. Darker shades of blue indicate larger areal ratios. β_α ranges from 0 at a dilation factor of 1 to 0.75 at the maximum dilation factor shown. (*B*) Areal ratios for $\chi = 100$ (red), 10 (purple), and 3 (blue). The dots portray the numerically calculated results and straight lines are shown for comparison. The black, dashed line marks $\mathcal{R}_\chi(h) = h$. (*C*) Areal ratios for $h = 1.8$ (green dots) and 1.2 (purple dots). (*D-F*) Same description as panels *A-C*, except for Model II. β_f ranges from 0 at a dilation factor of 1 to 110 pN at the maximum dilation factor shown. In panel *F*, $h = 3.5$ (green dots) or 2.0 (purple dots). The areal ratio calculations in panels *A* and *D* exclude the area of the self-oscillation region and were modified from [124].

5.6 Transient Responses

I have shown that robustness enhancement can be effected through homeostatic mechanisms. However, it remains to be determined whether actual hair bundles employ such a strategy. Obtaining direct evidence that homeostatic mechanisms improve the robustness of a bundle's responsiveness is complicated by the challenging nature of experimentally mapping the bundle's state diagram and by uncertainty about the homeostatic mechanism's identity. I therefore describe additional consequences of homeostasis that are more amenable to experimental testing. Because homeostasis produces systems whose behavior is governed by an additional timescale, identifying hair bundle behaviors that betray the presence of such a timescale would provide support for the presence of homeostasis.

One approach is to ask how a bundle poised to operate within the quiescent, underdamped region of the state diagram responds to force steps (Figure 5.9). A positive step is applied to shift the bundle from various initial operating points to the same reference operating point. An operating point at which the bundle possesses a peak sensitivity of 40 $\mathrm{km{\cdot}N^{-1}}$ is chosen as the reference operating point in both the homeostasis "off" and "on" cases. The relaxation time for small stimuli at the reference operating point is consequently similar with and without homeostasis. However, engaging the homeostatic mechanism alters the bundle's response to large stimuli. At the onset of each force step the bundle exhibits ringing whose magnitude and duration are similar for all initial operating points when homeostasis is inactive (Figure 5.9*B*). When homeostasis is turned on, the ringing behavior diminishes in amplitude and vanishes more quickly for initial operating points farther from the reference operating point. Homeostasis alters the relaxation dynamics associated with force steps.

A second stimulation protocol adds sinusoidal forcing to the force steps described above. The stimulus frequency is chosen to match the resonant frequency at the reference point. When homeostasis is turned off, the bundle's oscillation amplitude quickly reaches a steady state and the response time is not strongly affected by changing the initial operating point (Figure 5.9*C*). In contrast, when homeostasis is active the bundle requires more time to reach a steady state and this time delay grows systematically as the distance between the reference and initial operating points increases. Homeostasis retards the steady-state response to periodic stimuli.

In a final paradigm, force steps are delivered to a spontaneously oscillating hair bundle. In this protocol the bundle's initial operating point is the common reference point and the final operating point is varied. The bundle's amplitude of spontaneous oscillation at the reference operating point is chosen to be the same for the homeostasis "off" and "on" cases. Negative force steps are applied to shift the bundle's operating point closer to the edge of the oscillatory region. When homeostasis is inactive, spontaneous oscillations appear almost immediately after the onset and offset of the force step, regardless of the step's size (Figure 5.9*D*). In contrast, when homeostasis is active, the return of spontaneous oscillations is delayed. The delay lengthens as the size of the force step increases. Once again, homeostasis introduces a lag in the bundle's dynamics.

Figure 5.9: Hair bundle behaviors associated with homeostasis. (A) A schematic diagram showing the locations of the operating points and directions of the force steps used; labels indicate to which panel(s) each arrow applies. The Hopf bifurcation curve is colored purple when homeostasis is off (left) and orange when homeostasis is on (right). (B) The response to positive force steps for a bundle poised in the quiescent, underdamped region of the state diagram. Traces are labeled by the initial operating point's peak sensitivity in km·N^{-1}. All force steps brought the bundle to the same reference operating point (tip of B, C arrow in A), which possesses a peak sensitivity of 40 km·N^{-1}. The peak sensitivity at the reference point is a maximum as a function of the constant force. The stimulation protocols for the largest and smallest steps are shown schematically above the traces. When homeostasis is off, the ringing after the onset of the force step is not appreciably affected by the initial operating point (left). When homeostasis is on, the size and duration of the ringing diminish as the distance between the initial and reference operating points increases (right). (C) Schematic protocol of the force steps with a superimposed sinusoidal driving force delivered to a bundle. The frequency of the sinusoidal component is equal to the bundle's resonant frequency at the reference operating point (tip of B, C arrow in A) and the sinusoid's amplitude is 0.01 pN. The bundle's initial operating points and the size of the force steps are the same as in B. Representative traces are shown when homeostasis is off (left) or on (right). When homeostasis is off the bundle quickly reaches a steady state after the onset of the force step (left). When homeostasis is on, a greater interval is needed for the bundle to reach a steady state (right). (D) Response to negative force steps for a bundle poised in the self-oscillation region. Lighter shades of blue indicate larger step sizes. The schematic diagrams above the traces show the stimulation protocols for the largest and smallest force steps. The initial operating points for this protocol are chosen so that the bundle's oscillation amplitude is 17 nm in the absence or presence of homeostasis. The bundle's oscillation amplitude reaches a maximum as a function of the constant force at the initial operating points. The bundle's operating point is contained within the self-oscillation region throughout the entire protocol (D arrow in A). When homeostasis is off spontaneous oscillations are not interrupted by the force steps (left). When homeostasis is active a delay precedes the return of spontaneous oscillations at the onset and offset of the force step, and this delay lengthens as the size of the force step increases (right). All simulations are generated using Model II with parameter values listed in Table 4.2. From [124].

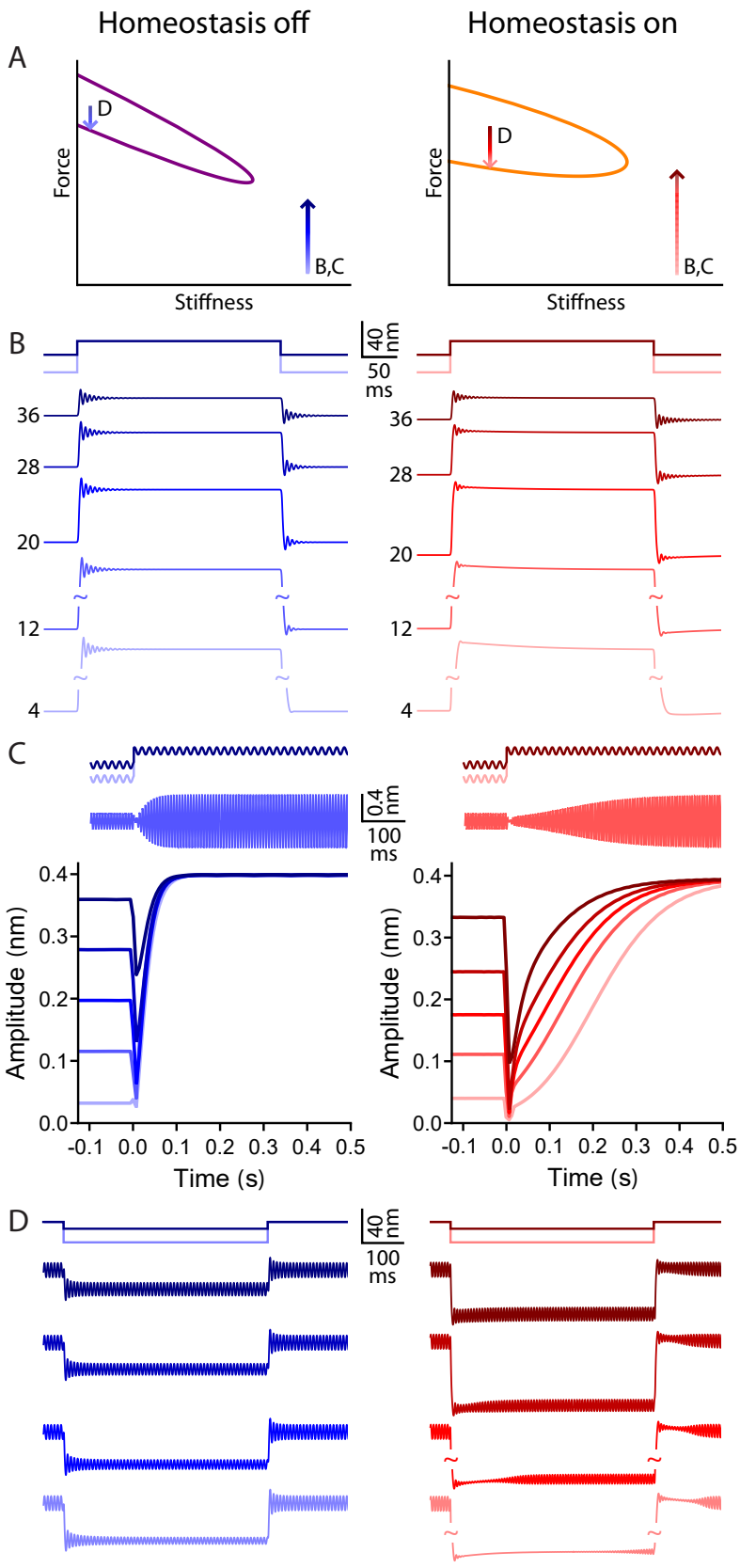

Figure 5.9: Hair bundle behaviors associated with homeostasis.

5.7 Robustness Enhancement by Mass Loading

The models of hair bundle motility employed in this work have so far neglected mass. When a hair bundle operates in isolation, its mass is indeed quite small. Within the organs where they function, however, many hair bundles are subjected to a mass load from an overlying accessory structure: the tectorial membrane rests on top of the hair bundles of outer hair cells, massive otoconia and an otolithic membrane weigh down bundles in the utricle and sacculus, and the ampullary cupulae lend substantial inertia to the bundles embedded within.

It was previously shown that the self-oscillation region in Model I is made larger by introducing mass into the equations [92]. Mass-loading could therefore constitute another means to achieve robustness of function. To this end, I introduce mass into Model II and subsequently analyze how this addition affects sensitivity contours.

Accounting for a mass load m in Model II without homeostasis yields the following system of differential equations

$$m\dot{v} = -\lambda_x v - k_{\mathrm{gs}}(x - y - DP_o) - kx + F_c + F(t)\,, \tag{5.7}$$

$$\dot{x} = v\,, \tag{5.8}$$

$$\lambda_y \dot{y} = k_{\mathrm{gs}}(x - y - DP_o) - k_{\mathrm{es}}(y - y_{\mathrm{es}}) - f(1 - SP_o)\,, \tag{5.9}$$

$$P_o = \frac{1}{1 + Ae^{-(x-y)/\delta}}\,, \tag{5.10}$$

in which v is the bundle's velocity. The conditions $T_1^3 = T_3$ and $T_2 < T_1^2$ (Eq. 2.44) reveal that a Hopf bifurcation occurs in this system when

$$F_{c,\mathrm{H}}(P_o^*) = \frac{1}{\delta}\ln\left[\frac{AP_o^*}{1 - P_o^*}\right]\left(k_{\mathrm{gs}} - k_{\mathrm{H}}(P_o^*)\left(1 + \frac{k_{\mathrm{gs}}}{k_{\mathrm{es}}}\right)\right)$$
$$+ k_{\mathrm{H}}(P_o^*)\left(\frac{k_{\mathrm{gs}}}{k_{\mathrm{es}}}DP_o^* - y_{\mathrm{es}} + \frac{f}{k_{\mathrm{es}}}(1 - SP_o^*)\right) - k_{\mathrm{gs}}DP_o^*, \tag{5.11}$$

$$k_{\mathrm{H}}(P_o^*) = \frac{1}{\delta^2\lambda_x\lambda_y^2}\Big[k_{\mathrm{gs}}(D\widehat{P}-\delta)\Big(mfS\widehat{P}(2\lambda_x+\lambda_y)+\lambda_x\delta[2mk_{\mathrm{es}}+\lambda_y(\lambda_x+\lambda_y)]\Big)$$

$$+mk_{\mathrm{gs}}^2(\lambda_x+\lambda_y)(D\widehat{P}-\delta)^2-\lambda_x[fS\widehat{P}+k_{\mathrm{es}}\delta][mfS\widehat{P}+\delta(mk_{\mathrm{es}}+\lambda_x\lambda_y)]\Big], \tag{5.12}$$

$\widehat{P} = P_o^*(1-P_o^*)$, as long as

$$\lambda_x[\widehat{P}(fS-Dk_{\mathrm{gs}})+\delta(k_{\mathrm{ge}}+k_{\mathrm{gs}})]^2 < \lambda_y k_{\mathrm{gs}}(D\widehat{P}-\delta)[\widehat{P}(fS-Dk_{\mathrm{gs}})+\delta k_{\mathrm{gs}}]. \tag{5.13}$$

Both $k_{\mathrm{H}}(P_o^*)$ and $F_{c,\mathrm{H}}(P_o^*)$ bear a linear dependence on m.

In accord with previous theoretical results, increasing the mass m effects a dilation of the self-oscillation region (Fig. 5.10*A*). The dilation factor h, defined as the square root of ratio the self-oscillation region's area with and without mass, grows in proportion to m (Fig. 5.10*C*).

The dilation of the self-oscillation region is accompanied by an expansion of the sensitivity contours (Fig. 5.10*D*). The expansion is unexpectedly large–supralinear, in fact–and significantly exceeds that resulting from adjusting other parameter values (c.f. Figs. 4.2 and 5.8). It is unclear why mass-loading effects such an enormous enlargement of the sensitivity contours, though two phenomena merit mention. One micrgram, which corresponds to a dilation factor of 1.5, appears to mark an important transition. For mass loads smaller than 1 μg the areal ratio grows more quickly for larger sensitivity values, as predicted by the analysis of Section 3.3 and as occurs when other parameter values are altered. For larger mass loads, however, the largest areal ratios are seen for the contours corresponding to the smallest sensitivity values. Additionally, for mass loads just over 1 μg the border of the underdamped region becomes discontinuous and the region normally contained within extends indefinitely; this might permit the very large expansion of the sensitivity contours.

A number of experimentally testable predictions arise from this theoretical analysis. Because imparting a mass load to a hair bundle is predicted to expand the bundle's self-oscillation region, it is predicted that mass-loading will enlarge the range of parameter values over which spontaneous oscillations can occur. Consequently, the bundle's sensitivity is also expected to exceed some specified threshold for a greater range of parameter values when the bundle is loaded. Lastly, it is anticipated that mass-loading can engender spontaneous oscillations by a previously quiescent bundle, even if that bundle lacks negative stiffness (Figs. 5.10*A* and *B*). State-diagram mapping experiments, such as those employed in references [89] and [90], are well-suited for testing these predictions.

The results portrayed in Figure 5.10 suggest that a large mass load might be required to appreciably dilate the self-oscillation region; 1 μg is substantially more massive than the few tens of nanograms that the tectorial membrane is thought to impart to an outer hair cell. However, large values of λ and λ_a were employed throughout this thesis to slow the bundle's oscillation frequency and consequently ease the computational demands of simulating the bundle's response to sinusoidal stimulation. If λ and λ_a are both reduced by a factor of five, only 50 nanograms of mass are needed to achieve a dilation factor of three.

These results also bear on another important and unresolved issue in the field. Spontaneous oscillations have not yet been detected in mammalian hair bundles. Technical difficulties may stand in the way: mammalian hair cells appear to be more fragile than their amphibian and reptilian counterparts, and a viable two-chamber preparation for cochlear hair cells is still lacking.

Discrepancies in biophysical properties might also provide an explanation for the absence of oscillation by mammalian hair bundles. Hair cells near the base of the

mammalian cochlea possess bundles that are nearly tenfold as stiff as those found in the bullfrog's sacculus [71, 86]. Mammalian bundles are therefore expected to be poised far from the self-oscillation region. That the force-displacement relation measured in such bundles lacks a region of negative stiffness, but nevertheless displays nonlinearity, supports this hypothesis [71]. Because negative stiffness is considered an essential ingredient for generating spontaneous oscillations, it is predicted that these bundles are quiescent.

This discussion has thus far neglected mass. To access an individual cochlear hair bundle one must remove the overlying tectorial membrane, which also frees the bundle from a significant inertial load. The preceding theoretical analysis suggests that a mass load can effect a sizable increase a bundle's self-oscillation region. The few tens of nanograms of mass imparted to bundles by the tectorial membrane [130] could therefore substantially reduce the distance in parameter space between a Hopf bifurcation and a cochlear hair bundle's operating point. Indeed, spontaneous otoacoustic emissions are stronger and more numerous in mice lacking otoancorin, a protein that affects the stiffness-to-mass ratio of the tectorial membrane by mediating this structure's attachment to the spiral limbus [131]. Considering that spontaneous otoacoustic emissions must arise from a vibration within the cochlea, this finding suggests that reducing the stiffness imparted by the tectorial membrane while maintaining its mass permits cochlear hair bundles to oscillate spontaneously. It is entirely plausible that the cochlea has evolved to employ mass-loading to ensure the robust operation of its hair bundles.

Because a bundle's spontaneous force-displacement relation does not depend on mass (Eq. 5.7 with $\dot{v} = v = 0$), mass-loading is predicted to engender spontaneous oscillations by hair bundles in the absence of negative stiffness. This suggests that

the ingredients required to generate spontaneous oscillations should be amended as follows. When a mass load is negligible, spontaneous oscillations can arise in bundles that possess negative stiffness and adaptation. For significant mass loads, it is instead sufficient for a bundle to exhibit adaptation and increased compliance over a range of bundle displacements (Figs. 5.10A and B). Oscillation of course ensures when both conditions are met.

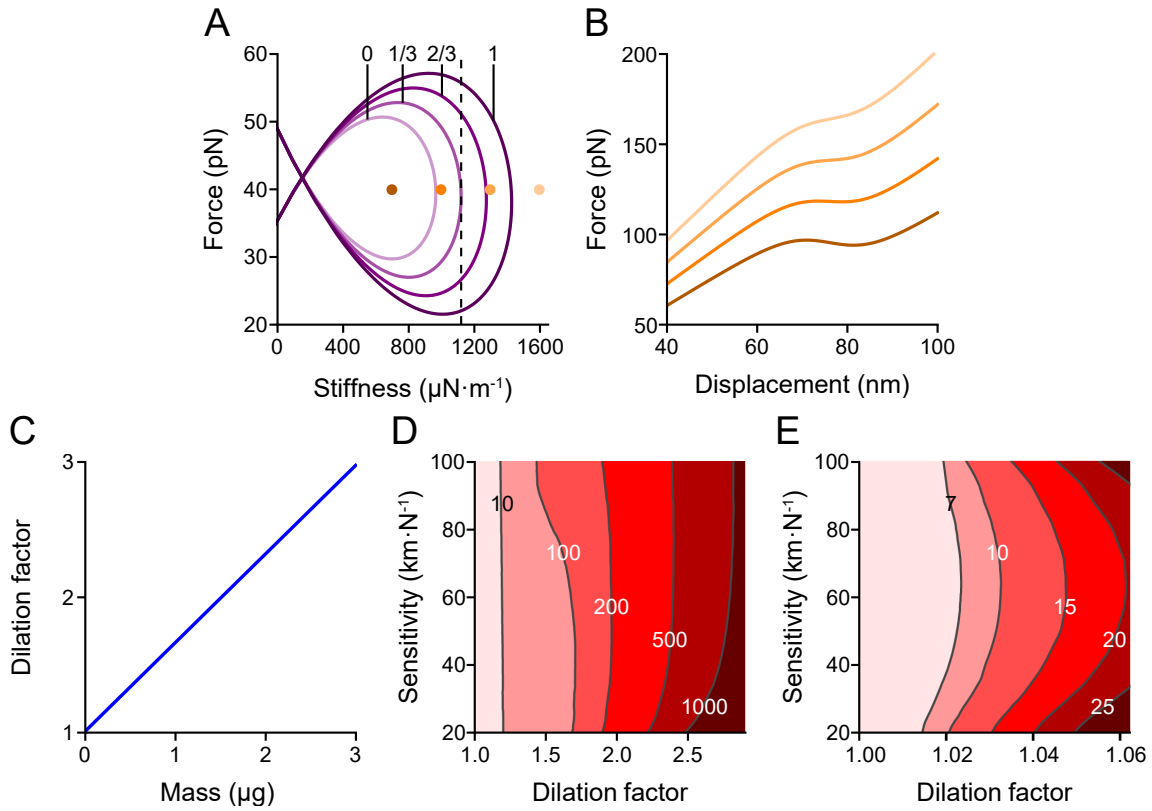

Figure 5.10: (*A*) Hopf bifurcation curves for mass loads of increasing size. Contours are labeled by the size of the mass (μg) loaded onto the bundle. Larger masses broaden the range of operating points at which the bundle oscillates spontaneously. The dashed line indicates the maximum load stiffness for which the bundle's force-displacement relation exhibits a region of negative stiffness. (*B*) Force-displacement relations for a hair bundle poised at each of the color-matched operating points in panel *A*. The operating point's stiffness (μN·m^{-1}) labels each curve. Only the lower two curves, corresponding to operating points situated to the left of the dashed line in panel *A*, possess regions of negative slope. That the operating point corresponding to the 1300 μN·m^{-1} curve falls within the 1 μg contour suggests that spontaneous oscillations can occur without negative stiffness when the bundle is loaded with a mass. (*C*) The dilation factor h for area of the self-oscillation region grows in proportion to the size of the mass load. (*D*) Areal ratios are displayed as a function of the dilation factor h and of the peak sensitivity χ corresponding to the contour of interest. (*E*) Expanded view of the portion of panel *D* that likely corresponds to physiologically relevant mass loads; a 100 ng mass load effected the largest dilation factor shown. Mass-loading effects an unexpectedly large increase in the areas between the Hopf bifurcation curve and the peak sensitivity contours (c.f. Figs. 4.2 and 5.8). The denominator of the areal ratios portrayed in panel *D* is given by the areas contained within the 50 ng sensitivity contours and by the areas contained within the 4 ng sensitivity contours for panel *E*.

Appendix F: Additional Analytical Expressions

Model I

$$\omega_{\pm}=\sqrt{\frac{2-(\widehat{a}-k)^2+2\alpha_*\widehat{a}b-\alpha_*^2\pm\sqrt{[2-(\widehat{a}-k)^2]^2+4\alpha_*\widehat{a}b[2-(\widehat{a}-k)^2]+2[2+(\widehat{a}-k)(\widehat{a}(4b-1)+k)]\alpha_*^2-4\widehat{a}b\alpha_*^3+\alpha_*^4}}{2}}. \tag{5.14}$$

Model II

$$k_{\mathrm{H}}(P_o^*)=-\frac{1}{2}\left(c_1-\sqrt{c_1^2-4c_2}\right), \tag{5.15}$$

$$\begin{aligned}c_1=\big\{&\tau_f^2\widehat{P}^2(Dk_{\mathrm{gs}}-f_0S+\beta_fP_o^*S)[S\lambda_x(\beta_fP_o^*-f_0)+Dk_{\mathrm{gs}}\lambda_T]+\delta^2[k_{\mathrm{gs}}\lambda_y\tau_f(2\lambda_y+2k_{\mathrm{es}}\tau_f+k_{\mathrm{gs}}\tau_f)+\lambda_x(\lambda_y+\tau_fk_{\mathrm{es}}+\tau_fk_{\mathrm{gs}})^2]\\&+\tau_f\widehat{P}\delta\big(S(f_0-\beta_fP0)[k_{\mathrm{gs}}\lambda_y\tau_f+2\lambda_x(\lambda_y+\tau_fk_{\mathrm{es}}+\tau_fk_{\mathrm{gs}})]-2Dk_{\mathrm{gs}}\lambda_T[\lambda_y+\tau_f(k_{\mathrm{es}}+k_{\mathrm{gs}})]\big)\big\}\Big/\\&\big(\delta\lambda_y\tau_f[\tau_f\widehat{P}(f_0S+\beta_fP_o^*S-Dk_{\mathrm{gs}})+\delta\lambda_y+\tau_f\delta(k_{\mathrm{es}}+k_{\mathrm{gs}})]\big),\end{aligned}$$

$$\begin{aligned}c_2=\big\{&\lambda_x^2\tau_f\beta_f^2\widehat{P}^2P_o^*S(2P_o^*S-1)+\beta_f\lambda_x\widehat{P}\big(\lambda_x\lambda_y\delta(1-2P_o^*S)-\tau_f(3P_o^*S-1)[\widehat{P}(f_0S\lambda_x-Dk_{\mathrm{gs}}\lambda_T)+k_{\mathrm{es}}\lambda_x\delta+k_{\mathrm{gs}}\lambda_T\delta]-\tau_f^2k_{\mathrm{es}}k_{\mathrm{gs}}P_o^*S[\delta+D\widehat{P}]\big)\\&+\big(\widehat{P}[f_0S\lambda_x-Dk_{\mathrm{gs}}\lambda_T]+k_{\mathrm{gs}}\lambda_T\delta+k_{\mathrm{es}}\lambda_x\delta\big)\big(\tau_f\widehat{P}[f_0S\lambda_x-Dk_{\mathrm{gs}}(\lambda_T+k_{\mathrm{es}}\tau_f)]+\delta[k_{\mathrm{gs}}\tau_f(\lambda_T+\tau_fk_{\mathrm{es}})+\lambda_x(\lambda_y+\tau_fk_{\mathrm{es}})]\big)\big\}\Big/\\&\big(\delta\lambda_y\tau_f[\tau_f\widehat{P}(f_0S+\beta_fP_o^*S-Dk_{\mathrm{gs}})+\delta\lambda_y+\tau_f\delta(k_{\mathrm{es}}+k_{\mathrm{gs}})]\big),\end{aligned}$$

$$\widehat{P}=P_o^*(1-P_o^*),\text{ and }\lambda_T=\lambda_x+\lambda_y,$$

The condition $T_2<T_1^2$ is satisfied when

$$k_{\mathrm{H}}(P_o^*)>\frac{P_o^*(1-P_o^*)[Dk_{\mathrm{gs}}(\lambda_x+\lambda_y+k_{\mathrm{es}}\tau_f)-f_0S\lambda_x+\beta_f(1-2P_o^*S)\lambda_x]-k_{\mathrm{gs}}\delta(\lambda_x+\lambda_y)-k_{\mathrm{es}}\delta(\lambda_x+k_{\mathrm{gs}}\tau_f)}{\tau_fP_o^*(1-P_o^*)(f_0S-Dk_{\mathrm{gs}}-\beta_fP_o^*S)+\lambda_y\delta+\tau_f\delta(k_{\mathrm{es}}+k_{\mathrm{gs}})}. \tag{5.16}$$

Chapter 6

Preliminary Experimental Results

This chapter contains the results of several preliminary experiments. Although my findings have been encouraging thus far, stronger evidence must be obtained through additional experiments.

6.1 Methods

The sacculus is a sensory organ that is responsible for communicating information about head position and vertical linear acceleration to the central nervous system. The sacculus comprises a sensory epithelium, in which hair cells reside, and an overlying load of calcium carbonate particles, or otoconia, lying atop an otolithic membrane. Because the tips of the hair bundles are embedded in the otolithic membrane, shifting the mass of crystals deflects the bundles (Fig. 1.3).

My approach is to use sacculi extracted from adult American bullfrogs, *Rana catesbiana*. This model system offers a number of technical advantages over hair cells from the inner-ear organs of mammals. The shape and position of the sacculus within the otic capsule makes extraction of the organ easier than that of the cochlea. The geometry of the saccular macula provides a large number of readily accessible bundles in a small area, and in appropriate physiological conditions the cells of this sensory epithelium remain viable for several hours [132], thus allowing an experimenter to perform many trials with the same specimen. So far these latter features have not been realized for the mammalian cochlea.

After removing the otoconia from a sacculus, I mount the isolated sensory epithelium in a two-compartment chamber (Fig. 6.1). In this configuration, hair bundles protrude upward from the apical surface of the sensory epithelium and into an open-top upper chamber whereas the basal surface of the sensory epithelium has access to the lower chamber. To simulate in vivo conditions during stimulation experiments I fill the lower chamber with oxygenated artificial perilymph (114 mM Na^+, 2 mM K^+, 2 mM Ca^{2+}, 118 mM Cl^-, 5 mM Hepes, and 3 mM D-glucose) and the upper chamber with oxygenated artificial endolymph (2 mM Na^+, 118 mM K^+, 250 μM Ca^{2+}, 118 mM Cl^-, 5 mM Hepes, and 3 mM D-glucose). Both solutions have an osmotic strength of 230 mOsmol·kg^{-1} and are titrated to a pH of 7.3. To finish the tissue preparation, I subject the apical surface of the sensory epithelium to 67 mg·L^{-1} of type XXIV protease (Sigma) at room temperature for 35 minutes. This enzyme solution frees the tips of the hair bundles from the overlying otolithic membrane and allows careful removal of this membrane with an eyelash.

I then visualize the preparation with differential-interference-contrast (DIC) optics in an upright microscope (60× water-immersion objective lens, 0.9 numerical aperture, BX51W, Olympus). Real-time images of the tissue are fed to a charge-coupled-device camera and a video processor (Argus-20, Hamamatsu Photonics), whereupon digital background subtraction aids in our ability to see hair bundle oscillations. This DIC microscopy allows me to confirm the viability of the sample, indicated by the presence of spontaneous oscillations [61] and the absence of tissue defects, and helps guide my approach to a hair bundle with a flexible glass probe.

To generate the probes I first use an electrode puller (P-2000, Sutter Instruments) to thin 1.2 mm diameter borosilicate capillaries and then make a 90° bend in each probe within 100 μm of its end with a 120 V solenoid apparatus. Next, probes are

sputter coated (Hummer 6.2, Anatech) with gold-palladium to make them less transparent. The power spectrum of each probe's thermal fluctuations while submerged in water is fit to a Lorentzian model; through the fluctuation-dissipation theorem, this allows calculation of the probe's stiffness and drag coefficient. Immediately before stimulation experiments, I soak the probes for 15 minutes in 200 μg·L^{-1} concanavalin A (Sigma), a lectin that encourages attachment of the probe to hair bundles.

Once coupled to a hair bundle, the probe serves two purposes. First, light from a 900 mW diode with a wavelength of 630 nm (UHP-Mic-LED-630, Prizmatix) is directed through the tissue. The shadow cast by the tip of the probe is magnified 1,350×, projected onto a dual photodiode, and then tracked as an indication of the position of the tip of the attached hair bundle. Second, the base of the probe is mounted to a piezoelectric actuator (PA 4/12, Piezosystem Jena GmbH) that is controlled by a mechanical-load clamp [89, 90]. This system allows me to command the stiffness of the bundle to a specified value while delivering a variety of force stimuli, including a constant offset force, force pulses, force ramps, and sinusoidal forces. In other words, I can use this clamp to poise a hair bundle at a desired operating point in the bundle's state diagram (k_{sp} vs. F_c space) and then deliver virtually any mechanical stimuli at this operating point. Finally, traces of the probe's position generated during hair bundle-stimulation experiments are saved and later analyzed using Matlab (R2015a, MathWorks). Additional details for the tissue preparation, stimulus apparatus, and data acquisition system employed in this work can be found in references [89, 90, 133].

All analytical calculations and simulations described in this work were performed using Mathematica (version 10.1, Wolfram).

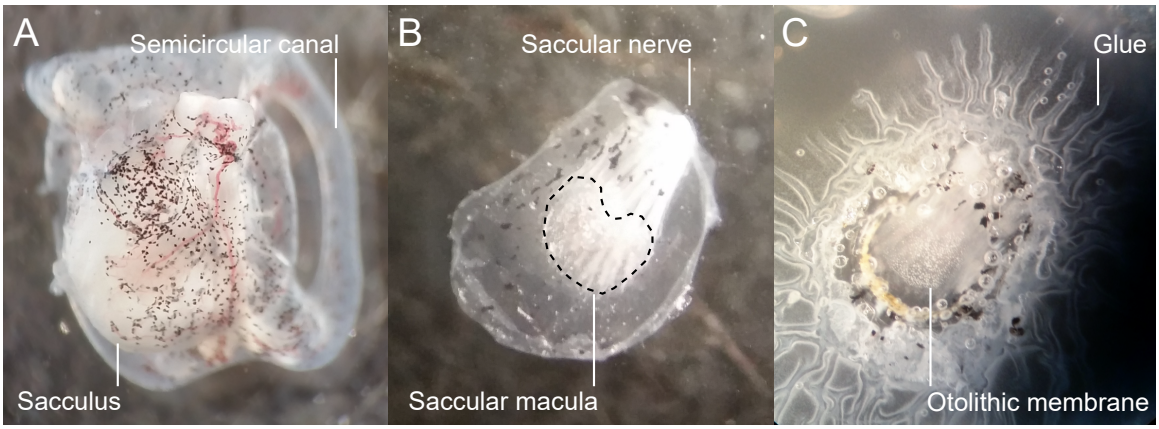

Figure 6.1: Tissue preparation. (A) Part of an inner ear extracted from a bullfrog. Visible are a semicircular canal and the sacculus. In this view the sensory epithelium of the sacculus is facing into the page and resting atop a mass of white otoconia. (B) Image portraying an isolated sacculus after the otoconial mass has been removed. The saccular nerve and saccular macula, which constitute the sensory epithelium of the sacculus (region enclosed by the dashed line) are visible. Compared to panel A, the sacculus has been flipped over in this view so that its sensory epithelium faces out of the page. (C) The tissue is mounted over a hole in a plastic cover slip. Peering through the hole, as in the image shown, permits a clear view of the otolithic membrane, distinguished by white speckles that represent residual otoconia embedded in its apical surface. Access to the hair bundles is obtained through this hole after the otolithic membrane has been removed. The exposed bundles are bathed in artificial endolymph and artificial perilymph fills the space underneath the coverslip. Cyanoacrylate glue applied around the tissue's perimeter secures the tissue to the cover slip and ensures a tight seal between the compartments of the two-chamber preparation. For mass-loading experiments, tungsten particles are placed near the hole's rim with a pipette. All images were captured by a cellular phone's camera (Samsung) through a dissecting microscope.

6.2 Responses to Force Pulses

Preliminary confirmation of the theoretically predicted responses to stimuli was sought by delivering force steps to individual hair bundles (Fig. 6.2). In accord with the findings of Section 5.6, force steps momentarily abolish spontaneous oscillations, and this delay lengthens as larger steps are applied to the bundle. Although consistent with the presence of a homeostatic mechanism, this result is nonspecific, for this phenomenon could arise from any dynamical process that adds a slow time scale to the system. Additionally, repetitions of this experiment are needed to verify the validity of the results.

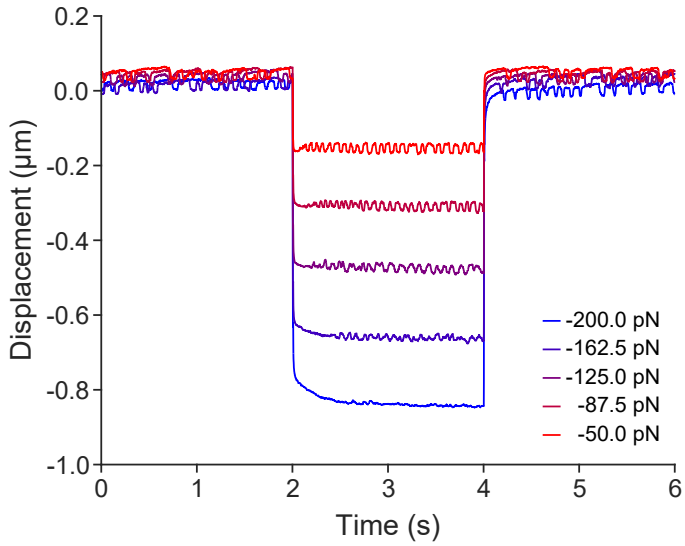

Figure 6.2: Hair bundle responses to force steps. Two-second force steps of various amplitudes were applied to a spontaneously oscillating hair bundle. After an initial delay at the onset of the step, spontaneous oscillations resume. This delay lengthens as the step size increases, which resembles the simulated responses for Model II when homeostasis is active (Fig. 5.9). The existence of three or more time scales in the bundle's dynamics likely underlies this behavior. Oscillations were entirely suppressed by a 200 pN force step.

6.3 Mass Loading

Tungsten particles were employed to impart mass loads to hair bundles. Because tungsten is 19.3 times as dense as water, small particles can deliver sizable masses: more than a nanogram of mass is contained within a tungsten particle that is five microns in diameter, an amount that is predicted to effect an appreciable change in the areas contained with bundle's sensitivity contours. Tungsten particles are also opaque, making them readily observable through DIC microscopy and allowing their shadows to be projected onto a dual photodiode.

Two methods were employed to deliver tungsten particles to hair bundles. In both approaches, 0.5 μL of tungsten particles solubilized in DMSO were soaked for 30 min in 200 $\mu g \cdot L^{-1}$ concanavalin A. In a first strategy, the particles were then pipetted directly onto the tissue. Consequently, many bundles sustained significant damage when impacted by a tungsten particle.

A more targeted approach is also possible. Because the plastic cover slip is transparent, the opaque tungsten particles are readily identifiable at the rim of the hole over which the tissue is affixed. The particles' concanavalin A coating allows them to adhere to a probe that has not been soaked in the lectin. In this way, a mass of tungsten of my choosing can be carried by the probe to any accessible bundle. The concanavalin A has a greater affinity for the hair bundle then for the probe, so that tungsten particles *carefully* placed on a bundle can detach from the transporting probe. A second probe coated in the lectin can then be coupled to the bundle and deliver stimuli (Figs. 6.3*A*,*B*).

Placing a tungsten particle on a spontaneously oscillating bundle demonstrated that oscillations can continue after mass-loading (Fig. 6.3*C*). Figures 6.4 and 6.5 ad-

ditionally show that mass-loading can engender spontaneous oscillations by quiescent bundles in the absence of negative stiffness and can effect larg-amplitude oscillations that are sustained over a greater range of parameter values. Mass-loading also led to an unexpected increase in the spontaneous oscillation frequency in the example shown (Figs. 6.5*A*,*B*). As is the case for a simple harmonic oscillator, increasing the mass was expected to *decrease* the oscillation frequency. These results suggest that robustness enhancement could be realized through mass loading.

Repetitions of these experiments are needed to verify the validity of these results. Owing to minute movements of the preparation and relaxation of the tissue, shadows projected onto the dual photodiode can become lightly out of focus over time. This decline in contrast artificially diminishes the amplitudes of spontaneous oscillations. To better quantify how mass-loading affects the oscillation amplitude, a calibration pulse should be included in every future record of hair bundle motion.

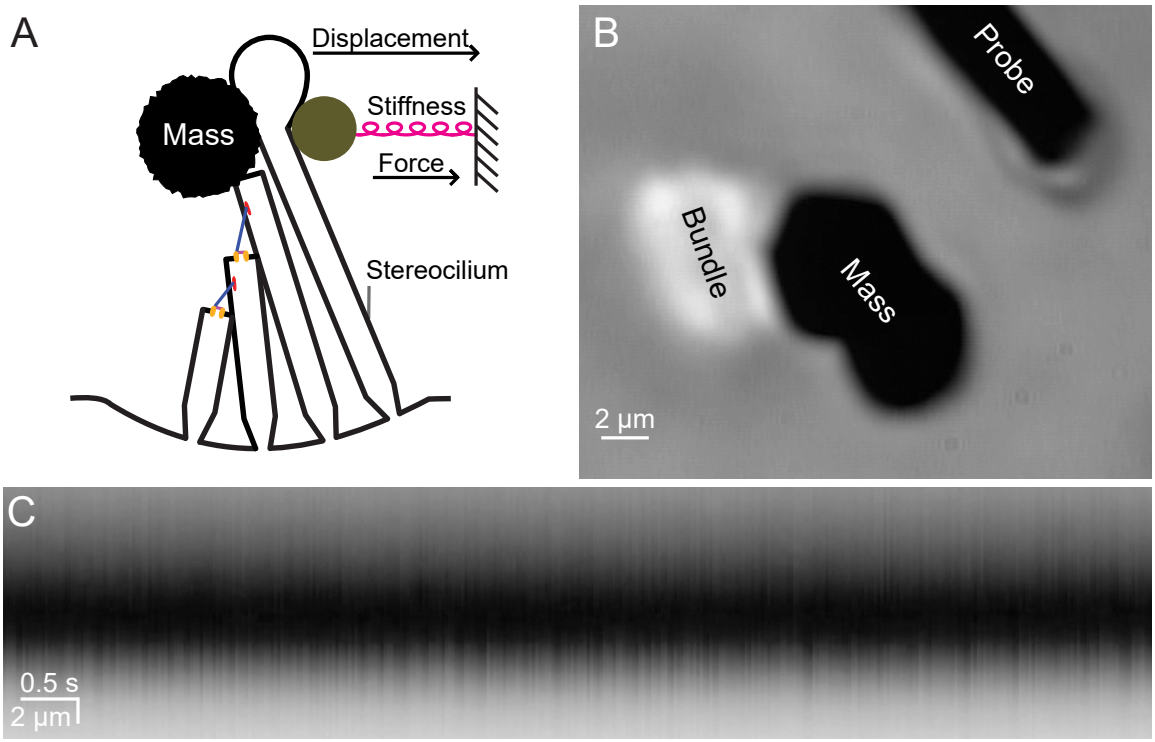

Figure 6.3: Mass-loading experiment. (A) A mechanical load clamp enables experimental adjustment of the constant force and stiffness applied to a bundle by an external load [89, 90]. To verify its predicted effect, a mass can be physically placed on an individual bundle. (B) Micrograph depicting a bundle loaded with a mass of tungsten. (C) Kymogram showing spontaneous oscillations of a mass-loaded bundle, demonstrating that the mass-loading process leaves intact the processes needed to generate spontaneous oscillations.

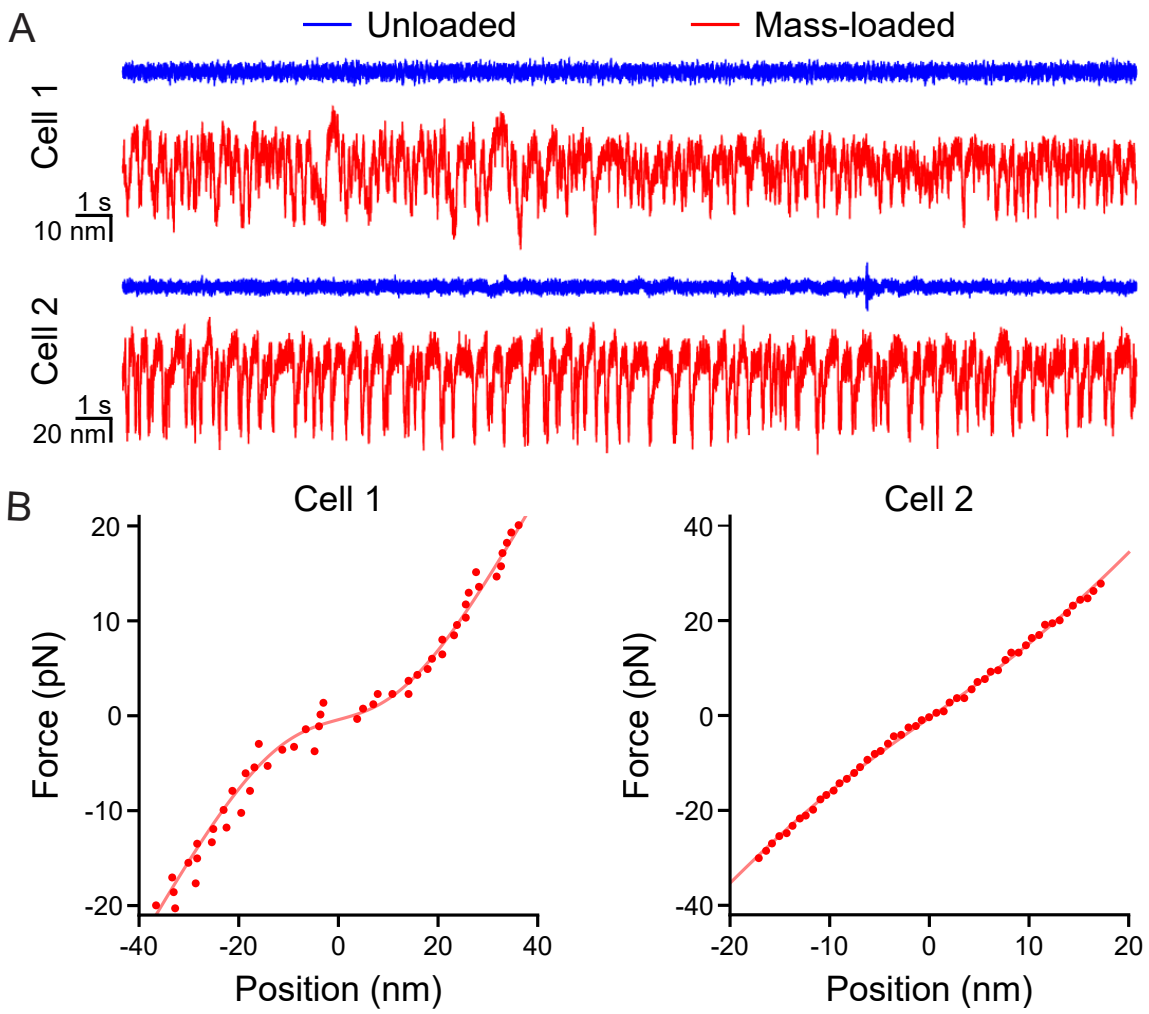

Figure 6.4: Mass loading engenders spontaneous oscillation by quiescent bundles. (*A*) Position traces for two bundles before (blue) and after (red) loading with tungsten masses of a few nanograms. (*B*) Force-displacement relations for the two cells in panel *A* following mass loading. These cells oscillated spontaneously despite the absence of a region of negative slope in their force-displacement relations. Unpublished results obtained by Dr. Joshua Salvi.

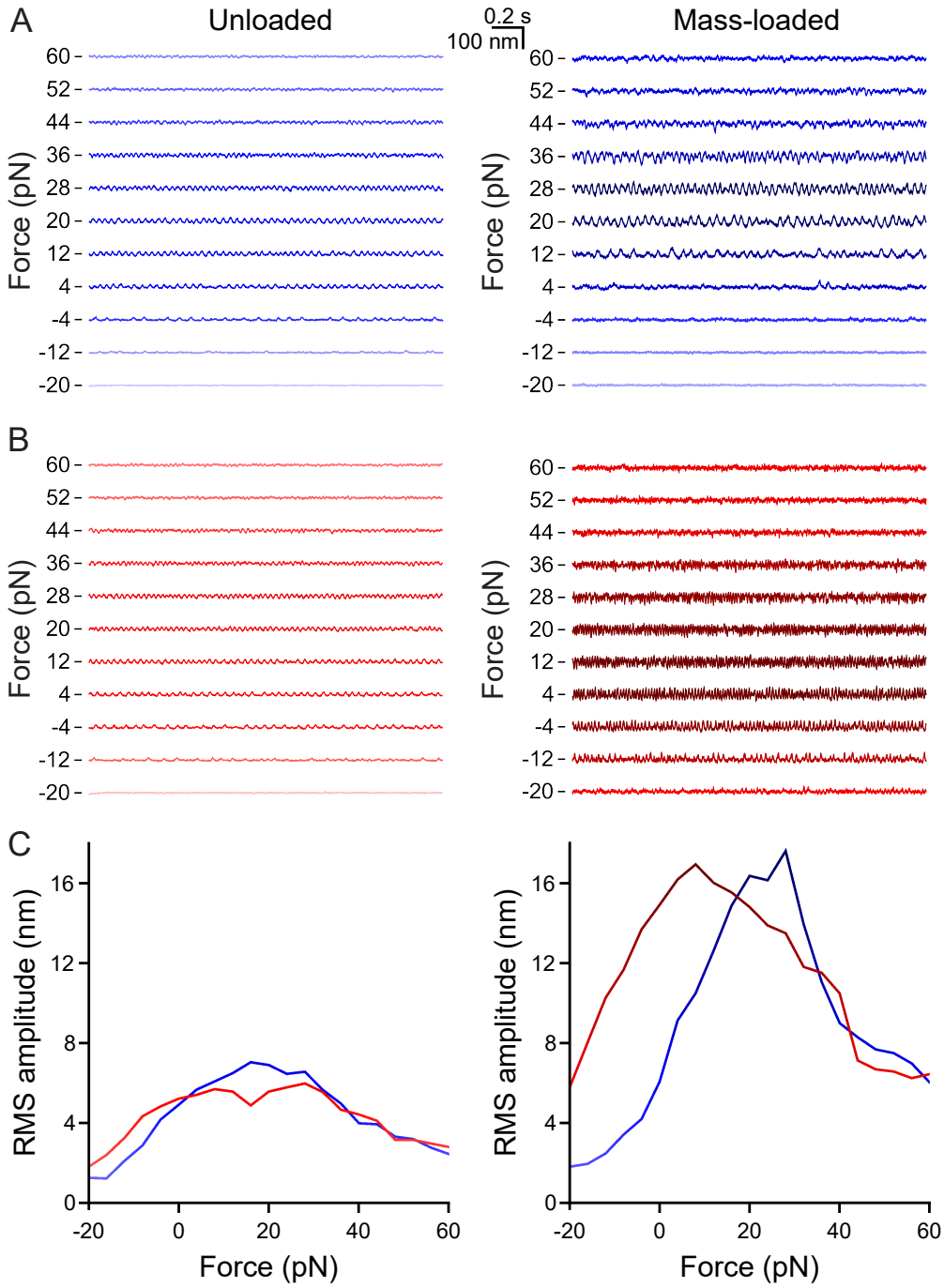

Figure 6.5: Mass loading enhances the robustness of spontaneous oscillations. (A, B) Position traces of a bundle commanded to operate at a load stiffness of 60 μN·m^{-1} (A) or 100 μN·m^{-1} (B) and at various constant forces before (left) and after (right) mass loading with a tungsten particle. (C) Root-mean-square (RMS) amplitude of spontaneous bundle oscillation as a function of constant force before (left) and after (right) mass loading at load stiffness values of 60 μN·m^{-1} (blue) and 100 μN·m^{-1} (red). Darker shading corresponds to larger amplitude oscillations in all panels.

Chapter 7

Discussion

Any biological system must contend with a host of constraints. Failing to operate within these constraints hinders the system's ability to function. In this work I have demonstrated how a hair bundle could employ homeostatic mechanisms to ease such constraints. Two homeostasis strategies, accounting for the dynamics of the adaptation rate or of the adaptation motor's strength, enhance the robustness of the hair bundle's sensitivity, frequency selectivity, and dynamic range to changes in parameter values. That these disparate homeostasis strategies produce qualitatively similar results suggests that enhancing robustness through homeostasis is a general principle. I conjecture that a homeostatic mechanism renders the bundle's signal-detection function more robust to changes in all parameter values and that equipping other systems with homeostasis would yield similar effects. The values of the parameters in the homeostasis equations could well have evolved to preserve the robustness of the bundle's function to changes in these parameter values (Section 4.4).

Although the two models that I investigate differ in a number of ways, their common features underlie the generality of the results. In the absence of homeostasis, the models possess topologically similar state diagrams, each characterized by a region of spontaneous oscillation bounded by a line of Hopf bifurcations. Moreover, each model involves a homeostatic mechanism that decreases the value of a target variable in response to an increasing measured variable. I show that these elements are sufficient to ensure robustness of function for an active periodic-signal detector. Together with a state diagram containing the aforementioned properties, a homeostatic mechanism

with this structure may constitute the minimal features needed to enhance a system's robustness of function.

For each control parameter that I evaluated, homeostasis renders the bundle's signal-detection ability more robust. The robustness enhancement is related to the factor by which the homeostatic mechanism dilates the size of the oscillatory region (Sections 4.3 and 5.5). The analyses undertaken in Sections 3.3 and 5.7 additionally suggest that expanding the self-oscillation region universally effects a concomitant increase in the areas contained by contours for various measures of a system's performance. Identifying a homeostatic mechanism that enlarges the self-oscillation region likely constitutes a general strategy for enhancing the robustness of an oscillator's function to changes in parameter values.

The forms of the homeostatic mechanisms are biologically plausible. Each employs information about the current state of the hair bundle; the homeostatic equation measures the bundle's oscillation amplitude through the mechanotransduction current. This information is rectified by a nonlinearity of the homeostatic process, which ensures that the process responds when the bundle is stimulated by a sinusoidal force. I show in Model I that a quadratic nonlinearity is sufficient to provide rectification, whereas Model II enacts rectification by employing a biophysically motivated nonlinearity, namely a Boltzmann function. Because the homeostatic mechanisms require few assumptions, either could be realized through several biological processes. For example, both homeostatic mechanisms could be effected through myosin-motor inhibition mediated by a Ca^{2+}-activated second messenger [134] or through regulation of Ca^{2+} buffers [45, 135] or pumps [135, 136].

The homeostatic mechanism operates on a timescale that greatly exceeds both the channels' relaxation time of a few milliseconds and the adaptation time constant of

tens of milliseconds [68, 137]. This timescale separation ensures that the homeostatic mechanism does not perturb the system's ability to detect periodic signals. When driven at the resonant frequency, the period of the bundle's oscillation was shorter than 20 in Model I or 20 ms in Model II for the vast majority of operating points in the underdamped region. I chose $\tau_\alpha = 10^3$ and $\tau_f = 200$ ms so that these timescales exceeded those of bundle oscillation, in accord with the timescales of the potential homeostatic mechanisms mentioned in the preceding paragraph.

Temporal resolution is sacrificed to attain robustness of function in two ways. First, by extending the range of parameter values over which the bundle exhibits sharply tuned frequency selectivity, the homeostatic mechanism also broadens the set of operating points at which the bundle's response is slow. This tradeoff poses a disadvantage only if a signal detector must strongly favor temporal resolution over frequency selectivity. Second, the bundle's transient responses to sinusoidal stimulation reveal that the homeostatic mechanism engenders delays on the order of hundreds of milliseconds (Fig. 5.9). That these delays are long reflects our decision to use parameter values that accord with measurements and estimates in saccular hair cells of the bullfrog. These cells are tuned to frequencies of a few tens of hertz, so their sensory function does not demand that they respond quickly to sinusoidal stimuli. Were I to use instead parameter values drawn from measurements in mammalian hair cells that are tuned to higher frequencies, the delays would be shorter and the homeostatic mechanism would not degrade the cells' temporal resolution below that required for higher-frequency hearing. There is some evidence, however, that homeostatic feedback within our cochlea is quite slow (see below).

Our models resemble a model that neglects adaptation but accounts for somatic motility, the change in length of an outer hair cell in response to a change in membrane

potential [121]. Feedback provided by somatic motility can engender spontaneous oscillations in cochlear models, yielding state diagrams similar to those discussed here. Enhancement of robustness through a homeostatic mechanism is not specific to models endowed with adaptation, but instead represents a principle that applies to models employing many forms of feedback.

Two types of hair cells are present within the mammalian cochlea: inner hair cells provide input to the brain, whereas outer hair cells amplify the vibrational response of the cochlea [138,139]. Feedback to the outer hair cells from efferent fibers originating in the medial olivocochlear nucleus could constitute a homeostatic mechanism similar to those that I describe [139]. Stimulation of efferents innervating outer hair cells alters the cochlea's mechanical response to acoustic stimulation, diminishing both sensitivity and dynamic range [138,140]. There is also evidence that efferent stimulation reduces the cochlea's frequency selectivity [141,142]. Moreover, feedback through efferents occurs in about 100 ms for fast effects and in tens of seconds for slow effects, timescales that are long compared to the response time of a few milliseconds for cochlear mechanics [108,140]. Because our models require only a resonant amplifier to which a homeostatic mechanism is added, they suggest how modulating efferent tone could enhance the robustness of cochlear function: If efferent neurons display a basal level of activity, then robustness enhancement could be realized through diminished efferent tone.

Noise diminishes a hair bundle's sensitivity, frequency selectivity, and dynamic range [143]. Through the feedback that it exerts, homeostasis propagates stochastic fluctuations of the bundle's position into the adaptation process. Accounting for noise may therefore decrease the degree of robustness enhancement. For sufficiently weak noise, the homeostatic mechanism should nonetheless improve the robustness of a

bundle's function to parameter variation.

Because bifurcations may be blurred or shifted by noise, it can be challenging to precisely locate them in noisy systems [144]. In experiments, this difficulty is addressed by employing a statistical test to delineate the boundary of a bundle's self-oscillation regime (Appendix B). Near the boundary, I predict that a hair bundle takes longer to relax after a constant force step when homeostasis is present than when it is absent.

Multiple timescales have been observed in the dynamics of hair bundle motion [87,145]. However, delays in a bundle's return to spontaneous oscillation were reported to depend on the duration rather than on the magnitude of the force steps, possibly because large force steps were employed [145]. Here I have shown that a homeostatic mechanism introduces an additional timescale whose signatures might be observed in the bundle's transient response (Figure 5.9). Noise may make it difficult to see in experiments the bundle's predicted transient responses to sinusoidal stimulation applied during force steps. The sizes of the force steps and amplitude of sinusoidal forcing can be adjusted, however, to maximize the predicted effects; it is hoped that a sufficiently large stimulus will evoke a behavior that is not obscured by noise. Alternatively, the long relaxation times owing to homeostasis might be evident only in the average over many stimulus trials. Evaluating transient responses in hair bundles or in cochlear vibrations evoked by the stimulation protocols described in this paper might provide evidence for a homeostatic mechanism in hearing.

Owing to homeostatic feedback, bursting oscillations arise in our models for low values of the stiffness . At these operating points the timescale for homeostatic feedback is similar to the hair bundle's period of spontaneous oscillation. Although these bursting oscillations can be entrained by sinusoidal forcing [87], the utility of

multimodal responses in hearing remains uncertain.

In this work I sought to achieve homeostasis of *function*, namely of a system's sensitivity, sharpness of tuning, and dynamic range. This strategy constitutes a conceptual departure from existing approaches that instead seek homeostasis of parameter values. Previous models have relied on a strong assumption: that the system's behavior is not significantly altered by conferring dynamics on a control parameter [51, 115–120, 125]. I show that this assumption does not hold in general: introducing homeostasis changes a system's state diagram and its dynamics. Further, our method does not require that the system maintain a representation of the set-point values to which parameters must be tuned.

The approach described in this work is general and likely applicable to any system whose function depends on oscillatory elements. A few examples drawn from biology include circadian clocks [146, 147], beating cardiomyocytes [148], and insulin-glucose oscillations [149]. The functions of these systems depend on their ability to detect and entrain to periodic stimuli. Homeostatic mechanisms may ensure that the function of these systems is robust to developmental and environmental variation.

Appendix G: Additional Completed Works

During my graduate training I engaged in a number of projects outside of the laboratory that explored my interest in human rights and a potential clinical interest in radiation oncology. This Appendix contains two manuscripts resulting from this work. The first, titled "Medical students' attitudes toward torture, revisited" describes the results of a survey of Weill Cornell medical students conducted by the Weill Cornell Center for Human Rights. This article appeared in the December 2017 issue of the *Health and Human Rights Journal* [150]. The second article, tentatively titled "Enhancement of external-internal correlation by phase-shift detection and correction based on concurrent external bellows and internal navigator signals," is currently under review at the *International Journal of Radiation Oncology·Biology·Physics*. This work investigates the phase difference between two components of respiratory motion and its correction allows surrogates to more faithfully represent the motions of tumors.

HHR
Health and Human Rights Journal

Medical Students' Attitudes toward Torture, Revisited

KRISTA DUBIN, ANDREW R. MILEWSKI, JOSEPH SHIN, AND THOMAS P. KALMAN

Abstract

This paper reports the findings of a survey of medical students' attitudes toward torture and discusses variables that may correlate with those attitudes. In late 2016, 483 enrolled medical and MD–PhD students at the Weill Cornell Medical College received an anonymous, institutional review board-approved survey that included questions about torture and its effectiveness, demographic questions, inquiries about personal experiences of harassment or discrimination, and questions regarding engagement in human rights activities. Some questions were drawn from a 2008 University of Illinois survey of medical students' attitudes toward torture, the only prior such survey at a US medical university. Of the 483 students who were contacted, 121 (25%) returned completed questionnaires, with responses indicating strong opposition to torture and skepticism about its usefulness. Respondents expressed greater opposition to torture in this survey than those who participated in the 2008 survey. Respondents' involvement in Weill Cornell's human rights program was associated with significantly stronger opposition to torture, while personal experiences of harassment were associated with a trend toward weaker opposition to torture. Respondents' answers closely approximate the clearly stated ethics of the profession, suggesting that human rights education during medical school may contribute to the development of proper values in young physicians even before they proceed into practice.

Krista Dubin, BA, is an MD–PhD candidate at the Weill Cornell/Rockefeller/Sloan-Kettering Tri-Institutional MD–PhD Program and a senior student advisor for the Weill Cornell Center for Human Rights, Weill Cornell Medical College, New York, NY, USA.

Andrew R. Milewski, BA, is an MD–PhD candidate at the Weill Cornell/Rockefeller/Sloan-Kettering Tri-Institutional MD–PhD Program and co-executive director of the Weill Cornell Center for Human Rights, Weill Cornell Medical College, New York, NY, USA.

Joseph Shin, MD, is an assistant professor in the Department of Medicine and co-medical director of the Weill Cornell Center for Human Rights, Weill Cornell Medical College, New York, NY, USA.

Thomas P. Kalman, MS, MD, is a clinical professor in the Department of Psychiatry and co-medical director of the Weill Cornell Center for Human Rights, Weill Cornell Medical College, New York, NY, USA.

Please address correspondence to Thomas Kalman. Email: tpkmd49@gmail.com.

Competing interests: None declared.

Introduction

Physicians are subject to broadly accepted standards governing ethical and professional conduct. The condemnation of physicians' direct or indirect participation in torture is one example. This is asserted by the World Medical Association, American Medical Association, American Psychological Association, World Psychiatric Association, American College of Physicians, American Psychiatric Association, and innumerable countries' medical societies.[1] However, as Steven Miles reminds us, many medical personnel continue to participate in and condone torture: "Many torture survivors report that clinicians monitored their mistreatment. The presence of a physician during torture compounds the victim's suffering by emphasizing that even the humanity of medicine is turned against the prisoner."[2] This paper explores the knowledge and attitudes of medical and MD–PhD students at one institution on matters relevant to the practice of torture and physician complicity with torture.

Many physicians and medical personnel who participate in torture do so as they succumb to conflicts between professional ethics and the demands of their work, superiors, and peers. The authorization of torture during the Bush administration by government authorities (Departments of State, Defense, and Justice) enabled its legitimization through the military chain of command. In military settings, many may fear retaliation or disciplinary consequences should they fail to follow orders. From a psychosocial perspective, Myles Balfe identifies factors that may contribute to a physician's participation in torture, such as the passionate assumption of the need to defend the United States from grave danger.[3] Balfe further notes that the capacity for rationalization (such as euphemistically referring to torture as "enhanced interrogation procedures") and cognitive distortions (such as the belief that without medical supervision, greater harm might ensue) are clear factors. Additionally, the splitting of roles such that responsibility can be diffused among many participants, each believing that their individual contribution to torture was minor or insignificant, creates an environment that enables medical personnel's participation in torture.

The present study explores future US physicians' attitudes toward the permissibility and utility of torture, as well as their beliefs about physicians' participation in torture. A previous survey of medical students' attitudes toward torture, conducted in 2008 at the University of Illinois College of Medicine-Chicago (UIC), provided a precedent for our project.[4] That six-question survey of 336 medical students across the four years of study revealed a level of support for torture that the authors reported as distressing, given medical associations' widespread condemnation of physicians' participation in torture. Specifically, the authors found that 35% of their sample would condone torture under certain circumstances; 24% agreed with the use of torture if a chance to elicit life-saving information existed; and 22% agreed that it was permissible for physicians to treat individuals so that torture could be initiated or continued. These and other findings led the authors to recommend the implementation of medical school curricular assessments to address ignorance or attitudes among students that are at odds with the universally and clearly stated ethics of the profession.

International surveys of medical students' attitudes toward torture or the mistreatment of prisoners have generally revealed a somewhat greater tolerance for such practices among medical students than in the UIC survey. For example, in a study conducted in Mauritius, 37.4% of surveyed medical students were in favor of beating individuals in police custody to obtain information, and in a study of New Delhi medical students, nearly 30% of respondents indicated approval of this practice.[5] Taken together, these studies demonstrate the importance of assessing medical students' attitudes toward such a major human rights issue.

The UIC survey has not, to our knowledge, been repeated at any other medical university in the eight years since it was administered. In addition to replicating the prior study, our project attempts to delineate personal and demographic factors that may be associated with attitudes toward torture. Clearly a question of great political, ethical, and medical sensitivity, this topic invites medical training institutions to examine curricula and human

rights educational efforts. It is important that medical students have solid grounding on matters such as torture and the obligations of the profession before they begin to practice independently in society.

Subjects and methods

The Institutional Review Board of the Weill Cornell Medical College in New York City approved this study. All enrolled four-year medical and MD–PhD students (483 total) received an email in November 2016, shortly after the conclusion of the national elections, containing links to a 28-item questionnaire (see Appendix). Their participation in the survey was anonymous and completely voluntary. Appropriate encryption procedures were employed to ensure that the identification of participant/non-participant status was impossible. Institutional review board-approved consent was obtained from all participants through encrypted procedures, and participants could access the survey only after first providing their consent.

The survey instrument contained 10 items addressing specific torture activities, justifications for torture, and ways that physicians might participate in torture. Five of these items matched questions from the 2008 UIC study. To identify factors that might influence students' attitudes, the survey also included demographic inquiries related to age, gender, ethnicity, religious affiliation, sexual orientation, and stage of medical school training; questions examining individual and family histories of exposure to trauma, harassment, or discrimination; and items surveying respondents' participation in student human rights activities at Weill Cornell, their familiarity with certain human rights statistics, and their opinions about human rights curricula in medical school. Participation in the survey was initiated by 146 students, but 19 were excluded because they did not complete any sections. Responses from six more participants were discarded, either because those respondents failed to complete the 10 torture-specific items or because they neglected to indicate their gender or age. The final sample size was thus 121 respondents.

We employed two methods to identify associations between participants' attitudes toward torture and their responses to the non-torture questions. In the first strategy, we used an aggregate metric, termed the "attitude toward torture scale" (ATS), to compare pools of participants grouped by their responses to individual non-torture questions. To calculate the ATS, we created a standardized scale of 0–4 for each of the 10 torture-specific items. Higher scores on this scale correspond to greater support for torture; "strongly agree," for example, was coded as a 4 if this response indicated the strongest support for torture (questions 1.1a-c, 1.2-1.5), whereas "strongly agree" was coded as a 0 if it instead corresponded to the greatest opposition to torture (questions 1.6-1.8). An individual's ATS was then calculated by summing that person's scores on these 10 questions. The ATS therefore ranged from 0 to 40, with a neutral position represented by 20. We performed Mann-Whitney U tests to compute p-values for the differences found between mean ATS values of paired subgroups. We employed the Bonferroni method to account for multiple hypothesis testing; differences in mean ATS values were considered statistically significant if their associated p-values fell below 0.05/N, in which N is the number of hypotheses tested. The ATS metric was developed solely for this study and has not been validated elsewhere.

Considering the 10 torture-specific items and ATS as dependent variables, the second method entailed creating a statistical model for each dependent variable as follows. We performed ordinal regressions between the dependent variable and each independent variable using the polr function of the MASS package in R. The false discovery rate was controlled at a level of 0.1 using the Benjamini-Hochberg method to account for testing multiple hypotheses. Those independent variables that did not survive the multiple hypothesis correction were then excluded. A final ordinal regression was performed on the dependent variable and all the remaining significant independent variables to arrive at a multivariate model for the dependent variable. Multivariate models were not computed for torture questions 1.6 and 1.7, as these questions were not found to have significant dependences on

any of the independent variables. Lastly, to investigate associations between individuals' attitudes toward various facets of torture, we calculated the Pearson correlation coefficient (r) for each pair of torture-specific questions.

Results

Of the 483 students who received the survey, 25.1% responded (Table 1). The lowest response rates were seen from the third-year medical school class and from MD–PhD students engaged in the PhD phase of their training. More females than males (75:46) completed the survey (the entire student body annually approximates a 50:50 male:female ratio).

The questionnaire began with ten items surveying respondents' attitudes toward torture, five of which were based on questions from the 2008 UIC study. Using a five-point Likert scale, participants were asked to indicate their agreement or disagreement with each statement. For ease of comparison between the studies at UIC and the Weill Cornell Medical College (WCM), the "strongly disagree" and "disagree" responses were pooled together, as were the "strongly agree" and "agree" responses.

A larger proportion of those surveyed in the present study expressed opposition to torture than in the 2008 UIC study (Figure 1). The most striking difference was seen in response to the statement "It is permissible for interrogators to use psychological intimidation (e.g. mock executions, sexual humiliation, religious humiliation, threatening loved ones)"; here, 93% of WCM respondents disagreed, compared to 30% of those surveyed at UIC (Figure 1A). In addition, 63% of WCM respondents disagreed that "the use of torture can be justified if the information obtained will save lives," compared to 51% of UIC respondents (Figure 1B). The item "It is permissible for physicians to treat individuals to verify their health so torture could begin or continue" garnered a disagreement rate of 83% at WCM and 58% at UIC (Figure 1C). Furthermore, 83% of

TABLE 1. Respondent demographics

Year†	Number of respondents	Response rate
1st	35	34.7%
2nd	37	40.2%
3rd	14	12.8%
4th	24	22.4%
MD–PhD	11	14.9%
Total	121	25.1%

Gender	
Female	75
Male	46
Age (yrs)	
Mean	25.4
Range	21–38

†Medical school year or MD–PhD students in PhD training

FIGURE 1. Comparison between survey results from the 2008 study at the University of Illinois College of Medicine–Chicago (UIC) and from the present study at the Weill Cornell Medical College (WCM)

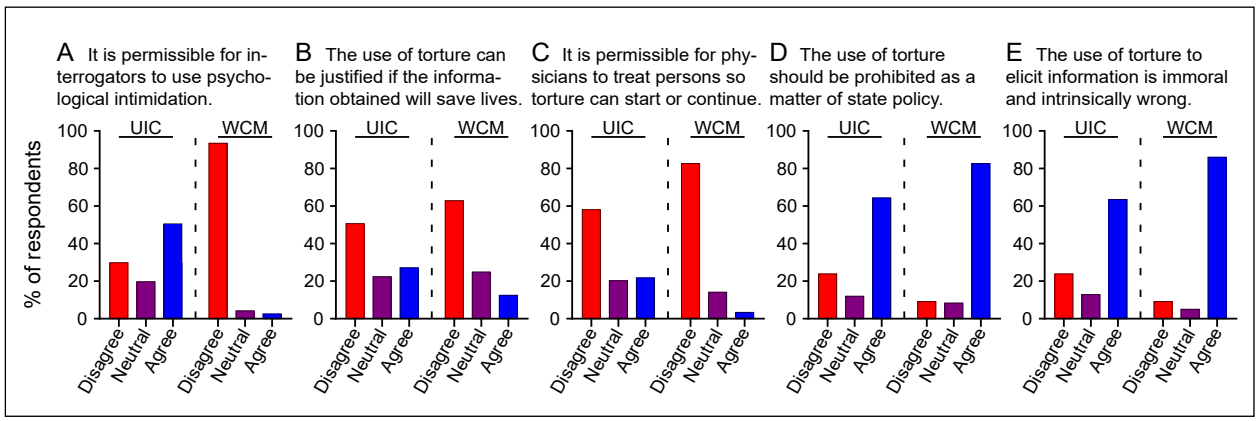

WCM respondents agreed that "the use of torture should be prohibited as a matter of state policy," compared to 64% of UIC respondents (Figure 1D). Finally, for the statement "The use of torture to elicit information is immoral and intrinsically wrong," the 86% agreement rate among WCM respondents exceeded the rate of 63% reported for UIC respondents (Figure 1E). WCM respondents' answers to these two final questions were strongly correlated (r = 0.84). Interestingly, the rate of neutral responses was lower among WCM respondents than among UIC students in all but one item: "The use of torture can be justified if the information obtained will save lives."

FIGURE 2. Medical students' attitudes toward torture

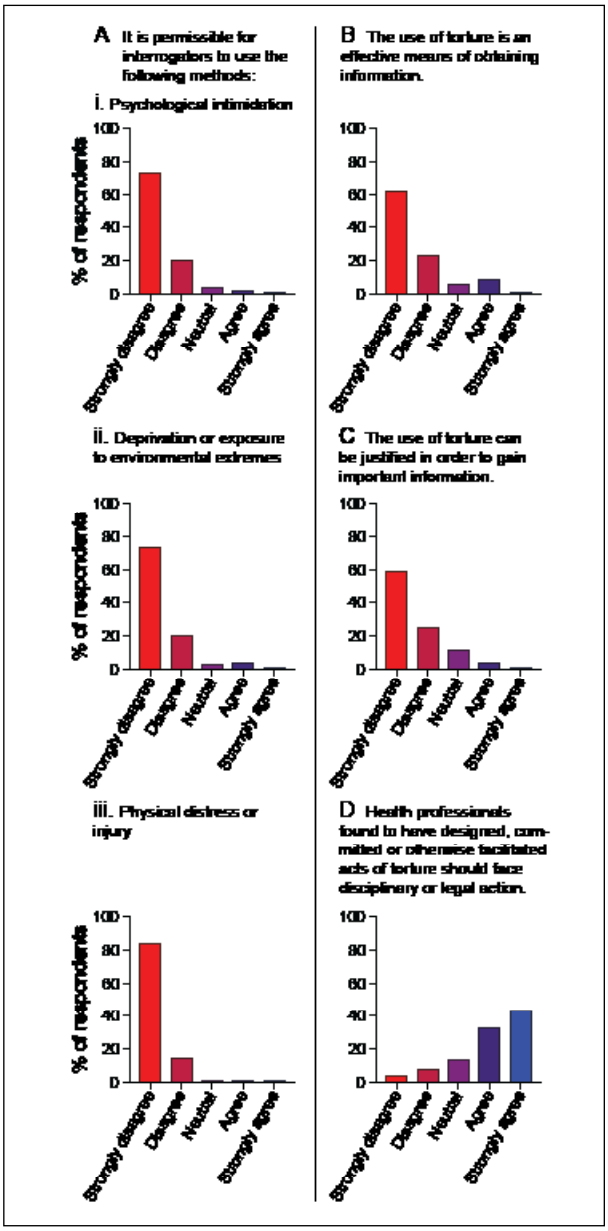

Our study sought to expand upon the 2008 UIC survey in several ways. First, because torture comes in different forms, we asked participants whether it is permissible for interrogators to employ "psychological intimidation (e.g. mock executions, sexual humiliation, religious humiliation, threatening loved ones)," "deprivation or exposure to environmental extremes (e.g. exposure to extreme heat/cold/noise, sensory deprivation, sleep deprivation, starvation, or forced feedings)," or "physical distress or injury (e.g. forced positions, asphyxiation, beating, electrocution)." More than 90% of WCM respondents disagreed that any of these three interrogation classes are permissible (Figure 2A). Approximately 8% of WCM students felt neutral or agreed that psychological intimidation and deprivation or exposure to environmental extremes are permissible interrogation strategies. Interestingly, WCM students were most opposed (97.5%) to interrogators employing tactics that would cause physical distress or injury. Respondents' answers to these three questions were strongly correlated ($r > 0.7$).

Believing that information elicited through torture is reliable will influence individuals' views on the justification of torture. Therefore, our survey also asked participants whether they agreed that "torture is an effective means of obtaining information"; more than 80% of students disagreed with this statement (Figure 2B). A similar percentage of respondents also disagreed with the premise that "torture can be justified to gain important information" (Figure 2C). Only 60%, however, disagreed with the statement that "torture can be justified if the information obtained will save lives" (Figure 1F), with 27.6% responding with a neutral answer. Participants who disagreed that torture is justified if it yields important information were also likely to disagree that life-saving information justifies torture (r = 0.75). Their responses to these two items, however, correlated less well with their belief in the effectiveness of torture as a means of obtaining information (r = 0.57 and 0.49, respectively).

Third, the 2008 questionnaire explored whether those surveyed believed it was acceptable for physicians to participate in torture. Taking this one step further, our study looked at whether respondents felt that physicians' participation in torture should warrant punishment. In this regard, 75% of WCM participants agreed that "health professionals who are found to have designed, committed, or otherwise facilitated torture should face disciplinary or legal action" (Figure 2D).

Finally, in an effort to identify factors that may inform individuals' beliefs about torture, our survey contained a number of additional questions (Appendix). Several items specifically addressed human rights issues, including whether respondents had participated in the existing programs at the medical college. Students involved with the Weill Cornell human rights program (item 5.3 of the survey) had significantly ($p < 10^{-4}$) lower mean ATS values (see "Subjects and methods" section), indicating greater opposition to torture than those who had not participated (Figure 3 and Table 2). Participants were also asked about individual or familial experiences of harassment or discrimination (item 4.3). A trend toward stronger pro-torture attitudes, as measured by mean ATS values, was seen among individuals who had experienced discrimination or harassment ($p = 0.0046$), but this trend did not reach statistical significance after applying a Bonferroni correction for multiple hypothesis testing (Figure 3 and Table 2). Strong correlations were seen between ATS values and responses to all of the torture-specific questions, with the strongest being for the item "The use of torture can be justified in order to gain important information" ($r = 0.85$).

Our multivariate regression analyses identified several additional factors that strongly predicted respondents' attitudes toward certain torture-specific items. Responses to the statement "Medical schools' curricula should include mandatory Human Rights coursework" (item 5.1) provided the strongest predictor for when individuals would express weaker opposition to torture. Those who disagreed with this statement were many times more likely to support the use of torture to obtain important information (odds ratio (OR) 42.14, 95% confidence interval (CI) {3.8,1059}) or life-saving information (OR 58.63, 95% CI {3.89,1752}), as well as the use of interrogation techniques that result in physical distress or injury (OR 18.22, 95% CI {2.22,183.7}). Conversely, those who agreed with mandatory human rights coursework were less likely to support the use of psychological intimidation (OR 0.27, 95% {0.09,0.79}), and those who strongly agreed were less likely to support the use of deprivation or exposure to environmental extremes compared to those who disagreed, felt neutral, or did not answer the question (OR 0.17, 95% CI {0.05,0.5}). The

FIGURE 3. A comparison of attitude-toward-torture scale values (error bars indicate standard error of the mean, and the asterisk denotes $p < 10^{-4}$)

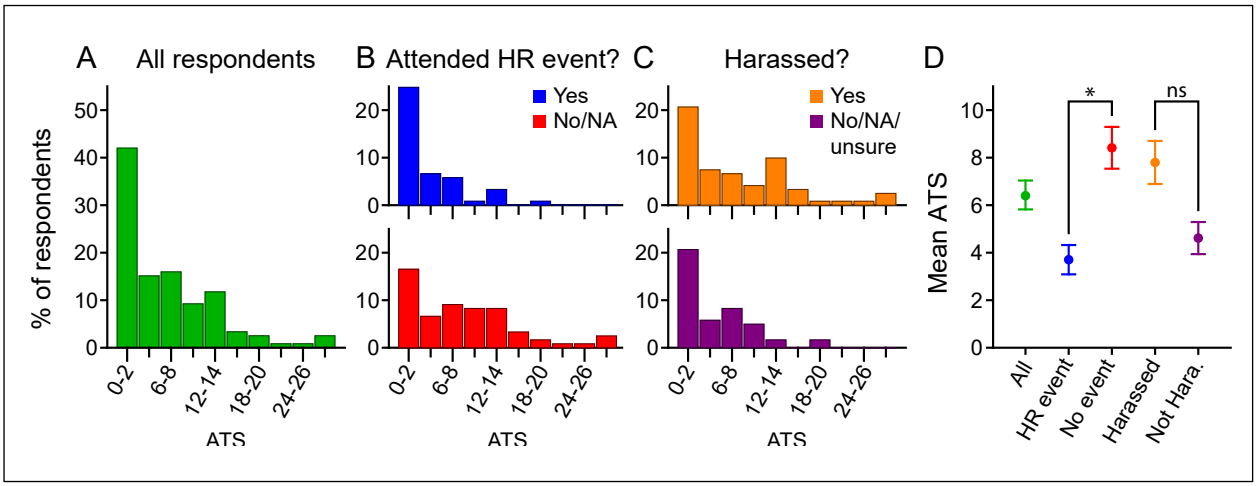

conclusions we can draw are limited, however, as only four individuals disagreed that medical school curricula should include mandatory human rights coursework.

Interestingly, students who were trained by the Weill Cornell Center for Human Rights to perform forensic evaluations of asylum seekers (item 5.3) were less likely to agree that obtaining life-saving information justifies the use of torture (OR 0.4, 95% CI {0.20,0.78}) or that it is permissible for physicians to treat individuals so that torture can begin or continue (OR 0.28, 95% CI {0.13,0.61}). We also found that the importance of an individual's belief system and experiences of harassment or gender-based discrimination yielded predictors of that person's attitude toward certain torture-specific items (data available upon request). Other factors, including ethnicity and age, were not found to be significant predictors for responses to individual torture questions (additional information available upon request).

Discussion

As part of their education, medical students would benefit from understanding that participation in torture may take active and passive forms.[6] Helping design torture programs that leave no physical evidence, such as those designed by James Mitchell and John Jessen for the US Department of Defense, would be considered active participation.[7] Passive physician participation can include ignoring torture when it occurs, deliberately failing to diagnose injuries caused by torture, and covering up occurrences through non-documentation or the alteration of medical records. When doctors condone and participate in torture, a demoralizing impact is felt both by victims and by staff—and given the respected authority of physicians, a strong message of support for torture may be inferred. The same can be said of physicians' participation in certain activities in correctional institutions, where human rights abuses often occur and where a doctor's behavior and attitude may convey tolerance for insensitive, inhumane conduct.[8] Given the parallels between torture and correctional medicine abuses, both topics should be central to any medical school's human rights curriculum.

Our results support the implementation of human rights educational programs in medical school curricula. However, beyond the one item in our survey that asked about support for disciplinary or legal action for physicians who have participated in torture (Figure 2D), we have not addressed an important aspect of the issue: professional accountability. The settlement, in August 2017, of a lawsuit brought by the American Civil Liberties Union (on behalf of three men who were kidnapped by the CIA in 2002 and tortured according to a protocol designed by psychologists Mitchell and Jessen) sends a clear message: health care personnel who violate professional codes of conduct may indeed be held accountable for their actions. The two psychologists had been paid millions by the CIA to design and implement an "enhanced interrogation program" to deal with post-9/11 terrorism suspects.[9] Whether a physician contributes actively to the conduct of torture, in the manner of Mitchell and Jessen, or passively, as might a prison MD who fails to contravene a course of solitary confinement, awareness that their actions or inaction will be scrutinized may help combat misbehavior.

TABLE 2. Mean attitude-toward-torture scale values

Condition	Number of respondents	Mean ATS ± SEM†
All	121	6.43 ± 0.61
WCCHR event[a]	51	3.71 ± 0.62
No WCCHR event[b]	70	8.41 ± 0.88
Harassed[c]	69	7.80 ± 0.91
Not harassed[d]	52	4.62 ± 0.68

† SEM = standard error of the mean. [a] Attended a human rights event hosted by the Weill Cornell Center for Human Rights (WCCHR). [b] Did not attend or left this question blank. [c] Respondent or family member experienced harassment (bullying/cyberbullying, stalking, intimidation, threats, etc.). [d] Was not harassed, was unsure, or left this question blank.

A recent global survey by the International Committee of the Red Cross reported that 46% of Americans approved of torture to obtain information from enemy combatants, with only slightly more than half indicating that torture was "wrong." Only Israelis, Palestinians, and Nigerians matched Americans in their endorsement of torture. By comparison, over 80% of Afghans and Colombians surveyed disapproved of torture.[10] The results of our survey of medical students at one American university reflect strongly divergent attitudes toward torture compared to this global survey.

Conclusive findings from our survey are limited by several factors. Our study, like the 2008 survey, was conducted at a single institution. The number of respondents (121) is relatively small, although our response rate of 25.1% is comparable to other survey response rates of physicians and medical students: 24% of medical students and 18.9% of medical residents completed the 2012 Canadian National Physician Survey, and 27% of medical students responded to Australia's 2013 National Mental Health Survey of Doctors and Medical Students.[11] The more robust response rates of first- and second-year students (34.7% and 40.2%, respectively) suggest that the pre-clinical years, before students disperse to disparate locations with different schedules, might be a more optimal time for surveying students.

The response rate of our study may have been affected by the very subject matter, torture being an uncomfortable topic for many. Questions about personal or familial experiences of discrimination, harassment, being a victim of a crime, or experiencing sexual or physical abuse may similarly have been too off-putting for some students.

Responses to some of our survey items may have been influenced by our detailing specific torture methods that were not made explicit in the UIC questionnaire (Figure 1A). Similarly, we attempted to ascertain whether respondents believed that torture is an effective way to obtain information, a question that was not included in the UIC study.

Although temporal, geographic, and compositional differences limit comparisons of responses to similar and identical questions between the 2008 UIC survey and our own, some limited observations seem merited. A trend toward stronger anti-torture attitudes was seen among students in 2016 (Figure 1). Why might such a trend be taking place? General contributing factors might include formal and informal human rights educational initiatives that have arisen in the intervening years; continued writing about Abu Ghraib and the role of medical personnel; the ongoing horrific human rights crises in Syria and in other countries; increased awareness of all human rights abuses, including torture; and the agitating polemics of the most recent presidential campaign, in which torture specifically and an atmosphere of hostility toward immigrants fleeing oppression generally may have seeped into the consciousness of medical students.[12]

Using the ATS metric, we examined whether students' participation in the school's student-run asylum clinic, the Weill Cornell Center for Human Rights, affected their views on torture.[13] Founded in 2010, this voluntary program attracts students interested in human rights activism and trains them in providing pro bono medical, mental health, and gynecologic evaluations to individuals seeking asylum in the United States. Between one-quarter and one-third of Weill Cornell students will have participated in this program by graduation. In the course of these evaluations, students have helped examine more than 300 asylum seekers, the majority of whom are survivors of torture, and have absorbed their histories. In our study, students who had participated in the human rights program had significantly lower (more opposed to torture) mean ATS values than students who had not been involved (Figure 3 and Table 2).

The medical education experience can be isolating for many students. Human rights education, formalized or not, can ameliorate such isolation and can enhance a student's preparedness for his or her life as a physician. A 2010 study documented deficits in medical students' knowledge of torture that could be remediated through a structured curriculum.[14] The experiences of Croatian medical students during the Croatian War of Independence (1991–1995) bears on the value of human rights experiences in medical school. As has been described:

> *Our experience during the five years of the wars… showed that the best option for the medical students was to continue their studies and engage very actively in a number of activities where their education and medical experience were important …Psychologically, intensive engagement in extracurricular activities related to their profession was of enormous benefit to the students … They became a symbol of safety, consolation, and help in many complicated situations.*[15]

Of course, torture is only one of many human rights issues that physicians will encounter in their careers. However, learning about torture equips clinicians to attend to victims of other abuses, including victims of human trafficking; domestic abuse; child abuse and child labor; bullying; religious, political, and ethnic persecution; LGBT discrimination; and, as previously mentioned, human rights abuses in prisons. Specifically, being able to elicit painful and difficult histories, developing empathy, and recognizing human resilience are skills that will serve all physicians in all settings.

Acknowledgments

The authors would like to thank the Weill Cornell Center for Human Rights for its role in generating interest in this topic among Weill Cornell medical students. K.D. and A.R.M were supported by a Medical Scientist Training Program grant from the National Institute of General Medical Sciences, NIH (award T32GM07739 to the Weill Cornell/Rockefeller/Sloan Kettering Tri-Institutional MD-PhD Program).

Ethical approval

Ethical approval for this study, protocol number 1507016384, was received from the Weill Cornell Medical College Institutional Review Board on November 19, 2016.

References

1. World Medical Association, 29th World Medical Assembly, Declaration of Tokyo: Guidelines for Physicians concerning Torture and Other Cruel, Inhuman or Degrading Treatment or Punishment in relation to Detention and Imprisonment, Tokyo, October 1975; American Medical Association, *Torture, coercive interrogations and physicians* (December 2014); American Psychological Association, *Timeline of APA Policies and Actions Related to Detainee Welfare and Professional Ethics in the Context of Interrogation and National Security.* Available at http://www.apa.org/news/press/statements/interrogations.aspx; World Psychiatric Association, General Assembly of the World Psychiatric Association, Madrid Declaration on Ethical Standards for Psychiatric Practice, August 1996; L. Snyder, "American College of Physicians ethics manual: Sixth edition," *Annals of Internal Medicine* 156 (2012), pp. 73–104.

2. S. Miles, "Torture: The bioethics perspective," *Hastings Center.* Available at http://www.thehastingscenter.org/briefingbook/torture-the-bioethics-perspective.

3. M. Balfe, "Why did U.S. healthcare professionals become involved in torture during the War on Terror?" *Journal of Bioethical Inquiry* 13 (2016), pp. 449–460.

4. J. Bean, D. Ng, H. Demirtas, and P. Guinan, "Medical students' attitudes toward torture," *Torture* 18/2 (2008) pp. 99–103.

5. S. K. Verma and G. Biswas, "Knowledge and attitude on torture by medical students in Delhi," *Torture* 15/1 (2005), pp. 46–50; A. K. Agnihotri, B. Purwar, and N. Jeebun, "Awareness of issues related to torture among medical students in Mauritius," *Indian Journal of Medical Ethics* 4 (2007).

6. G. Maio, "History of medical involvement in torture—then and now," *Lancet* 357/9268 (2001), pp. 609–1611.

7. S. Fink, "Settlement reached in C.I.A. torture case," *New York Times* (August 17, 2017). Available at https://www.nytimes.com/2017/08/17/us/cia-torture-lawsuit-settlement.html?mcubz=1.

8. J. Pont, H. Stöver, and H. Wolff, "Dual loyalty in prison health care," *American Journal of Public Health* 102/3 (2012), pp. 475–480; American Civil Liberties Union, *ACLU affiliates send advisements to 100+ healthcare facilities detailing rights to hospital personnel not to condone invasive searches requested by CBP agents* (Houston: ACLU of Texas, 2016); M. Marizco "Lawsuit alleges 'invasive' body cavity search by Arizona hospital, CBP," *Fronteras* (June 13, 2016). Available at http://fronterasdesk.org/content/10336/lawsuit-alleges-invasive-body-cavity-search-arizona-hospital-cbp.

9. American Civil Liberties Union, *Out of the darkness.* Available at https://www.aclu.org/issues/national-security/torture/out-darkness?redirect=feature/out-darkness.

10. S. Sengupta, "Torture can be useful, nearly half of Americans in poll say," *New York Times* (December 5, 2016). Available at https://www.nytimes.com/2016/12/05/world/americas/torture-can-be-useful-nearly-half-of-americans-in-poll-say.html.

11. National Physician Survey, *2012 response rates.*

Available at http://nationalphysiciansurvey.ca/surveys/2012-survey/response-rates/; beyondblue, *National mental health survey of doctors and medical students* (Hawthorn: beyondblue, 2013).

12. Physicians for Human Rights, *Student asylum clinics*. Available at http://physiciansforhumanrights.org/asylum/student-asylum-clinics.html?referrer=http://physiciansforhumanrights.org; J. Risen, "Outside psychologists shielded U.S. torture program, report finds," *New York Times* (July 10, 2015). Available at www.nytimes.com/2015/07/11/us/psychologists-shielded-us-torture-program-report-finds; J. Kitfield, "The lingering stench of torture," *New York Times* (January 13, 2017). Available at https://www.nytimes.com/2017/01/13/opinion/the-lingering-stench-of-torture.html?_r=0; Human Rights Watch, *World report 2017: Syria*. Available at https://www.hrw.org/world-report/2017/country-chapters/syria; J. Diamond, "Trump on torture: 'We have to beat the savages'," *CNN* (March 6, 2016). Available at http://www.cnn.com/2016/03/06/politics/donald-trump-torture/index.html.

13. E. Emery, C. Stellar, K. Dubin, et al., "Student leadership in the creation and operation of an asylum clinic," *Health and Human Rights Journal*, Perspectives (2015). Available at https://www.hhrjournal.org/2015/11/student-leadership-in-the-creation-and-operation-of-an-asylum-clinic.

14. M. Husain, U. B. Ghaffar, J. A. Usmani, and S. J. Rivzi. "A study to determine whether targeted education significantly improves the perception of human torture in medical students in India," *Journal of the Indian Medical Association* 108 (2010) pp. 491–494.

15. V. Gluncic, D. Pulanic, M. Prka, et al. "Curricular and extracurricular activities of medical students during war, Zagreb University School of Medicine, 1991–1995," *Academic Medicine* 76/1 (2001) pp. 82–87.

APPENDIX

Medical Students' Attitudes toward Torture survey

The numbering of the questions discussed in Figures 1 and 2 of the main text correspond to questions in Part 1 of the original survey as follows:

Main text figure	1A	1B	1C	1D	1E	2A	2B	2C	2D
Survey, Part 1 question	1.a	4	5	6	7	1	2	3	8

Questions 5–7 of the survey were taken verbatim from the UIC study, while questions 1a and 4 are modified versions of UIC questions.

SURVEY

Please complete the following brief, *confidential* survey. You may skip any questions you do not feel comfortable answering.

Part 1

Please note that once you select 'Submit', you cannot return to this section of the survey.

1. It is permissible for interrogators to use the following methods:

   a. Psychological intimidation (e.g. mock executions, sexual humiliation, religious humiliation, threatening loved ones).

   ☐ Strongly disagree ☐ Disagree ☐ Neutral ☐ Agree ☐ Strongly agree

   b. Deprivation or exposure to environmental extremes (e.g. exposure to extreme heat/cold/noise,

sensory deprivation, sleep deprivation, starvation or forced feedings).

☐ Strongly disagree ☐ Disagree ☐ Neutral ☐ Agree ☐ Strongly agree

c. Physical distress or injury (e.g. forced positions, asphyxiation, beating, electrocution).

☐ Strongly disagree ☐ Disagree ☐ Neutral ☐ Agree ☐ Strongly agree

2. The use of torture is an effective means of obtaining important information.

☐ Strongly disagree ☐ Disagree ☐ Neutral ☐ Agree ☐ Strongly agree

3. The use of torture can be justified in order to gain important information.

☐ Strongly disagree ☐ Disagree ☐ Neutral ☐ Agree ☐ Strongly agree

4. The use of torture can be justified if the information obtained will save lives.

☐ Strongly disagree ☐ Disagree ☐ Neutral ☐ Agree ☐ Strongly agree

5. It is permissible for physicians to treat individuals to verify their health so that torture could begin or continue.

☐ Strongly disagree ☐ Disagree ☐ Neutral ☐ Agree ☐ Strongly agree

6. The use of torture should be prohibited as a matter of state policy.

☐ Strongly disagree ☐ Disagree ☐ Neutral ☐ Agree ☐ Strongly agree

7. The use of torture to elicit information is immoral and intrinsically wrong.

☐ Strongly disagree ☐ Disagree ☐ Neutral ☐ Agree ☐ Strongly agree

8. Health professionals who are found to have designed, committed or otherwise facilitated acts of torture should face disciplinary or legal action (e.g. loss of one's professional license).

☐ Strongly disagree ☐ Disagree ☐ Neutral ☐ Agree ☐ Strongly agree

Part 2

Please note that once you select 'Submit', you cannot return to this section of the survey.

1. What is your age? _____

2. What is your gender?

☐ Male ☐ Female ☐ Transgender ☐ Intersex ☐ Other

3. What is your home state (abbrev.) in the United States, or country of origin if not the United States?

_____

4. What year of medical education are you in?

☐ 1st year ☐ 2nd year ☐ 3rd year ☐ 4th year ☐ MD/PhD (if currently in PhD stage)

Part 3

Please note that once you select 'Submit', you cannot return to this section of the survey.

1. What ethnicity do you consider yourself?

☐ American Indian or Alaskan Native ☐ Native Hawaiian or Pacific Islander

☐ Non-Hispanic White ☐ African-American ☐ Hispanic/Latino ☐ Middle Eastern
☐ Asian ☐ Multiracial ☐ Other

2. Do you identify as:

☐ Heterosexual ☐ Lesbian ☐ Gay ☐ Bisexual ☐ Questioning ☐ Asexual ☐ Not Sure

3. Do you identify with any one of the following?

☐ Christian ☐ Jewish ☐ Muslim ☐ Hindu ☐ Buddhist ☐ Atheist
☐ Agnostic ☐ Spiritual ☐ Other

4. How important is this religion or belief system in your daily life?

☐ Not at all ☐ Slightly important ☐ Important ☐ Very Important ☐ No opinion

5. Have you served in the military or with affiliated organizations/contractors?

☐ Yes ☐ No

6. Has a member of your family served in the military or with affiliated organizations/contractors?

☐ Yes ☐ No

Part 4

Please note that once you select 'Submit', you cannot return to this section of the survey.

1. Have you or a member of your family ever been a victim of a crime that caused physical or emotional injury?

☐ Yes ☐ No ☐ Not sure

2. Have you or a member of your immediate family ever experienced physical or sexual abuse?

☐ Yes ☐ No ☐ Not sure

3. Have you or a member of your immediate family ever experienced harassment (including, but not limited to, bullying/cyber bullying, stalking, intimidation, threats, etc.)?

☐ Yes ☐ No ☐ Not sure

a. If you answered "yes" to question 3: Was the perpetrator(s) acting in an official capacity (e.g. security personnel, law enforcement, military, etc.)?

☐ Yes ☐ No ☐ Not sure

4. Do you believe that you or a member of your immediate family have ever experienced discrimination based on the following (select all that apply)?

☐ Race ☐ Ethnicity ☐ Nationality ☐ Religion
☐ Sexual orientation ☐ Gender ☐ Political opinion ☐ Membership in a specific group

Part 5

Please note that once you select 'Submit', you cannot return to this section of the survey.

1. Please indicate how strongly you agree or disagree with the following statement: Medical schools' curricula should include mandatory Human Rights coursework.

☐ Strongly disagree ☐ Disagree ☐ Neutral ☐ Agree ☐ Strongly agree

2. Have you participated in a *Weill Cornell volunteer/community service activity?

   ☐ Yes ☐ No

*Such as with the Weill Cornell Center for Human Rights (WCCHR), Weill Cornell Community Clinic (WCCC), Motivating Action through Community Health Outreach (MAChO), etc.

   a. If you answered "yes" to question 2: Please indicate which activity: _____

3. If you have participated with the Weill Cornell Center for Human Rights (WCCHR), please indicate if you attended a WCCHR-sponsored educational event (select all that apply):

   ☐ Student training ☐ WCCHR Elective ☐ SafeZone training ☐ Other

   a. If you answered "student training" to question 3: Please indicate the year you attended the student training: _____

   b. If you answered "other" to question 3: Please describe what other WCCHR-sponsored educational event(s) you have participated in _____

4. Have you participated in human rights training, education or other activities in the past?

   ☐ Yes ☐ No

   a. If you answered "yes" to question 4: Please describe: _____

5. If you have participated with the Weill Cornell Center for Human Rights (WCCHR), how many evaluations have you observed?

   ☐ 0 ☐ 1 ☐ 2 ☐ 3 or more

6. How many applications for asylum were submitted in the United States in 2015?

   ☐ < 10,000 ☐ 10,000-49,999 ☐ 50,000-249,999 ☐ >=250,000

7. How many survivors of torture are estimated to be residing in the United States?

   ☐ < 10,000 ☐ 10,000-49,999 ☐ 50,000-249,999 ☐ >=250,000

Enhancement of external-internal correlation by phase-shift detection and correction based on concurrent external bellows and internal navigator signals

Running Title: Phase-shift correction for improved external-internal correlation

Key Words: Four-dimensional MRI, Radiotherapy planning and delivery, external-internal motion phase shift

PACS:

treatment strategy in, 87.55.-x

Treatment planning, 87.55.D-

in medical imaging, 87.57.Q-

Respiration, 87.19.Wx

Cancer, 87.19.xj

ABSTRACT

Purpose: To enhance the correlation between external and internal respiratory motions by dynamically determining and correcting the patient-specific phase shift between external and internal respiratory waveforms acquired concurrently during respiratory-correlated (RC) four-dimensional magnetic resonance imaging (4DMRI) scans.

Methods: Internal-navigator and external-bellows waveforms were acquired simultaneously during 6 to 15-minute RC-4DMRI scans in ten healthy volunteers under an IRB-approved protocol. The navigator was placed at the right lung-diaphragm interface while the bellows was placed ~5cm inferior to the sternum. Three segments of each respiratory waveform, at the beginning, middle, and end of a scan, were analyzed. Three phase-domain methods were employed to estimate the phase shift, including analytic signal analysis, phase-space oval fitting, and principal component analysis. A robust strategy for estimating the phase shift was realized by combining these methods in a weighted average and by eliminating outliers ($>2\sigma$) owing to breathing irregularities. Whether phase-shift correction affects the external-internal correlation was evaluated. The cross-correlation between the two waveforms in the time domain provided an independent check of the correlation enhancement.

Results: Phase-shift correction significantly enhanced the external-internal correlation in all volunteers across the entire 6-15min scans. On average, the correlation increased from 0.45±0.28 to 0.85±0.15 for the combined method. The combined method exhibits a 99.5% success rate and reveals that the phase of the external waveform leads that of the internal waveform in all ten subjects by 57 ± 17^{o} (1.6±0.5 bins) on average. Seven volunteers exhibit highly reproducible phase shifts over time, evidenced by standard deviations (σ) below 4^{o}, whereas $8^{o}<\sigma<12^{o}$ in the

remaining three subjects. Regardless, phase-shift correction significantly improved the correlation in all volunteers.

Conclusions: Correcting the phase shift estimated by the phase-domain methods provides a new approach for enhancing the correlation between external and internal respiratory motions. This strategy holds promise for improving the accuracy of respiratory-gated radiotherapy.

INTRODUCTION

Despite substantial progress made in the past 2-3 decades, including the advent of fluoroscopic motion-monitoring techniques employing implanted fiducial markers (1-5), respiratory-correlated (RC) four-dimensional computed tomography (4DCT) (6-9), and, more recently, 4D magnetic resonance imaging (4DMRI) (10-14), managing clinical motion remains one of the biggest challenges in using conventional linear accelerators to treat thoracic and upper abdominal cancers (15-17). Breathing irregularities are common in lung cancer patients and degrade both the quality of 4DCT images and the fidelity of tumor delineation (18-21). Because breathing irregularities also reduce the correlation between the motions of an external-surface surrogate and a mobile tumor, the position of the tumor cannot be reliably inferred from that of the surrogate during treatment delivery without radiographic verification (22-24). Three general approaches have been advanced to overcome this problem, but none are without caveats: (1) Updating an adaptive, correlation-based model with frequent x-ray imaging presents a viable solution (2-4, 25-28), but this approach entails the invasive implantation of radio-opaque fiducial markers. (2) Models that employ physical principles to predict respiratory motion should be insensitive to breathing irregularities (29-32), but require a better understanding and more thorough validation of patient-specific breathing patterns. (3) MR-guided radiotherapy (33, 34) offers real-time 2D cine imaging, but demands substantial investment, staff training, and maintenance resources.

Respiration-induced motions often exhibit nonlinear behaviors, including phase shifts between the motions of an external body surface and internal structures, such as lung or liver tumors. The phase shift can be substantial (10, 15, 35) and has been advanced as the most critical irregularity for external-internal models (36). Such a phase shift engenders ellipsoidal trajectories in phase space: this nonlinear relationship illuminates the cause for the low correlation between the two

motion waveforms (1). Because they arise from asynchronized muscle engagement and tissue elasticity, phase shifts are known to be patient-specific and location-dependent (13, 15, 32, 35-38). A better understanding and more thorough characterization of the nonlinear features of organ movement are thus essential for building a model that accurately predicts tumor motion (29-31). Such a model may find application in respiratory gating, in tumor tracking, and in motion-compensated treatment delivery.

In this study, we report the feasibility of determining and correcting patient-specific phase shifts to enhance the correlation between external and internal respiratory waveforms. Quantitative estimates of the phase shift were obtained using three individual methods, including phase-space oval fitting (POF), principal component analysis (PCA), and analytic signal analysis (ASA). A fourth method excluded outliers (>2σ) from the individual methods and combined the remaining phase-shift estimates in a weighted average. This approach improved the phase-shift calculation's robustness to breathing irregularities. Maximizing the time-domain cross-correlation between the motion waveforms and between the diaphragm-motion trajectories extracted from navigator-triggered and bellows-rebinned 4DMRI images provided two additional strategies to verify the results obtained by the phase-domain methods. The respiratory waveforms were acquired concurrently by an internal navigator and by external bellows during 4DMRI scans of ten healthy volunteers under an IRB-approved protocol.

METHODS AND MATERIALS

Simultaneous external and internal waveforms acquired during 4DMRI

Respiratory-correlated 4DMRI scans that employed T2-weighted fast spin-echo sequences were acquired using a 3T MR scanner (Ingenia, Philips Healthcare, Amsterdam, Netherland) in ten healthy volunteers under an IRB-approved protocol. During each scan, external bellows (496Hz) and internal navigator (20Hz) waveforms were acquired concurrently (13). The bellows was placed inferior to the sternum and the navigator ($3x3x6cm^3$) was placed on the dome of the right diaphragm. The initial timestamps (in milliseconds) in the scanner and bellows log files were used to synchronize the two waveforms. A 4DMRI scan lasted 6-15 minutes, during which 2D coronal slice images were acquired. The navigator signal was used to prospectively sort these slices into 10 respiratory cycle bins using an amplitude-binning method (13).

Three waveform segments (10-300s) at the beginning, middle, and end of a scan were divided into 10 or 12.5-second windows that were used for phase-shift assessment. Multiple windows (12.5s) were used in the middle and end segments (Table S1), and each window overlapped with 5s of the subsequent window. The navigator signal was continuous except at times when slice images were acquired. The bellows waveform was down-sampled to match the navigator's 20-Hertz frame rate, and both waveforms were normalized and centered. The occurrence of ellipsoidal trajectories in phase-space (navigator vs. bellows) confirmed the existence of a phase shift between the waveforms (1). Estimates of the phase shift were obtained through phase-space oval fitting (POF), principal component analysis (PCA), and analytic signal analysis (ASA) methods. After correcting the calculated phase shift, the resulting correlation between the two waveforms was compared with their original correlation and with the maximum value of their time-domain cross-correlation (TCC) (Fig. 1).

Phase-domain methods to assess the phase shift

Three phase-domain methods were implemented in Mathematica (Version 10.1; Wolfram) and also combined to yield a fourth robust and adaptive strategy for estimating the phase shift.

(1) Phase-Space Oval Fitting (POF): The phase shift between the bellows $\boldsymbol{x(t)}$ and navigator $\boldsymbol{y(t)}$ waveforms was calculated from the best–fit oval in phase space (Fig. S1A). In this space, an ellipse centered at (0,0) is described by

$$\frac{(\boldsymbol{x}\cos\boldsymbol{\theta}+\boldsymbol{y}\sin\boldsymbol{\theta})^2}{\boldsymbol{a^2}}+\frac{(\boldsymbol{y}\cos\boldsymbol{\theta}-\boldsymbol{x}\sin\boldsymbol{\theta})^2}{\boldsymbol{b^2}}=\mathbf{1}, \qquad (\mathbf{1})$$

where $\boldsymbol{a}$ and $\boldsymbol{b}$ are the major and minor half-axis lengths and $\boldsymbol{\theta}$ is the angle by which the major axis is tilted clockwise from the positive $\boldsymbol{x}$-axis. For simplicity, we modeled the waveforms as two sinusoidal functions $\boldsymbol{x(t)}=\boldsymbol{r_1}\cos(\boldsymbol{\omega_1 t})$ and $\boldsymbol{y(t)}=\boldsymbol{r_2}\cos(\boldsymbol{\omega_2 t}+\boldsymbol{\phi})$ with phase shift $\boldsymbol{\phi}$ and assuming $\boldsymbol{\omega_1}=\boldsymbol{\omega_2}=\boldsymbol{\omega}$. The phase shift is given by

$$\boldsymbol{\phi}=\tan^{-1}\left[\frac{\boldsymbol{ab}\sec\boldsymbol{\theta}}{(\boldsymbol{a^2}-\boldsymbol{b^2})\sin\boldsymbol{\theta}}\right]. \qquad (\mathbf{2})$$

The residual error $\boldsymbol{RE}$ in phase-space ellipse's fit of the data points $\{\boldsymbol{x_j},\boldsymbol{y_j}\}$ is given by

$$\boldsymbol{RE}=\frac{\mathbf{1}}{\boldsymbol{n}}\sum_{\boldsymbol{j=1}}^{\boldsymbol{n}}\min_{\boldsymbol{\alpha_j}}\sqrt{(\boldsymbol{x_j}-\boldsymbol{r_1}\cos(\boldsymbol{\alpha_j}))^2+(\boldsymbol{y_j}-\boldsymbol{r_2}\cos(\boldsymbol{\alpha_j}+\boldsymbol{\phi}))^2}\ . \qquad (\mathbf{3})$$

An explanation of how the sign of $\boldsymbol{\phi}$ is determined and detailed deviations of Eqns. 2 and 3, are provided in Appendix A1.

(2) Principal Component Analysis (PCA): A $\mathbf{2}\times\boldsymbol{n}$ matrix $\boldsymbol{A}=$ [bellows: $\boldsymbol{x(t)}$, navigator: $\boldsymbol{y(t)}$] was constructed from the two concurrent waveforms and the covariance matrix for this dataset was formed by the multiplication $\boldsymbol{AA^T/(n-1)}$. The principal components, $\vec{\boldsymbol{p}}_{\boldsymbol{1}}$ and $\vec{\boldsymbol{p}}_{\boldsymbol{2}}$, were given by the eigenvectors of the covariance matrix. The square roots of the eigenvalues, $\sqrt{\boldsymbol{\lambda_1}}$

and $\sqrt{\boldsymbol{\lambda_2}}$, represented the standard deviation in the dataset in the directions of the principal component vectors. An ellipse was then constructed with major and minor axes pointing in the directions of $\vec{\boldsymbol{p}}_{\boldsymbol{1}}$ and $\vec{\boldsymbol{p}}_{\boldsymbol{2}}$ and with half lengths $\boldsymbol{a} = \sqrt{\boldsymbol{\lambda_1}}$ and $\boldsymbol{b} = \sqrt{\boldsymbol{\lambda_2}}$, respectively (Fig. S1A). The tilt angle of the ellipse was given by $\boldsymbol{\theta} = \mathbf{tan^{-1}}\left[\vec{\boldsymbol{p}}_{\boldsymbol{1},\boldsymbol{y}}/\vec{\boldsymbol{p}}_{\boldsymbol{1},\boldsymbol{x}}\right]$ and the phase shift $\boldsymbol{\phi}$ by Eq. 2. See Appendix A2 for additional details.

(3) Analytic Signal Analysis (ASA): An analytic representation of a real-valued function, called the function's analytic signal, can be constructed as follows:

$$\boldsymbol{f_A(t) = f(t) + if_H(t)},$$

where $\boldsymbol{f(t)}$ is the original function, $\boldsymbol{f_H(t)}$ is the Hilbert transform of $\boldsymbol{f(t)}$, and $\boldsymbol{f_A(t)}$ is the analytic signal of $\boldsymbol{f(t)}$. The discrete Fourier ($\boldsymbol{\mathcal{F}}$) and inverse Fourier ($\boldsymbol{\mathcal{F}^{-1}}$) transforms were employed to calculate the Hilbert transforms for the discrete signals:

$$\boldsymbol{f_H(t) = \mathcal{F}^{-1}\{-i\,\mathbf{sign}(\omega)\mathcal{F}\{f(t)\}(\omega)\}(t)}; \quad \boldsymbol{sign(\omega)} = \begin{cases} \mathbf{1}, & \boldsymbol{if\ \omega > 1}; \\ \mathbf{0}, & \boldsymbol{if\ \omega = 0}; \\ \mathbf{-1}, & \boldsymbol{if\ \omega < 1}. \end{cases}$$

The instantaneous phase of a signal at time $\boldsymbol{t_k}$, $\boldsymbol{\varphi(t_k)}$, is found from its analytic signal:

$$\boldsymbol{\varphi(t_k) = \mathbf{tan^{-1}}\left[\frac{\mathbf{Im}\, f_A(t_k)}{\mathbf{Re}\, f_A(t_k)}\right] = \mathbf{tan^{-1}}\left[\frac{f_H(t_k)}{f(t_k)}\right]}. \quad (\mathbf{4})$$

Then $\boldsymbol{\Delta\varphi(t_k) = \varphi_1(t_k) - \varphi_2(t_k)}$ is the instantaneous phase shift between these two signals and averaging over a set of data points yields the mean phase shift $\boldsymbol{\phi = \langle \Delta\varphi(t_k)\rangle_{t_k}}$ for the interval containing the time points $\boldsymbol{t_k}$ (Fig. S1B).

A combined method to calculate a mean phase shift (MPS):

Breathing irregularities may cause the individual methods to yield unreliable results. More reliable estimates can therefore be obtained from a combined method that excludes individual-method outliers. A moving average was initialized by weighting the phase-shift estimates at time

zero by the reciprocal of their $\boldsymbol{RE}$ (see Appendix A). At each successive time point, the phase-shift was estimated by halving the weighted average of the phase shifts calculated by the individual methods at the current time point and adding the result to half of the previous moving average value. A moving standard deviation $\boldsymbol{\sigma}$ was calculated as the average standard deviation of the individual phase shifts found at all the previous time points. Numerical simulations of noisy sinusoids revealed a strong correlation between the $\boldsymbol{RE}$ and the true error in the phase-shift estimate (Figs. S1C,D). This analysis also informed the choice that $\boldsymbol{RE}$ = 0.2 would serve as the maximum tolerable threshold (Appendix B). An outlier was defined to be a phase shift estimated by an individual method whose value was more than $\boldsymbol{2\sigma}$ away from the running average and whose $\boldsymbol{RE}$ for the associated phase-space ellipse exceeded 0.2.

Time-Domain Cross-Correlation (TCC) method:

The cross-correlation in the time domain, $\mathbf{TCC}(\boldsymbol{\tau_j})$, between the two signals was calculated as follows:

$$\mathbf{TCC}(\boldsymbol{\tau_j}) = \frac{\sum_{k=1}^{N} \boldsymbol{s_I}(\boldsymbol{t_k}+\boldsymbol{\tau_j})\boldsymbol{s_E}(\boldsymbol{t_k}) - \sum_{k=1}^{N} \boldsymbol{s_I}(\boldsymbol{t_k}+\boldsymbol{\tau_j}) \sum_{i=1}^{N} \boldsymbol{s_E}(\boldsymbol{t_i})}{\sqrt{\sum_{k=1}^{N}\left[\boldsymbol{s_I}(\boldsymbol{t_k}+\boldsymbol{\tau_j}) - \sum_{i=1}^{N} \boldsymbol{s_I}(\boldsymbol{t_i}+\boldsymbol{\tau_j})\right]^2} \sqrt{\sum_{k=1}^{N}[\boldsymbol{s_E}(\boldsymbol{t_k}) - \sum_{i=1}^{N} \boldsymbol{s_E}(\boldsymbol{t_i})]^2}}, \qquad (\mathbf{5})$$

where the number of points $\boldsymbol{N}$ was a subset of that contained within the time window, $\boldsymbol{s_I}$ is the navigator signal, and $\boldsymbol{s_E}$ is the bellows signal. $\mathbf{TCC}(\mathbf{0})$ gives the original correlation between the external and internal waveforms. Multiplying the frequency of the bellows or navigator waveforms by the value of $\boldsymbol{\tau_j}$ that maximizes $\mathbf{TCC}(\boldsymbol{\tau_j})$ provides another estimate of the phase shift between the two signals. The frequency of the waveforms was found in four ways: the frequency at which the power spectrum of the 1. bellows or 2. navigator signals achieved their maximum value, and the average slope of the 3. bellows' or 4. navigator's instantaneous phase. The correlation coefficient between each pair of frequency estimates exceeded 0.9, indicating that any

of the four estimates works equally well at most time points. When a discrepancy existed between these estimates, the frequency that maximized the phase-shift corrected correlation, described below, was chosen.

Diaphragm-motion phase shifts between navigator-triggered and bellows-rebinned 4DMRI

Following previously reported methods, two binning strategies were employed to produce two different 4DMRI images (13). Sorting the 2D slices into phase bins based on the amplitude of the internal navigator generated the navigator-triggered 4DMRI image. The bellows-rebinned 4DMRI image was constructed by instead using the phase of the concurrently acquired external-bellows signal to sort the 2D slices into phase bins. Two diaphragm-motion trajectories were then obtained by manually tracking the position of the right diaphragm dome's apex in both 4DMRI images through the breathing cycle. The two trajectories are functions of phase-bin number. A cross-correlation analysis was performed to identify the phase shift that arises between the two different 4DMRI images for each subject.

2.4 1D phase-shift correction for improved external-internal correlation

To correct the phase shift estimated by the 1D methods within each time window, the navigator signal was shifted in time by an amount equal to the calculated phase shift divided by the waveform's frequency. The frequency of the waveform was estimated in four ways, as described in the previous section. At each time point, the frequency estimate was chosen to maximize the correlation between the waveforms following phase-shift correction. By comparing the correlation coefficient for the original waveforms to that of the phase-shift corrected waveforms, we assessed whether correcting the phase shift enhances the correlation between the internal and external signals.

RESULTS

Patient-specific phase-shifts

The calculated phase shifts spanned a broad range of 0.5–1.7 radians using the MPS method (Table 1). By excluding outliers and averaging the phase shifts obtained by the ASA, POF, and PCA methods, the MPS method yields a smoother and more robust estimate (Fig. 2A, Fig S2). Owing to their different assumptions and varied sensitivity to noise and breathing irregularities, each method yields slightly different phase-shift estimates. However, these phase shifts are strongly correlated: Pearson's correlation coefficient r exceeded 0.8 for every pair of methods, except $r = 0.77$ for the maximum TCC and ASA methods.

The external bellows signal was found to lead the motion acquired by the internal navigator in the ten subjects by all five waveform methods (Table 1, Fig. 2). The analysis also reveals that an individual's phase shift can be relatively stable over several minutes (Fig. 2B). Changes in the phase shift may occur, however, when a volunteer alters his or her breathing pattern. For example, asking subjects 4 and 9 to take deep breaths near the end of the scans precipitated a nearly 0.5-radian change in their phase shifts.

Phase shift determined from tracking points in 4DMRI images

The phase shift measured between the diaphragm trajectories based on navigator-triggered and bellows-rebinned RC-4DMRI images also revealed that the phase of the bellows waveform leads that of the navigator signal (Fig. 2C, Table 1). Because it collects into bins images at various times throughout the scan, this approach can estimate only an average phase shift. That close agreement between the 4D-imaging and 1D-waveform methods was seen for 6 volunteers indicates that the phase shift is stable in time for these individuals. The discrepancy observed for the other 4 volunteers may stem from breathing irregularities and the fact that the 4D image and 1D signal

were not acquired exactly at the same time, namely the navigator waveforms were not recorded during image acquisition. The 4D-imaging method can accurately estimate the average phase shift only if the shapes of the navigator and bellows waveforms are similar and are stable in time. Pronounced irregularities in the bellows waveform acquired for volunteer 4 led to a relatively flat diaphragm-motion trajectory in the bellows-rebinned 4DMRI image. Owing to these large uncertainties, the cross-correlation analysis yielded an unreliable phase-shift estimate in this subject (Table 1).

Enhanced motion correlation with phase-shift correction

An improved correlation between the internal navigator and external bellows signals after phase-shift correction was found for every subject. On average, the correlation was enhanced from 0.45±0.28 to 0.85±0.15, and to above 0.9 for five subjects (Table 2, Fig. 3B). The improvement appeared to be systematic as an enhanced correlation was found in nearly every time window (Fig. S3). Interestingly, an improved correlation was achieved even in the only time window that all three methods failed.

The time-domain cross-correlation analysis provided comparable values to those obtained by correcting the phase shift (Table 2, Fig. 3B). The maximum TCC and MPS results are in close agreement, except for subjects 4 and 8, the individuals with the largest phase shifts (1.27 and 1.29 radians) and thus the lowest uncorrected correlations (r=0.19 and 0.09). Although correcting their phase shifts effected the greatest relative correlation enhancement, the maximum TCC results suggest that further improvement may be possible for these subjects.

Correcting the phase shift causes the ellipsoidal phase-space trajectory to collapse into a more linear shape, which graphically illustrates the improved correlation (Fig. 3C, Supplemental Video).

The phase-space representation also grants a view into breathing irregularities: Although the positions or orientations of the phase-space trajectories may vary considerably, the phase shift remains stable. The Mann-Whitney U Test revealed that the difference between the original and phase-shift-corrected correlations as well as that between the original correlation and the maximum TCC was statistically significant in all volunteers (Fig. 4A). The phase-shift estimation strategy is also robust: the combined method failed in only a single time window and the success rate exceeded 95% for each of the individual methods (Table S1, Fig. 4B).

DISCUSSION

Based on clinical observations (1, 13, 29), it was reasonable to hypothesize that some patient-specific respiratory features, including the phase shift, may remain invariant over several minutes during a single imaging or treatment session. Correcting the persistent patient-specific phase shift was therefore expected to improve the correlation between the internal and external respiratory motions.

Subject-specific phase shift in phase, time, and image domains

In total, six different methods (POF, PCA, ASA, MPS, maximum TCC, and image-based trajectory), drawn from the phase, time, and image domains, were employed to determine the patient-specific phase shift between concurrent external bellows and internal navigator waveforms. Unlike the maximum TCC method that operates in the time-domain, assessing phase shifts in the phase domain does not require estimates of the breathing frequency. In the image domain, an averaged phase shift can be extracted retrospectively. The close agreement found for the

correlation enhancement among these methods suggests an accurate assessment of the phase shift and accords with the proposition that the phase shift constitutes the primary cause of the original weak correlation.

Phase shifts, which should depend on the nature of the subject's breathing pattern (30) and on the placement of the external bellows (38, 39), were observed in all 10 subjects. The thoracoabdominal movements are initiated by the diaphragm and intercostal muscles. These structures therefore bear on the breathing pattern, which refers to the ratio of thoracic to abdominal involvement during respiration. Even when placed inferior to the xiphoid of the sternum, the bellows may detect the motion of the inferior ribs, resulting in a complex motion pattern. This might explain the large phase shifts found for several volunteers, similar to previous reports (13, 15, 35, 38). Lastly, the MR navigator echo allows us to monitor respiratory motion for 6-15 minutes, a timeframe that is similar in length to radiotherapy treatments and much longer than the 30 to 60-second windows usually employed in fluoroscopic imaging (2, 40).

The subject-specific phase shift is stable and correctable

Two periodic waveforms with differing phases will consistently move in opposite directions at certain times during their cyclical motions. Such a phase shift was recognized as the most critical irregularity for external-internal models (36). We demonstrated that the phase shift is stable in time and that the phase shift—not random irregularities—is the primary cause for the low correlation between the internal and external waveforms (0.45±0.28). Following phase-shift correction, the correlation was significantly improved in all volunteers (0.85±0.16). This finding demonstrates the importance and feasibility of detecting and correcting a dynamic phase shift to establish a robust external-internal motion model for respiratory-gated radiotherapy.

Obtaining similar correlation enhancements through disparate methods provided solid cross verification that the phase shifts were accurately estimated. Because the PCA method performed best (Fig. 4B) and produced results that were nearly identical to those produced by the MPS method (Table 2), it is possible to simplify the phase-shift estimation strategy to employ this single approach. However, the POF and ASA methods yielded greater correlation improvements than the PCA method in several time windows. By incorporating all three estimates, the MPS method is thus equipped to attain greater robustness than any individual method.

The temporal resolution of the phase-shift calculation

The temporal resolution of the phase-shift calculation is approximately equal to the length of the time window, which can reasonably be made as small as 5s. The methods therefore track slow changes in the phase shift well, but lag behind abrupt changes by the length of one time window. The close agreement between the phase shifts estimated by the phase-domain and time-domain methods together with the small number of sharp declines observed in the corrected correlation suggest, however, that rapid changes in the phase shift occur only rarely and that the temporal resolution of the combined method is adequate to track changes in the phase shift.

In the single time window that all three phase-space methods failed, the phase-space trajectory resembles two disparately oriented ovals that, together, cannot be accurately represented by a single ellipse. After subdividing this time window into two parts that each contained only one of these ovals, the combined method succeeded in estimating phase shifts of approximately 1.45 radians, values that are similar to phase shifts found for subsequent time windows. The sudden reorientation of the phase-space trajectory during this time window may reflect an abrupt change in the subject's breathing pattern or in the baseline position of the diaphragm or epigastrium.

Although the phase shift seems unaffected, these changes can result in failure of the phase-shift estimation strategy.

The implication of phase-corrected external surrogate for respiratory gating

In this study of healthy volunteers, the internal motion target is the diaphragm, which can serve only as an internal motion surrogate for a lung or liver tumor. In a future patient study, we can explore the feasibility of placing the internal navigator on a sizable tumor to obtain a direct measurement of the phase shift between the motions of the tumor and bellows. Alternatively, we can employ the super-resolution, time-resolved 4DMRI in a patient study, as it can measure a tumor's motion at a 2-Hertz frame rate (14). To meet various clinical needs, the dynamic MR imaging data can be used to build either a simple phase-shift-corrected respiratory model or a sophisticated physics-based perturbation model that incorporates the movement of the entire torso's surface through optical imaging (41, 42).

Recent reports suggest that patients' breathing irregularities may cause tumor underdosing when the internal tumor volume is used to plan the treatment (40). Guidance for managing clinical motion is therefore urgently needed. Further study of the external-internal motion relationship and tumor-motion monitoring during treatment will thus be critical for improving the accuracy and outcomes of existing therapeutic strategies.

CONCLUSION

Significantly enhanced correlation between the movement of external and internal structures during free breathing has been achieved by correcting a patient-specific phase shift. Three phase-domain methods were developed to dynamically estimate the phase shift and a more robust technique was realized by combining these individual methods. The value of the phase shift tends to be stable over 6 to 15 minutes, and possibly longer, suggesting that the phase shift can be determined and corrected immediately prior to treatment and periodically monitored for changes. Employing the phase-space technique to boost the external-internal motion correlation thus offers a promising strategy for guiding respiratory-gated radiotherapy.

REFERENCES:

1. Seppenwoolde Y, Shirato H, Kitamura K, et al. Precise and real-time measurement of 3D tumor motion in lung due to breathing and heartbeat, measured during radiotherapy. International journal of radiation oncology, biology, physics. 2002;53(4):822-834.
2. Hoisak JD, Sixel KE, Tirona R, et al. Correlation of lung tumor motion with external surrogate indicators of respiration. Int J Radiat Oncol Biol Phys. 2004;60(4):1298-1306.
3. Ozhasoglu C, Murphy MJ. Issues in respiratory motion compensation during external-beam radiotherapy. International journal of radiation oncology, biology, physics. 2002;52(5):1389-1399.
4. Pepin EW, Wu H, Zhang Y, Lord B. Correlation and prediction uncertainties in the cyberknife synchrony respiratory tracking system. Med Phys. 2011;38(7):4036-4044.
5. Kupelian P, Willoughby T, Mahadevan A, et al. Multi-institutional clinical experience with the Calypso System in localization and continuous, real-time monitoring of the prostate gland during external radiotherapy. Int J Radiat Oncol Biol Phys. 2007;67(4):1088-1098.
6. Low DA, Nystrom M, Kalinin E, et al. A method for the reconstruction of four-dimensional synchronized CT scans acquired during free breathing. Medical physics. 2003;30(6):1254-1263.
7. Vedam SS, Keall PJ, Kini VR, et al. Acquiring a four-dimensional computed tomography dataset using an external respiratory signal. Physics in medicine and biology. 2003;48(1):45-62.
8. Ford EC, Mageras GS, Yorke E, Ling CC. Respiration-correlated spiral CT: a method of measuring respiratory-induced anatomic motion for radiation treatment planning. Medical physics. 2003;30(1):88-97.
9. Sonke JJ, Zijp L, Remeijer P, van Herk M. Respiratory correlated cone beam CT. Medical physics. 2005;32(4):1176-1186.
10. Cai J, Chang Z, Wang Z, et al. Four-dimensional magnetic resonance imaging (4D-MRI) using image-based respiratory surrogate: a feasibility study. Med Phys. 2011;38(12):6384-6394.
11. Hu Y, Caruthers SD, Low DA, et al. Respiratory amplitude guided 4-dimensional magnetic resonance imaging. Int J Radiat Oncol Biol Phys. 2013;86(1):198-204.
12. Kauczor HU, Plathow C. Imaging tumour motion for radiotherapy planning using MRI. Cancer Imaging. 2006;6:S140-144.
13. Li G, Wei J, Olek D, et al. Direct Comparison of Respiration-Correlated Four-Dimensional Magnetic Resonance Imaging Reconstructed Using Concurrent Internal Navigator and External Bellows. Int J Radiat Oncol Biol Phys. 2017;97(3):596-605.
14. Li G, Wei J, Kadbi M, et al. Novel Super-Resolution Approach to Time-Resolved Volumetric 4-Dimensional Magnetic Resonance Imaging With High Spatiotemporal Resolution for Multi-Breathing Cycle Motion Assessment. Int J Radiat Oncol Biol Phys. 2017;98(2):454-462.
15. Keall PJ, Mageras GS, Balter JM, et al. The management of respiratory motion in radiation oncology report of AAPM Task Group 76. Med Phys. 2006;33(10):3874-3900.
16. Li G, Mageras G, Dong L, Mohan R. Image-guided radiation therapy. In: Khan FM, Gerbi BJ, editors. Treatment Planning in Radiation Oncology. 4th Edition ed. Philadelphia, PA: Lippincott Williams & Wilkins; 2016. p. 229-258.
17. Kerkmeijer LG, Fuller CD, Verkooijen HM, et al. The MRI-Linear Accelerator Consortium: Evidence-Based Clinical Introduction of an Innovation in Radiation Oncology Connecting Researchers, Methodology, Data Collection, Quality Assurance, and Technical Development. Front Oncol. 2016;6:215.

18. Yamamoto T, Langner U, Loo BW, Jr., et al. Retrospective analysis of artifacts in four-dimensional CT images of 50 abdominal and thoracic radiotherapy patients. Int J Radiat Oncol Biol Phys. 2008;72(4):1250-1258.
19. Watkins WT, Li R, Lewis J, et al. Patient-specific motion artifacts in 4DCT. Med Phys. 2010;37(6):2855-2861.
20. Persson GF, Nygaard DE, Af Rosenschold PM, et al. Artifacts in conventional computed tomography (CT) and free breathing four-dimensional CT induce uncertainty in gross tumor volume determination. Int J Radiat Oncol Biol Phys. 2011;80(5):1573-1580.
21. Li G, Cohen P, Xie H, et al. A novel four-dimensional radiotherapy planning strategy from a tumor-tracking beam's eye view. Phys Med Biol. 2012;57(22):7579-7598.
22. Fayad H, Pan T, Clement JF, Visvikis D. Technical note: Correlation of respiratory motion between external patient surface and internal anatomical landmarks. Medical physics. 2011;38(6):3157-3164.
23. Korreman SS, Juhler-Nottrup T, Boyer AL. Respiratory gated beam delivery cannot facilitate margin reduction, unless combined with respiratory correlated image guidance. Radiother Oncol. 2008;86(1):61-68.
24. Ionascu D, Jiang SB, Nishioka S, et al. Internal-external correlation investigations of respiratory induced motion of lung tumors. Med Phys. 2007;34(10):3893-3903.
25. Seppenwoolde Y, Berbeco RI, Nishioka S, et al. Accuracy of tumor motion compensation algorithm from a robotic respiratory tracking system: a simulation study. Med Phys. 2007;34(7):2774-2784.
26. Hoogeman M, Prevost JB, Nuyttens J, et al. Clinical accuracy of the respiratory tumor tracking system of the cyberknife: assessment by analysis of log files. Int J Radiat Oncol Biol Phys. 2009;74(1):297-303.
27. Malinowski K, McAvoy TJ, George R, et al. Incidence of changes in respiration-induced tumor motion and its relationship with respiratory surrogates during individual treatment fractions. Int J Radiat Oncol Biol Phys. 2012;82(5):1665-1673.
28. Nishioka T, Nishioka S, Kawahara M, et al. Synchronous monitoring of external/internal respiratory motion: validity of respiration-gated radiotherapy for liver tumors. Jpn J Radiol. 2009;27(7):285-289.
29. Low DA, Parikh PJ, Lu W, et al. Novel breathing motion model for radiotherapy. Int j radiat oncol biol phys. 2005;63(3):921-929.
30. Yuan A, Wei J, Gaebler CP, et al. A novel respiratory motion perturbation model adaptable to patient breathing irregularities. Int J Radiat Oncol Biol Phys. 2016;96(5):1087-1096.
31. Ackerley EJ, Cavan AE, Wilson PL, et al. Application of a spring-dashpot system to clinical lung tumor motion data. Med Phys. 2013;40(2):021713.
32. Seregni M, Cerveri P, Riboldi M, et al. Robustness of external/internal correlation models for real-time tumor tracking to breathing motion variations. Phys Med Biol. 2012;57(21):7053-7074.
33. Li HH, Rodriguez VL, Green OL, et al. Patient-Specific Quality Assurance for the Delivery of Co Intensity Modulated Radiation Therapy Subject to a 0.35-T Lateral Magnetic Field. Int J Radiat Oncol Biol Phys. 2014.
34. McPartlin AJ, Li XA, Kershaw LE, et al. MRI-guided prostate adaptive radiotherapy - A systematic review. Radiother Oncol. 2016.
35. Mukumoto N, Nakamura M, Sawada A, et al. Accuracy verification of infrared marker-based dynamic tumor-tracking irradiation using the gimbaled x-ray head of the Vero4DRT (MHI-TM2000). Med Phys. 2013;40(4):041706.

36. Seregni M, Kaderka R, Fattori G, et al. Tumor tracking based on correlation models in scanned ion beam therapy: an experimental study. Phys Med Biol. 2013;58(13):4659-4678.
37. Li R, Mok E, Han B, et al. Evaluation of the geometric accuracy of surrogate-based gated VMAT using intrafraction kilovoltage x-ray images. Med Phys. 2012;39(5):2686-2693.
38. Cai J, Chang Z, O'Daniel J, et al. Investigation of sliced body volume (SBV) as respiratory surrogate. J Appl Clin Med Phys. 2013;14(1):3987.
39. Li G, Arora NC, Xie H, et al. Quantitative prediction of respiratory tidal volume based on the external torso volume change: a potential volumetric surrogate. Phys Med Biol. 2009;54(7):1963-1978.
40. Dhont J, Vandemeulebroucke J, Burghelea M, et al. The long- and short-term variability of breathing induced tumor motion in lung and liver over the course of a radiotherapy treatment. Radiother Oncol. 2017;126:in press.
41. Li G, Huang H, Wei J, et al. Novel spirometry based on optical surface imaging. Med Phys. 2015;42(4):1690.
42. Li G, Wei J, Huang H, et al. Characterization of optical-surface-imaging-based spirometry for respiratory surrogating in radiotherapy. Med Phys. 2016;43(3):1348.

FIGURES:

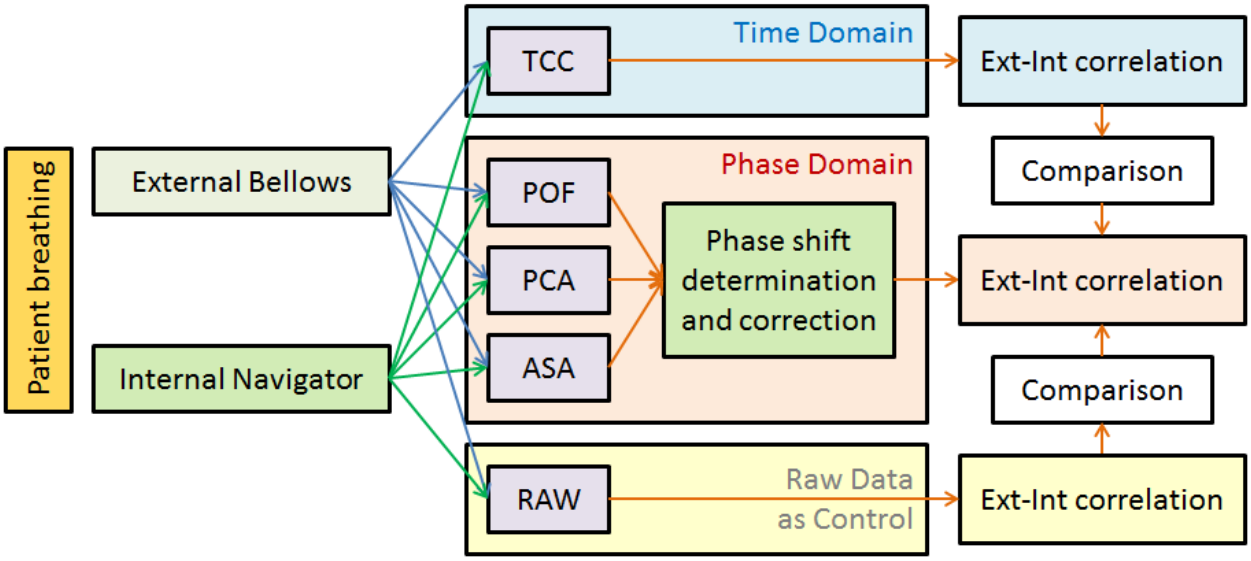

Figure 1. Workflow for determining and correcting the phase shift to enhance the correlation between the internal and external waveforms. Three quantitative phase-domain methods were applied, including phase-space oval fitting (POF), principal component analysis (PCA), and analytic signal analysis (ASA). The correlation between the phase-shift corrected external and internal waveforms was compared to the original correlation and to the waveforms' maximum time-domain cross-correlation (TCC).

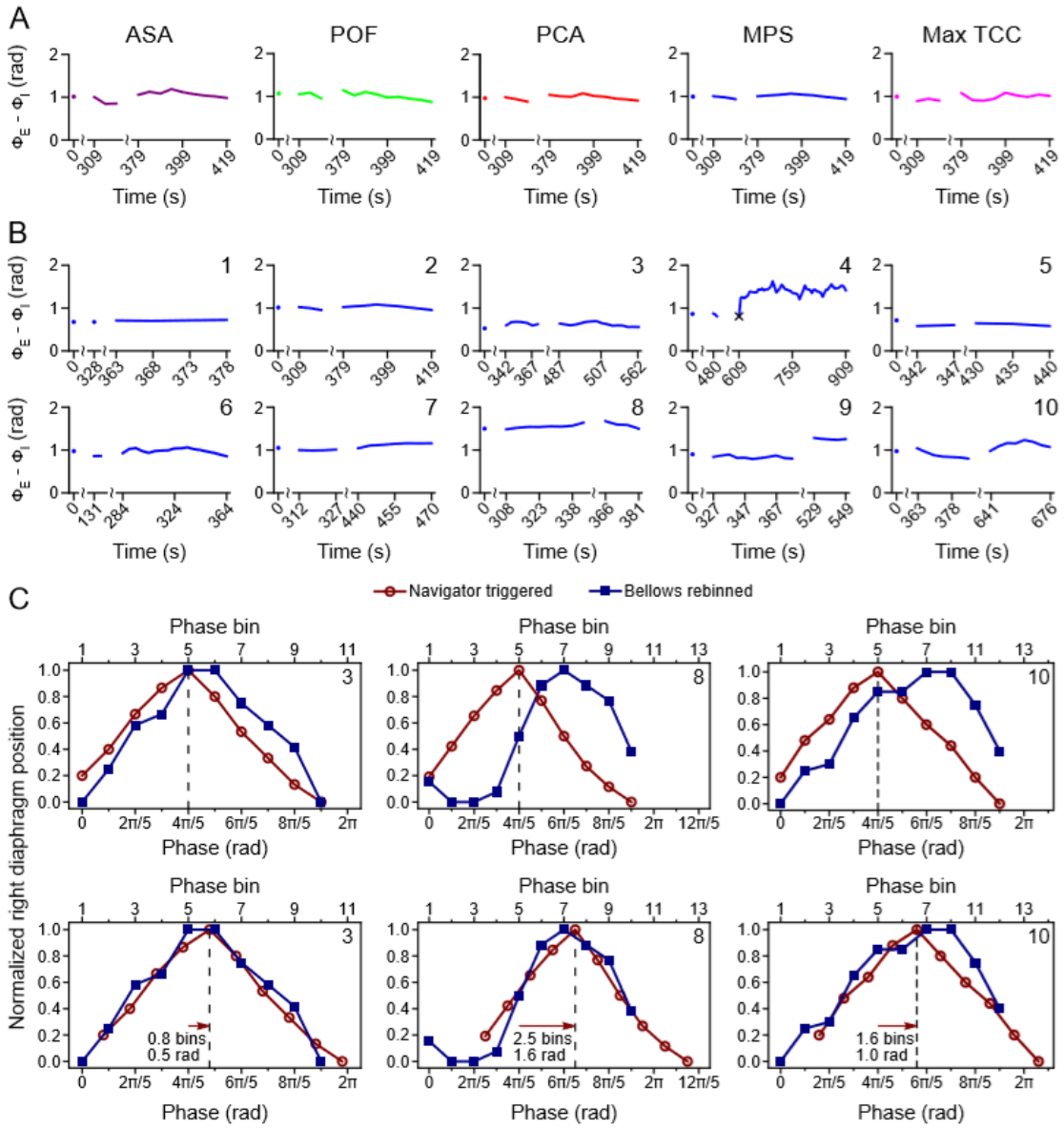

Figure 2. Volunteer-specific phase shifts determined by six methods. (A) Phase shift over time for volunteer 2 calculated every 5s using the analytic signal analysis (purple), phase space oval-fitting (red), principal component analysis (green), combined mean phase shift (blue), or maximum time-domain cross-correlation (magenta) method. (B) Phase shifts over time for 10 volunteers calculated using the combined method. The × in the panel for volunteer 4 indicates the single time point across all volunteers at which the combined method failed. (C) Representative phase shifts estimated from measured diaphragm motions. Trajectories were obtained from navigator-triggered (dark-red circles) and bellows-rebinned (dark-blue squares) 4DMRI images before (upper panels) and after (lower panels) phase alignment for subjects 3 (left), 8 (middle), and 10 (right). The dark-red arrows indicate the estimated phase shift.

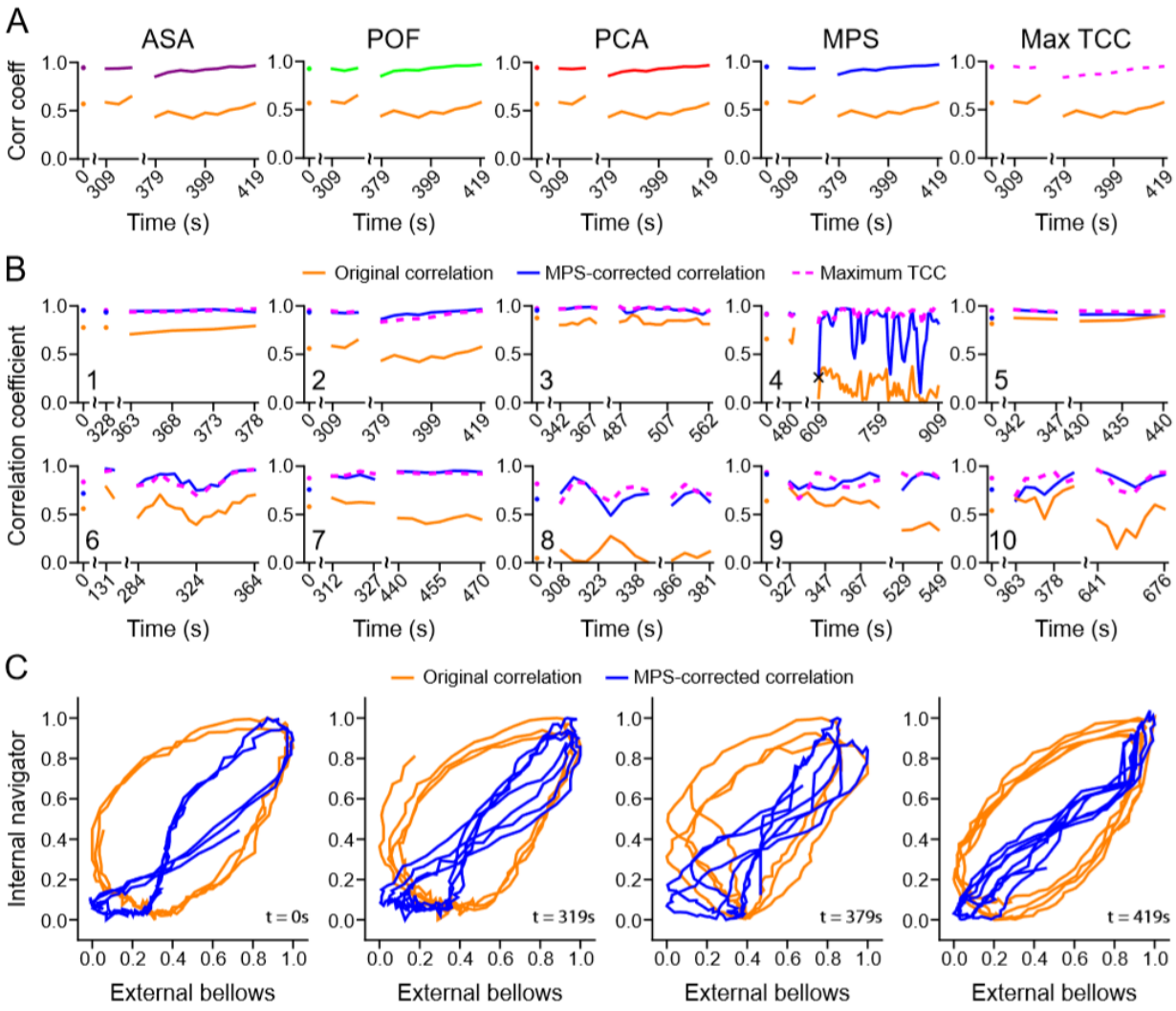

Figure 3. Correlation enhancement via phase-shift correction calculated every 5s. (A) Correlation over time between the internal-navigator and external-bellows signals for subject 2 before (orange) and after phase-shift correction using the ASA (purple), POF (red), PCA (green), MPS (blue) and maximum TCC (dashed, magenta) methods. (B) Correlation enhancement over time for all subjects using the MPS method (blue). The cross-correlation is also shown for comparison (dashed, magenta). (C) Phase-shift correction causes the phase-space oval (orange) to collapse (blue) for subject 2, providing a visual indication of the improved correlation. The enhanced correlation is stable (B2) despite breathing irregularities (C, Supplemental Video).

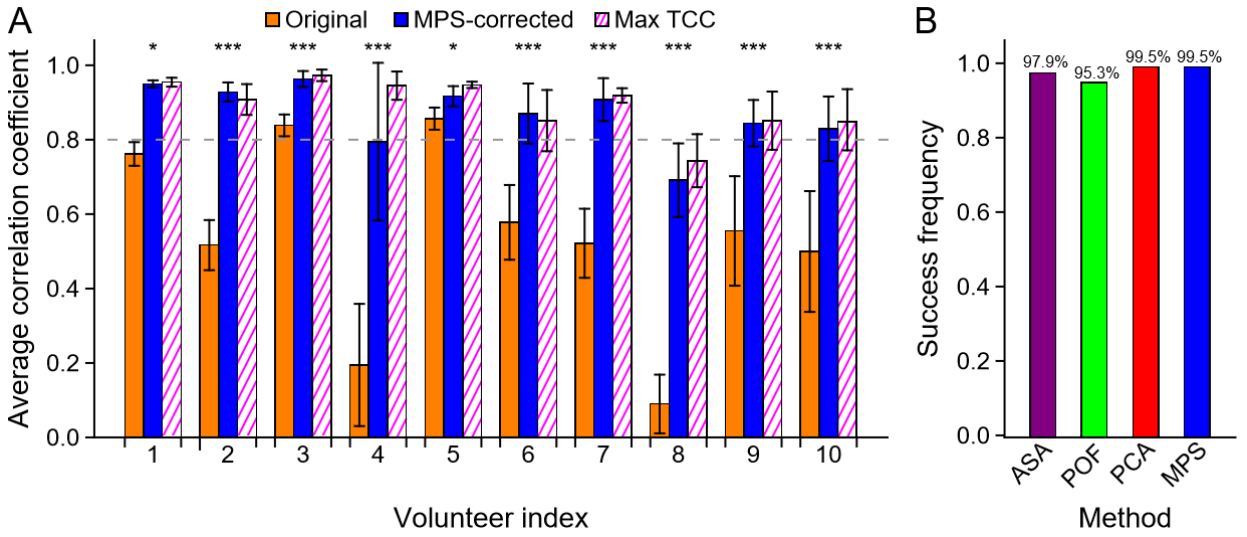

Figure 4. (A) Correlation coefficient averaged across all time points before (orange) and after (blue) phase-shift correction, together with the average maximum TCC value (striped, magenta). Phase-shift correction yields a statistically-significant enhancement of the correlation in all subjects (* $p<0.05$, *** $p<0.005$, Mann-Whitney U Test). The error bars represent one standard deviation. (B) Robustness (99.5% success rate) of the combined phase-domain method compared to the individual methods.

TABLES

Table 1. Phase shifts (mean±standard deviation in radians) estimated in the phase, time, and image domains[†]

Volunteer	ASA	POF	PCA	MPS	Max TCC	Image
1	0.65 ± 0.03	0.83 ± 0.04	0.65 ± 0.02	0.70 ± 0.02	0.68 ± 0.06	0.6
2	1.03 ± 0.10	1.03 ± 0.08	0.99 ± 0.05	1.02 ± 0.04	0.98 ± 0.07	1.0
3	0.52 ± 0.06	0.84 ± 0.12	0.59 ± 0.06	0.62 ± 0.05	0.60 ± 0.05	0.5
4	1.31 ± 0.22	1.47 ± 0.17	1.34 ± 0.19	1.37 ± 0.17	1.27 ± 0.19	--*
5	0.49 ± 0.09	0.73 ± 0.14	0.59 ± 0.10	0.62 ± 0.05	0.48 ± 0.07	0.3
6	0.91 ± 0.20	1.05 ± 0.10	0.87 ± 0.11	0.97 ± 0.06	0.67 ± 0.17	0.8
7	1.05 ± 0.17	1.13 ± 0.06	1.08 ± 0.11	1.08 ± 0.07	0.97 ± 0.18	0.4
8	1.50 ± 0.32	1.54 ± 0.06	1.63 ± 0.10	1.56 ± 0.06	1.29 ± 0.42	1.6
9	0.84 ± 0.25	1.12 ± 0.15	0.97 ± 0.19	0.96 ± 0.20	0.86 ± 0.21	0.7
10	1.05 ± 0.15	1.11 ± 0.26	0.89 ± 0.19	1.01 ± 0.14	0.72 ± 0.13	1.0
Mean[#]	0.93 ± 0.33	1.08 ± 0.26	0.96 ± 0.33	0.99 ± 0.30	0.85 ± 0.27	0.77

[†] Analytic signal analysis (ASA); phase-space oval fitting (POF); principal component analysis (PCA); mean phase shift (MPS); and time-domain cross-correlation (TCC).
[#] Averaged over all volunteers' mean phase shifts.
* Severe breathing irregularities make the peak of the bellows waveform difficult to discern.

Table 2. Correlation (mean±standard deviation) before and after phase-shift correction[†]

Volunteer	Original	ASA	POF	PCA	MPS	Max TCC
1	0.76 ± 0.03	0.95 ± 0.01	0.93 ± 0.02	0.95 ± 0.01	0.95 ± 0.01	0.95 ± 0.01
2	0.52 ± 0.07	0.93 ± 0.03	0.92 ± 0.03	0.93 ± 0.03	0.93 ± 0.03	0.91 ± 0.04
3	0.84 ± 0.03	0.97 ± 0.02	0.92 ± 0.04	0.97 ± 0.02	0.96 ± 0.02	0.97 ± 0.02
4	0.19 ± 0.16	0.75 ± 0.20	0.80 ± 0.17	0.80 ± 0.19	0.78 ± 0.21	0.93 ± 0.04
5	0.86 ± 0.03	0.93 ± 0.03	0.88 ± 0.05	0.92 ± 0.03	0.92 ± 0.03	0.95 ± 0.01
6	0.58 ± 0.10	0.86 ± 0.11	0.86 ± 0.09	0.88 ± 0.08	0.87 ± 0.08	0.85 ± 0.08
7	0.52 ± 0.09	0.91 ± 0.05	0.89 ± 0.07	0.91 ± 0.06	0.91 ± 0.06	0.92 ± 0.02
8	0.09 ± 0.08	0.69 ± 0.10	0.69 ± 0.10	0.69 ± 0.10	0.69 ± 0.10	0.74 ± 0.07
9	0.56 ± 0.14	0.86 ± 0.06	0.83 ± 0.07	0.85 ± 0.07	0.84 ± 0.06	0.85 ± 0.08
10	0.52 ± 0.18	0.75 ± 0.16	0.81 ± 0.11	0.85 ± 0.07	0.83 ± 0.09	0.85 ± 0.08
Mean[#]	0.45 ± 0.28	0.83 ± 0.16	0.84 ± 0.14	0.85 ± 0.14	0.85 ± 0.15	0.90 ± 0.08

[†] Analytic signal analysis (ASA); phase-space oval fitting (POF); principal component analysis (PCA); mean phase shift (MPS); and time-domain cross-correlation (TCC).
[#] Averaged over all 192 time windows

APPENDIX A: Phase-space methods for determining phase shifts

A1 Phase-Space Oval Fitting (POF): The phase shift between the two concurrent waveforms was found from the oval that best fits the data in a 2D phase space [bellows: $\boldsymbol{x(t)}$ and navigator: $\boldsymbol{y(t)}$] (Fig. S1A). In this space, an ellipse centered at (0,0) is described by

$$\boldsymbol{c_1x^2 + c_2xy + c_3y^2 = \frac{(x\cos\theta + y\sin\theta)^2}{a^2} + \frac{(y\cos\theta - x\sin\theta)^2}{b^2} = 1,} \qquad \boldsymbol{(1\ or\ A1)}$$

where $\boldsymbol{a}$ and $\boldsymbol{b}$ are the major and minor half-axis lengths and $\boldsymbol{\theta}$ is the angle by which the major axis is tilted clockwise from the positive $\boldsymbol{x}$-axis. Equating the coefficients of the $\boldsymbol{x^2}$, $\boldsymbol{xy}$, and $\boldsymbol{y^2}$ terms in Eq. A1 yields:

$$\boldsymbol{\theta = \frac{1}{2}\tan^{-1}\left(\frac{c_2}{c_1 - c_3}\right),\ a = \sqrt{\frac{\cos(2\theta)\sin^2(\theta)}{c_1\cos(2\theta) - \cos^2(\theta)\left((c_1+c_3)\cos^2(\theta) - c_1\right)}},\ b = \sqrt{\frac{\cos(2\theta)}{(c_1+c_3)\cos^2(\theta) - c_1}}}$$

The linear least squares method was used to fit the ellipse to the data to obtain the coefficients $\{\boldsymbol{c_1, c_2, c_3}\}$:

$$\begin{bmatrix} x_1^2 & x_1y_1 & y_1^2 \\ x_2^2 & x_2y_2 & y_2^2 \\ x_3^2 & x_3y_3 & y_3^2 \end{bmatrix} \begin{bmatrix} c_1 \\ c_2 \\ c_3 \end{bmatrix} = \begin{bmatrix} 1 \\ 1 \\ 1 \end{bmatrix} \rightarrow \boldsymbol{M\vec{c} = \vec{v}} \rightarrow \boldsymbol{\vec{c} \approx (MM^T)^{-1}M^T\vec{v}}. \qquad \boldsymbol{(A2)}$$

For simplicity, we modeled the waveforms as two sinusoidal functions $\boldsymbol{x(t) = r_1\cos(\omega_1 t)}$ and $\boldsymbol{y(t) = r_2\cos(\omega_2 t + \phi)}$ with phase shift $\boldsymbol{\phi}$ and assuming $\boldsymbol{\omega_1 = \omega_2 = \omega}$. The trajectory $\{\boldsymbol{r_1\cos(\alpha), r_2\cos(\alpha + \phi)}\}$, in which $\boldsymbol{\phi \neq 0}$ is the phase shift between the two signals, describes an ellipse in phase space**.** The distance from this ellipse to the phase-space origin at some value $\boldsymbol{\alpha = \omega t}$ is given by:

$$\boldsymbol{r_1^2\cos^2(\alpha) + r_2^2\cos^2(\alpha + \phi)}$$

$$\boldsymbol{= \frac{1}{4}\left[r_1^2(e^{2i\alpha} + 2 + e^{-2i\alpha}) + r_2^2\left(e^{2i(\alpha+\phi)} + 2 + e^{-2i(\alpha+\phi)}\right)\right]} \qquad \boldsymbol{(A3)}$$

This expression takes its extreme values at:

$$\boldsymbol{\alpha_k = \frac{1}{4i}\ln\left[\frac{r_1^2 + r_2^2 e^{-2i\phi}}{r_1^2 + r_2^2 e^{2i\phi}}\right] - \frac{\pi}{2}k,\ \ k \in \mathbb{Z}\,.} \qquad (\boldsymbol{A4})$$

At $\boldsymbol{\alpha_0}$, when $\boldsymbol{k = 0}$, the distance from the ellipse to the origin in phase space is maximized, while at $\boldsymbol{\alpha_1}$ the distance is minimized. At these two points on the ellipse we have:

550 **1**). $\boldsymbol{r_1 \cos(\alpha_0) = a\cos(\theta)}$, **2**). $\boldsymbol{r_2 \cos(\alpha_0 + \phi) = a\sin(\theta)}$,

3). $\boldsymbol{r_1 \cos(\alpha_0 - \pi/2) = -b\sin(\theta)}$, **4**). $\boldsymbol{r_2 \cos(\alpha_0 + \phi - \pi/2) = b\cos(\theta)}$,

where $\boldsymbol{a}$ and $\boldsymbol{b}$ are half the length of the major and minor axes of the ellipse, respectively, and $\boldsymbol{\theta}$ is the clockwise tilt of the ellipse with respect to the positive $\boldsymbol{x}$-axis. Solving this system of equations yields the phase shift between the two waveforms as well as the amplitude of each:

555 $$\boldsymbol{\phi = \tan^{-1}\left[\frac{ab\sec\theta}{(a^2-b^2)\sin\theta}\right],\ r_1 = \sin\theta\sqrt{a^2 + b^2\cot^2\theta},\ r_2 = \cos\theta\sqrt{a^2 + b^2\tan^2\theta}}.\ (\boldsymbol{A5})$$

Any given phase-space ellipse corresponds to two possible phase shifts: clockwise traversal around the ellipse occurs if the phase of the bellows leads that of the navigator, whereas the converse is true for counter-clockwise trajectories. The temporal order of the points in phase space was therefore employed to orient the ellipse. Finally, the residual error (***RE***) in the best-

560 fit ellipse was quantified by calculating the average distance between a data point and the best-fit ellipse. Let $\boldsymbol{d_j(\alpha_j)}$ give the distance from the data point $\boldsymbol{\{x_j, y_j\}}$ to the point on the ellipse $\boldsymbol{\{r_1\cos(\alpha_j), r_2\cos(\alpha_j + \phi)\}}$. Then the residual error is:

$$\boldsymbol{\frac{1}{n}\sum_{j=1}^{n}\min_{\alpha_j} d_j(\alpha_j) = \frac{1}{n}\sum_{j=1}^{n}\min_{\alpha_j}\sqrt{(x_j - r_1\cos(\alpha_j))^2 + (y_j - r_2\cos(\alpha_j + \phi))^2}}\,. \quad (\boldsymbol{A6})$$

In the above expression, $\boldsymbol{n}$ is the number of data points in the window and is given by the

565 duration of the window times the 20-Hertz sampling frequency. The minimization with respect to $\boldsymbol{\alpha_j}$ is accomplished by differentiating $\boldsymbol{d_j}$ with respect to $\boldsymbol{\alpha_j}$ and setting the result equal to 0. Rearranging and letting $\boldsymbol{z_j = e^{i\alpha_j}}$ produces the following quartic:

$$z_j^4\left(r_1^2 + r_2^2 e^{2i\phi}\right) - 2z_j^3\left(r_1 x_j + r_2 y_j e^{i\phi}\right) + 2z_j\left(r_1 x_j + r_2 y_j e^{-i\phi}\right) - \left(r_1^2 + r_2^2 e^{-2i\phi}\right) = 0. \quad (A7)$$

This equation has four solutions, call them $\{z_j^*\}$, and the argument of each, $\alpha_j^* = \arg z_j^* = -i \ln z_j^*$, must be plugged into $d_j(\alpha_j)$ to determine which minimizes the distance between the data point $\{x_j, y_j\}$ and the best-fit ellipse.

A2 Principal Component Analysis (PCA): A $2 \times n$ matrix $A =$ [bellows: $x(t)$, navigator: $y(t)$] was constructed from the two concurrent waveforms and the covariance matrix for this dataset was formed by the multiplication $AA^T/(n-1)$. The principal components, $\vec{p}_1$ and $\vec{p}_2$, were given by the eigenvectors of the covariance matrix. The square roots of the eigenvalues, $\sqrt{\lambda_1}$ and $\sqrt{\lambda_2}$, represented the standard deviation in the dataset in the directions of the principal component vectors. An ellipse was then constructed with major and minor axes pointing in the directions of $\vec{p}_1$ and $\vec{p}_2$ and with half lengths $a = \sqrt{\lambda_1}$ and $b = \sqrt{\lambda_2}$, respectively (Fig. S1A). The tilt angle of the ellipse was given by $\theta = \tan^{-1}\left[\vec{p}_{1,y}/\vec{p}_{1,x}\right]$ and the phase shift ϕ by Eq. A5. As above, the temporal order of the data points in phase space sets the sense of the ellipse's orientation.

Because $\sqrt{\lambda_1}$ and $\sqrt{\lambda_2}$ give only the relative sizes of a and b and not their absolute values, a scaling factor f was introduced into the RE calculation to resize the calculated ellipse to match the dimensions of the data. The RE can be expressed as

$$RE = \min_f \left[\frac{1}{n} \sum_{j=1}^{n} \min_{\alpha_j} \sqrt{\left[x_j - f r_1 \cos(\alpha_j)\right]^2 + \left[y_j - f r_2 \cos(\alpha_j + \phi)\right]^2} \right], \quad (A8)$$

where minimizations were performed over the parameters f and α_j.

APPENDIX B: Numerical simulation and analysis of the phase-shift calculation methods

Gaussian noise was added to the amplitudes and phases of two cosine waves that possessed equal oscillation frequencies and amplitudes but differed in phase by one radian. For high to moderate signal-to-noise-ratio (SNR) values, the analytic signal analysis (ASA), phase-space oval fitting (POF), and principal component analysis (PCA) methods yielded accurate estimates of the phase shift (Fig. S1C). At lower SNR levels the ASA method becomes least reliable while the PCA method remains the most robust. Because it requires that the data points are ordered in time, the ASA method is expected to be more sensitive to noise than the other two methods. As the simulated noise level approaches zero, the error in the ASA and POF methods' estimates decreases linearly, whereas the PCA method's estimate levels off, approaching a small lower bound (<3%). Because the density of data points in phase space is greater at the poles of the ellipse, the PCA method slightly underestimates the magnitude of the oval's minor axis relative to that of the major axis, which in turn introduces a small error into the phase-shift estimate.

Numerical simulations reveal strong correlations between the error in the phase-shift estimate and the fit residual for the phase-space ellipses constructed using each method: $r = 0.74$, 0.96, and 0.86 for the ASA, POF, and PCA methods, respectively (Fig. S1D). Based on these correlations, the ellipse-fit residuals were used to estimate a method's accuracy. The best-fit curves in doubly logarithmic space demonstrate that setting an upper bound of 0.2 on the ellipse-fit residual limits the phase-shift error to approximately 30% (Fig. S1D). Residual values beyond this threshold were therefore chosen to indicate a method's failure when applied to data obtained from the volunteers. Because the waveforms obtained from the ten volunteers contain multiple frequency components, residual values for ovals that are fit to these data sets will reach 0.2 at higher SNRs than for simple sinusoidal waves. The threshold residual value of 0.2 therefore limits the error in any method's estimation of the phase shift more conservatively than is suggested by the simulation results.

SUPPLEMENT

Table S1. 4DMRI scan durations and analysis parameters

Volunteer index	Gender	Scan length min′ sec″	# of time windows[†] (early, middle, late)	Total time analyzed (s)	# of method failures (ASA,POF,PCA,MPS)[$]
1	♀	6′ 33″	1,1,4	38.4	0,0,0,0
2	♂	6′ 51″	1,3,9	74.3	0,0,0,0
3	♂	9′ 23″	1,7,16	130.7	0,3,0,0
4	♂	14′ 44″	1,3,61	340.8	3,4,1,1
5	♀	8′ 51″	1,2,3	38.4	0,0,0,0
6	♀	5′ 20″	1,2,17	110.2	1,0,0,0
7	♂	8′ 10″	1,4,7	69.2	0,0,0,0
8	♀	6′ 33″	1,8,4	74.3	0,0,0,0
9	♂	9′ 43″	1,11,5	94.8	0,2,0,0
10	♀	11′ 04″	1,7,8	89.7	0,0,0,0

[†] There are 192 time windows in total and each contains 10 or 12.5 seconds.

[$] Analytic signal analysis (ASA); phase-space oval fitting (POF); principal component analysis (PCA); mean phase shift following the elimination of individual method outliers (MPS)

615

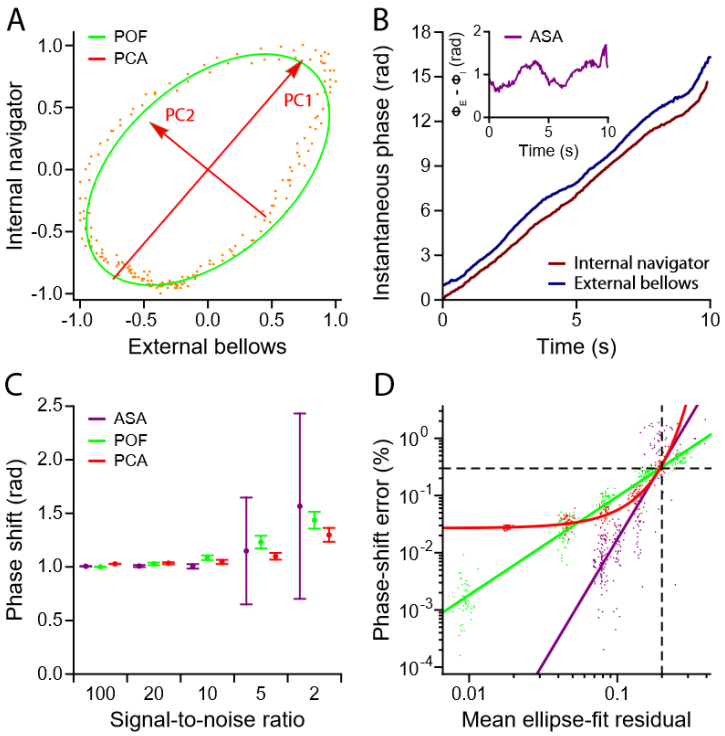

620 **Figure S1**. Methods for estimating the phase shift between the external bellows and internal navigator signals. (A) Representative ellipse and principal components found for volunteer 2 through the phase-space oval-fitting (POF) and principal component analysis (PCA) methods, respectively. (B) Representative instantaneous phases of and the phase shift between (inset) the internal and external waveforms calculated for volunteer 2 using the analytic signal analysis (ASA) 625 method. (C) Dependence of the phase-shift estimation methods on the signal-to-noise ratio for simulated waveforms. As the Gaussian noise level increases relative to the amplitude of the simulated waveforms, the methods' accuracy in estimating the 1-radian phase shift between the two sinusoids diminishes. Each point represents the average of 50 trials and error bars indicate one standard deviation. (D) Numerical simulations also reveal that the ASA (purple), POF (green), and 630 PCA (red) methods are less accurate when the phase-space ellipses constructed from each bear a large mean residual (***RE***). Residuals were averaged over the simulated data points in a trial. Each dot represents a single trial and every cloud of dots corresponds to one of the signal-to-noise levels depicted in panel C. The curves that best fit the ASA, POF, and PCA points in doubly logarithmic space are $2.60 + 4.35x$, $0.71 + 1.72x$, and $20.38 \times 10^{1.81x} - 1.57$, respectively. The 635 intersection of the three curves approximately occurs at a residual of 0.2 and a phase-shift error of 30%. A mean residual of 0.2 or greater was chosen to indicate a method's failure when applied to the data sets obtained from human volunteers.

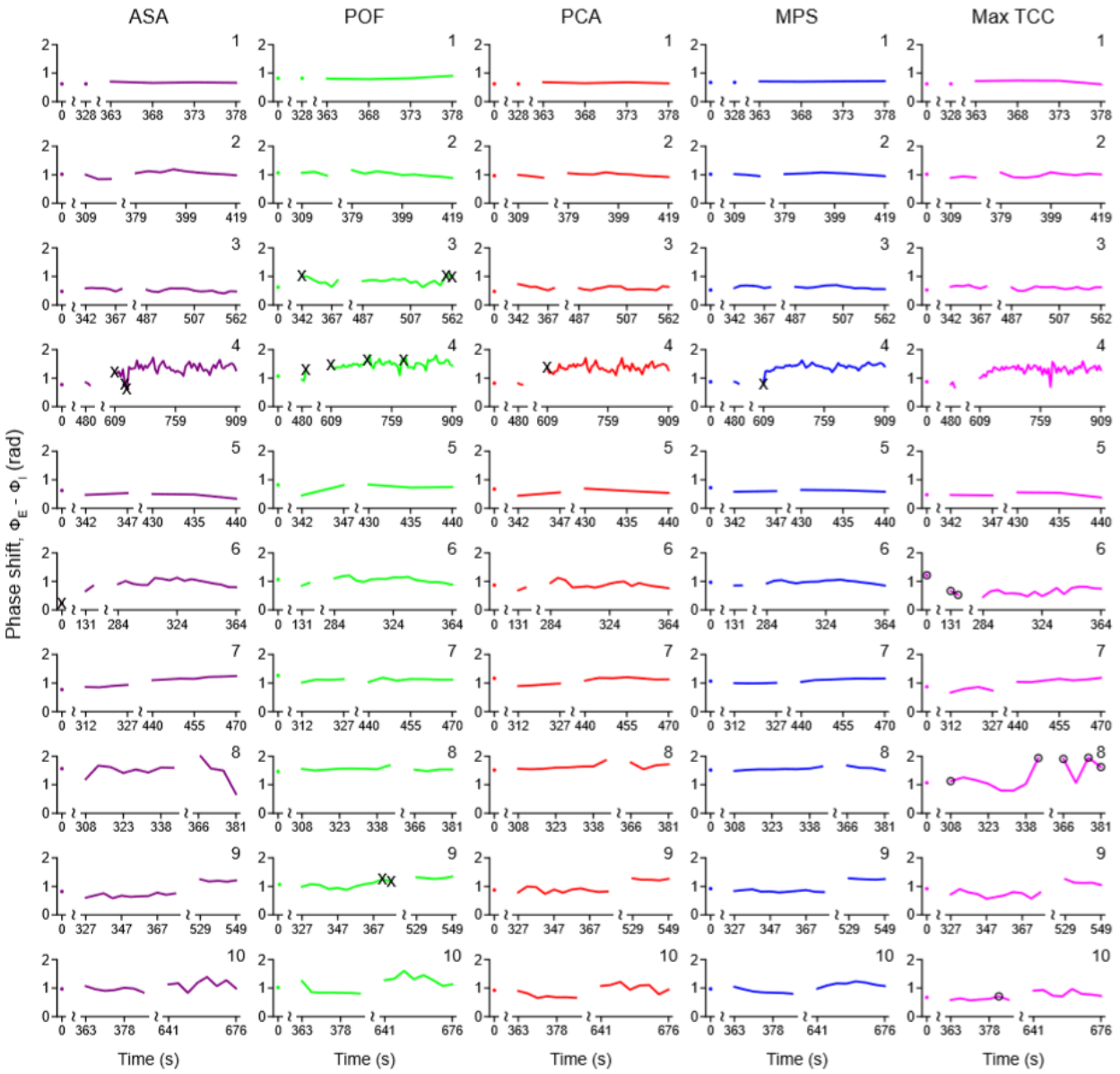

Figure S2. Phase shifts estimated by the analytic signal analysis (ASA, purple), phase-space oval fitting (POF, green), principal component analysis (PCA, red), combined (MPS, blue), and maximum time-domain cross-correlation (TCC, magenta) methods. The × symbols indicate time points at which a method failed; these phase-shift estimates were excluded from the combined method calculation. The ○ symbols indicate time points at which the standard deviation among the four frequency estimates exceeded 0.05Hz. The frequency estimate that maximized the phase-shift-corrected correlation was employed at each time point. The volunteer's index labels the top-right corner of each panel. The phase of the external bellows was found to lead that of the internal navigator at all time points in every volunteer.

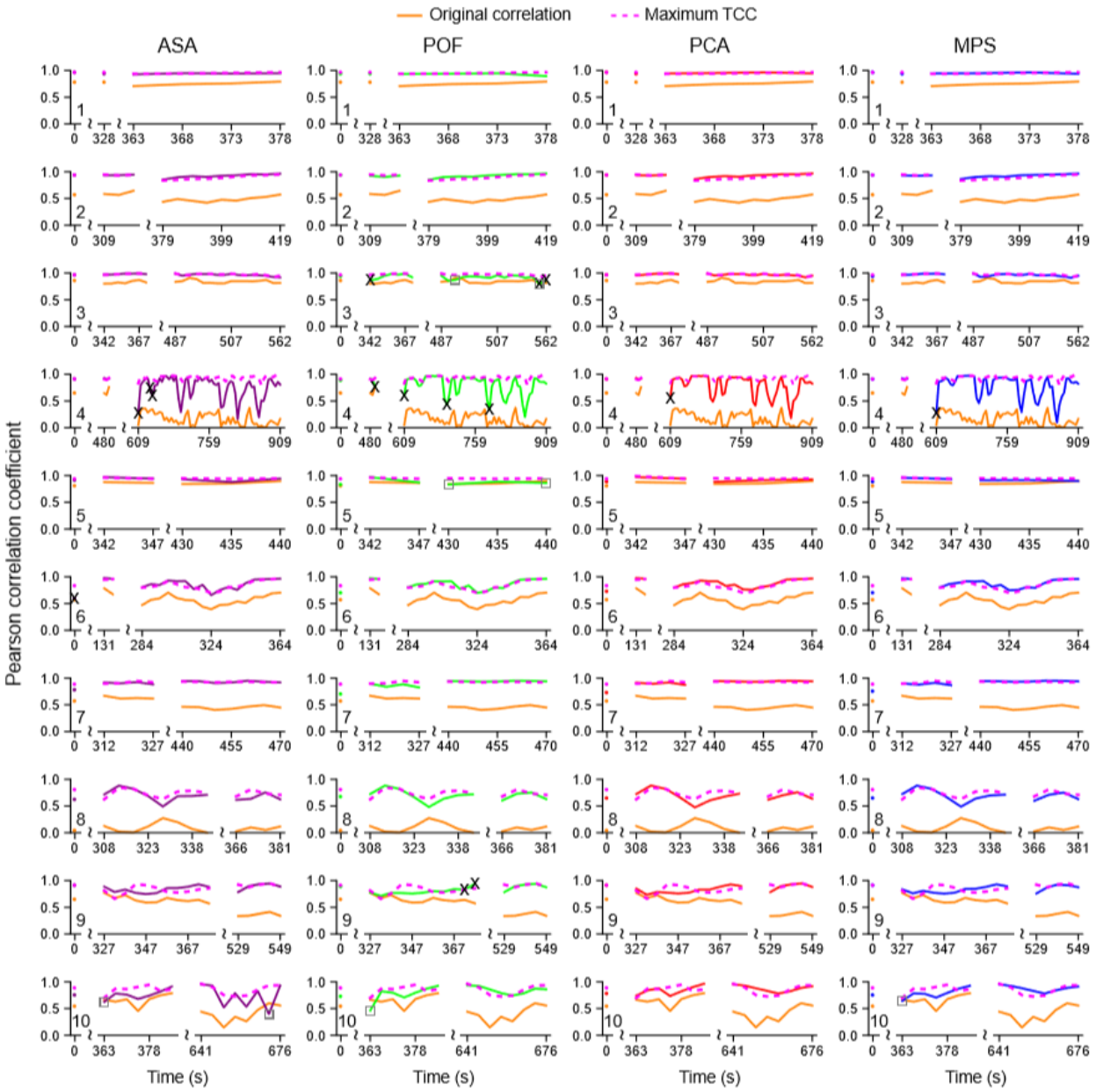

Figure S3. Correlation enhancement following phase-shift correction using the analytic signal analysis (ASA, purple), phase-space oval fitting (POF, green), principal component analysis (PCA, red), and combined (MPS, blue) phase-shift estimates. The original correlation between the uncorrected waveforms (orange) and the maximum time-domain cross-correlation (TCC, dashed magenta) are shown for comparison in each panel. The × symbols indicate time points at which a method failed. The volunteer's index labels the bottom-left corner of each panel. The gray boxes mark the 2, 5, and 1 points at which correcting the phase shift calculated by the ASA, POF, and MPS methods, respectively, failed to enhance the correlation. The correlation was enhanced in all time windows for the PCA method.

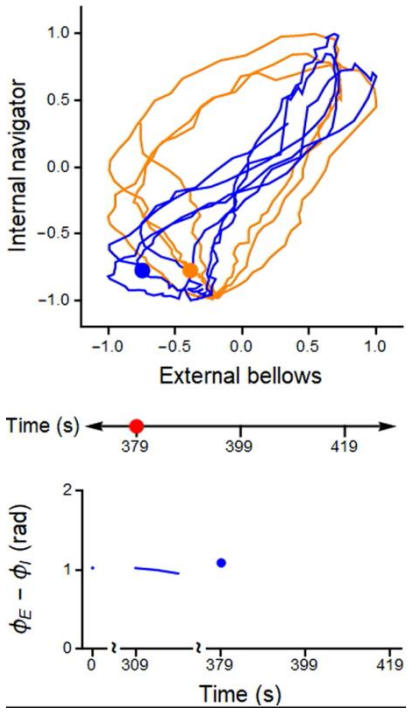

Supplemental Video. Correcting the phase shift estimated by the MPS method effects a collapse of the original phase-space ellipse (orange) into a more linear trajectory (blue). The red dot tracks the progression of time and the blue dot in the lower panel gives the estimated phase shift for the dataset shown at the same time in the upper panel. Each frame of the movie represents 0.5s of real time, which constitutes the amount of time by which the 12.5-second time window was shifted to generate each point in the phase-shift curve (the window was instead shifted by 5s for every other figure). At $t = 379$s the phase-space trajectory is moderately irregular and, as evidenced by the greater uniformity and overlap of the ovals, becomes more regular in the ensuing 40s. During this time, the estimated phase shift remains nearly constant, illustrating the stability of this measure and the robustness of the estimation strategy to breathing irregularities.

Bibliography

[1] Spiegel M F and Watson CS. Performance on frequency-discrimination tasks by musicians and nonmusicians. *The Journal of the Acoustical Society of America*, 76(6):1690–1695, December 1984.

[2] Sivian LJ and White SD. On minimum audible sound fields. *The Journal of the Acoustical Society of America*, 4(4):288–321, 1933.

[3] De Vries HL. Brownian movement and hearing. *Physica*, 14(1):48–60, 1948.

[4] Harris GG. Brownian motion in the cochlear partition. *The Journal of the Acoustical Society of America*, 44(1):176–186, 1968.

[5] Dalhoff E, Turcanu D, Zenner H-P, and Gummer AW. Distortion product otoacoustic emissions measured as vibration on the eardrum of human subjects. *Proceedings of the National Academy of Sciences*, 104(5):1546–1551, 2007.

[6] Knudsen VO. The sensibility of the ear to small differences of intensity and frequency. *Physical Review*, 21(1):84, 1923.

[7] Hudspeth AJ. Integrating the active process of hair cells with cochlear function. *Nature Reviews Neuroscience*, 15(9):600, 2014.

[8] Berryman M. Research photo gallery, 2017. [Online; accessed March 17, 2018, Photo credit: Leonardo Rodrigues Andrade].

[9] Fuchs PA and Glowatzki E. Synaptic studies inform the functional diversity of cochlear afferents. *Hearing research*, 330:18–25, 2015.

[10] Dallos P and Fay RR. *The cochlea*, volume 8. Springer Science & Business Media, 2012.

[11] Dallos P. The active cochlea. *Journal of Neuroscience*, 12(12):4575–4585, 1992.

[12] Fettiplace R and Hackney CM. The sensory and motor roles of auditory hair cells. *Nature Reviews Neuroscience*, 7(1):19, 2006.

[13] Ciganović N, Wolde-Kidan A, and Reichenbach T. Hair bundles of cochlear outer hair cells are shaped to minimize their fluid-dynamic resistance. *Scientific Reports*, 7(1):3609, 2017.

[14] Lim DJ. Cochlear anatomy related to cochlear micromechanics. a review. *The Journal of the Acoustical Society of America*, 67(5):1686–1695, 1980.

[15] Koeppen BM and Stanton BA. *Berne and Levy Physiology E-Book*. Elsevier Health Sciences, 2017.

[16] Hearing Aids Wizard. Human ear diagram. http://www.hearing-aids-wizard.com/human-ear-diagram.html, 2014.

[17] Von Békésy G and Wever EG. *Experiments in hearing*, volume 8. McGraw-Hill New York, 1960.

[18] Emadi G, Richter C-P, and Dallos P. Stiffness of the gerbil basilar membrane: radial and longitudinal variations. *Journal of neurophysiology*, 91(1):474–488, 2004.

[19] Teudt IU and Richter CP. Basilar membrane and tectorial membrane stiffness in the cba/caj mouse. *Journal of the Association for Research in Otolaryngology*, 15(5):675–694, 2014.

[20] Lim DJ. Functional structure of the organ of corti: a review. *Hearing research*, 22(1-3):117–146, 1986.

[21] Beurg M, Evans MG, Hackney CM, and Fettiplace R. A large-conductance calcium-selective mechanotransducer channel in mammalian cochlear hair cells. *Journal of Neuroscience*, 26(43):10992–11000, 2006.

[22] Furness DN, Mahendrasingam S, Ohashi M, Fettiplace R, and Hackney CM. The dimensions and composition of stereociliary rootlets in mammalian cochlear hair cells: comparison between high-and low-frequency cells and evidence for a connection to the lateral membrane. *Journal of Neuroscience*, 28(25):6342–6353, 2008.

[23] Patel SH, Salvi JD, Ó Maoiléidigh D, and Hudspeth AJ. Frequency-selective exocytosis by ribbon synapses of hair cells in the bullfrog's amphibian papilla. *Journal of Neuroscience*, 32(39):13433–13438, 2012.

[24] Patuzzi R and Robertson D. Tuning in the mammalian cochlea. *Physiological Reviews*, 68(4):1009–1082, 1988.

[25] Ruggero MA, Narayan SS, Temchin AN, and Recio A. Mechanical bases of frequency tuning and neural excitation at the base of the cochlea: comparison of basilar-membrane vibrations and auditory-nerve-fiber responses in chinchilla. *Proceedings of the National Academy of Sciences*, 97(22):11744–11750, 2000.

[26] Müller M, von Hünerbein K, Hoidis S, and Smolders JWT. A physiological place–frequency map of the cochlea in the cba/j mouse. *Hearing research*, 202(1-2):63–73, 2005.

[27] Kössl M and Vater M. The cochlear frequency map of the mustache bat, *Pteronotus parnellii*. *Journal of Comparative Physiology A*, 157(5):687–697, 1985.

[28] Müller M. Frequency representation in the rat cochlea. *Hearing research*, 51(2):247–254, 1991.

[29] Müller M, Wess F-P, and Bruns V. Cochlear place-frequency map in the marsupial *Monodelphis domestica*. *Hearing research*, 67(1-2):198–202, 1993.

[30] Coombs S, Braun CB, and Donovan B. The orienting response of lake michigan mottled sculpin is mediated by canal neuromasts. *Journal of Experimental Biology*, 204(2):337–348, 2001.

[31] Bleckmann H and Zelick R. Lateral line system of fish. *Integrative zoology*, 4(1):13–25, 2009.

[32] Brandt T. Vertigo: its multisensory syndromes. chapter 17, pages 285–289. Springer Science & Business Media, 2004.

[33] Ratcliff G and Nathan PW. Human nervous system, May 2017.

[34] Van Trump WJ and McHenry MJ. The morphology and mechanical sensitivity of lateral line receptors in zebrafish larvae (*Danio rerio*). *Journal of Experimental Biology*, 211(13):2105–2115, 2008.

[35] Tilney LG, Derosier DJ, and Mulroy MJ. The organization of actin filaments in the stereocilia of cochlear hair cells. *The Journal of cell biology*, 86(1):244–259, 1980.

[36] Flock Å, Flock B, and Murray E. Studies on the sensory hairs of receptor cells in the inner ear. *Acta oto-laryngologica*, 83(1-6):85–91, 1977.

[37] Kachar B, Parakkal M, Kurc M, Zhao Y-D, and Gillespie PG. High-resolution structure of hair-cell tip links. *Proceedings of the National Academy of Sciences*, 97(24):13336–13341, 2000.

[38] Siemens J, Lillo C, Dumont RA, Reynolds A, Williams DS, Gillespie PG, and Müller U. Cadherin 23 is a component of the tip link in hair-cell stereocilia. *Nature*, 428(6986):950, 2004.

[39] Ahmed ZM, Goodyear R, Riazuddin S, Lagziel A, Legan PK, Behra M, Burgess SM, Lilley KS, Wilcox ER, Riazuddin S, et al. The tip-link antigen, a protein associated with the transduction complex of sensory hair cells, is protocadherin-15. *Journal of Neuroscience*, 26(26):7022–7034, 2006.

[40] Kazmierczak P, Sakaguchi H, Tokita J, Wilson-Kubalek EM, Milligan RA, Müller U, and Kachar B. Cadherin 23 and protocadherin 15 interact to form tip-link filaments in sensory hair cells. *Nature*, 449(7158):87, 2007.

[41] Sotomayor M, Weihofen W A, Gaudet R, and Corey DP. Structure of a force-conveying cadherin bond essential for inner-ear mechanotransduction. *Nature*, 492(7427):128, 2012.

[42] Assad JA, Shepherd GMG, and Corey DP. Tip-link integrity and mechanical transduction in vertebrate hair cells. *Neuron*, 7(6):985–994, 1991.

[43] Beurg M, Fettiplace R, Nam J-H, and Ricci AJ. Localization of inner hair cell mechanotransducer channels using high-speed calcium imaging. *Nature neuroscience*, 12(5):553, 2009.

[44] Kozlov AS, Andor-Ardó D, and Hudspeth AJ. Anomalous brownian motion discloses viscoelasticity in the ear's mechanoelectrical-transduction apparatus. *Proceedings of the National Academy of Sciences*, 109(8):2896–2901, 2012.

[45] Ricci AJ, Wu YC, and Fettiplace R. The endogenous calcium buffer and the time course of transducer adaptation in auditory hair cells. *Journal of Neuroscience*, 18(20):8261–8277, 1998.

[46] Patuzzi R and Rajan R. Does electrical stimulation of the crossed olivo-cochlear bundle produce movement of the organ of corti? *Hearing research*, 45(1-2):15–32, 1990.

[47] Legan PK, Lukashkina VA, Goodyear RJ, Kössl M, Russell IJ, and Richardson GP. A targeted deletion in α-tectorin reveals that the tectorial membrane is required for the gain and timing of cochlear feedback. *Neuron*, 28(1):273–285, 2000.

[48] Hudspeth AJ. The hair cells of the inner ear. *Scientific American*, 248(1):54–65, 1983.

[49] Holton T and Hudspeth AJ. The transduction channel of hair cells from the bull-frog characterized by noise analysis. *The Journal of physiology*, 375(1):195–227, 1986.

[50] Markin VS and Hudspeth AJ. Gating-spring models of mechanoelectrical transduction by hair cells of the internal ear. *Annual review of biophysics and biomolecular structure*, 24(1):59–83, 1995.

[51] Nadrowski B, Martin P, and Jülicher F. Active hair-bundle motility harnesses noise to operate near an optimum of mechanosensitivity. *Proceedings of the*

National Academy of Sciences of the United States of America, 101(33):12195–12200, 2004.

[52] Martin P, Mehta AD, and Hudspeth AJ. Negative hair-bundle stiffness betrays a mechanism for mechanical amplification by the hair cell. *Proceedings of the national academy of sciences*, 97(22):12026–12031, 2000.

[53] Kozlov AS, Risler T, and Hudspeth AJ. Coherent motion of stereocilia assures the concerted gating of hair-cell transduction channels. *Nature neuroscience*, 10(1):87, 2007.

[54] Karavitaki KD and Corey DP. Sliding adhesion confers coherent motion to hair cell stereocilia and parallel gating to transduction channels. *Journal of Neuroscience*, 30(27):9051–9063, 2010.

[55] Kozlov AS, Baumgart J, Risler T, Versteegh CPC, and Hudspeth AJ. Forces between clustered stereocilia minimize friction in the ear on a subnanometre scale. *Nature*, 474(7351):376, 2011.

[56] LeBoeuf AC, Ó Maoiléidigh D, and Hudspeth AJ. Divalent counterions tether membrane-bound carbohydrates to promote the cohesion of auditory hair bundles. *Biophysical journal*, 101(6):1316–1325, 2011.

[57] Kozlov AS, Risler T, Hinterwirth AJ, and Hudspeth AJ. Relative stereociliary motion in a hair bundle opposes amplification at distortion frequencies. *The Journal of physiology*, 590(2):301–308, 2012.

[58] Kroese ABA, Das A, and Hudspeth AJ. Blockage of the transduction channels of hair cells in the bullfrog's sacculus by aminoglycoside antibiotics. *Hearing research*, 37(3):203–217, 1989.

[59] Marcotti W, Van Netten SM, and Kros CJ. The aminoglycoside antibiotic dihydrostreptomycin rapidly enters mouse outer hair cells through the mechano-electrical transducer channels. *The Journal of physiology*, 567(2):505–521, 2005.

[60] Howard J and Hudspeth AJ. Compliance of the hair bundle associated with gating of mechanoelectrical transduction channels in the bullfrog's saccular hair cell. *Neuron*, 1(3):189–199, 1988.

[61] Martin P, Bozovic D, Choe Y, and Hudspeth AJ. Spontaneous oscillation by hair bundles of the bullfrog's sacculus. *Journal of Neuroscience*, 23(11):4533–4548, 2003.

[62] Hudspeth AJ. Making an effort to listen: mechanical amplification in the ear. *Neuron*, 59(4):530–545, 2008.

[63] Iwasa KH and Ehrenstein G. Cooperative interaction as the physical basis of the negative stiffness in hair cell stereocilia. *The Journal of the Acoustical Society of America*, 111(5):2208–2212, 2002.

[64] Corey DP and Holt JR. Are tmcs the mechanotransduction channels of vertebrate hair cells? *Journal of Neuroscience*, 36(43):10921–10926, 2016.

[65] Gianoli F, Risler T, and Kozlov AS. Lipid bilayer mediates ion-channel cooperativity in a model of hair-cell mechanotransduction. *Proceedings of the National Academy of Sciences*, 114(51):E11010–E11019, 2017.

[66] Corey DP and Hudspeth AJ. Kinetics of the receptor current in bullfrog saccular hair cells. *Journal of Neuroscience*, 3(5):962–976, 1983.

[67] Corey DP and Hudspeth AJ. Analysis of the microphonic potential of the bullfrog's sacculus. *Journal of Neuroscience*, 3(5):942–961, 1983.

[68] Howard J and Hudspeth AJ. Mechanical relaxation of the hair bundle mediates adaptation in mechanoelectrical transduction by the bullfrog's saccular hair cell. *Proceedings of the National Academy of Sciences*, 84(9):3064–3068, 1987.

[69] Eatock RA, Corey DP, and Hudspeth AJ. Adaptation of mechanoelectrical transduction in hair cells of the bullfrog's sacculus. *Journal of Neuroscience*, 7(9):2821–2836, 1987.

[70] Holt JR, Corey DP, and Eatock RA. Mechanoelectrical transduction and adaptation in hair cells of the mouse utricle, a low-frequency vestibular organ. *Journal of Neuroscience*, 18(16):1–1, 1998.

[71] Kennedy HJ, Crawford AC, and Fettiplace R. Force generation by mammalian hair bundles supports a role in cochlear amplification. *Nature*, 433(7028):880, 2005.

[72] Gillespie PG, Wagner MC, and Hudspeth AJ. Identification of a 120 kd hair-bundle myosin located near stereociliary tips. *Neuron*, 11(4):581–594, 1993.

[73] Garcia JA, Yee AG, Gillespie PG, and Corey DP. Localization of myosin-iβ near both ends of tip links in frog saccular hair cells. *Journal of Neuroscience*, 18(21):8637–8647, 1998.

[74] Steyger PS, Gillespie PG, and Baird RA. Myosin iβ is located at tip link anchors in vestibular hair bundles. *Journal of Neuroscience*, 18(12):4603–4615, 1998.

[75] Holt JR, Gillespie SKH, Provance Jr DS, Shah K, Shokat KM, Corey DP, Mercer JA, and Gillespie PG. A chemical-genetic strategy implicates myosin-1c in adaptation by hair cells. *Cell*, 108(3):371–381, 2002.

[76] Gillespie PG and Cyr JL. Myosin-1c, the hair cell's adaptation motor. *Annu. Rev. Physiol.*, 66:521–545, 2004.

[77] Kros CJ, Marcotti W, Van Netten SM, Self TJ, Libby RT, Brown SDM, Richardson GP, and Steel KP. Reduced climbing and increased slipping adaptation in cochlear hair cells of mice with myo7a mutations. *Nature neuroscience*, 5(1):41, 2002.

[78] Grati M and Kachar B. Myosin viia and sans localization at stereocilia upper tip-link density implicates these usher syndrome proteins in mechanotransduction. *Proceedings of the National Academy of Sciences*, 108(28):11476–11481, 2011.

[79] Fettiplace R and Kim KX. The physiology of mechanoelectrical transduction channels in hearing. *Physiological reviews*, 94(3):951–986, 2014.

[80] Yu I-M, Planelles-Herrero VJ, Sourigues Y, Moussaoui D, Sirkia H, Kikuti C, Stroebel D, Titus MA, and Houdusse A. Myosin 7 and its adaptors link cadherins to actin. *Nature communications*, 8:15864, 2017.

[81] Hacohen N, Assad JA, Smith WJ, and Corey DP. Regulation of tension on hair-cell transduction channels: displacement and calcium dependence. *Journal of Neuroscience*, 9(11):3988–3997, 1989.

[82] Assad JA, Hacohen N, and Corey DP. Voltage dependence of adaptation and active bundle movement in bullfrog saccular hair cells. *Proceedings of the National Academy of Sciences*, 86(8):2918–2922, 1989.

[83] Rüsch A and Thurm U. Spontaneous and electrically induced movements of ampullary kinocilia and stereovilli. *Hearing research*, 48(3):247–263, 1990.

[84] Benser ME, Marquis RE, and Hudspeth AJ. Rapid, active hair bundle movements in hair cells from the bullfrog's sacculus. *Journal of Neuroscience*, 16(18):5629–5643, 1996.

[85] Martin P and Hudspeth AJ. Active hair-bundle movements can amplify a hair cell's response to oscillatory mechanical stimuli. *Proceedings of the National Academy of Sciences*, 96(25):14306–14311, 1999.

[86] Crawford AC and Fettiplace R. The mechanical properties of ciliary bundles of turtle cochlear hair cells. *The Journal of physiology*, 364(1):359–379, 1985.

[87] Roongthumskul Y, Fredrickson-Hemsing L, Kao A, and Bozovic D. Multiple-timescale dynamics underlying spontaneous oscillations of saccular hair bundles. *Biophysical journal*, 101(3):603–610, 2011.

[88] Meenderink SWF, Quiñones PM, and Bozovic D. Voltage-mediated control of spontaneous bundle oscillations in saccular hair cells. *Journal of Neuroscience*, 35(43):14457–14466, 2015.

[89] Salvi JD, Ó Maoiléidigh D, Fabella BA, Tobin M, and Hudspeth AJ. Control of a hair bundle's mechanosensory function by its mechanical load. *Proceedings of the National Academy of Sciences*, 112(9):E1000–E1009, 2015.

[90] Salvi JD, Ó Maoiléidigh D, and Hudspeth AJ. Identification of bifurcations from observations of noisy biological oscillators. *Biophysical journal*, 111(4):798–812, 2016.

[91] Faber J and Bozovic D. Chaotic dynamics of inner ear hair cells. *Scientific reports*, 8(1):3366, 2018.

[92] Ó Maoiléidigh D, Nicola EM, and Hudspeth AJ. The diverse effects of mechanical loading on active hair bundles. *Proceedings of the National Academy of Sciences*, 109(6):1943–1948, 2012.

[93] Ruggero MA and Rich NC. Application of a commercially-manufactured doppler-shift laser velocimeter to the measurement of basilar-membrane vibration. *Hearing research*, 51(2):215–230, 1991.

[94] Gold T. Hearing. ii. the physical basis of the action of the cochlea. *Proceedings of the Royal Society of London B: Biological Sciences*, 135(881):492–498, 1948.

[95] Kemp DT. Stimulated acoustic emissions from within the human auditory system. *The Journal of the Acoustical Society of America*, 64(5):1386–1391, 1978.

[96] Kemp DT. Evidence of mechanical nonlinearity and frequency selective wave amplification in the cochlea. *Archives of oto-rhino-laryngology*, 224(1-2):37–45, 1979.

[97] Zurek PM. Spontaneous narrowband acoustic signals emitted by human ears. *The Journal of the Acoustical Society of America*, 69(2):514–523, 1981.

[98] Burns EM, Strickland EA, Tubis A, and Jones K. Interactions among spontaneous otoacoustic emissions. i. distortion products and linked emissions. *Hearing research*, 16(3):271–278, 1984.

[99] Wit HP, Van Dijk P, and Segenhout JM. An electrical correlate of spontaneous otoacoustic emissions in a frog, a preliminary report. In *Cochlear Mechanisms: Structure, Function, and Models*, pages 341–347. Springer, 1989.

[100] Manley GA and Köppl C. Phylogenetic development of the cochlea and its innervation. *Current opinion in neurobiology*, 8(4):468–474, 1998.

[101] Manley GA and Gallo L. Otoacoustic emissions, hair cells, and myosin motors. *The Journal of the Acoustical Society of America*, 102(2):1049–1055, 1997.

[102] Vilfan A and Duke T. Frequency clustering in spontaneous otoacoustic emissions from a lizard's ear. *Biophysical journal*, 95(10):4622–4630, 2008.

[103] Gelfand M, Piro O, Magnasco MO, and Hudspeth AJ. Interactions between hair cells shape spontaneous otoacoustic emissions in a model of the tokay gecko's cochlea. *PLoS One*, 5(6):e11116, 2010.

[104] Brownell WE, Bader CR, Bertrand D, and De Ribaupierre Y. Evoked mechanical responses of isolated cochlear outer hair cells. *Science*, 227(4683):194–196, 1985.

[105] Zheng J, Shen W, He DZZ, Long KB, Madison LD, and Dallos P. Prestin is the motor protein of cochlear outer hair cells. *Nature*, 405(6783):149, 2000.

[106] Liberman MC, Gao J, He DZZ, Wu X, Jia S, and Zuo J. Prestin is required for electromotility of the outer hair cell and for the cochlear amplifier. *Nature*, 419(6904):300, 2002.

[107] Liberman MC, Zuo J, and Guinan Jr JJ. Otoacoustic emissions without somatic motility: can stereocilia mechanics drive the mammalian cochlea? *The Journal of the Acoustical Society of America*, 116(3):1649–1655, 2004.

[108] Ruggero MA, Rich MC, Recio A, Narayan SS, and Robles L. Basilar-membrane responses to tones at the base of the chinchilla cochlea. *The Journal of the Acoustical Society of America*, 101(4):2151–2163, 1997.

[109] Martin P and Hudspeth AJ. Compressive nonlinearity in the hair bundle's active response to mechanical stimulation. *Proceedings of the National Academy of Sciences*, 98(25):14386–14391, 2001.

[110] Strogatz S, Friedman M, Mallinckrodt AJ, and McKay S. Nonlinear dynamics and chaos: With applications to physics, biology, chemistry, and engineering. *Computers in Physics*, 8:532, 1994.

[111] Kuznetsov YA. Elements of applied bifurcation theory. *Applied mathematical sciences*, 1998.

[112] Rössler OE. An equation for continuous chaos. *Physics Letters A*, 57(5):397–398, 1976.

[113] VM Eguíluz, Ospeck M, Choe Y, Hudspeth AJ, and Magnasco MO. Essential nonlinearities in hearing. *Physical Review Letters*, 84(22):5232, 2000.

[114] Choe Y, Magnasco MO, and Hudspeth AJ. A model for amplification of hair-bundle motion by cyclical binding of ca2+ to mechanoelectrical-transduction channels. *Proceedings of the National Academy of Sciences*, 95(26):15321–15326, 1998.

[115] Camalet S, Duke T, Jülicher F, and Prost J. Auditory sensitivity provided by self-tuned critical oscillations of hair cells. *Proceedings of the National Academy of Sciences*, 97(7):3183–3188, 2000.

[116] Jülicher F. Mechanical oscillations at the cellular scale. *Comptes Rendus de l'Académie des Sciences-Series IV-Physics-Astrophysics*, 2(6):849–860, 2001.

[117] Vilfan A and Duke T. Two adaptation processes in auditory hair cells together can provide an active amplifier. *Biophysical journal*, 85(1):191–203, 2003.

[118] Moreau L and Sontag E. Balancing at the border of instability. *Physical Review E*, 68(2):020901, 2003.

[119] Moreau L, Sontag E, and Arcak M. Feedback tuning of bifurcations. *Systems & control letters*, 50(3):229–239, 2003.

[120] Balakrishnan J. Self-tuning to the hopf bifurcation in fluctuating systems. *Journal of Physics A: Mathematical and General*, 38(8):1627, 2005.

[121] Ó Maoiléidigh D and Jülicher F. The interplay between active hair bundle motility and electromotility in the cochlea. *The Journal of the Acoustical Society of America*, 128(3):1175–1190, 2010.

[122] Blackwell DL, Lucas JW, and Clarke TC. Summary health statistics for us adults: national health interview survey, 2012. *Vital and health statistics. Series 10, Data from the National Health Survey*, (260):1–161, 2014.

[123] Daniel E. Noise and hearing loss: a review. *Journal of School Health*, 77(5):225–231, 2007.

[124] Milewski AR, Ó Maoiléidigh D, Salvi JD, and Hudspeth AJ. Homeostatic enhancement of sensory transduction. *Proceedings of the National Academy of Sciences*, page 201706242, 2017.

[125] Shlomovitz R, Fredrickson-Hemsing L, Kao A, Meenderink SWF, Bruinsma R, and Bozovic D. Low frequency entrainment of oscillatory bursts in hair cells. *Biophysical journal*, 104(8):1661–1669, 2013.

[126] Hartigan JA and Hartigan PM. The dip test of unimodality. *The Annals of Statistics*, pages 70–84, 1985.

[127] Shepherd GM and Corey David P. The extent of adaptation in bullfrog saccular hair cells. *Journal of Neuroscience*, 14(10):6217–6229, 1994.

[128] Corns LF, Johnson SL, Kros CJ, and Marcotti W. Calcium entry into stereocilia drives adaptation of the mechanoelectrical transducer current of mammalian cochlear hair cells. *Proceedings of the National Academy of Sciences*, 111(41):14918–14923, 2014.

[129] Robles L and Ruggero MA. Mechanics of the mammalian cochlea. *Physiological reviews*, 81(3):1305–1352, 2001.

[130] Edge RM, Evans BN, Pearce M, Richter C-P, Hu X, and Dallos P. Morphology of the unfixed cochlea. *Hearing research*, 124(1-2):1–16, 1998.

[131] Cheatham MA, Ahmad A, Zhou Y, Goodyear RJ, Dallos P, and Richardson GP. Increased spontaneous otoacoustic emissions in mice with a detached tectorial membrane. *Journal of the Association for Research in Otolaryngology*, 17(2):81–88, 2016.

[132] Gale JE, Meyers JR, Periasamy A, and Corwin T. Survival of bundleless hair cells and subsequent bundle replacement in the bullfrog's saccule. *Developmental Neurobiology*, 50(2):81–92, 2002.

[133] Azimzadeh JB and Salvi JD. Physiological preparation of hair cells from the sacculus of the american bullfrog (*Rana catesbeiana*). *Journal of visualized experiments: JoVE*, (121), 2017.

[134] Hirono M, Denis CS, Richardson GP, and Gillespie PG. Hair cells require phosphatidylinositol 4, 5-bisphosphate for mechanical transduction and adaptation. *Neuron*, 44(2):309–320, 2004.

[135] Lumpkin EA and Hudspeth AJ. Regulation of free ca2+ concentration in hair-cell stereocilia. *Journal of Neuroscience*, 18(16):6300–6318, 1998.

[136] Yamoah EN, Lumpkin EA, Dumont RA, Smith PJS, Hudspeth AJ, and Gillespie PG. Plasma membrane ca2+-atpase extrudes ca2+ from hair cell stereocilia. *Journal of Neuroscience*, 18(2):610–624, 1998.

[137] Vollrath MA and Eatock RA. Time course and extent of mechanotransducer adaptation in mouse utricular hair cells: comparison with frog saccular hair cells. *Journal of neurophysiology*, 90(4):2676–2689, 2003.

[138] Pickles JO. An introduction to the physiology of hearing. 2008.

[139] Goutman JD, Elgoyhen AB, and Gómez-Casati ME. Cochlear hair cells: The sound-sensing machines. *FEBS letters*, 589(22):3354–3361, 2015.

[140] Guinan Jr JJ. Olivocochlear efferents: anatomy, physiology, function, and the measurement of efferent effects in humans. *Ear and hearing*, 27(6):589–607, 2006.

[141] Cooper NP and Guinan Jr JJ. Medial olivocochlear efferent effects on basilar membrane responses to sound. In *Auditory Mechanisms: Processes And Models: (With CD-ROM)*, pages 86–92. World Scientific, 2006.

[142] Brown MC and Nuttall AL. Efferent control of cochlear inner hair cell responses in the guinea-pig. *The Journal of Physiology*, 354(1):625–646, 1984.

[143] Lindner B, Dierkes K, and Jülicher F. Local exponents of nonlinear compression in periodically driven noisy oscillators. *Physical review letters*, 103(25):250601, 2009.

[144] Arnold L. *Random dynamical systems*. Springer Science & Business Media, 2013.

[145] Kao A, Meenderink SWF, and Bozovic D. Mechanical overstimulation of hair bundles: suppression and recovery of active motility. *PLoS One*, 8(3):e58143, 2013.

[146] d'Eysmond T, De Simone A, and Naef F. Analysis of precision in chemical oscillators: implications for circadian clocks. *Physical biology*, 10(5):056005, 2013.

[147] Woller A, Gonze D, and Erneux T. The goodwin model revisited: Hopf bifurcation, limit-cycle, and periodic entrainment. *Physical biology*, 11(4):045002, 2014.

[148] Qu Z, Xie L-H, Olcese R, Karagueuzian HS, Chen P-S, Garfinkel A, and Weiss JN. Early afterdepolarizations in cardiac myocytes: beyond reduced repolarization reserve. *Cardiovascular research*, 99(1):6–15, 2013.

[149] Sturis J, Knudsen C, O'Meara NM, Thomsen JS, Mosekilde E, Van Cauter E, and Polonsky KS. Phase-locking regions in a forced model of slow insulin and glucose oscillations. *Chaos: An Interdisciplinary Journal of Nonlinear Science*, 5(1):193–199, 1995.

[150] Dubin K, Milewski AR, Shin J, and Kalman TP. Medical students' attitudes toward torture, revisited. *Health and human rights*, 19(2):265, 2017.